



**HAL**  
open science

# Comprehension of cellulose depolymerisation mechanisms induced by iron ions

Alice Gimat

► **To cite this version:**

Alice Gimat. Comprehension of cellulose depolymerisation mechanisms induced by iron ions. Material chemistry. Université Pierre et Marie Curie - Paris VI, 2016. English. NNT : 2016PA066579 . tel-01654429

**HAL Id: tel-01654429**

**<https://theses.hal.science/tel-01654429>**

Submitted on 3 Dec 2017

**HAL** is a multi-disciplinary open access archive for the deposit and dissemination of scientific research documents, whether they are published or not. The documents may come from teaching and research institutions in France or abroad, or from public or private research centers.

L'archive ouverte pluridisciplinaire **HAL**, est destinée au dépôt et à la diffusion de documents scientifiques de niveau recherche, publiés ou non, émanant des établissements d'enseignement et de recherche français ou étrangers, des laboratoires publics ou privés.

**THÈSE DE DOCTORAT  
DE L'UNIVERSITÉ PIERRE ET MARIE CURIE**

**Spécialité : Chimie**

**École doctorale : ED397, Physique et chimie des matériaux**

réalisée

**au Laboratoire de Réactivité de Surface (LRS) et au Centre de Recherche  
sur la Conservation (CRC)**

présentée par

**Alice GIMAT**

pour obtenir le grade de :

**DOCTEUR DE L'UNIVERSITÉ PIERRE ET MARIE CURIE**

Sujet de la thèse :

**Comprehension of cellulose depolymerisation mechanisms  
induced by iron ions**

soutenue le 1 décembre 2016

devant le jury composé de :

<b>Pr.</b>	<b>Philippe REFAIT</b>	<b>Rapporteur</b>
<b>Pr.</b>	<b>Antje POTTHAST</b>	<b>Rapporteur</b>
<b>Dr.</b>	<b>Thibaud CORADIN</b>	<b>Président du jury</b>
<b>Dr.</b>	<b>Ira RABIN</b>	<b>Examineur</b>
<b>Pr.</b>	<b>Didier GOURIER</b>	<b>Examineur</b>
<b>Dr.</b>	<b>Pascale MASSIANI</b>	<b>Directeur de thèse</b>
<b>Pr.</b>	<b>Véronique ROUCHON</b>	<b>Directeur de thèse</b>



# Contents

<b>Abbreviations</b>	<b>v</b>
<b>Acknowledgements</b>	<b>ix</b>
<b>Introduction</b>	<b>1</b>
<b>I Literature review</b>	<b>5</b>
I.1 Paper . . . . .	5
I.1.1 Historical context . . . . .	5
I.1.2 Composition of european rag papers . . . . .	5
I.1.3 Paper fibers organisation from molecular level to macrostructure . .	6
I.1.4 Paper porosity and water diffusion . . . . .	6
I.1.5 Gelatin sizing . . . . .	9
I.2 Iron gall inks . . . . .	10
I.2.1 Historical context . . . . .	10
I.2.2 What are iron gall inks made of? . . . . .	11
I.2.3 The color of ink . . . . .	12
I.2.4 Stability of the complex/precipitate . . . . .	14
I.3 Iron gall inks corrosion . . . . .	15
I.3.1 Overview . . . . .	15
I.3.2 Acid-catalyzed hydrolysis of cellulose . . . . .	17
I.3.3 Oxidation mechanisms . . . . .	18
I.3.4 Impact of several parameters on IGI corrosion . . . . .	23
I.4 PhD thesis outline . . . . .	25
<b>II Investigation of reactive oxygen species (ROS)</b>	<b>27</b>
II.1 Introduction . . . . .	27
II.2 Methods . . . . .	29
II.2.1 Sample preparation: From paper impregnation to liquid samples . .	29
II.2.2 Electron spin resonance spectroscopy coupled with spin-trapping . .	30
II.2.3 Determination of hydroxyl radicals by RP-HPLC . . . . .	34
II.2.4 Iron quantification by UV-visible spectroscopy . . . . .	36
II.3 Results and discussion . . . . .	36
II.3.1 Spectroscopic signatures of spin traps adducts . . . . .	36
II.3.2 Conditions for spin traps adducts detection . . . . .	39
II.3.3 Effect of paper ageing on DMPO-formate adducts concentrations and leaching phenomena . . . . .	40
II.3.4 From leached to model solutions . . . . .	44

II.3.5	Influence of pH and iron(II) concentration on TEMPOL . . . . .	46
II.3.6	Roles of oxidation processes and of iron(II) in radicals production . . . . .	48
II.3.7	Reactive oxygen species (ROS) involved in the DMPO-formate adduct formation and impact on cellulose depolymerization . . . . .	49
II.3.8	Does hydroxyl radicals have an impact on cellulose depolymerization? . . . . .	51
II.4	Conclusion . . . . .	51
<b>III</b>	<b>Glycosidic bond scission</b>	<b>53</b>
III.1	Depolymerisation of inked papers: a kinetic study . . . . .	53
III.1.1	Evaluation of the degree of polymerization ( <i>DP</i> ) by viscosimetry . . . . .	53
III.1.2	Ekenstam model and Arrhenius law . . . . .	54
III.1.3	Inked paper model: conditions of experiments . . . . .	55
III.1.4	Main outcomes of the kinetic study paper model . . . . .	56
III.2	Degradation of cellobiose in solid state . . . . .	57
III.2.1	Bibliographic recalls . . . . .	57
III.2.2	Experimental aspects . . . . .	58
III.2.3	Results . . . . .	59
III.3	Degradation of cellobiose in solution . . . . .	62
III.3.1	Experimental factorial design . . . . .	62
III.3.2	Sample preparation . . . . .	64
III.3.3	Analytical techniques . . . . .	66
III.3.4	Influence of pH, iron and oxygen on cellobiose conversion into glucose . . . . .	69
III.3.5	Investigation of degradation products . . . . .	74
III.3.6	Analysis of the results with experimental design . . . . .	81
III.4	Conclusion . . . . .	81
<b>IV</b>	<b>The distribution of ink components in paper fibers</b>	<b>83</b>
IV.1	Introduction . . . . .	83
IV.2	Material . . . . .	85
IV.2.1	Preparation of fiber samples . . . . .	85
IV.2.2	Preparation of model compounds for STXM . . . . .	87
IV.2.3	Ultra-thin cross-sections preparation . . . . .	89
IV.2.4	Diversity and quality of cross-sections. . . . .	90
IV.3	Analytical techniques . . . . .	94
IV.3.1	Atomic force microscopy coupled with infrared spectroscopy . . . . .	94
IV.3.2	Scanning transmission X-ray microscopy (STXM) . . . . .	95
IV.4	Model compounds analysis and protocol optimization . . . . .	99
IV.4.1	XANES signatures of model compounds . . . . .	99
IV.4.2	Influence of X-ray beam on iron oxidation state . . . . .	103
IV.5	Components penetration into fibers . . . . .	106
IV.5.1	Gelatin penetration into fibers . . . . .	106
IV.5.2	Ink penetration into unsized fibers . . . . .	112
IV.5.3	Ink penetration into sized fibers . . . . .	117
IV.5.4	The impact of a gelatin top layer on ink distribution . . . . .	121
IV.6	Conclusion . . . . .	125
<b>Conclusion</b>		<b>129</b>

---

<b>Appendices</b>	<b>131</b>
<b>A Carbonyl content analysis</b>	<b>133</b>
<b>B ESR spectroscopy</b>	<b>139</b>
B.1 ESR principle . . . . .	139
B.2 Hyperfine coupling . . . . .	140
B.3 Spin-trapping artefacts . . . . .	141
B.4 Complementary tests to investigate hydroxyl radicals . . . . .	142
B.4.1 Tests using POBN . . . . .	142
B.4.2 Investigation of DMPO hydroxylamine formation without scavenger	144
<b>C Iron dosage by UV-vis spectroscopy</b>	<b>145</b>
C.1 State of the art . . . . .	145
C.2 Iron(II) quantification in solution . . . . .	148
C.3 Iron(III) quantification . . . . .	149
<b>D Iron chemistry in solution</b>	<b>151</b>
D.1 Pourbaix diagram . . . . .	151
D.2 Iron(II) oxidation . . . . .	151
<b>E HPLC-TPP method</b>	<b>155</b>
E.1 Calibration . . . . .	155
E.2 Test of ink component interferences . . . . .	155
<b>F HTPA calibration by HPLC</b>	<b>157</b>
<b>G SECM</b>	<b>159</b>
G.1 Principle of scanning electro-chemical microscopy . . . . .	159
G.1.1 Substrate and ultra micro electrode preparation . . . . .	159
G.1.2 Principle of the experiment . . . . .	160
G.2 Test of degradation of a organic layer by localized formation of hydroxyl radicals . . . . .	161
G.3 Test of degradation of a fiber by localized formation of hydroxyl radicals . . . . .	162
<b>H Paper depolymerisation: a kinetic study</b>	<b>165</b>
<b>I Sugar calibration by electrophoresis</b>	<b>175</b>
<b>J Test of iron elimination with cation exchange resin</b>	<b>177</b>
J.1 Estimation of the amount of resin needed . . . . .	177
J.2 Test in batch mode . . . . .	177
<b>K STXM</b>	<b>179</b>
K.1 Conversion of exposure times to dose . . . . .	179
K.2 Critical doses estimation . . . . .	182
K.3 Parameters for stack acquisition . . . . .	183
K.3.1 Iron edge . . . . .	183
K.3.2 Carbon edge . . . . .	183
K.3.3 Nitrogen edge . . . . .	183

---

<b>Résumé</b>	<b>185</b>
<b>Bibliography</b>	<b>195</b>
<b>List of Figures</b>	<b>217</b>
<b>List of Tables</b>	<b>225</b>

# Abbreviations

ABEE	4-aminobenzoic acid ethyl ester, also called benzocaine
AD	anno domini
AFM	atomic force microscopy
ATR	attenuated total reflectance
BET	Brunauer-Emmett-Teller
CTAB	Cetyltrimethylammonium bromide
DMPO	5,5-Dimethyl-1-Pyrroline-N-Oxide
DMSO	dimethyl sulfoxide
EOF	electro-osmotic flux
ERO	Espèce réactive de l'oxygène
ESR	electron spin resonance
FIB	focussed ion beam
FLD	fluorescence detector
FT	Fourier transform
HPLC	high performance liquid chromatography
HTPA	hydroxyterephthalic acid
IR	infrared

LINAC	linear accelerator
MNP	1-methyl-1-nitrosopropane
NHE	normal hydrogen electrode
<i>O.D.</i>	optical density
OSA	order sorting aperture
PBN	$\alpha$ -(phenyl)-N-t-butylnitron
PDA	photodiode array detector
PDAc	2,6-pyridinedicarboxylic acid
PIXE	particule-induced X-ray emission
POBN	$\alpha$ -(4-pyridyl-1-oxide)-N-tert-butylnitron
PTFE	polytetrafluoroethylene
RGB	red green blue
ROS	reactive oxygen species
RP	reverse phase
RPE	Résonance paramagnétique électronique
RP-HPLC	reverse phase liquid chromatography
SEM	scanning electron microscopy
SP	spin-trap
STXM	scanning transmission X-ray microscopy
TEM	transmission electron microscopy
TEMPOL	4-hydroxy-2,2,6,6-tetramethylpiperidin-1-oxyl

TPA	terephthalic acid
UV	ultra-violet
XANES	X-ray absorption near edge structure



# Acknowledgements

This work was carried out between 2013 and 2016, between the center of research on conservation (Centre de recherche sur la conservation des collections, CRCC), attached to the natural history museum of Paris (Museum national d'Histoire naturelle, MNHN) and the LRS, laboratoire de réactivité de surface, attached to the university Pierre et Marie Curie (UPMC, Paris 6). Working between these two different entities was rewarding, both on a scientific and cultural point of view and I am glad these was made possible in the framework of the LabeX Matisse, which offered financial support for this thesis.

This PhD thesis would not have been possible without the help, advices, or support of a lot of people.

First of all, I would like to express my deep gratitude to my promoters and advisors Pr. Véronique Rouchon and Dr. Pascale Massiani, who trusted me with this work. They both made them available to discuss and shared with me the quality of their reflections, their scientific rigor and skills.

I would like to thank also Anne-Laurence Dupont, who gave me precious advices, especially regarding separative techniques and initiated me to capillary electrophoresis.

Thanks to all the eminent scientists who accepted to read this manuscript and be part of my jury.

I would like to thank Helène Pernot and Bertrand Lavédrine for welcoming me in their respective laboratory during this PhD.

A special thank to Valeryia Kasneryck, who started this work during her internship.

I am also deeply grateful to all the people that helped me carrying out with my experiments:

- Oulfa Belhadj (CRCC), for her help with viscometry and SEM;
- Anne Michelin (CRCC), for her advice with STXM and her help during the shifts on the SM Beamline at CLS;
- Jiang Wang, from the SM Beamline at CLS, who gave presious advice and helped with data treatment;
- Frédéric Averseng, Jeanine Fournier and Christophe Calers (LRS) for their technical help with ESR spectroscopy;
- Jérémy Henin, Matthieu Thoury (IPANEMA) and Shakib Djediat (MNHN), for their help in cross-section preparation with ultramicrotomy;
- Ariane Deniset and Alexandre Dazzi (LCP, Orsay University), for accepting my uncommon samples and initiating me to AFM-IR technique;
- David Troadec (IEMN, Lille university) for the cross-section preparation by FIB;

- Vincent Losinho (LRS), for his advice regarding pressure regulator and gas pipes for my experiment;
- Mohamed Selmane (LCMCP), for his advice with DRX;
- Sandra Casale (LRS), for the SEM analysis at LRS;
- Jean-Marc Noel, Jérôme Médard, Jean Pinson and Catherine Combellas, for welcoming me at ITODYS laboratory (University Paris 7), and a particular thanks to JMN who always cheered me up with his enthusiasm and had the patience to teach me SECM and encourage me.
- Arul Marie, for the tests in mass spectrometry on the MNHN platform;
- Audrey Soukhavong, for her kindness and her help during her one-month internship, which transformed into great friendship;
- Sabrina Paris (CRCC), for helping with HPLC leaks but foremost for her friendship and support... and the time travel into Middle Ages.

I thank all the colleagues from both laboratories for their sympathies and especially:

- Guillaume Laugel, Frédérique Fournier and Julien Reboul for the jokes and laughs in the office we shared in Ivry;
- Laurie Ballerini, Denis Réau for their support, friendship and also for the endless board games in company of Camille and Florian L.
- Karam, Olf, Marie-Nour, Noemie, Mariame, Achraf, Maya, other PhD students and Laetitia who all gave the atmosphere to the LRS first floor in Ivry.

I would also like to thank Guillaume B., for his perseverance in teaching me L<sup>A</sup>T<sub>E</sub>X; my family, for their support; and last but not least, Florian, for his support during the end of my PhD, his jokes to relax me and his love.

# Introduction

Heritage artefacts have crossed the ages and a large number of them lay now in public or private collections. They are, however, not always in good condition as the materials they are made of may degrade with time. These degradations are in the focus of Heritage science research. Understanding the decay mechanisms of the materials gives indeed important clues to propose preventive and curative preservation strategies that take into account the specificity and the constraints of heritage items.

Regarding more particularly graphic documents, the case of iron gall ink bearing papers remains a challenging issue for conservators. Iron gall inks were used for writing and, to a lesser extent, for drawing till the 20<sup>th</sup> century. Plenty of recipes exist that mostly include three main ingredients: gall nuts extracts, iron(II) sulfate and gum arabic. Gall nuts extracts are rich in polyphenol, and more specifically in gallic acid. In aerated environment, gallic acid reacts with iron(II) leading to the formation of a deep blue iron(III)-gallate precipitate. Gum Arabic is added as a binder to create a suspension and make the ink suitable for writing.

Under certain circumstances, iron gall inks provoke degradation of the paper sheet, a phenomenon referred to as iron gall ink corrosion. It starts with the migration of some ink components into the paper sheet, either at the moment of writing because the paper is insufficiently sized, or later on because of inappropriate exposure to high humidity conditions. Then chemical reactions take place, provoking a degradation of the paper behind and around the ink line. It turns brown, becomes brittle and cannot bear any bending. When the sheet is handled without specific care, cracks appear in the ink line, leading sometimes to holes formation under repetitive handling.

The degradation of paper is attributable to the alteration of its main constituent, cellulose, that is also the major structural component of the plants used as raw materials. It is a polysaccharide made of anhydroglucose units, assembled through  $\beta(1-4)$  linkage, also called “glycosidic bond”. As a result cellobiose (a dimer of glucose) is the building block of cellulose. Upon degradation, cellulose depolymerizes, resulting, at a macroscopic scale, in a loss of mechanical properties of the paper. Regarding the particular case of iron gall ink corrosion, there is still a controversial issue about the main mechanism involved in this depolymerization. Two main mechanisms are pointed out: acid hydrolysis due to ink acidity and radical oxidation.

Considering degradation of blank papers (without any interference with iron based products), a consensus has been reached on the fact that acid-catalysed hydrolysis is the main pathway of acidic paper degradation below 100 °C while oxidation prevails over 100 °C. It is also often considered that the predominant degradation route in dark at mild environmental conditions is that of hydrolysis, and that potential oxidation mechanism could play merely a synergistic role.

In the case of iron gall inks, the presence of iron may substantially change this scenario as iron(II) is known to promote the formation of highly reactive hydroxyl radicals through Fenton reactions. These radicals, often put forward as one of the major cause of iron gall ink corrosion, can provoke radical chain reactions, leading to chain scissions. The predominance of oxidative mechanism was evidenced on deacidified iron gall ink impregnated papers in mild alkaline conditions but not in acidic conditions. Moreover, in a previous study conducted in the *Centre de Recherche sur la Conservation*(CRC) it was shown that the combined presence of iron and oxygen had a strong impact on paper degradation that was perceptible within few days at ambient temperature. These observations directly questioned the predominance of hydrolysis over oxidation in the case of iron gall ink corrosion. This also opened the route to the present thesis work which aims at getting a better understanding of the main degradation mechanism of cellulose in the presence of iron.

The first chapter of this manuscript corresponds to a literature review tackling the composition of paper, of iron gall inks, and the possible degradation mechanisms. Chapters II,III and IV are then successively dedicated to the three complementary approaches developed along the work to investigate iron-induced depolymerization of cellulose: both chapters II and III concern chemical aspects of the degradation, namely the formation of radicals (chapter II) and bond breaking reactions (chapter III), while chapter IV is dealing with the distribution of ink components in paper fibers. Each of these three chapters details the specific methodologies used and discusses the results obtained.

The first approach, described in Chapter II, more precisely targeted the identification of reactive oxygen species (ROS) potentially involved in iron gall ink corrosion. It was motivated by the previously observed impact of oxygen on depolymerization. Hydroxyl radicals were of particular interest since they are often put forward as main vector of degradation, but the study included as well all other types of ROS potentially present. For the experiments, model Whatman papers were impregnated and stored during several months at 23 °C and 50 % relative humidity. ROS in the sample systems were then analyzed by spin trapping coupled with electron spin resonance (ESR) and high performance liquid chromatography (HPLC). In this part, iron leaching was also carefully analyzed since it was shown to be an important factor to consider for correct understanding of the results.

The second approach (chapter III) consisted first in a kinetic study of the degradation of paper samples in which the depolymerization was monitored by viscosity measurement and the loss of mechanical properties by zero-span measurements. The validity of the Arrhenius model was tested taking advantage of the fact that depolymerization was measurable at ambient temperature. Following these experiments, cellobiose was chosen as a model molecule to study the effect of different parameters (iron, acidity, oxygen) on the degradation. Cellobiose presents the great advantages to be a simpler molecule than cellulose, to be water soluble (which guarantees a good interaction with ink components) and to include a glycosidic bond. Cleavage of this bond leads to the formation of two glucose units and this process could be quantitatively monitored by capillary electrophoresis.

The last approach, detailed in chapter IV, investigated the distribution of ink ingredients inside a paper fiber. These physical aspects are believed to be key parameters to understand possible interactions between iron gall inks and paper. In order to be closer to original manuscripts, a rag paper prepared according to a traditional process was chosen. Some tests were performed by atomic force microscopy coupled with infrared spectroscopy

(AFM-IR) to evaluate the potentiality of this technique to provide relevant information. In addition, Scanning Transmission X-ray Microscopy (STXM) at the iron L-Edge was investigated as it allows mapping at a nano-scale (resolution approx. 30 nm) not only the distribution of iron but also its speciation. The measurements were performed at the 10ID-1 line of the Canadian Light Source. Because papers are also sized, a specific attention was also paid to the distribution of gelatin around or in paper fibers. To this end, mappings were recorded as well at the carbon and nitrogen K-Edges.

Several Appendixes provided at the end of the document complete the experimental descriptions. They give calibration curves of the analytical tools reported in this thesis, along with the analysis parameters. They also present and some additional experiments that were attempted. These last parts are preceded by a short “conclusion and perspective” section that summarizes the main contribution of this work in terms of better chemical comprehension of the phenomena taking place in paper fibers in the presence of iron.



# Chapter I

## Literature review

### I.1 Paper

#### I.1.1 Historical context

Paper was first produced in China. Its making dates back to a few centuries before Christ as attested by recent archeological excavations linked to the Han dynasties [1]. It passed over the islamic world (Middle East and North Africa) in the Middle Ages (since around the 8<sup>th</sup> century). Then it was traded in Italy and Spain (via North Africa) around the 11<sup>th</sup> century. European paper making started a few centuries later, mostly at the instigation of crusaders on their return from Middle East : paper mills established in the 13<sup>th</sup> century [2] in Italy, Fabriano being one of the most famous example. In France, papermaking started in the mid 14<sup>th</sup> century.

Paper was first considered as a cheap substitute for parchment. This new and easy-to-make material however progressively spread up to face the needs of the society, in particular those issued from the emerging printing activity of the 15<sup>th</sup> century. At the 17<sup>th</sup> century, paper making was a flourishing industry, which processes are fully described in the Diderot and d'Alembert Encyclopedia. In first approximation, European papermaking know-hows remained more or less similar from the 15<sup>th</sup> to the 18<sup>th</sup> century (gelatin sized rag papers), then the processes significantly changed in the first part of the 19<sup>th</sup> century thanks to several technological inventions (introduction of the papermaking machine by the French Louis-Nicolas Robert, introduction of new sizing agents, introduction of wood as raw material, etc.) [2].

#### I.1.2 Composition of european rag papers

European rag papers are made with old cotton, linen or hemp rags that are worked on so as to obtain a network of individual fibers. A few percent of mineral charges (mostly calcium carbonates) are usually added to the fibrous network to whiten the paper and make it more stable through ageing.

Paper fibers mostly contain cellulose, with some proportions of hemi-cellulose and lignin (TAB. I.1). These compounds are highly hydrophilic, meaning that a paper exclusively composed of these fibers would be permeable to any kind of water based ink. This is the reason why papers are also commonly sized, a process to make them less permeable and thus suitable for writing. Gelatin was largely used for this purpose from the beginning of European papermaking until the 19<sup>th</sup> century [3]. As attested by measurements on 15<sup>th</sup>

Vegetal	Cellulose content	Hemicellulose content	Lignin content
Cotton	88 – 94%	2 – 4%	
Flax	71 %	18.6 – 20.6%	2.2 %
Hemp	72 %	10 %	3 %
Wood	30 – 64%	20 – 40%	14 – 37%

TAB. I.1 – Main composition of cotton, flax, hemp and wood [7].

century papers, light element sulphate salts (alum) were also added by papermakers [4, 5] in order to control the gelatin viscosity and the eventual biological contamination (mold and bacteria) of gelatin and to prevent its dissolution during the application of ink [6].

### I.1.3 Paper fibers organisation from molecular level to macrostructure

On a molecular level, cellulose is a linear polymer made of anhydroglucose units linked to each other by an osidic bond between carbon  $C_1$  and  $C_4$  of the pyranose ring (FIG. I.1). In this thesis, the position of carbon atoms of the pyranose ring will be numbered  $C_x$  and oxygen atoms of cellulose attached to the carbon  $C_x$  will be numbered  $O_x$ . The repetition unit made of two anhydroglucose units is named cellobiose [8, 9].

Cellulose has a high native degree of polymerization (DP between 5000-15000) and its structured network involves two types of hydrogen bonding [10, 11]: firstly, intramolecular hydrogen bondings between i)  $O_6$  and  $O_2H$  or ii)  $O_3H$  and cyclic O (FIG. I.2, blue dotted lines); secondly, intermolecular hydrogen bondings through  $O_3$  and  $O_6H$  (FIG. I.2, red dotted lines).

These bondings act in combination with van der Waals forces and dipole interactions (orange arrows) and favor the cellulose arrangement in layers (FIG. I.2) leading to a compact structure of elementary fibrils composed of amorphous and crystalline parts (FIG. I.3). These elementary fibrils aggregate and form microfibrils (width of 10 – 30 nm) leading to macrofibrils (width of 100 – 400 nm). These fibrils are structured in different cell walls layers of the vegetal fibers (FIG. I.4A) and these latter are matted together in a paper sheet (FIG. I.4B).

### I.1.4 Paper porosity and water diffusion

The ability of raw paper fibers to adsorb gas is negligible (specific area of  $0.45 \text{ m}^2 \cdot \text{g}^{-1}$  to  $1.3 \text{ m}^2 \cdot \text{g}^{-1}$ ), as attested by some previous works (see TAB. I.2). But these fibers are highly hydrophilic and able to absorb water due to the hydroxylic groups present in

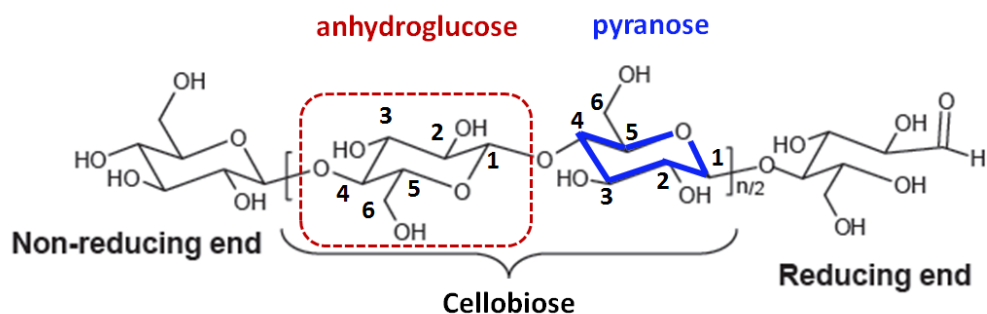


FIG. I.1 – 3-D representation of cellulose macromolecule.

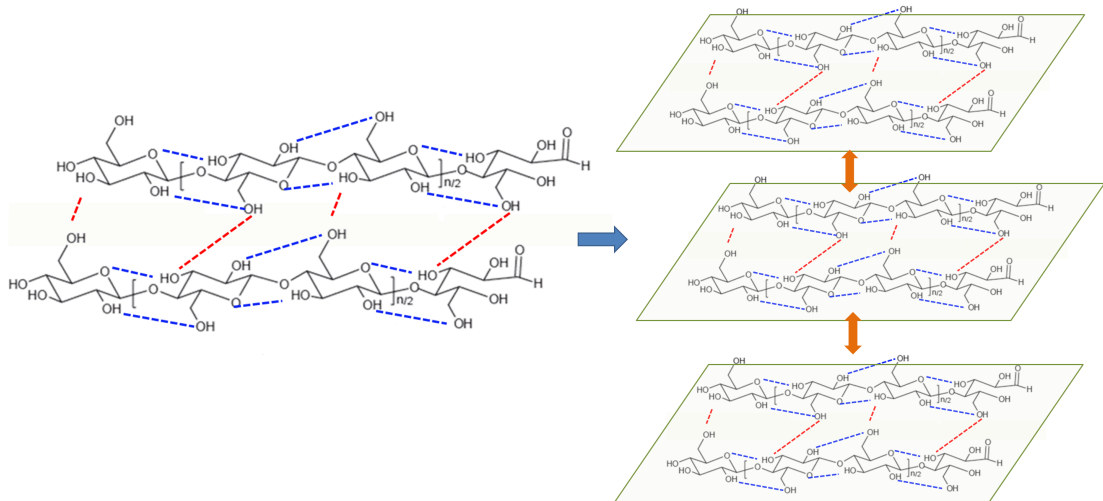


FIG. I.2 – Cellulose arrangement in parallel layer.

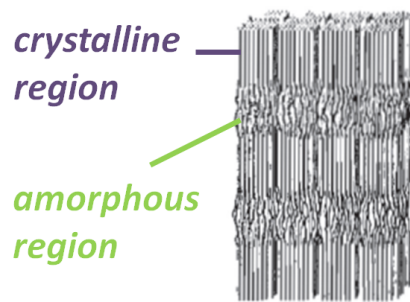


FIG. I.3 – Cellulose arrangement in crystalline and amorphous regions.

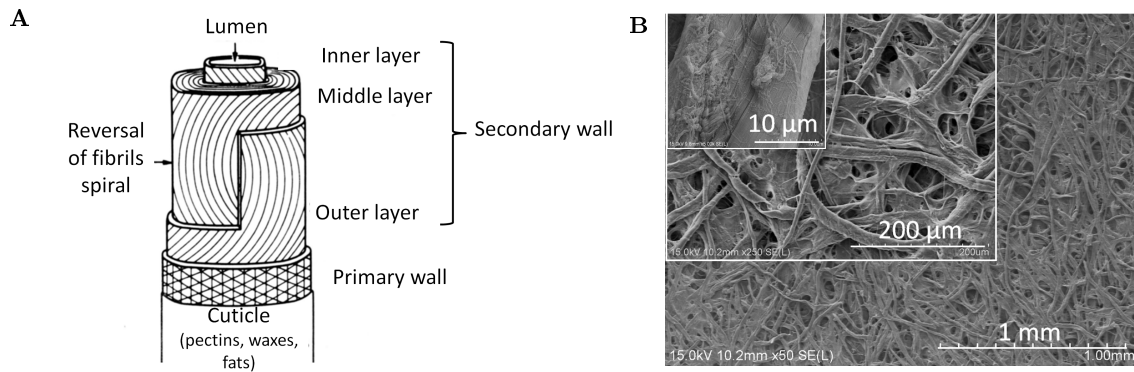


FIG. I.4 – (A) Representation of morphological structure of a cotton fiber and B Scanning electron microscopy images of Whatman paper I.

cellulose that interact with  $\text{H}_2\text{O}$  through hydrogen bonding. At the macroscopic scale of a paper sheet, this hydrophilicity leads to a length expansion upon humidity exposure and this hydrophilic character can be estimated from water vapor sorption measurements. This is for instance illustrated on FIG. I.5 in which the water uptake of a Whatman paper followed from its mass change upon the increase or decrease in relative humidity (RH). This example, as for most cellulosic samples, shows an hysteresis loop: sorption and desorption curves do not superimpose that reveals a water retention upon drying. The amount of adsorbed water can be interpreted in terms of “specific area” which can be estimated with the Brunauer-Emmett-Teller (BET) model. For cotton linters (which Whatman papers are made of), a satisfactory interpolation of data is obtained in the range 0 % to 40 % RH considering an area of about  $110 \text{ m}^2 \cdot \text{g}^{-1}$ , a value corresponding to significant absorption capacity.

Upon exposure to increasing humidity values, especially above 70 %, the water uptake is progressively more and more accentuated (FIG. I.6) which has been attributed to different configurations of water adsorption and consequently change in water mobility inside the cellulosic matter [16]: i) below 25 %, water is present as a monolayer between cellulose chains; ii) between 25 % and 70 %, multi layers of water are present between cellulose chains allowing some water mobility between the water layers; iii) above 70 %,

Fluid	Sample	Specific area ( $\text{m}^2 \cdot \text{g}^{-1}$ )	sample mass (g)	Apparatus	Pretreatment	Source
$\text{N}_2$	Cotton fibers	0.72	40 – 50		25 °C $1 \cdot 10^{-6}$ mmHg	[12]
	Cotton fibers	0.45	10	Sorptomatic 1990 (FISONS)	100 °C 0.9 Pa	[13]
	$\mu$ -crystalline cellulose	1.3	0.4	Quantasorb Sorption system	test with various conditions	[14]
$\text{H}_2\text{O}_v$	Cotton fibers	108	5	scale	–	[12]
	Whatman 2	117.8	0.04	CISorp Analyzer	–	[15]
	Whatman 1	118	0.014	DVS Advantage	–	

TAB. I.2 – Literature review of nitrogen and water sorption by cellulosic substrates.

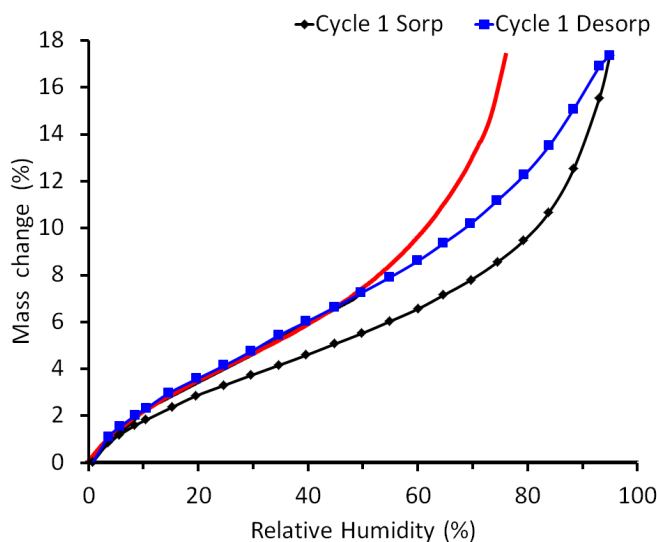


FIG. I.5 – Water vapor sorption (in black) and desorption (in blue) curves of Whatman paper upon humidity exposure. The red curve represents the BET model.

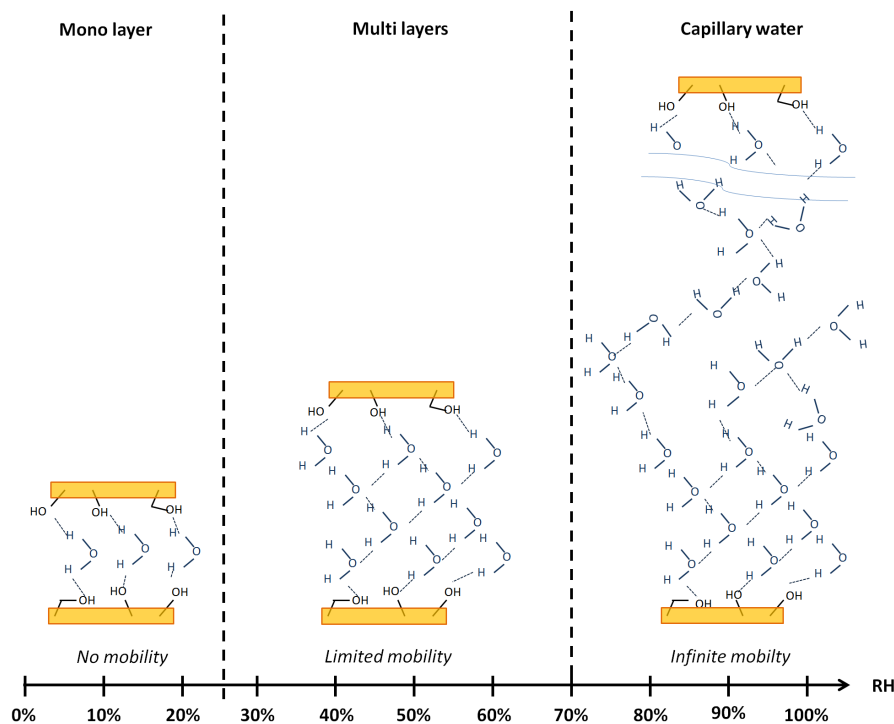


FIG. I.6 – Water arrangements between cellulose chains depending on relative humidity (adapted from [16]).

capillary water is formed and water mobility is high.

Other authors [17, 18] have suggested that, in wood and cork, sorption was not following this monolayer/multilayers description. Sorption proceeds in two steps: first an absorption of water vapor in clusters around hydrophilic sites and then water diffuses into the cell wall. These considerations probably prevail at the microscale of a paper fiber. At the macro scale of a paper sheet, according to Leisen et al. [19] moisture is first transported as vapor through the void spaces between fibers. It is then adsorbed by the fibers on a longer time scale. This approach is coherent with other publications which showed that pore diffusion is a dominant mechanism over surface diffusion in paper samples [20, 21].

### I.1.5 Gelatin sizing

Gelatin is obtained by the partial hydrolysis of collagen derived from the skin, white connective tissue or bones of animals. Gelatin is composed of several polypeptide chains made of a sequence of amino-acids and contains many glycine, proline and 4-hydroxyproline residues (FIG. I.7). Consequently, gelatin is classified as a derived protein. Due to its chemical functions (amino and carboxylic groups), gelatin can behave as an acid or a base. Two types of gelatin exist depending on production pathways : Type A gelatin is obtained by acid hydrolysis and Type B gelatin is obtained from an alkali-treatment [22]. Those two types of gelatins differ slightly in composition but mainly in their physical properties (isoelectric point, gel strength, viscosity).

A gelatin solution is able to form a gel upon drying due to partial coiling of the peptidic chains. Regarding paper sizing, gelatin interacts with the cellulose chains of paper through hydrogen bonding. However, its distribution inside paper is still under question. Indeed, the formation of a film above the paper surface preventing the water penetration has been described [16]. This description is valid at the macro scale of the paper sheet, but to our

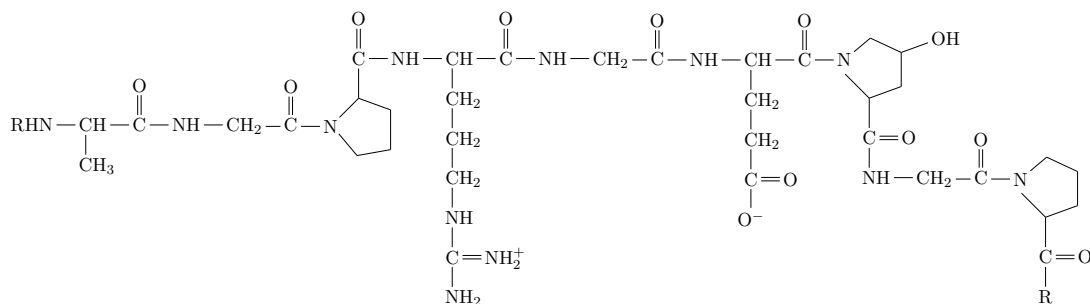


FIG. I.7 – Typical structure of gelatin.

knowledge, there was no investigation of the gelatin distribution at the scale of paper fibers.

While preventing the water permeation, gelatin sizing has some protective effect against paper degradation. Indeed, gelatin sized papers were shown to be more resistant to ageing than unsized papers [23]. Moreover, higher contents of gelatin were found on better preserved historical papers than on deteriorated ones [24]. However, the presence of alum can alter the size. Alum is indeed known to increase significantly paper degradation rate [25], while increasing paper acidity.

## I.2 Iron gall inks

### I.2.1 Historical context

The chemical reaction between iron salts and gall nuts extracts to form dark products is known since antiquity. It was for instance reported in 77 anno domini (AD), by Pliny-the-elder in his *Naturalis Historia*. Pliny was not aware about the chemical nature of the metallic salt that he called *paraphoron* and classified under the term of *aluminis*. At that time, there were indeed a lot of confusions between different sulfate phases that were mainly recognized by taste, shape and color. The *paraphoron* here above mentioned is very probably related to rozenite ( $\text{Fe}^{\text{II}}\text{SO}_4 \cdot 4\text{H}_2\text{O}$ ). Other iron sulfates, such as melanterite ( $\text{Fe}^{\text{II}}\text{SO}_4 \cdot 7\text{H}_2\text{O}$ ) are also found under the appellation of *Atramentum* and confused with copper salts.

Iron gall inks have probably been used for writing from antiquity to middle ages in a large geographical area including Europe, Middle East and North Africa. Yet, few recipes of iron gall inks are available. One early record of an ink obtained by mixing iron salts and tannin can be found in a encyclopedia from Theophilus, who describes among other things the preparation of ink by mixing green vitriol with thorn wood extract[26]. Others recipes of Middle age have been described by [27]. Gum arabic can be found in 11<sup>th</sup> century islamic recipes and was probably introduced later in Europe [28].

Iron gall inks have been used in western countries until the 20<sup>th</sup> century. From the nineteenth century onwards, with the industrial revolution and development of chemistry, ink-makers progressively mixed these inks with other types of inks and with synthetic dyes [29, 30], in order to gather in one product the benefit of each ink. Examination of ink-making recipes also shows that iron sulfate was a common ingredient of nib writing inks until the 1960s. Therefore many of the manuscripts written in the 19<sup>th</sup> and 20<sup>th</sup> century contain iron sulfate bearing inks. They are acidic and relatively rich in iron.

## I.2.2 What are iron gall inks made of?

Iron gall inks are made of three main components (FIG. I.8) which proportion varies according to recipes [28, 27]:

- *an iron salt*: often assimilated to iron sulfate such as melanterite ( $\text{Fe}^{\text{II}}\text{SO}_4 \cdot 7\text{H}_2\text{O}$ ) that has a characteristic blue-green color. Iron salts were rarely pure and often included some proportions of copper and zinc. Depending of the period to be considered, and the way to prepare or collect these materials, several appellations have been used to name these salts (atramentum sutorium, stalagma, copperas, vitriol, ...);
- *tannins aqueous extracts*: tannins are natural polyphenolic biomolecules mainly composed of galloyles, catechin and of flavonol units. They also include some triterpenoide or polyol units (such as glucose) (see FIG. I.9). For ink production, hydrolysable tannins were used. Their nature depends on the plant from which they come from. Iron gall inks were mostly prepared with gall nuts<sup>1</sup> that are rich in gallo-tannins. During aqueous extraction, these tannins are hydrolyzed and the resulting solution contains a high proportion of mono-, di- and tri-gallic acids in combination with other minor products (ex. glucose). Ellagitannins, issued from fruits or pods extracts, are more rarely used for ink making (FIG. I.9). During hydrolysis, they release a significant proportion of ellagic acid in addition to gallic acid and sugars [31];
- *a binder*: gums were mostly used. They are complex mixtures of water soluble polysaccharides with a few percent of glycoproteins. Gum Arabic, a secretion from a cut of acacia trees, was largely used for ink making. It is a high molecular weight polymer (Mw from 240.000 to 580.000) that contains units of (-)arabinose, (-f)galactose, (-)rhamnose and (-f) glucuronic acid.

The dark color of the ink is due to a strong interaction between soluble iron(II) and released carboxy-phenol molecules, a model of which is mono-gallic acid. In presence

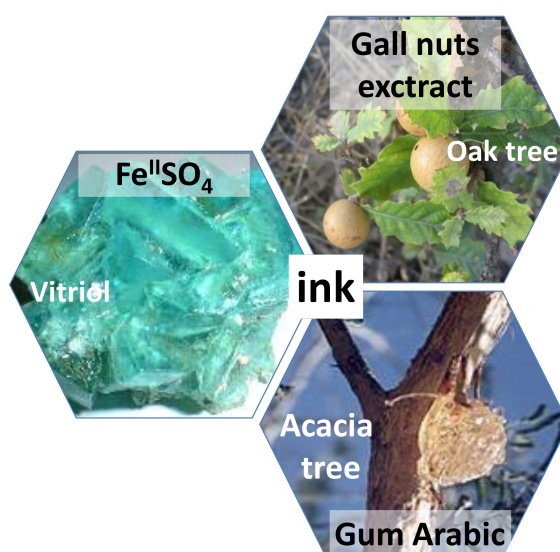
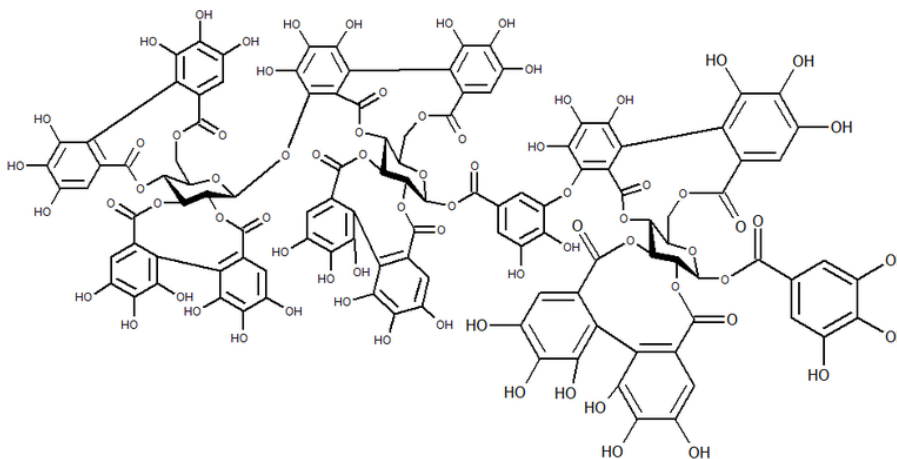


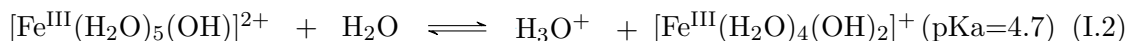
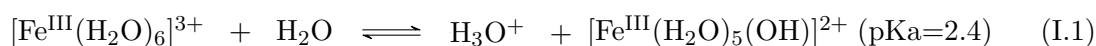
FIG. I.8 – Iron gall ink main composition.

<sup>1</sup>abnormal outgrowths of plant tissues caused by various parasites

FIG. I.9 – *Raspberry ellagotannins*.

of oxygen, this interaction leads to a formation of small particles of a dark precipitate involving iron(III). The introduction of gum as a thickener prevents deposition of these particles and maintains some homogeneity of the ink solution.

It is important to note that iron gall inks are acidic due i) to the presence of organic acids in the tannin extracts (gallic acid has a pKa value close to 4.41) and ii) also due to soluble iron(III) which behaves as an acid, releasing hydronium ions (monohydrated protons) through hydration reactions (EQ. I.1 and EQ. I.2) [32]:



One has to note that the chemistry of iron gall ink solutions still remains poorly understood, the question of complexation/precipitation in the presence of gallic acid being one point. Yet, the high reactivity of iron allows many other interactions with surrounding components, such as chelation with saccharides [33], redox reactions with gallic acid [34], oxidation by dissolved oxygen, etc. All these reactions obviously compete with each other.

### I.2.3 The color of ink

The color of diluted iron gall inks ranges from blue to brown depending on the kind of gall nut used. When gallic acid is the major component of aqueous extracts, a blue color is obtained on freshly prepared inks, which turn toward a black aspect upon ageing because of increasing amount of precipitate. Although it is acknowledged in literature that the ink color comes from precipitation of iron with phenolic compounds, the detailed structure of the precipitate has been a debate for several decades. The involvement of hydroxyl groups in the precipitate formation was empirically deduced by Darbour[35] who tested mixtures of different phenolic compounds with iron(II) sulfate and showed that the presence of two adjacent hydroxyl groups was necessary to obtain a colored solution.

All authors agree with the fact that the precipitate involves more or less equimolar quantities of iron(II) sulfate and gallic acid (TAB. I.3) and that it mainly contains iron(III)

Sample	Elemental analysis				Atomic ratios	Sources
	Fe (%)	C (%)	H (%)	O (%)		
Feller's iron gallate	– <sup>a</sup>	29.95 (32.46) <sup>b</sup>	2.70 (2.73) <sup>b</sup>	– <sup>a</sup>	FeC <sub>7</sub> H <sub>7</sub> O <sub>7</sub>	[37]
Wunderlich's iron gallate	22.3	34.43	1.24	41.4	FeC <sub>7.18</sub> H <sub>3.07</sub> O <sub>6.48</sub>	[38]
Ponce's IGI ppt	20.7	30.89	2.74	45.62	FeC <sub>6.9</sub> H <sub>7.4</sub> O <sub>7.7</sub>	[39, 40]

TAB. I.3 – Composition of iron gall ink precipitate (adapted from Ponce, Gaskell, and Brostoff [39])

in octahedral sites. Yet, two different structures have been proposed. The first one, suggested by Krekel [36], was until recently widely accepted in the cultural heritage field. It involves a three step mechanism (see FIG. I.10):

- *step 1*: addition of one gallic acid to iron(II) sulfate leading to a colorless Fe<sup>II</sup>-gallate complex and to protons release;
- *step 2*: reaction of two equivalents of the Fe<sup>II</sup>-gallate complex with 0.5 equivalent of oxygen to form a tetrahedral Fe<sup>III</sup>-bis-gallate complex;
- *step 3*: decarboxylation of the gallate ligands to produce a black insoluble Fe<sup>III</sup> octahedral pyrogallin complex.

Another structure was proposed by Wunderlich, Weber, and Bergerhoff [38] who considered that chelation of iron does not only occur with the hydroxyls groups of gallic acid but also with its carboxylic functions [38]. However, as iron(III) chloride was used in their study as precursor instead of iron(II) chloride, their findings aroused skepticism among the cultural heritage community. More recently Feller and Cheetham [37], found a similar structure using iron(II) chloride as precursor. They proposed a polymeric organization in which iron(III) gallate is a dihydrate FeC<sub>7</sub>O<sub>5</sub>H<sub>2</sub>,2H<sub>2</sub>O.

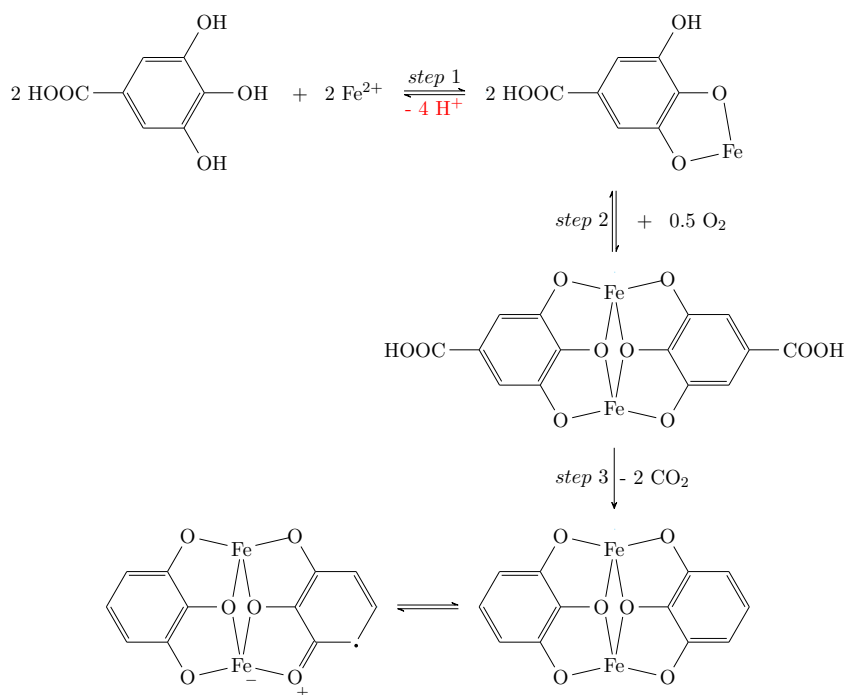


FIG. I.10 – Iron gall ink complex formation according to Krekel [36]. Note the release of two protons in step 1.

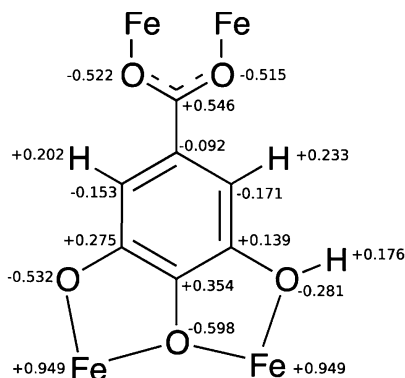


FIG. I.11 – Structure and partial charge of the iron gallate complex proposed by Ponce et al. [40].

The recent work of Ponce et al.[40] unambiguously confirmed this scenario. These authors showed that the ratio Fe:C is always 7:1, whichever the initial molar ratio between Fe(II) sulfate and gallic acid, and that the carboxylic functions of gallic acid are still present in the precipitate [40]. Their work also confirmed that the color of the precipitate does not come from an intervalence charge transfer between Fe(II) and Fe(III), but rather from the charge transfer between aromatic rings and Fe(III) which generates a conjugated double bond system responsible for energy absorption in the visible range (620 nm). Interestingly, this latest knowledge regarding the structure of the iron gall ink precipitate clearly established deprotonation of phenolic groups (FIG.I.11) thus offering an additional explanation to the acidification of ink solutions with ageing.

#### I.2.4 Stability of the complex/precipitate

The stability of iron gall complexes has been addressed in the literature, several studies being performed in iron sulfate and gallic acid solutions to determine the stoichiometry of the formed complexes and their constants of complexation. The lack of a uniformed nomenclature brings some confusion but some main conclusions can be drawn from these works:

- a 1:1 Fe to gallic acid soluble complex forms in the pH range 3 to 5 [41, 42, 43] while 1:2 and 1:3 complexes predominantly form above pH 5 and 7, respectively [41, 42];
- in the complex 1:1, iron is bound to the two adjacent hydroxyls groups of gallic acid [41, 42, 43, 44], the last hydroxyl remaining intact due to a higher value of pKa [45]. Several authors proposed that the carboxylic acid group is involved in the iron binding [41, 42]. Also, Hynes and Ó Coinceanainn [43] mentioned the decomposition of the complex into semiquinone and quinone;
- the binding of iron by gallic acid is relatively low in comparison to other phenolic acids [46, 47] or other iron specific chelates.

Fewer studies deal with the stability of the iron gall ink precipitate. Sistach, Gibert, and Areal [48] mentioned a decomposition of the iron gall ink precipitate leading to a change in color from blue to brown due to the formation of quinone structures. Ponce, Gaskell, and Brostoff [39] have also evidenced a change in the structure of the crystalline precipitate upon ageing leading to an amorphous compound.

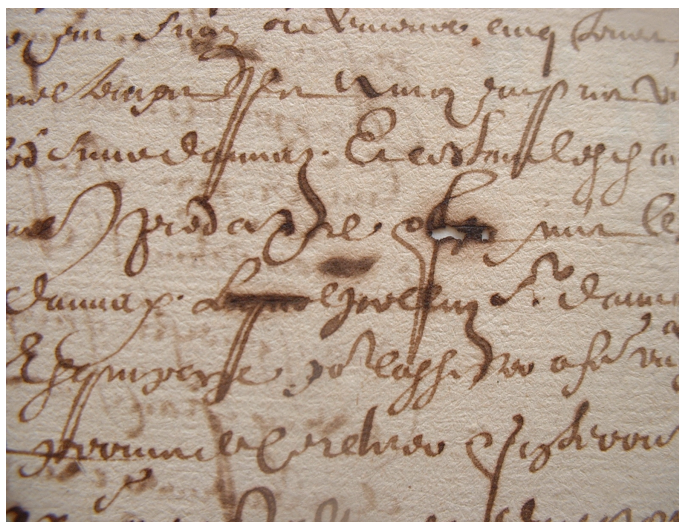


FIG. I.12 – Manuscripts corroded by iron gall ink.

### I.3 Iron gall inks corrosion

#### I.3.1 Overview

Most archivists and librarians are fully aware of the harmful nature of iron gall inks, which, during their ageing, can progressively destroy their cellulosic support (paper). This alteration, referred to as “Iron Gall Ink Corrosion”, is often substantiated by the existence of cracked zones or, even worse, holes in ancient manuscripts (FIG. I.12).

The first step of degradation corresponds to migration of ink ingredients in the carrier. This may occur during the ink writing process if the paper is insufficiently sized. It then behaves as a chromatographic support, Fe(III) gallate precipitate remaining at the surface while free Fe(II) ions migrate with the solvent largely around the ink spot (FIG. I.13). Migration of some of the ink components can also be achieved when the document is exposed to high humidity conditions (above 80-85 % RH) [49, 50, 51]: condensation of water in the paper then leads to dissolution of water soluble compounds, which migrate in the paper. Whether these migrations occur in the sheet (between fibers) or in the fibers

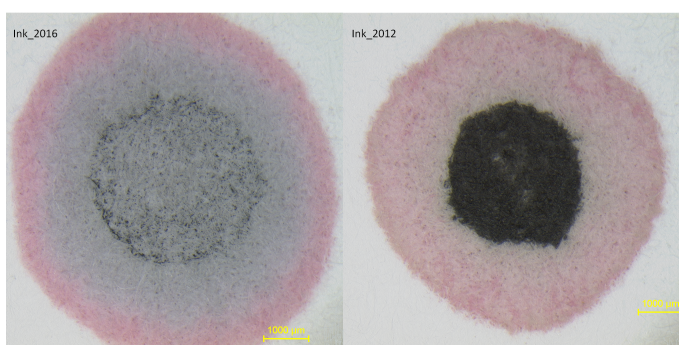


FIG. I.13 – Ink diffusion on a paper previously impregnated with Fe(II) specific chelate (bathophenanthroline) which gives a pink color with Fe(II). Model ink was made of iron(II) sulphate,  $7 \text{ H}_2\text{O}$ ,  $40 \text{ g} \cdot \text{L}^{-1}$  and gallic acid,  $9 \text{ g} \cdot \text{L}^{-1}$ . Aspect of the diffusion depends on the age of the ink.  
 Left: ink of six months, the grey halo corresponds to iron(III) gallate formed during ink drying.  
 Right: ink of four years, the grey halo is almost absent due to the completion of iron(III) gallate precipitate formation prior ink use.

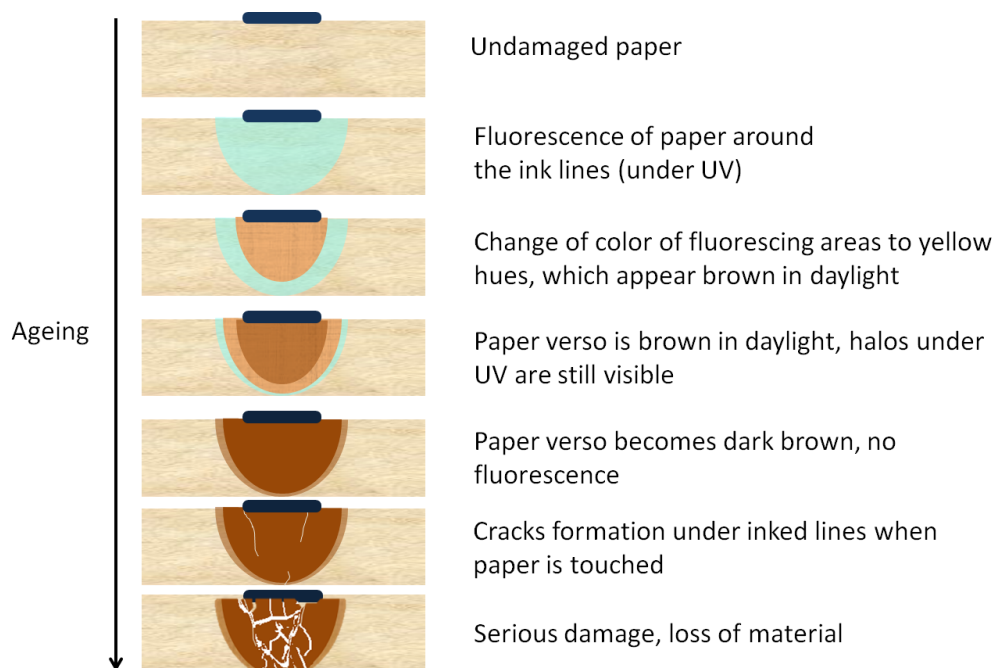


FIG. I.14 – Steps of progression in degradation of a manuscript by iron gall ink according to *Reissland*[52].

themselves remains an open question. Yet, these migrations induce some fluorescence of the paper in the early stage of the degradation, then some browning.

When ink components impregnate the paper (and/or the fibers), chemical degradation can take place. There is a consensus on the fact that this degradation leads to browning and loss of mechanical properties. Near the ink line, the paper becomes fragile, but far from the ink line, it is still strong. Damaged documents are often handled without specific care because people are not aware that the paper is locally brittle. Yet turning pages, even carefully, implies bending sheets. This action may induce locally an unbearable mechanical solicitation, provoking cracks and finally holes in the fragile area [52] (FIG. I.14).

The chemistry of iron gall ink corrosion has been a matter of discussion for several decades [53, 54, 55] not to say centuries. The first occurrence we could find of this debate is a conference in Sankt Gallen, Switzerland, in 1898. The acidic nature of iron gall inks was in the early times identified as the main cause of paper alteration. In 1876, Fenton discovered the ability of iron to produce powerful oxidants (hydroxyl radicals) from hydrogen peroxide [56]. This study was followed by the work of Haber and Weiss in 1934 [57, 58]. Some decades later, other works aroused a clear awareness of the necessity to take into account free metallic ions as additional potential degradation factors, such as copper in green pigments [59, 60, 61] or iron in the case of iron gall ink corrosion [62, 63, 64]. This point is all the more crucial that a survey performed on 104 recipes of iron gall inks dating from the 15<sup>th</sup> to the 19<sup>th</sup> century pointed out a large excess of iron over gallic acid, meaning that the formation of the iron gall precipitate cannot consume all iron [65, 64]. In these conditions, there is still some Fe(II) ions left in solution, even when the formation of precipitate is completed.

Regarding iron gall ink corrosion, it is at the end of the 20<sup>th</sup> century, that several studies more precisely addressed the chemistry of the degradation that is currently attributed to a combination of acid-catalyzed hydrolysis and of iron-catalyzed oxidation of cellulose [55, 66, 67, 68, 69]. However, the dominant degradation mechanism (if any) remains unclear.

In the following sections are presented the general mechanisms of acid-catalyzed hydrolysis and oxidation in the case of blank papers. The potential impact of iron is then discussed in each section, to finish by previous studies of iron gall ink corrosion which highlight several parameters impacting the paper depolymerisation.

### I.3.2 Acid-catalyzed hydrolysis of cellulose

The degradation of blank paper in acidic medium is a complex subject that motivated numerous studies [70, 71, 72, 73]. On a general point of view, cellulose hydrolysis takes place in three steps [74, 75, 76] (FIG. I.15): first, the attack of an acidic proton at an oxygen site (glycosidic or ring oxygen) leading to the formation of a cyclic or noncyclic carbonium cation, then a rearrangement by bond cleavage, and finally a step of water addition to close the reaction pathway. Because of steric effects, the mechanism put forward in most cases is the one that involves proton attack on the glycosidic oxygen and subsequent carbonium formation.

The hydrolytic scissions of the cellulose chains lead to an increase of the number of cellulose reducing ends (FIG. I.1), i.e. to the formation of one carbonyl group per scission (without modifying the carboxyl groups content) [77]. Experiments done in aerated conditions on acidic paper samples have shown that the carbonyl groups content reflected the changes in the average chains length [77, 78]. This led to the proposal that ageing in acidic medium almost exclusively occurs through acid-catalyzed hydrolysis, both in humid and dry atmosphere.

Regarding more especially iron gall ink corrosion, the hypothesis of the acid hydrolysis as predominant pathway in litterature lies on the fact that the pH of iron gall ink is acidic with typical values between 2 and 3. These low pH values are due both to the presence of gallic acid and to the presence of iron(III), which behaves as an acid through solvation (see section I.2.2). In addition, the pH value of an ink solution is not stable. It slowly decreases upon natural aging in aerated conditions meaning that there is a release of protons. This can be attributed to i) the formation of iron gall products (complexes or precipitate) on which two adjacent phenol groups are deprotonated (see section I.2.2) and/or ii) to the oxidation and precipitation of iron in excess (EQ. III.13):

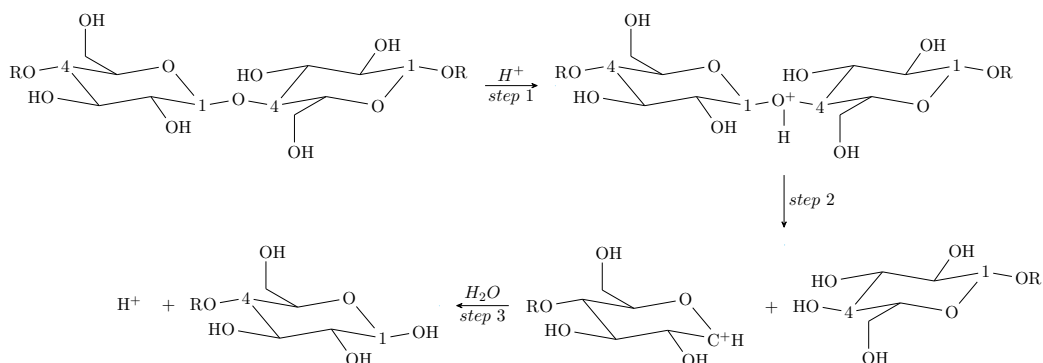


FIG. I.15 – Acid catalyzed hydrolysis of cellulose.

### I.3.3 Oxidation mechanisms

Regarding blank (ink free) paper degradation, oxidation is often considered as a secondary degradation pathway (compared to acid hydrolysis) that does not directly lead to an osidic bond scission but rather to the formation of carbonyl, carboxylic acid, and peroxy groups, which could rearrange in a second step. In mild alkaline conditions, when there is no acid-catalyzed hydrolysis, oxidation is considered as the predominant route of paper degradation [79] through carbonyl groups formation followed by beta-alkoxy elimination [80] and bond cleavage.

Even if the impact of oxygen on paper degradation has been the subject of several studies, this has not led to a general consensus: some authors concluded to a negligible impact of oxygen on paper ageing [81], while others observed either slower cellulose degradation in the absence of oxygen [82] or more rapid loss of paper strength during ageing upon increasing oxygen concentration [83]. The reason of this confusion might lie in the difficulty to obtain properly controlled oxygen free conditions during long periods of ageing. In this section, hydroxilic groups in cellulose potentially sensitive to oxidation will be first introduced. Then, the radical mechanism of auto-oxidation along with the impact of iron on the production of radicals will be presented.

#### a Oxidation of cellulose alcohol groups

Cellulose contains hydroxyls groups and (although less numerous) aldehyde terminal groups. They can undergo oxidation reactions leading to the formation of carbonyl and carboxylic groups that can be evidenced by infrared spectroscopy [84, 85, 86] or with gel permeation chromatography coupled with fluorescence detection. This last technique allows carbonyl [87, 88, 89] and carboxyl groups [90] quantification after specific labelling reactions.

Depending on the location of the attacked carbon [91] different functions can be obtained (see FIG. I.16): 1) attack on aldehyde terminal groups that forms a carboxylic acid; 2) attack on C<sub>2</sub> and C<sub>3</sub>, either simultaneously or individually, form carbonyl groups without ring cleavage and produces an oxidized cellulose of the reducing type; 3) attack on C<sub>6</sub> to form an aldehyde group, which can in turn be oxidized to form 4) a carboxyl group.

Carbon atoms reactivity towards oxidation depends on their involvement in the hydro-

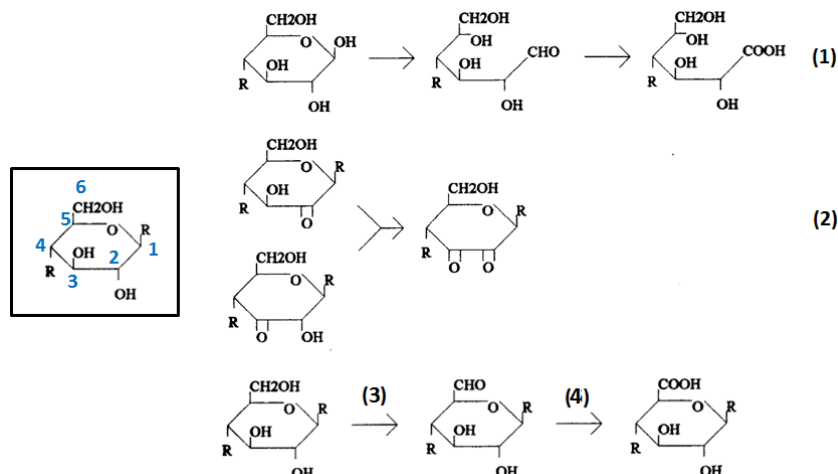


FIG. I.16 – Sites of possible oxidation on cellulose[91].

gen bonding network (see section I.1.3). Thus, C<sub>3</sub> carbons, for which all the attached OH groups are involved in hydrogen bondings appear less sensitive to oxidation than C<sub>2</sub> and C<sub>6</sub> carbons for which only half of attached OH groups participate in hydrogen bondings [92]. Moreover, in alkaline medium, formation of carbonyl groups on C<sub>2</sub>, C<sub>3</sub> and C<sub>6</sub> can provoke the cleavage of the glycosidic linkage by  $\beta$ -alkoxy-elimination [93].

Oxidation can happen simultaneously with acid-catalyzed hydrolysis and both mechanisms can reinforce each other. For instance, the reducing end groups formed by acid-catalyzed hydrolysis were found to be involved in peroxide formation [94]. They can also be oxidized to carboxylic acid which in return participates to acid-catalyzed hydrolysis. Similarly, the above mentioned oxidation pathways (4) and (6) lead to formation of carboxylic acids and thus promote hydrolysis.

Moreover, oxidation can process through different mechanisms and the products shown in FIG. I.16 can be obtained as well through a redox reaction on alcohol groups provided the presence of a strong enough oxidant or after free radical chain reactions. These latter, that are described in the next section, can imply all carbon atoms (and not only hydroxyl bearing carbons). They frequently occur on organic polymers provided the presence of a radical initiator I.

### b Auto-oxidation of cellulose

The general scheme of autoxidation was first proposed in 1946 by Bolland and Gee [95] on synthetic polymers. It has been conveyed as a possible mechanism for cellulose degradation by Entwistle, Cole, and Wooding [96] (FIG. I.17). This mechanism consists in three main steps:

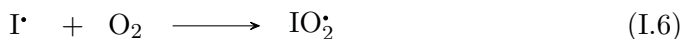
- the initiation step, that is also a limiting step, involves an initiator I, molecular oxygen and cellulose to form radicals. It has been shown that only the terminal aldehyde groups of cellulose are able to react spontaneously with oxygen to form such radicals [93];
- the propagation step in which radicals react with cellulose (Cell-H), forming carbohydrate radicals (Cell•) that can react with oxygen to form peroxy radicals (Cell-O<sub>2</sub>•). These latter can abstract a hydrogen atom from another cellulose chain leading to formation of new Cell• radicals and peroxycellulose (Cell-O<sub>2</sub>H) that decomposes into peroxy radicals (Cell-O<sub>2</sub>•), alkoxy radicals (Cell-O•) and hydroxyl radicals (HO•);
- the termination step caused by the recombination of two radicals.

Hydroxyl radicals produced in the propagation step of this mechanism are amongst the most powerful oxidants ( $E^\circ(\text{HO}\cdot, \text{H}^+/\text{H}_2\text{O}) = +2.31$ ) [98]. They can quickly react with organic molecules in a non-selective manner. As an example, the constant rate of hydroxyl radicals on glucose in aqueous solution is around  $1 \text{ GL} \cdot \text{mol}^{-1} \cdot \text{s}^{-1}$  [99]. More generally, with these radicals, three types of reactions can be foreseen: addition to C=C double bonds, electron transfer and H-abstraction [100]. On carbohydrates, since C-H bonds have a lower dissociation energy than O-H bonds, hydroxyl radicals preferentially abstract hydrogens linked to carbon atoms that bear an alcohol group. This leads through reactions 1 and 2 of FIG.I.18 to an intermediate peroxy radical that immediately loses a hydroperoxy radical (reaction 3, FIG.I.18) and forms a carbonyl group. Yet, hydrogen abstraction may also concern a carbon that does not bear a hydroxyl, such as those that

Initiation:



Propagation:



Termination:

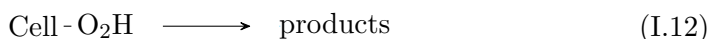
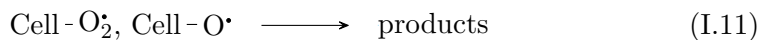
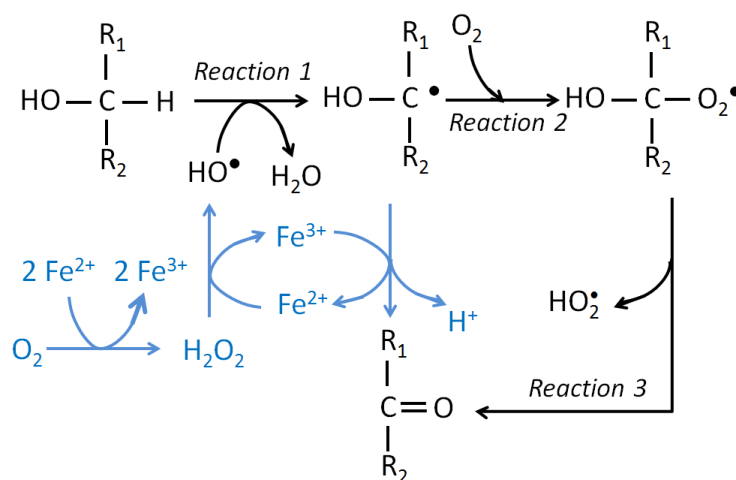
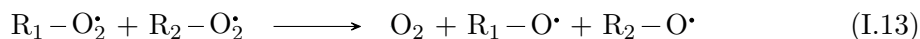
FIG. I.17 – Cellulose autoxidation adapted from [97]. *I* stands for an initiator.

FIG. I.18 – Radical oxidation of carbohydrate (black scheme) and the impact of iron and Fenton reaction (blue scheme).

are close to the glycosidic bond ( $C_1$  and  $C_4$ ). Formation of these radicals will then lead to a scission of the glycosidic linkage at some point. Guay et al. [101] obtained experimental evidences of the ability of hydroxyl radicals to cleave the glycosidic bond by a direct substitution reaction at the anomeric carbon ( $C_1$ ) creating an oxy radicals at  $C_4$  while breaking the osidic bond (FIG. I.19).

In radiation chemistry, formation of peroxy radicals has also been mentioned on cellobiose [102][103]. When those peroxy radicals are formed on  $C_1$ ,  $C_2$ ,  $C_6$ ,  $C_{2'}$ ,  $C_{3'}$  or  $C_{6'}$  quick elimination of  $\text{HO}_2^-$  occurs leading to a carbonyl group formation (reactions 1 to 3, FIG. I.18, black scheme). For peroxy radicals formed on  $C_{1'}$ ,  $C_4$  or  $C_{5'}$  (FIG. I.20) longer lifetimes were found, which enables them to react with other peroxy radicals forming alkoxy radicals EQ. I.13. These radicals are unstable and may rearrange with the scission of the glycosidic bond by fragmentation.



The occurrence of the Bolland-Gee scenario on cellulose was confirmed recently in alkaline conditions with the detection of hydroxyl radicals [80, 104]. Formation of peroxides during natural ageing [105, 94] and during artificial ageing of cellulose [106, 107] has also

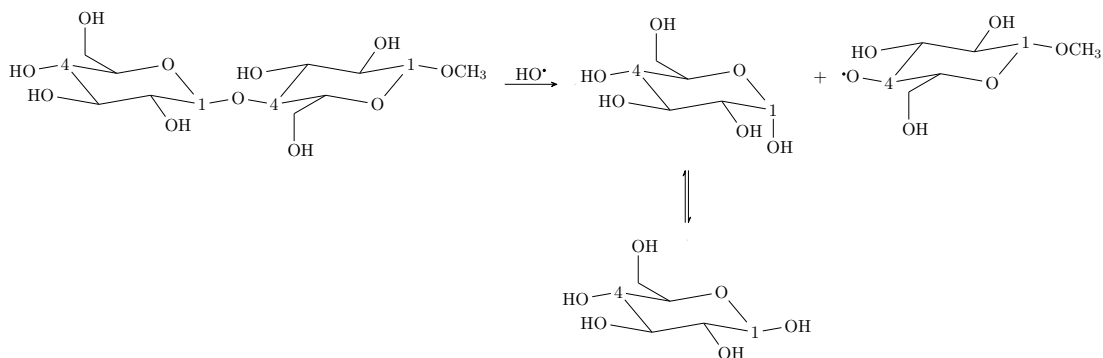


FIG. I.19 – *Hydroxyl radical attack at the anomeric carbon during delignification proposed by Guay et al.[101].*

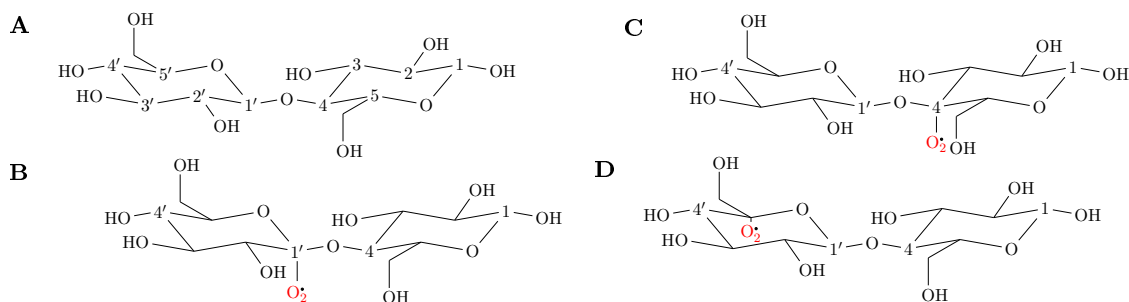
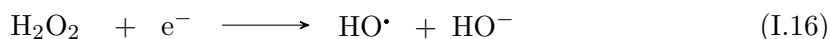
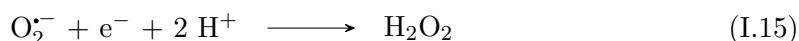


FIG. I.20 – (A) *Cellobiose molecule with carbon numbered and peroxyl radicals of cellobiose on (B) C<sub>1'</sub>, (C) C<sub>4</sub> and (D) C<sub>5'</sub>, that can be at the origin of osidic bond cleavage.*

been evidenced along with formation of hydroxyl radicals [104, 107]. For alkaline paper, a link between depolymerisation and hydroxyl radicals production has been evidenced [104]. However, to our knowledge, no similar observation has been made in acidic medium.

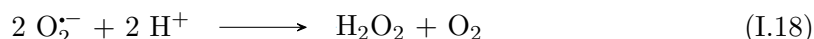
### c Production of reactive oxygen species by free iron

The reduction of a molecule of oxygen to water implies the transfer of 4 electrons. If we suppose that these electrons are transferred one by one, three oxygen reactive species are then produced as intermediates : superoxide or hydroperoxyl radicals ( $O_2^{\bullet-}$  or  $HO_2^{\bullet}$ ) (Eq. I.14), hydrogen peroxide ( $H_2O_2$ ) (Eq. I.15) and hydroxyl radicals ( $HO^{\bullet}$ ) (Eq. I.16).



The reduction potential of the  $O_2/O_2^{\bullet-}$  redox couple is rather low ( $-0.33$  V at pH 7) with respect of reduction potentials of the other intermediate couples. This is consistent with the fact that the formation of peroxyl or hydroperoxyl radicals is the limiting step of the reduction. Once  $O_2^{\bullet-}$  is formed, a disproportionation reaction is thermodynamically

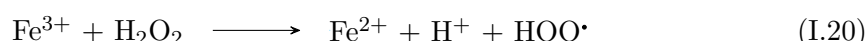
possible that leads to the production of hydrogen peroxide (EQ. I.18 )



The presence of iron(II) considerably enhances oxygen reduction, and thus formation of intermediate oxygen reactive species. In particular, iron(II) easily reacts with hydrogen peroxide through Fenton reaction (EQ. I.19), leading to the formation of highly reactive hydroxyl radicals  $\text{HO}\cdot$ . Those radicals could then react with cellulose and contribute to the auto-oxidation scheme previously described (FIG. I.17).



The impact of iron is not limited to iron(II). Iron (III) can also oxidize hydrogen peroxide to superoxide radicals (EQ. I.20).

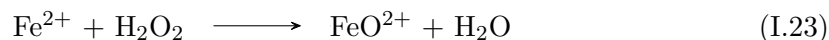


The combination of reactions EQ. I.19 and I.20 shows that iron may have a catalytic impact on the production of superoxide and hydroxyl radicals. These reactions can also be considered with an organic peroxide instead of hydrogen peroxide (EQ. I.21 and I.22):



In presence of oxygen, iron can then promote the formation of ROS, either directly by acting on cellulose peroxides, or indirectly through oxygen reduction steps reactions. Interestingly, it has been shown that Fenton reaction can also involve chelated iron(II) (and not free iron(II) only) as it is not inhibited by the presence of chelating agents such as EDTA [108].

The Fenton reaction (EQ. I.19) has motivated numerous studies, most of them dealing with solution systems. The nature of the produced oxygen species has been the object of some controversy. For instance iron oxo species have been suggested as alternative products of the Fenton reaction at pH 6-7 in a recent study [109] (EQ. I.23):



Activation of oxygen by iron has often been suggested as a major cause of iron gall ink corrosion [64, 65]. Indeed the degradation of a model compound of cellulose (methyl- $\beta$ -D-glucopyranoside) by the Fenton reagents (mixture of iron(II) and hydrogen peroxide) was studied, leading to the proposal of a mechanism [110] in which several degradation products would be possible depending on the site of hydroxyl attack: i) if a radical is formed on  $\text{C}_1$  or  $\text{C}_4$ , a cleavage of the glycosidic bond happens, leading to gluconic acid formation or glucoside fragments respectively; ii) if  $\text{C}_2$  and  $\text{C}_3$  undergo the attack, keto groups will be formed by electron transfer with iron(III); iii) finally attack on  $\text{C}_6$  will give aldehyde groups and lead to glucuronic acids [48, 91].

The Fenton-Hamilton hypothesis, a variation of the Fenton mechanism, has been suggested by Sistach, Gibert, and Areal [48] as a possible mechanism implying iron gall precipitate and cellulose: in presence of hydrogen peroxide, the iron gallate dissociates to

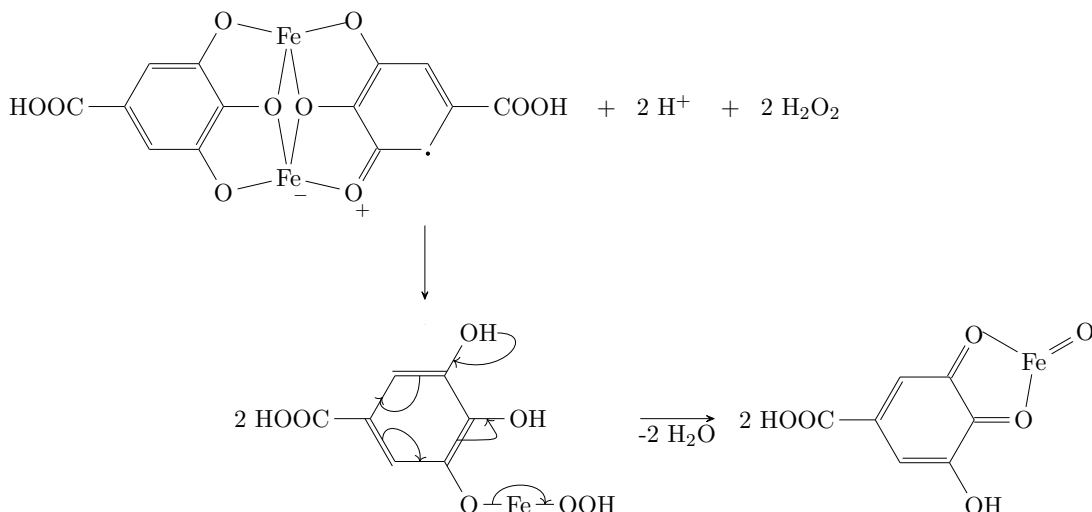


FIG. I.21 – The Fenton-Hamilton hypothesis [48].

an iron hydrogeno-peroxide compound forming in the end a quinone/ferryl like structure upon water loss (FIG. I.21). This last hypothesis appears however relatively unlikely.

### 1.3.4 Impact of several parameters on IGI corrosion

Several experiments aimed at clarify the parameters impacting the iron gall ink corrosion of papers. The influence of ink ingredients, but also the one of pH, oxygen and humidity were respectively investigated on model samples or solutions.

#### a Influence of ink ingredients

Several studies aimed at determining the respective roles of the main components of iron gall inks (gum arabic, iron sulfate and gallic acid) on paper ageing. Especially, unsized papers were impregnated with different combinations of these components and their depolymerization was followed versus natural ageing in ambient conditions [111]. This was done by following the decrease of the average chain length (average number of monomers per macromolecule, called degree of polymerisation: DP) of the cellulose macromolecule due to glycosidic bond breaking, leading to the following observations:

- no significant drop of the DP was observed on the samples impregnated with gum Arabic and/or gallic acid (despite the fact that the pH of the gallic acid solution was close to 2.8) (FIG.I.22, black line);
- conversely, all samples impregnated with iron sulfate underwent a fast depolymerization perceptible in the first days of ageing (FIG. I.22, orange line). The degradation was faster with additional presence of gallic acid (FIG. I.22, dark blue line).

The faster degradation with gallic acid could be due to i) the reducing power of gallic acid (which is able to reduce iron(III) to iron(II) [112] and thus to maintain a large amount of iron(II) in the sample) or ii) to the fact that the pH of these papers is approximately 0.2 point lower.

On a general point of view, gallic acid has a twofold behavior that can be anti or pro oxidant [113, 114]. It can behave as an antioxidant because of its capacity to scavenge free radicals [114, 115]. It can also be prooxidant most likely because of its strong ability to reduce iron [116]. According to Strlic et al. [114], this behavior is driven by the molar ratio

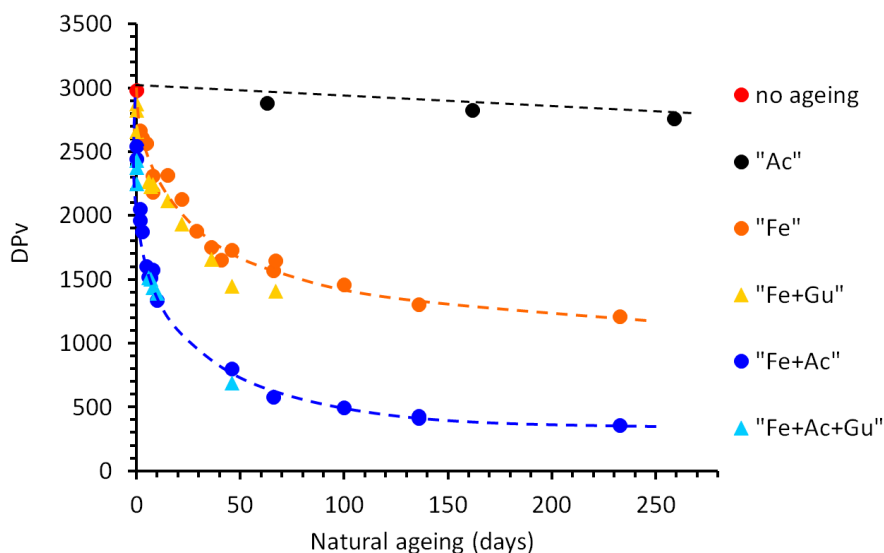


FIG. I.22 – *Viscosimetric measurements of the degree of polymerisation ( $DP_v$ ) of Whatman 1 papers samples during natural ageing at 50 % relative humidity, 23 °C.*

*Papers samples were impregnated with gallic acid (Ac, in black), by iron sulfate without gum arabic (Fe, in orange) or with gum arabic (Fe Gu, yellow) and by model iron gall ink (Ac Fe, in dark blue) without gum arabic and with gum arabic (Ac Fe Gu, pale blue) [111].*

of gallic acid to iron(III). They showed in a Fenton medium, that the effect is pro-oxidative if the ratio is smaller than 2 and anti-oxidant if the ratio is greater than 2.

### b Influence of pH

Shahani and Hengemihle[60] have studied the influence of iron on paper degradation at different pH values. A decrease in the effect of iron was observed after a neutralization treatment, suggesting that acid hydrolysis promoted by the acidity of the ink could be the predominant degradation mechanism. However, the rich chemistry of iron allows imagining alternative pathways. In particular, standard reduction potential of dioxygen and iron significantly vary with the pH, meaning that oxidation reactions are pH dependent. Moreover, an increase of pH has a direct impact on conversion of iron(II) to iron(III) and precipitation of this latter.

The impact of pH on Fenton reactions has been the object of several studies without leading to a general consensus : hydroxyl radicals production has been measured at circum neutral pH (range 5.5-9.5) on Fenton-like systems consisting in solutions of hydrogen peroxide and iron(III) chloride using (N, N'-(5-nitro-1,3-phenylene) bisglutaramide) as probe molecule [117]. The maximum production of hydroxyl radicals was found to take place at pH 8.5, suggesting that oxidation could be a major route at this pH. In other studies, the Fenton reaction was yielding a maximum hydroxyl radicals production around pH 3 [118, 119, 120] a pH value close to that of iron gall inks. Below pH 3, hydroxyl radicals would be scavenged by protons, and above pH 5, iron(II) would be oxidized to iron(III) that readily precipitates.

### c Influence of oxygen and humidity

Oxygen and humidity are also parameters that could have an impact on degradation processes. Humidity has unquestionably a strong physical impact on the diffusion of com-

ponents from the ink deposit, to the paper. But it could also have a chemical impact: high humidity conditions are usually considered as promoting hydrolysis [70] but it can also increase peroxides content in iron free papers as it has been demonstrated on bleached pulp [105]. During thermoluminescence measurements [121], increase of humidity led to an increase in the signal suggesting that humidity could promote oxidation mechanisms. Conversely, on papers impregnated with different combinations of ink ingredients [111], it was observed that conditioning at high humidity condition (80 % RH) did not promote degradation. On similar papers aged in aerobic or anoxic conditions, it has been observed that oxygen, in addition to iron, had a strong impact on cellulose depolymerization, suggesting a significant involvement of oxygen reactive species in the degradation pathway. Moreover, some unpublished measurements made at the BOKU center with the CCOA method [87, 88, 89] on similar iron(II)sulphate and gallic acid impregnated samples (see appendix IV.6) revealed that ageing in aerated conditions led to significant chain scissions and increase of carbonyl groups (different from the reducing end groups).

## **I.4 PhD thesis outline**

The degradation of paper by iron gall inks results from the combined action of physical and chemical parameters and remains poorly understood in its details. Many questions remain open. In particular: does oxidation prevail on acid catalyzed hydrolysis? Is there a synergetic effect between these two possible pathways? What is the impact of temperature, of moisture, of oxygen, of iron speciation and concentration? How do ink ingredients interact with cellulose? Can they fully impregnate a paper fiber or do they remain at the surface? The present work was undertaken to give some answers to these questions.

The literature detailed above shows a clear involvement of oxygen and iron, suggesting oxidation mechanisms and potentially radical formation. The first step of our investigation, exposed in next chapter, also deals with the presence of reactive oxygen species (and especially hydroxyl radicals) potentially involved in the degradation. This will be done by electron spin resonance (ESR) spectroscopy using 5,5-Dimethyl-1-pyrroline N-oxide (DMPO) as spin trap and by high performance liquid chromatography (HPLC) using terephthalic acid (TPA) as a radical scavenger.



# Chapter II

## Investigation of reactive oxygen species (ROS)

### II.1 Introduction

ROS are highly reactive species involving oxygen atoms. They can be classified into three categories: i) *species from oxygen activation*: singlet oxygen, superoxide ion  $O_2^{\cdot-}$ , hydroxyl radicals  $OH^{\cdot}$ , hydrogen peroxide  $H_2O_2$ ; ii) *organic species*: hydroperoxide  $R-OOH$ , hydroperoxyl radicals  $R-OO^{\cdot}$ ; iii) *metal-oxo species*: perferryl ion  $(Fe^V-O_2)^{2+}$ , ferryl ion  $(Fe^{IV}=O)^{2+}$ , superoxo radical anion  $Fe^{III}-O_2^{\cdot-}$ , or other species like  $\mu$  peroxo,  $\mu$  oxo, alkylperoxo, hydroperoxo, described in FIG. II.1. The occurrence of this last category has been proposed and largely debated in the 90's but still remains controversial since metal-oxo species were never directly and unambiguously evidenced, except in porphyrin structure. ROS are highly electrophilic and quickly react with the surrounding organic molecules. They can be evidenced by different analytical techniques. For the detection of peroxides and hydrogen peroxide that have a relatively long lifetime, a large variety of techniques are available:

- the techniques of hydrogen peroxide titration are based on the use of iodide, permanganate or ceric sulfate. These techniques rely on the reduction of peroxide and are usually not accurate at low concentrations [123];

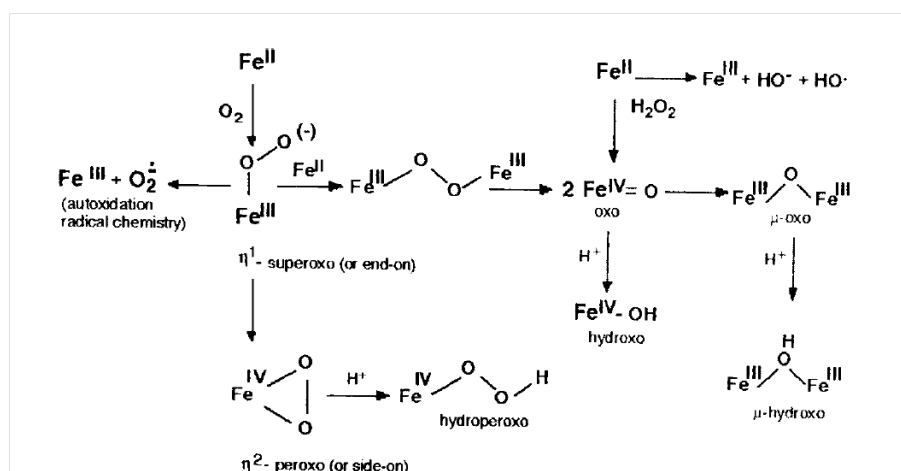


FIG. II.1 – Iron oxo species formation [122].

- spectroscopic methods can also be used, one of the oldest using iodine and ammonium molybdate in acidic solutions [124]. A more recent one is based on the formation of a peroxovanadate complex from the reaction of hydrogen peroxide with vanadium pentoxide. This method has a high detection limit and has been shown to be efficient in quantifying hydrogen peroxide in pulp bleaching effluents [125];
- chemiluminescence in presence of luminol has been used in the case of paper to study iron gall ink corrosion and the peroxide emission from paper [69]. However the emitted signal is not specific to peroxides and can be also attributed to charge transfer, transglycosilation and singlet oxygen emission;
- gas chromatography is another technique of choice as illustrated by the detection of hydrogen peroxide using phenylglyoxylic acid during oxygen delignification of kraft pulp [126]. This technique was also found appropriate for organic peroxides quantification after a reduction with  $H_2$  or  $NaBH_4$  followed by a derivatization [127]. Liquid chromatography has been successfully employed as well for cellulose peroxides quantification on paper samples using reverse phase liquid chromatography (RP-HPLC) and triphenylphosphine (TPP) for cellulose peroxides quantification [107].

A common problem encountered with the identification of radicals lies in their short lifetimes (1 ns) which compromises their direct observation. A general way to bypass this drawback is to use trapping reactions to stabilize the radicals and allow their detection. Regarding hydroxyl radicals, different target molecules are proposed in the literature. Many of them undergo hydroxylation reactions. For instance terephthalic acid (TPA) [107] and N,N-(5-nitro-1,3-phenylene)bisgluramide (NPG) [69, 128, 117] proved to be efficient for the quantification of hydroxyl radicals with HPLC. In alkaline medium,  $\gamma$ -tocopheryl-isopropyl ether was proposed for the trapping of hydroxyl radicals [80], the hydroxylated product showing a characteristic red-colored quinone that was quantified by photospectroscopy. In the field of catalysis, coumarin has also been used producing a fluorescent compound (umbelliferone) after hydroxyl radical addition [129].

A method of choice to detect radicals is ESR spectroscopy (see section II.2.2 and appendix B) that the only technique allowing a direct detection of radicals and paramagnetic species. Again, as the lifetimes of ROS are much shorter than the time necessary to record an ESR spectrum (several minutes), it is necessary to use spin-trapping techniques based on the formation of radical-adducts with longer lifetimes.

ESR has been widely used to study oxidative and/or antioxidant properties in a number of scientific fields including biology [130], inorganic toxicochemistry [131, 132], food chemistry [133], environment [134] and catalysis [135]. ESR has also been applied to study in-situ formation of unidentified organic radicals in solutions containing cellulose and cellobiose [136]. It does not only work on liquid samples, but also on solid ones, and has been used in the field of cultural heritage for direct measurements on solid paper samples [137, 138], showing the occurrence of paramagnetic Iron(III) and unidentified organic radicals.

In this work, hydroxyl radicals were investigated both through ESR and reverse phase (RP)-HPLC with the terephthalic acid (TPA) method, this latter being specific to hydroxyl radicals and having a good sensitivity (very low limit of detection). Although the ESR detection limit is higher, this spectroscopic technique was also chosen because of the larger spectrum of the reactive oxygen species that can be investigated. Few ESR experiments were done directly on paper samples to assess the nature of the iron sites, but the majority

of the ESR experiments were done using spin-traps in aqueous solutions put in contact with paper samples previously impregnated with combinations of iron gall ink components. Some other sample solutions with the iron gall ink components were also prepared (section II.2.1) and used as useful model to interpret the results.

## II.2 Methods

### II.2.1 Sample preparation: From paper impregnation to liquid samples

#### a Impregnation of paper samples

Different types of solutions were prepared in milli-Q water (Millipore) using purified compounds: iron(II) sulfate heptahydrate  $\text{Fe}^{\text{II}}\text{SO}_4 \cdot 7 \text{H}_2\text{O}$  (99 %, Aldrich), iron(III) sulfate pentahydrate  $\text{Fe}_2^{\text{III}}(\text{SO}_4)_3 \cdot 5 \text{H}_2\text{O}$  (97 %, Sigma Aldrich) and gallic acid monohydrate (98 %, Sigma-Aldrich). The corresponding solutions will be hereafter called Fe2, Fe3 and Ac, respectively. Fe2 and Ac were also used in combination and the mixture will be referred to as Ink. This modern ink is, of course, not representative of all the past recipes and procedures which mentioned various ingredients and proportions; especially, gum arabic was not added to the model ink solution, because its role was shown to be mainly that of a physical barrier changing the diffusion of ink in paper but not the chemistry of the cellulose depolymerisation.

The aqueous solutions used for paper impregnation contained Fe2 or Fe3 ( $144 \text{ mmol} \cdot \text{L}^{-1}$  iron(II) or iron(III), respectively), Ac ( $53 \text{ mmol} \cdot \text{L}^{-1}$  gallic acid) or Ink ( $144 \text{ mmol} \cdot \text{L}^{-1}$  and  $53 \text{ mmol} \cdot \text{L}^{-1}$  Ac). Concentrations were among ranges found in original recipes and we considered such composition to be at least realistic in terms of chemistry of the degradation. A molar ratio of 3 was chosen for the ink solution. It corresponds to a large excess of iron, by analogy with what is believed to be the case for former iron gall inks [64]. Before impregnation, the ink solution was stirred for 3 days in a closed vessel to ensure formation of some iron(III) gallate compounds to which the blue color of the ink is attributed. Note that during the formation of this precipitate, the ink acidifies, as illustrated by FIG. II.2.

Impregnation consisted in immersing sheets of Whatman n°1 paper (100 % cotton) in the solutions for 10 min, then placing them between two Cobb blotting papers [139, 140]

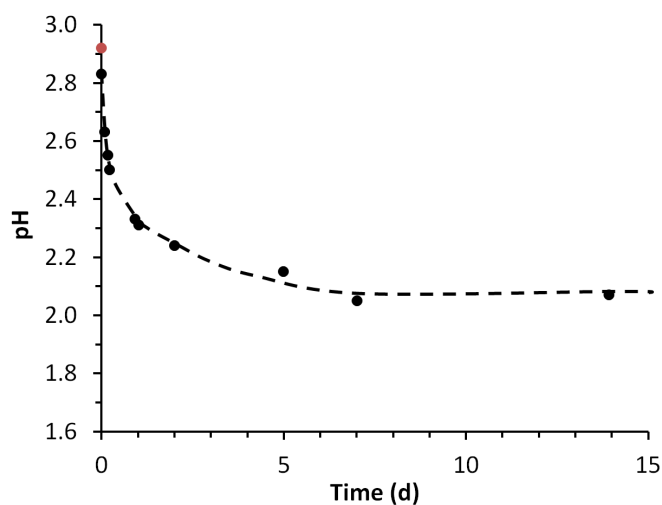


FIG. II.2 – Monitoring of model ink pH with time (black circle). Red circle represents pH of gallic acid solution.

and mopping up the excess of solution with a 10 kg roll back and forth. Each paper sheet was finally dried and naturally aged up to 70 days in a controlled atmosphere (23 °C and 50 % relative humidity).

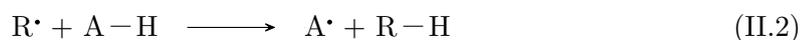
## b Liquid samples

Three types of sample solutions were prepared. The first type was obtained by placing 40 mg of paper (fresh or aged  $y$  days) in 0.5 mL of water in a vial; these samples are hereafter referred to as X-P $_y$  (paper solutions) where X is the impregnation component (Fe2, Fe3, Ac or Ink). The second type was prepared by putting 80 mg of X-impregnated paper (aged  $y$  days) in 1 mL of water; after 30 min under stirring, 0.5 mL of the supernatant was sampled, hereafter referred to as X-L $_y$  (leaching solutions). The third type consisted in model solutions (hereafter referred to as X-M $_z$ ) obtained by direct dissolution in 0.5 mL of water of the X ingredient at a given  $z$  concentration ( $\text{mmol} \cdot \text{L}^{-1}$ ); the Ink model solutions (Ink-M $_z$ ) correspond to diluted solutions of the ink used for paper impregnation, with varying Fe2 concentrations ( $z$  in  $\text{mmol} \cdot \text{L}^{-1}$ ), keeping the  $\frac{Fe}{Ac}$  ratio to 3.

## II.2.2 Electron spin resonance spectroscopy coupled with spin-trapping

### a Spin-trapping principle

On a general point of view, spin-trapping is achieved by the addition of the sought free radical (R $\cdot$ ) on the double bond of a diamagnetic spin-trap (SP) thus forming a relatively stable free radical (SP-R $\cdot$ ) (EQ. II.1), detectable by ESR and referred to as radical-adduct. In addition to spin-traps, intermediate target molecules H-A (commonly an alcohol or a formate anion) are often used: they react with a large spectrum of radicals and electrophilic species by homolytic scission of the H-A bond, providing an easier (yet unspecific) way of detection because the spin-trap adduct formed has a longer life-time (in the order of several tens of minutes instead of a few). The use of these target molecules is modeled by (EQ. II.2). Then, the new formed radical A $\cdot$  reacts with the spin-trap according to EQ. II.1.



Nitroxide spin-traps are commonly used as spin-traps. They lead to a multiple line spectrum due to their structure allowing an hyperfine coupling (see Appendix B). Indeed the unpaired electron (which is mainly localized on N and O atoms from N=O) interacts with the  $^{14}\text{N}$  nitrogen atom (spin  $I = 1$ ) and gives three lines of equivalent intensity separated from  $a_N$ , coupling constant proportionnate to spin density on nitrogen. If other paramagnetic nuclei are present in positions  $\alpha$ ,  $\beta$  or  $\gamma$  from the nitrogen atom, other splitting can occur. In general,  $\gamma$  couplings are not observed.

Two main categories of compounds are used as spin-traps:

- *nitroso based compounds*: 1-methyl-1-nitrosopropane (MNP) is one the nitroso trap the most used. With such a nitroso trap, the radical is added directly onto the nitrogen atom, allowing additionnal hyperfine coupling that helps identifying the trapped specie. However they have many drawbacks: i) nitroso compounds are

in equilibrium with a dimer inactive for spin-trapping and which is majoritary in water; ii) their oxygenated adducts are unstable, so it is not possible to use them for hydroxyl radicals detection for example; iii) they decompose with light and heat; iv) they are toxic.

- *nitrones*: pyrrolidines (such as 5,5-Dimethyl-1-Pyrroline-N-Oxide (DMPO)) or  $\beta$ -arylnitrones (as for example  $\alpha$ -(phenyl)-N-t-butylnitron (PBN) or  $\alpha$ -(4-pyridyl-1-oxide)-N-tert-butylnitron (POBN) ) are commonly used. They are rather stable and can be used in various media. They are specifically interesting to study oxygen-centered radicals, like reactive oxygen species. Their main drawback is the lack of information about the nature of the radicals since these latter are fixed on the carbon of the nitronyl group and not directly on the nitrogen. Thus, different radicals can lead to the same ESR signature.

In this study, a pyrrolidine type nitron was chosen among commercially available spin-traps because, as described,  $\beta$ -arylnitrones are not adequate to detect hydroxyl radicals (adduct decomposition) and differentiation of oxygen centred radicals is difficult. More specifically, DMPO was chosen because of its water solubility and of its ability to detect oxygen and carbon-centered radicals [132]. With hydroxyl radicals it forms a specific adduct which lifetime is around 5 min [141, 132, 142, 131] (FIG. II.3A). Formate anion was additionally used as target molecule in some of the experiments. This molecule reacts with radicals (including hydroxyl radicals) and non-radicals (such as iron oxo entities) electrophilic species according to reaction EQ.II.2 in which  $A^*$  is  $CO_2^-$  (FIG. II.4A). The produced carboxylate radicals (lifetime 1  $\mu$ s) are then trapped by the spin-trap, forming a final radical adduct ( $DMPO - CO_2^-$ ) whose lifetime is expected to be around 1 h (FIG. II.4B). As spin-trapping occurs in liquid phase, the experiments were carried out in solutions in which paper sheets had been previously immersed for a given period of time. For a better understanding of the measured signal, leaching and model solutions were additionally investigated to evaluate the impact of oxygen and pH on adducts formation.

## b Protocol

ESR experiments were carried out using several protocols (TAB.II.1) that differed by the type of sample (X- $P_y$ , X- $L_y$  or X- $M_z$ ), and by the nature and amounts of reactants solutions obtained by using: purified DMPO [132] (97 %, Sigma Aldrich) and POBN (99 %, Sigma Aldrich) as spin traps, sodium formate as target molecule (99 %, Merck) and 4-hydroxy-2,2,6,6-tetramethylpiperidin-1-oxyl (TEMPO) as stable radical (97 %, Sigma Aldrich). All solutions were prepared in milli-Q water (Millipore). The concentrations of DMPO ( $100 \text{ mmol} \cdot \text{L}^{-1}$ ) and sodium formate ( $4 \text{ mol} \cdot \text{L}^{-1}$ ) were chosen to ensure enough quantity of spin trap and target molecule in the medium as defined in a previous study[132].

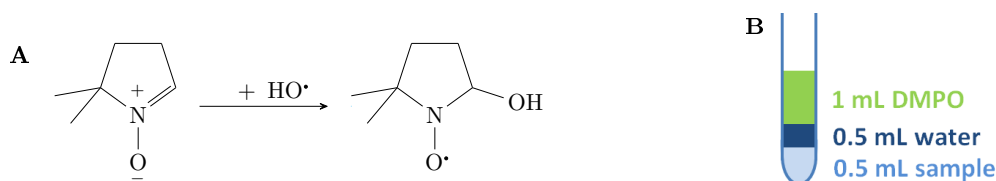


FIG. II.3 – The spin-trapping of hydroxyl radicals by DMPO: (A) reaction of spin-trapping and (B) protocol 1.

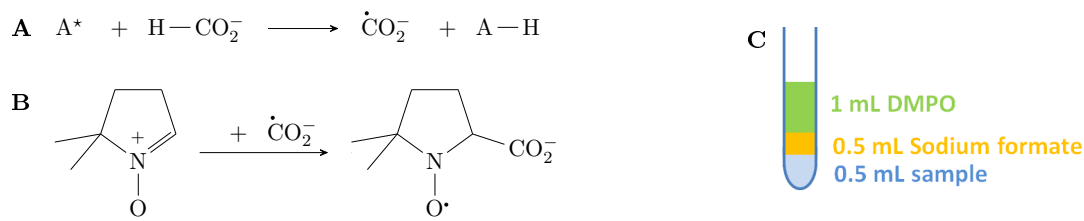


FIG. II.4 – Detection of electrophilic species with DMPO and sodium formate: (A) reaction of the electrophilic specie with formate, (B) reaction of spin-trapping and (C) protocol 2.

Protocol	Sample <sup>a</sup>		Reactant solutions <sup>b</sup>				Contact time <sup>c</sup>
	Type	Volume	Spin trap	TEMPOL (stable radical)	Sodium formate (target molecule)	water	
1	X-P <sub>y</sub>	0.5	1			0.5	5 and 30 min
2	X-P <sub>y</sub> ; X-L <sub>y</sub>	0.5	1		0.5		30 and 60 min
2'	X-M <sub>z</sub>	0.5	1		0.5		2 min
3	X-M <sub>z</sub>	0.5		1		0.5	2 min
4	X-M <sub>z</sub>	0.5		1	0.5		2 min

<sup>a</sup> sample solutions prepared i) by keeping the paper in contact with the DMPO/formate till analysis (paper sample solutions X-P<sub>y</sub>); ii) by taking only the supernatant (leaching solutions X-L<sub>y</sub>) and iii) by dissolving controlled concentrations of the X component (model solutions X-M<sub>z</sub>); X is the model component (X=Fe<sup>2+</sup>, Fe<sup>3+</sup>, Ac or Ink); y is the aging time of paper (in days); z is the iron concentration (in mmol · L<sup>-1</sup>)

<sup>b</sup> the concentrations of the aqueous reactant solutions were 100 mmol · L<sup>-1</sup> (DMPO), 27 μmol · L<sup>-1</sup> (TEMPOL) and 4 mol · L<sup>-1</sup> (sodium formate);

<sup>c</sup> time between spin trap/formate addition and aliquot sampling for ESR recording (solutions were kept under stirring in the dark).

TAB. II.1 – Protocols and compositions of the mixed solutions used for the ESR analyses (the total analyzed volume is 2 mL in each protocol).

The TEMPOL concentration (27 μmol · L<sup>-1</sup>) was selected to have high enough ESR signal intensity.

In each protocol, the sample was mixed with one (or two) reactant solution(s) then water was added, if needed, until completion to a total volume of 2 mL (TAB. II.1). Then, the mixed solution was kept at 23 °C under continuous stirring for given durations till ESR analysis. These steps were done in the dark to avoid photo-decomposition of DMPO and of DMPO radical adducts. Protocol 1 was dedicated to X-P<sub>y</sub> samples and involved only DMPO (FIG. II.3B). Protocols 2 and 2' were applied to X-P<sub>y</sub>, X-L<sub>y</sub> and X-M<sub>z</sub> samples using both DMPO and formate (FIG. II.4C). Protocols 3 and 4 concerned X-M<sub>z</sub> model solutions in presence of TEMPOL either with water (protocol 3) or with formate solution (protocol 4). Note that, in the above procedures, paper was still present in the X-P<sub>y</sub> samples (but not in the X-L<sub>y</sub> and X-M<sub>z</sub> samples) when DMPO (and eventually formate) was added. For all protocols, the pH of the analyzed solution was monitored (microelectrode Inlab Micro, Mettler Toledo).

### c Instrumentation

An ESR spectrometer is composed of various elements (FIG. II.5):

- an electromagnet creates the magnetic field  $B$ . The variation of current intensity in the coil allows scanning in magnetic field;
- a Gunn diode (generator) gives the microwave radiation;
- a cavity resonator contains the sample. The radiation creates a stationary wave

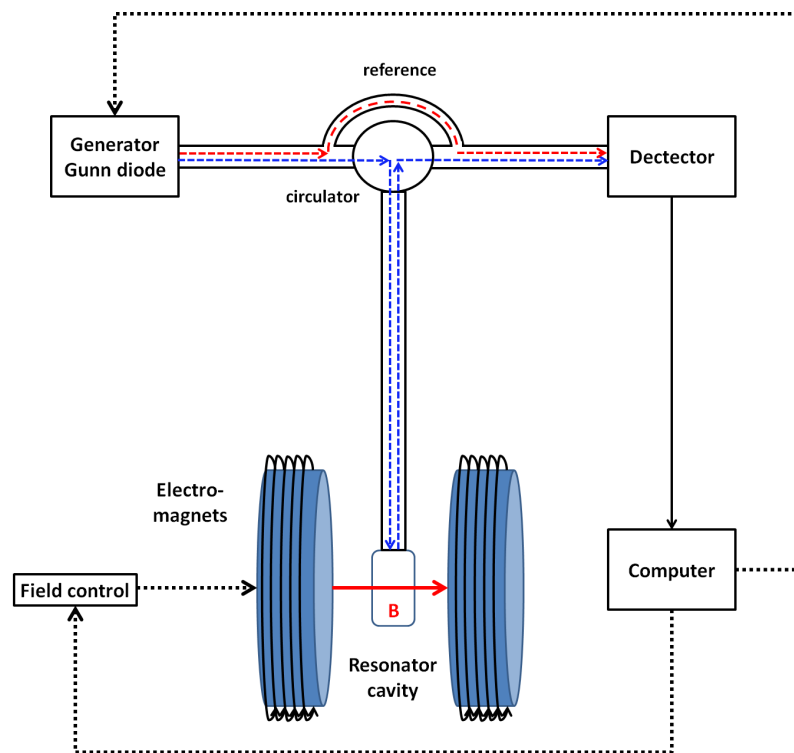


FIG. II.5 – Scheme of ESR spectrometer principle.

with a magnetic component perpendicular to the  $B$  field and an amplitude maximum at the center of the cavity;

- the dectector is a diode which has to work in the linear part in order to ensure that the absorption signal is proportional to the sqarred root of the power. To improve the sensitivity of the spectrometer, the detection technique is based on the modulation of the magnetic field. Under these conditions, the detector gives a signal proportional to the derivative  $\frac{ds}{dB}$  and not to the absorption;
- a special dewar can be used in the cavity to perform measurements at 77 K (with liquid nitrogen for example) in order to reach better resolution.

In the present study, the spectra were recorded on a JEOL  $FA - 300$  series ESR spectrometer working at the X band equipped with a  $TE011$  cylindrical cavity (FIG. II.6 A).

For liquid phase ESR experiments, an aqueous quartz flat cell (cell ES-LC12, JEOL, FIG. II.6B ) was used after milli-Q water washing. Approximately 1 mL of the 2 mL samples solutions was filtered through a filter with 0.2  $\mu\text{m}$  pore diameter (cellulose acetate, CHROMAFIL®CA, Macherey-Nagel) and placed in the analysis cell after previous rinsing. For liquid samples, the parameters were: 9.4 GHz microwave frequency, 100 kHz field modulation, 0.05 mT modulation width, 2 mW microwave power, 335.65 mT central field and sweep time of 2 min. The ESR signal intensity was obtained by double integration of the first peak (lowest  $B$  field) of the  $SP - R^{\bullet}$  multiplet signal. Before each series of measurements, blank experiments were systematically done with the spin-trap solution (DMPO) alone or with formate, in the same conditions as for the samples and the eventual small signals (impurity), when present, were subtracted from the measured solutions signals. A 10  $\mu\text{mol} \cdot \text{L}^{-1}$  TEMPOL stable radical solution was used as external



FIG. II.6 – (A) JEOL FA – 300 series ESR spectrometer and (B) JEOL quartz flat cell.

standard to convert signal intensity into adduct concentration (expressed in  $\mu\text{mol} \cdot \text{L}^{-1}$ , unless otherwise stated).

For the solid-state ESR experiments carried out on paper samples (in solid state without spin-trap), the paper sheet was cut into tiny pieces and inserted into quartz tubes of 5 mm diameter. The measurements were done both at room temperature and at 77 K (liquid  $\text{N}_2$ ) using a quartz dewar inserted into the cavity. The same spectrometer as above was used at 9.1 GHz microwave frequency. The parameters were: 100 kHz field modulation, 0.07 mT modulation width, 2 mW microwave power, 410.00 mT central field and sweep time of 4 min for solid samples.

### II.2.3 Determination of hydroxyl radicals by RP-HPLC

#### a HPLC principle

Liquid chromatography is a separation technique that is based on a tripartite interaction: interaction of the solute with a mobile phase (solvent) and stationary phase (porous particles stock in a column). The separation of different analytes in the column comes from their different affinity for the mobile and stationary phases. In HPLC, the porous particles are tiny (diameter of 3  $\mu\text{m}$  to 5  $\mu\text{m}$ ) and the mobile phase is forced through the column by high pressure delivered by a pump. The detection is made with a detector, such as a photodiode array detector (PDA)[143].

Regarding more especially reverse phase liquid chromatography (RP-HPLC), the stationary phase is non-polar (e.g.  $\text{C}_{18}$ ,  $\text{C}_8$ ,  $\text{C}_3$ , phenyl, ...) and the mobile phase is composed of a mixture of water (buffered) and water-miscible organic solvent, such as methanol or acetonitrile. It can be used for a wide range of molecules: non-polar, polar, ionizable and ionic. A gradient elution is often used to ease the separation: the composition of the mobile phase is changing with elution time. First, the mobile phase contains mainly water and then organic solvent is added to increase the solvent strength and allows the elution of strongly retained solute [143].

#### b Terephthalic acid (TPA) hydroxylation assay

TPA (98 %, Sigma Aldrich) was used to quantify hydroxyl radicals in papers using RP-HPLC with ultra-violet (UV) and fluorescence detection according to a method detailed elsewhere [107]. One hour after their pre-impregnation with ink or  $\text{Fe}_2$  solutions, the paper samples were impregnated with a methanolic solution of TPA (2 mL,  $0.41 \text{ g} \cdot \text{L}^{-1}$ , resulting TPA uptake of  $7 \mu\text{mol} \cdot \text{g}^{-1}$  of paper), as illustrated FIG. II.7). They were then

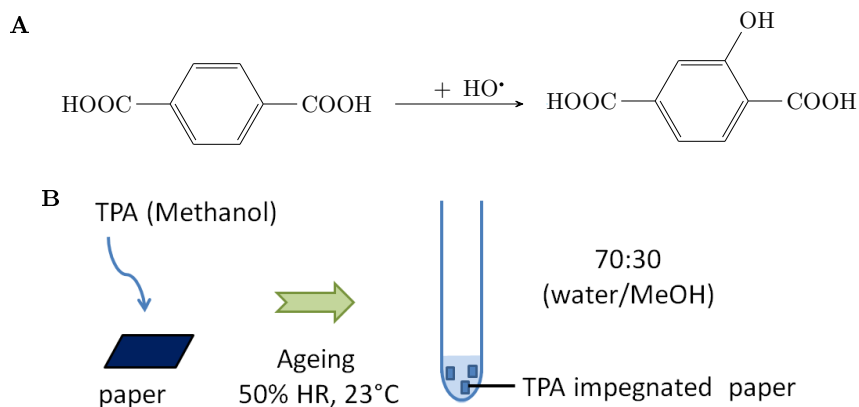


FIG. II.7 – Hydroxyl radicals detection on paper samples: (A) reaction of terephthalic acid (TPA) hydroxylation and (B) protocol for hydroxyl radicals detection on paper.



FIG. II.8 – Agilent 1100 series HPLC system.

dried and stored at 23 °C and 50 % relative humidity (referred hereafter as natural ageing, similar to ageing conditions described in section 2.1).

After given periods of ageing, the remaining TPA and the formed hydroxyterephthalic acid (HTPA) (produced by reaction of TPA with  $\text{HO}^\bullet$ ) were extracted from paper and HTPA was quantified by RP-HPLC/UV/fluorescence detector (FLD). This was done by immersing 40 mg of paper for three hours under constant stirring at room temperature in 1.2 mL of a 7:3 water:methanol (HPLC grade) mixture, then filtering the extract on 0.2  $\mu\text{m}$  pores polytetrafluoroethylene (PTFE) syringe filters (Macherey Nagel). Analysis was done with an Agilent 1100 series HPLC system (FIG. II.8) equipped with a vacuum degasser, a quaternary pump, a FLD (excitation and emission wavelengths of 250 nm and 440 nm, respectively) and a PDA (245 nm). Separation was carried out at 30 °C on a Pursuit  $C_{18}$  column ((2.1 mm  $\times$  100 mm, 5  $\mu\text{m}$  particle-diameter, Varian) preceded by a guard cartridge (Security-Guard, Phenomenex). The system was operated in an isocratic mode with a mixture of 70 %  $\text{KH}_2\text{PO}_4$  (50  $\text{mmol} \cdot \text{L}^{-1}$ , pH 3.2 adjusted with phosphoric acid 1  $\text{mol} \cdot \text{L}^{-1}$ ) and 30 % methanol, a flow rate of 0.2  $\text{mL} \cdot \text{min}^{-1}$  and a sample injection volume of 10  $\mu\text{L}$ . The system operation, data acquisition, calibration and quantitation were performed using ChemStation software for LC 3D systems (Agilent). The HTPA amounts were normalized with respect to paper weight and expressed in  $\text{nmol} \cdot \text{g}^{-1}$ . TPA analysis is known to be highly sensitive towards  $\text{HO}^\bullet$  detection (through HTPA formation), of the order of the nanomole per gram of paper (limit of detection of 1.5  $\text{nmol} \cdot \text{L}^{-1}$  and limit of quantification of 3  $\text{nmol} \cdot \text{L}^{-1}$ )[107]. Thanks to the chemical stability of

TPA and HTPA, it enables the quantification of all hydroxyl radicals formed after TPA impregnation and accumulated during ageing time. Despite these encouraging points, application of TPA hydroxylation assay to the study of iron impregnated papers since the iron leaching occurring during the experiments (see section II.3.3) provoked obstruction of the chromatographic columns. Solving this problem with commercial filtration cartridges was attempted but induced a lot of impurities in our sample, so it was not used further. For this reason, only a few hydroxylation assays were performed.

## II.2.4 Iron quantification by UV-visible spectroscopy

In order to evaluate possible iron leaching in solution, iron concentrations in solution were measured by UV-Visible spectroscopy, using 2,2-bipyridyl (99.5 %, Merck) and potassium thiocyanate (99 %, Sigma-Aldrich), which are chelating agents able to form specific colored complexes with  $\text{Fe}^{2+}$  and  $\text{Fe}^{3+}$ , respectively (stability constants of 17 [144, 145] and 2.3 [146, 147], respectively). This was done on leaching solutions that were prepared as described above, but in higher volumes (total volume 8 mL), in order to allow UV-Visible spectroscopic measurements. These solutions were moreover appropriately diluted (as in protocol 2, TAB. II.1) to reach a final “paper/volume of solution” ratio identical to that of the ESR analyzed final solutions.

The solutions were sampled and placed into 50 mL flasks that already contained the reactants for iron dosage. For iron(II) determination, the bipyridyl final concentration was  $0.45 \text{ mmol} \cdot \text{L}^{-1}$ , after completion with a phosphate buffer ( $25 \text{ mmol} \cdot \text{L}^{-1}$ ) prepared with sodium phosphate monobasic anhydrous (99 %, Merck) and with sodium phosphate dibasic anhydrous (99 %, Merck). The pH of the final solution was 6. For iron(III) determination, the reactants were sulfuric acid and potassium thiocyanate with final concentrations at  $4 \text{ mmol} \cdot \text{L}^{-1}$  and  $0.85 \text{ mol} \cdot \text{L}^{-1}$ , respectively. The pH of the solution was 2. Spectroscopic measurements were done with a V-570 JASCO UV-Visible spectrometer. Quantifications were done from previously established calibration curves (see appendix C), by converting to concentration the absorbance at 523 nm for iron(II) and at 479 nm for iron(III) (signal maxima,  $\lambda_{max}$ ).

## II.3 Results and discussion

### II.3.1 Spectroscopic signatures of spin traps adducts

#### a Investigation of hydroxyl radicals

The first ESR spectroscopy experiments were carried out on Ink- $\text{P}_y$ , Fe2- $\text{P}_y$  and Ac- $\text{P}_y$  solutions according to protocol 1 (presence of only DMPO as reactant, TAB. II.1) with the aim to identify possible hydroxyl radicals formation during cellulose degradation. Whatever paper ageing, no signal was detected (FIG. II.9A, upper part). Especially, the four lines with 1:2:2:1 relative intensities characteristic of the DMPO–OH• adduct (see appendix B,  $g = 2.0054$ ;  $a_N = a_{H\beta} = 1.49 \text{ mT}$ ) [132] were not observed, revealing that, even if present, hydroxyl radicals remained at concentrations below detection limits (estimated in our experiments close to  $1 \text{ } \mu\text{mol} \cdot \text{L}^{-1}$ , i.e.  $50 \text{ nmol} \cdot \text{g}^{-1}$  of paper). Similarly, tests performed with POBN as spin trap, did not show any formation of POBN–OH• adduct (FIG. II.10), in line with the fact that half-life is around 30 times shorter for POBN–OH• adducts than for DMPO–OH• ones.

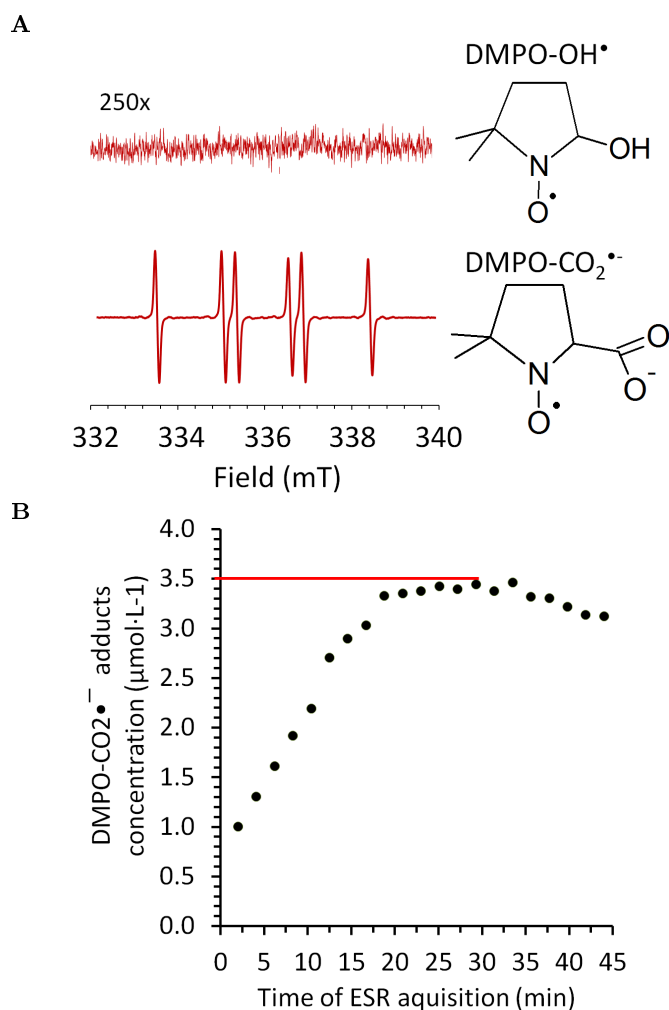


FIG. II.9 – (A) Typical ESR signals of Ink- $P_7$  solutions in presence of DMPO alone (top) or used in combination with formate (bottom) and schemes of the related expected DMPO-OH• and DMPO-COO•<sup>-</sup> radical adducts, if present; (B) Typical evolution with time of the DMPO-COO•<sup>-</sup> signal intensity (taking as example the Ink- $P_7$  solution after 60 min of mixing).

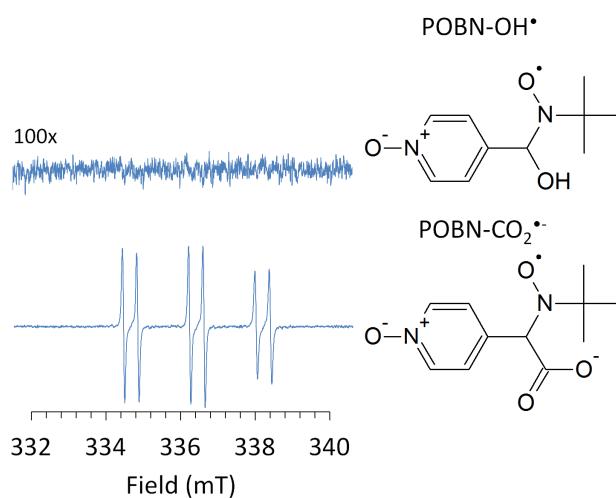


FIG. II.10 – Typical ESR signals of Ink- $P_7$  solutions in presence of POBN alone (top) or used in combination with formate (bottom) and schemes of the related expected POBN-OH• and POBN-COO•<sup>-</sup> radical adducts, if present.

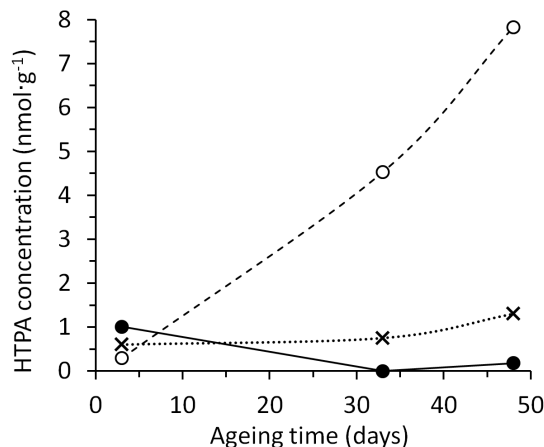


FIG. II.11 – HTPA concentrations (normalized with respect to paper weight) detected by HPLC upon ageing of a blank paper (cross) and paper impregnated with Ink (full circle) or Fe2 (empty circle).

The plausible formation of DMPO – OH• adduct immediately followed by decomposition into ESR silent molecule (hydroxylamine) was investigated (see appendix B.4 section B.4.2) and inconclusive. Such absence of ESR detectable HO• is also coherent with the low hydroxyl radicals content that was found by TPA hydroxylation experiments performed on Ink and Fe2 impregnated papers at different ageing durations (FIG. II.11). On the inked paper, the amount of HTPA (full circles, FIG. II.11) was below control curve (cross, FIG. II.11) and also negligible. On the Fe2 impregnated paper (empty circles, FIG. II.11), some HTPA was found at concentrations that increased with storage time, in line with the cumulative nature of the measurement. Nevertheless, the cumulative amount of OH• formed within fifty days was about 8 nmol · g<sup>-1</sup>, a value below the DMPO/ESR detection limit (in accordance with above absence of ESR signal). All these data reveal that, even if present, hydroxyl radicals always remain at very low (negligible) concentrations.

## b Investigation of other radicals

On the contrary, the addition of formate in the Ink-P<sub>y</sub> solutions containing DMPO (protocol 2) systematically gave rise to a well identified spectrum with six hyperfine lines of same intensity (FIG. II.9A, lower part) and constants ( $g = 2.0041$ ,  $a_N = 1.581$  mT and  $a_{H\beta} = 1.894$  mT) typical of the DMPO – CO<sub>2</sub><sup>-</sup> radical anion adduct [132]. These six hyperfine lines result i) from a primary triplet splitting due to the N nucleus and ii) from a secondary doublet splitting due to the β-hydrogen present in the adduct molecule.

A typical evolution of the ESR signal intensity as a function of time is represented in FIG. II.9B, showing an initial increase of the signal, then a stabilization at a maximum value, afterwards the DMPO – CO<sub>2</sub><sup>-</sup> adduct content progressively decreases. This arises from the fact that the DMPO – CO<sub>2</sub><sup>-</sup> concentration in the medium results from a combination of i) adducts formed by spin-trapping that accumulate with radical production and ii) of adducts progressively lost by decomposition due to their half-life (of the order of one hour)[132].

Comparable tests, performed with POBN and formate, similarly resulted in the emergence of an ESR six lines spectrum of same relative intensity with signature ( $g = 2.0030$ ,  $a_N = 1.560$  mT and  $a_{H\beta} = 0.344$  mT) characteristic of the POBN adduct in presence of scavengers (FIG. II.10).

Sample	DMPO – CO <sub>2</sub> <sup>•-</sup> concentrations ( $\mu\text{mol} \cdot \text{L}^{-1}$ )
Ink-P <sub>1</sub>	12.2 ± 1.6
Ink-P <sub>7</sub>	8.2 ± 0.6
Ink-P <sub>21</sub>	7.0 ± 1.0
Ink-L <sub>7</sub>	7.8 ± 0.4
Ink-M <sub>2,1</sub>	11.2 ± 2.6
Fe2-P <sub>1</sub>	9.6 ± 3.4
Fe2-P <sub>7</sub>	6.2 ± 1.2
Fe2-P <sub>21</sub>	4.8 ± 0.2
Fe2-L <sub>7</sub>	4.4 ± 1.0
Fe2-M <sub>2,1</sub>	2.6 ± 0.4
Fe2-M <sub>1</sub>	4.2 ± 1.0
Fe3-P <sub>7</sub>	<i>n.d.</i>
Fe3-M <sub>2,1</sub>	0.4 ± 0.4
Ac-P <sub>7</sub>	<i>n.d.</i>
Ac-M <sub>0.71</sub>	<i>n.d.</i>

TAB. II.2 – Concentration of DMPO – CO<sub>2</sub><sup>•-</sup> adducts in solution samples as estimated from ESR measurements carried out with protocol 2. Reported values are average values of 3 samples with standard deviations. *n.d.* : no detected signal.

For quantitative comparison purpose, the maximum intensity values (as highlighted by the red line in FIG. II.9) were considered and converted, from TEMPOL calibration to DMPO – CO<sub>2</sub><sup>•-</sup> adduct concentrations in solution. TAB. II.2 lists all DMPO – CO<sub>2</sub><sup>•-</sup> concentrations thus measured in the three series of samples (X-P<sub>y</sub>, X-L<sub>y</sub> and X-M<sub>z</sub>). Except for few of them, which will be discussed in next sections, the concentrations are significant, revealing the presence of DMPO – CO<sub>2</sub><sup>•-</sup> adducts in most samples, in contrast with the DMPO – OH• adducts that were not detected (as seen above). Interestingly, hydroxyl adducts were similarly not found in former studies [131, 148] on iron(II) containing solutions, neither with DMPO in water [131] nor with phosphate buffer [131, 148], whereas a significant amount of them appeared when formate anions [131] or ethanol [148] were added as scavengers to the medium.

It has been proposed in the literature that iron(III) (an oxidant) could facilitate nucleophilic addition of water on DMPO and lead to DMPO – OH• adduct formation without any input from “true” hydroxyl radicals [149, 150, 151, 152] (see appendix B.3). From experimental data discussed above, it is clear that such hypothesis can be ruled out in our samples since no significant DMPO – OH• adduct signature could be found. Then, the species at the origin of the DMPO – CO<sub>2</sub><sup>•-</sup> adducts should differ from solely hydroxyl radicals and the question of their nature and of the possible role of iron in their formation is raised.

### II.3.2 Conditions for spin traps adducts detection

Before comparing the DMPO – CO<sub>2</sub><sup>•-</sup> concentrations found in the different solution samples, it should be recalled that protocol 2 differed from protocol 1 not only in the addition of formate but also in pH value. Indeed, formate at high concentration acts as a buffer, giving a circumneutral medium in protocol 2 (pH 6.5), while it is acidic with protocol 1

(pH 3.5). Since pH may have an effect on signal intensity, it appeared necessary, before discussing the data, to evaluate such possible effect.

To this end, comparative ESR spectroscopy measurements were done on the same Ink-P<sub>7</sub> solution while changing the pH, either by buffering the medium (with phosphate, in protocol 1, to reach pH of 7 instead of 3.5 without buffer) or by acidifying it (with sulfuric acid in protocol 2, to reach pH 4.7 instead of 6.5 without acid addition). In both cases, no ESR signal was observed, giving two information: firstly, pH is not responsible for the non-detection of DMPO – OH•, these adducts being never observed, whatever the conditions; secondly, DMPO – CO<sub>2</sub><sup>•-</sup> adducts formation is pH dependent since it occurred in neutral conditions (section II.3.1) but is no longer detected in acidic ones, even at a pH value of 4.7 that is one unit above the 3.75 pKa value of formic acid (in principle high enough to have excess formate anions in the solution). Hence, it appears that great care should be taken with experiments, for proper quantitative study of adducts formation, two prerequisite being neutral pH and the presence of a scavenger.

Another important factor is oxygen, which role on the signal intensity was proved by performing again protocol 2 on the Ink-P<sub>7</sub> solution, but under argon bubbling, so as to achieve oxygen concentrations below 1.7 mg · L<sup>-1</sup> (instead of approximately 8 mg · L<sup>-1</sup> under ambient atmosphere). This resulted in the total signal disappearance, showing that DMPO – CO<sub>2</sub><sup>•-</sup> production is oxygen dependent as well.

For the sake of completion, measurements were also carried out with protocol 2 to identify which of the ink components is involved in adducts production (TAB. II.2 ). No signal was detected with the Ac-P<sub>7</sub> and Fe3-P<sub>7</sub> liquid samples. Conversely, Fe2-P<sub>7</sub> led to an adduct content of 6.2 μmol · L<sup>-1</sup>, similar (within the error bars) to that obtained with Ink-P<sub>7</sub> (8.2 μmol · L<sup>-1</sup>). Therefore, the initial use of ferrous iron to impregnate the paper seems to be determinant as well for adducts production.

### Spin-traps adducts observed with ESR spectroscopy and condition for their detection.

Adducts characteristic from hydroxyl radicals were not evidenced by spin-trapping coupled with ESR spectroscopy. This point is coherent with the HPLC experiments with TPA that allowed detection of hydroxyl radicals in some samples (Fe2 papers) but in much smaller quantities than the ESR detection limit. However, the combined use of a spin-trap (DMPO) with a target molecule (formate anions) allowed to evidence a signal in all the iron(II) bearing samples, suggesting the presence of another ROS than hydroxyl radicals. The formation of the DMPO – CO<sub>2</sub><sup>•-</sup> adduct is linked to a close to neutral pH, to the presence of oxygen, but also on the initial presence of iron(II) in the medium.

### II.3.3 Effect of paper ageing on DMPO-formate adducts concentrations and leaching phenomena

#### a Evolution of DMPO-formate adducts concentrations with paper ageing

Having above detection limitations in mind (need of a neutral pH, of a scavenger and of oxygen), protocol 2 was used to investigate the influence of ageing time of paper on the amount of detected radicals. The curve of DMPO – CO<sub>2</sub><sup>•-</sup> concentrations in the Ink-P<sub>y</sub> solutions versus ageing time y (FIG. II.12A) shows a rapid increase within the first ten

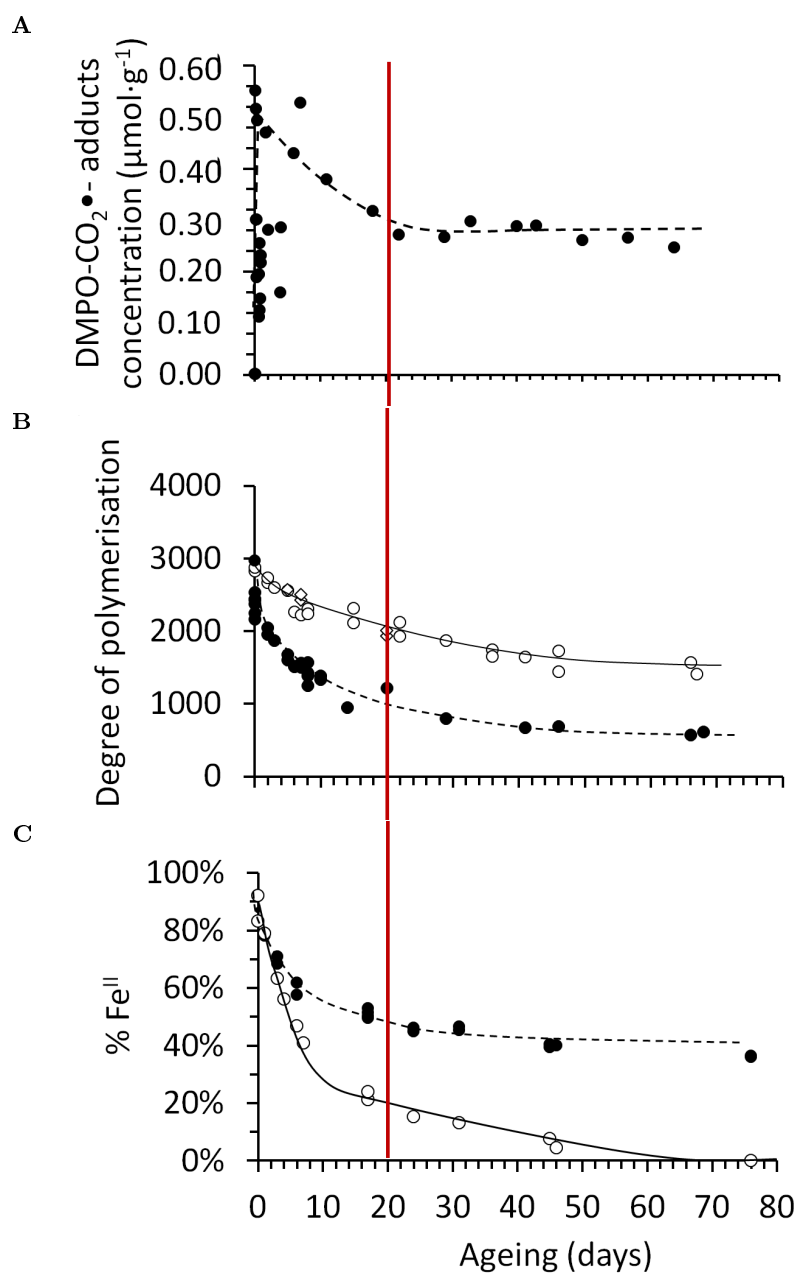


FIG. II.12 – Evolution with paper ageing of ESR measurements (A), degree of polymerization (B) and proportion of ferrous iron (C). (A) DMPO – CO<sub>2</sub><sup>•-</sup> concentrations determined by ESR on ink-P<sub>y</sub> solutions following protocol 2. Values are normalized with respect to paper weight; (B) Viscosimetry measurements; (C) XANES measurements at the Fe K-Edge (from Rouchon et al.[111]). Inked (full circle) or Fe<sub>2</sub> impregnated papers (empty circle).

Sample	iron concentrations ( $\text{mmol} \cdot \text{L}^{-1}$ )			$\% \text{Fe}^{2+} / \text{Fe}_{\text{total}}$	%Fe leached <sup>a</sup>
	$\text{Fe}^{2+}$	$\text{Fe}^{3+}$	$\text{Fe}_{\text{total}}$		
Ink-L <sub>1</sub>	2.39	<i>n.d.</i> <sup>b</sup>			
Ink-L <sub>7</sub>	2.19	<i>n.d.</i> <sup>b</sup>			
Ink-L <sub>21</sub>	1.94	<i>n.d.</i> <sup>b</sup>			
Fe2-L <sub>1</sub>	2.58	0.05	2.63	98 %	87 %
Fe2-L <sub>7</sub>	1.12	0.54	1.66	67 %	55 %
Fe2-L <sub>21</sub>	0.75	0.74	1.49	50 %	50 %

<sup>a</sup> estimation based on an initial iron concentration in the paper of  $8.5 \text{ mg} \cdot \text{g}^{-1}$ .

<sup>b</sup> not determined because gallic acid–iron chelates (present in Inks) compete with thiocyanate–iron chelates (complex allowing iron quantification), prohibiting the quantitative analysis.

TAB. II.3 – Iron quantification in leaching solutions as determined by UV/VIS spectroscopy (precision  $\pm 0.05$ ).

hours of ageing, followed by a slow decrease, then a stabilization after twenty days of ageing. Moreover, the data are largely scattered within the first twenty days of ageing, but more stable afterwards.

Interestingly, these trends show some similarities with the evolutions of the degree of polymerization of cellulose (FIG. II.12B, full circles) and iron(II) contents (FIG. II.12C, full circles) recently discussed for analogous inked papers aged in similar conditions [111]. This could suggest that the three processes originate from a common degradation mechanism possibly involving radicals formed in the paper sheet during storage. Nevertheless, it has to be reminded that the ESR spin trap data (FIG. II.12A) were obtained from experiments performed in solution while the two other measurements (FIG. II.12B and FIG. II.12C) were done in the solid phase. Moreover, the ink ingredients are water-soluble. Hence, it appeared necessary to check if the radicals evaluated in FIG. II.12A indeed come from species constitutive of the inked paper sheets themselves, or if they could be related to other species possibly leached in solution under the ESR analysis conditions.

#### DMPO – CO<sub>2</sub><sup>-</sup> ESR signal intensities evolution with paper ageing.

The concentration of the DMPO – CO<sub>2</sub><sup>-</sup> adducts evolved depending on the duration of the paper storage: within the first day of ageing, the production of the maximum adducts increase and then decrease to stabilized. This phenomenon might be linked to depolymerisation of cellulose which is also important within the first day of ageing.

### b Leaching phenomena

In fact, the occurrence, and even the importance of leaching phenomena in the conditions of spin trapping experiments was demonstrated by the iron concentrations evaluated by UV-Visible spectroscopy in the X-L<sub>y</sub> samples (X=Ink or Fe2), which consist in paper extracts (section II.2.1). In TAB. II.3, the concentrations in Fe<sup>2+</sup> (column 2), Fe<sup>3+</sup> (column 3), total soluble iron (column 4) and the molar Fe<sup>2+</sup>/Fe<sub>total</sub> ratio (column 5) are successively reported, together with the percentage of leached iron (column 6) calculated by considering an initial iron concentration of  $8.5 \text{ mg} \cdot \text{g}^{-1}$  in the paper as previously determined by atomic absorption spectroscopy [153]. These data lead to several observations.

Firstly, iron was always detected in solution, indicating that leaching systematically took place and involved an important amount of iron. Considering the Fe2-L<sub>y</sub> samples,

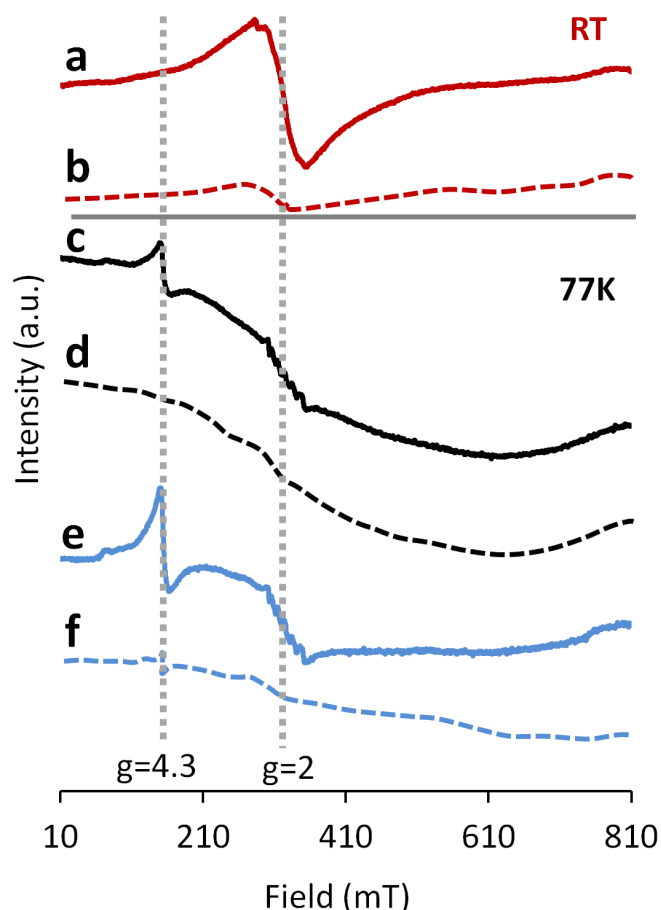


FIG. II.13 – Solid-state ESR spectra recorded at room temperature (a,b) and at 77 K (c-f) before (plain lines) and after (dotted lines) water washing. Red (a,b) and blue curves (e,f) correspond to  $Fe_2-P_{21}$  sample and black curves (c,d) to  $Fe_2-P_1$  sample.

the percentage of leached iron was between 50 % and 87 %, depending on paper ageing.

Secondly, the iron release systematically decreased versus paper ageing (TAB. II.3, column 4) revealing that the iron containing phases present in the impregnated papers became, on average, less soluble with time. In the first phase of ageing, iron was mainly leached as  $Fe^{2+}$  (TAB. II.3, column 2), yet  $Fe^{3+}$  release gradually increased to become comparable to  $Fe^{2+}$  release (21 days ageing, TAB. II.3, column 3).

These trends were also confirmed by solid-state ESR measurements performed directly on papers impregnated with Fe2 and carried out before and after water washing. The first measurement taken at ambient temperature (FIG. II.13, spectra a and b) allowed to reveal the presence of pseudo-octahedral  $Fe^{III}$  complexes (possibly hydrated complexes where  $Fe^{III}$  is bound to one or more water molecules or hydroxyl groups of cellulose)[154]. Afterwards, the spectra were recorded at 77 K (FIG. II.13, spectra c to f), which enabled the detection of isolated rhombic  $Fe^{III}$  sites (signature at  $g=4.3$ ) [154]. An additional signature around  $g=2$  with six-hyperfine lines was assigned to  $Mn^{2+}$  impurities coming from iron sulfate. More importantly, FIG. II.13 shows that a great part of  $Fe^{III}$  was leached during water washing. This concerned both octahedral  $Fe^{III}$  (FIG. II.13, spectrum b) and rhombic sites (FFIG. II.13, spectra d and f). These latter totally disappeared when washing was performed on the paper aged one day (FIG. II.13, spectrum d), and only

part of them remained attached to the paper for the paper aged twenty-one days (FIG. II.13, spectrum f). All these data clearly evidence that substantial iron leaching takes place during preparation of the X-P<sub>y</sub> solution samples for ESR analysis.

#### Leaching phenomenon.

The protocol of spin-trapping being carried out in solution, the determination of possible iron leaching in solution was necessary. Determination of iron concentrations by UV-visible spectroscopy revealed that iron leaching from the paper samples was important and decreased with the ageing time of the paper. This latter point was illustrated by a stronger attachment of the iron(III) to the paper samples.

### II.3.4 From leached to model solutions

The important iron leaching in the X-P<sub>y</sub> solution samples strongly questions its impact on ESR signals. This question is easily answered by comparing the DMPO – CO<sub>2</sub><sup>•-</sup> adducts concentration in the X-P<sub>y</sub> (paper solution) and X-L<sub>y</sub> (leached solution) samples (TAB. II.2) : firstly, this concentration in Ink-P<sub>7</sub> ( $8.2 \pm 0.6 \mu\text{mol} \cdot \text{L}^{-1}$ ) is very close to the one in Ink-L<sub>7</sub> ( $7.8 \pm 0.4 \mu\text{mol} \cdot \text{L}^{-1}$ ); secondly, the value in Fe2-P<sub>7</sub> ( $6.2 \pm 1.2 \mu\text{mol} \cdot \text{L}^{-1}$ ) is only slightly above the one in Fe2-L<sub>7</sub> ( $4.4 \pm 1.0 \mu\text{mol} \cdot \text{L}^{-1}$ ), the difference being within margin error. Hence, the ESR signals detected in the Ink-P<sub>y</sub> solution samples seem not to come from the paper itself (neither from paper degradation processes) but rather predominantly from soluble iron species leached from it. Yet, measuring the impact of the leached species and understanding their origin and their behaviour remains of keen interest for a better comprehension of paper degradation processes since iron dissolution can as well happen at a micro scale in paper fibers when these latter are exposed to high humidity conditions [49, 155]. The leached species as those identified above could be present and play a role in the degradation.

To further investigate the impact of iron leached species on radical adducts formation, complementary measurements were undertaken on model X-M<sub>z</sub> solutions prepared by direct dissolution in water of the X ingredient, with no paper involved. The chosen iron concentration in Ink-M<sub>z</sub>, Fe2-M<sub>z</sub> and Fe3-M<sub>z</sub> was  $2.1 \text{ mmol} \cdot \text{L}^{-1}$ , as inspired by the Fe<sup>II</sup> content in Ink-L<sub>7</sub> (TAB. II.3), and the gallic acid concentration in Ac-M<sub>z</sub> was taken equal to  $0.7 \text{ mmol} \cdot \text{L}^{-1}$  (to keep a Fe/Ac molar ratio of 3 as in Ink-M<sub>z</sub>). Fe<sup>II</sup> free solutions (Fe3-M<sub>2.1</sub> and Ac-M<sub>0.7</sub>) yielded no ESR signal (TAB. II.2) whereas DMPO – CO<sub>2</sub><sup>•-</sup> adducts were systematically detected in iron(II) based solutions, respectively at  $2.6 \mu\text{mol} \cdot \text{L}^{-1}$  and  $11.2 \mu\text{mol} \cdot \text{L}^{-1}$  for Fe2-M<sub>2.1</sub> and Ink-M<sub>2.1</sub> (TAB. II.2). These observations, as well as the similar concentration ranges in Fe2-M<sub>2.1</sub> and Ink-M<sub>2.1</sub> than in X-P<sub>y</sub> samples (TAB. II.2), demonstrate again the essential role of leached Fe<sup>II</sup> ions in the detected ESR signals. This is consistent with former studies reporting (i) no formation of DMPO – CH<sub>3</sub>CHOH• adducts in iron(III) solutions [148] and (ii) weaker DMPO – CO<sub>2</sub><sup>•-</sup> adduct formation with higher Fe<sup>III</sup>/Fe<sup>II</sup> ratio [131].

Additional ESR spectroscopy measurements were done on model solutions (protocol 2', TAB. II.1) to identify the effect of iron concentration on adducts production. To this end, Ink-M<sub>z</sub> and Fe2-M<sub>z</sub> solutions were prepared to reach iron concentrations in the range  $0.01 \text{ mmol} \cdot \text{L}^{-1}$  to  $10 \text{ mmol} \cdot \text{L}^{-1}$  for the analyzed spin trapping solution (after DMPO and eventually formate addition). At low Fe<sup>II</sup> concentrations, the DMPO – CO<sub>2</sub><sup>•-</sup>

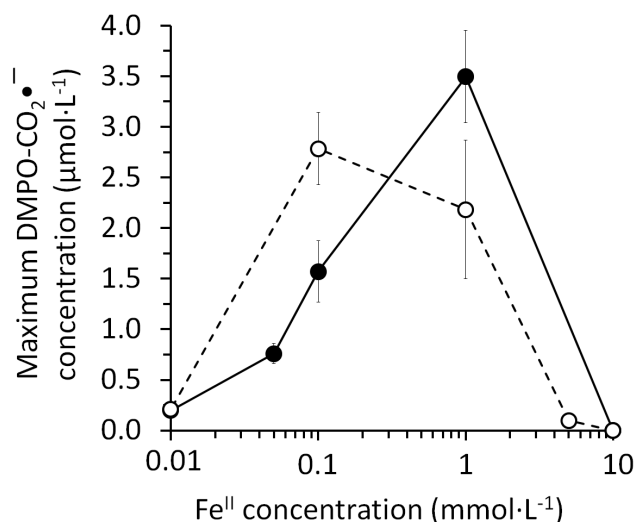


FIG. II.14 – DMPO – CO<sub>2</sub><sup>-</sup> adducts concentrations versus initial iron II sulfate concentration in Fe2-M<sub>z</sub> (empty circle) and Ink-M<sub>z</sub> (full circle) solutions.

signal increased with Fe<sup>II</sup> content, for both Fe2-M<sub>z</sub> and Ink-M<sub>z</sub> (FIG. II.14), but it drastically dropped at higher contents (concentrations above 0.1 mmol · L<sup>-1</sup> for Fe2-M<sub>z</sub> and 1 mmol · L<sup>-1</sup> for Ink-M<sub>z</sub>) till disappearing when the Fe<sup>II</sup> concentration reached 10 mmol · L<sup>-1</sup>. Although amazing, such two-phase behavior was already reported for DMPO – CO<sub>2</sub><sup>-</sup> [131] and DMPO – CH<sub>3</sub>CHOH<sup>-</sup> [148] adducts production in presence of Fe<sup>II</sup>. The initial increase (left of FIG. II.14, low Fe<sup>II</sup> concentration) was a priori expected since it follows the concentration in the medium of the Fe<sup>II</sup> ions that are responsible for adducts production. The rapid decrease at Fe<sup>II</sup> concentrations above 1 mmol · L<sup>-1</sup> was however hardly expectable.

A possible explanation for this decrease could be an interaction between iron and formate, potentially leading to formate consumption, but such hypothesis can be ruled out because formate was present in great excess (1 mol · L<sup>-1</sup>) compared to iron (<10 mmol · L<sup>-1</sup>), in the analysed solution, hence enough formate is always available for DMPO – CO<sub>2</sub><sup>-</sup> adducts formation. More probably, the decrease of the signal could be related to some interaction between iron and DMPO leading to a degradation of the DMPO-radical adducts. Such type of interaction has already been proposed in term of formation of a chelate between Fe<sup>III</sup> and DMPO [149]. Another option would be to attribute such disappearance to pH changes since i) pH was shown above to potentially affect adducts concentrations (II.3.2) and ii) pH decreased (though slowly) upon increase of iron(II) concentration in both Fe2-M<sub>z</sub> (empty circles, FIG. II.15) and Ink-M<sub>z</sub> solutions (full circles, FIG. II.15). Such pH effect would be in accordance with a previous report in which the ESR signal of 5 mmol · L<sup>-1</sup> Fe<sup>II</sup> solutions (with ethanol as target molecule) was affected by a pH decrease from over 6 down to 5 [131].

Above considerations question which of the pH decrease and Fe<sup>II</sup> concentration is the main factor impacting DMPO – CO<sub>2</sub><sup>-</sup> disappearance. As pH and Fe<sup>II</sup> concentration are correlated, the present system appears inappropriate to study their respective roles. This is why additional experiments were performed (next section) using a stable radical, TEMPOL.

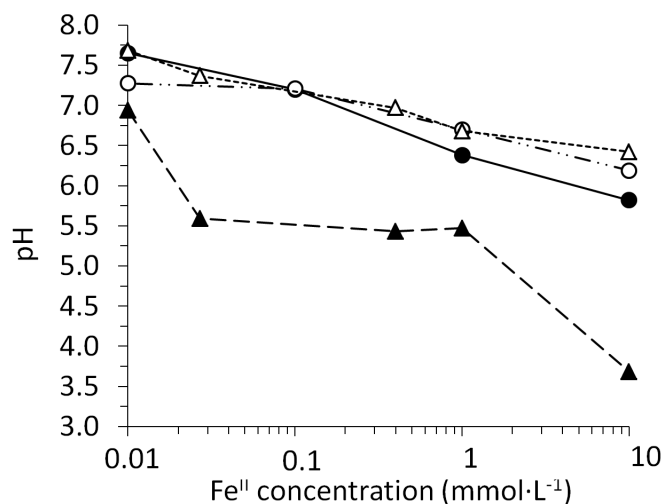


FIG. II.15 – Final pH versus initial  $Fe^{II}$  concentrations in the  $Ink-M_z$  (full circle) and  $Fe2-M_z$  (empty circle) solutions studied by ESR with protocol 2, and in the  $Fe2-M_z$  solution analyzed according to protocols 3 (full triangle) and 4 (empty triangle).

### Study of the effect of iron(II) on the concentrations of the $DMPO-CO_2^-$ adducts.

The use of model solutions showed that the signal of the  $DMPO-CO_2^-$  adducts was linked to iron(II) leached in solution. The concentration of iron(II) had a strong impact on the concentrations detected in solutions. Below  $1 \text{ mmol} \cdot \text{L}^{-1}$ , the adduct concentration increase with the iron(II) one. However, above this value, there is a decrease in adducts concentrations detected, which might be due to a pH decrease or to iron(II).

### II.3.5 Influence of pH and iron(II) concentration on TEMPOL

To identify the respective effects of pH and  $Fe^{II}$  on radical adducts disappearance, complementary tests were performed on TEMPOL, a stable nitroxide radical with a structure (FIG. II.16A) similar to that of the  $DMPO-CO_2^-$  adduct (FIG. II.9A). When dissolved in water ( $27 \text{ } \mu\text{mol} \cdot \text{L}^{-1}$  in our conditions), this radical has a typical ESR signature (FIG. II.16A) which intensity remained fully stable within the duration of the experiment (cross, FIG. II.16B). It is thus a good probe for independently studying the effects of pH and  $Fe^{II}$ .

After mixing the TEMPOL solution with model  $Fe2-M_z$  solutions, the TEMPOL concentration was no longer stable but regularly decreased with time (see typical evolution for  $Fe2-M_1$ , FIG. II.16B, full triangles). For quantitative comparisons purpose, the intensity values at 30 min of recording (red lines, FIG. II.16B) will be considered in what follows.

On one hand, the effect of pH was evaluated by adjusting the pH of the TEMPOL solution (initially at 6.7) between 1 and 8.5 by addition of sulfuric acid (FIG. II.17A, full squares) or of sodium hydroxide (FIG. II.17A, empty square). For pH values between 3.8 and 6.7, the TEMPOL concentration was not affected. Therefore, acidity, by itself, seems to have a negligible effect on TEMPOL radical concentration.

On the other hand, the effect of iron was studied by preparing mixed TEMPOL and  $Fe2-M_z$  solutions with different iron contents that were next analyzed according to proto-

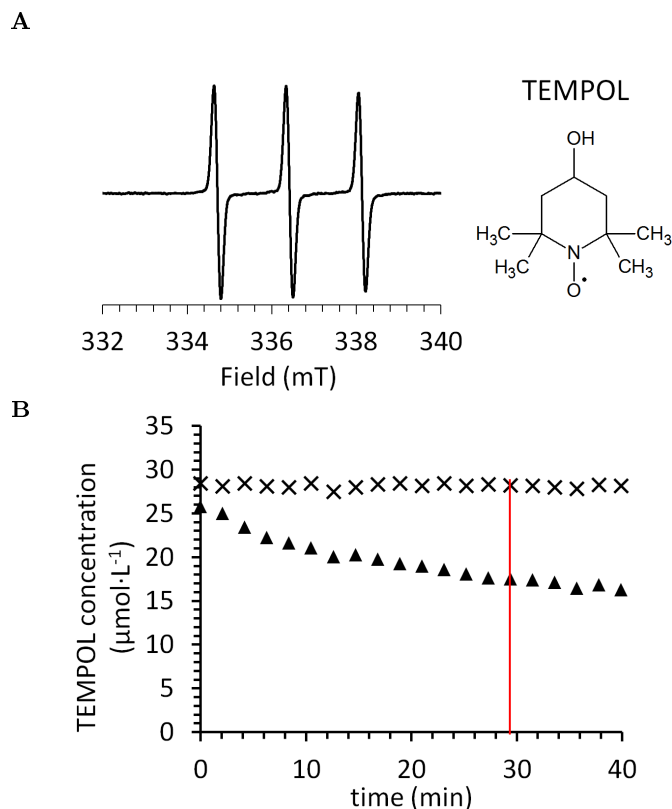


FIG. II.16 – (A) ESR signal and scheme of the TEMPOL stable radical; (B) evolution with time of its concentrations in the  $27 \mu\text{mol}\cdot\text{L}^{-1}$  TEMPOL solution left alone (cross) or mixed with the  $\text{Fe}2\text{-M}_1$  solution (full triangle). Values at 30 min were chosen to compare the samples.

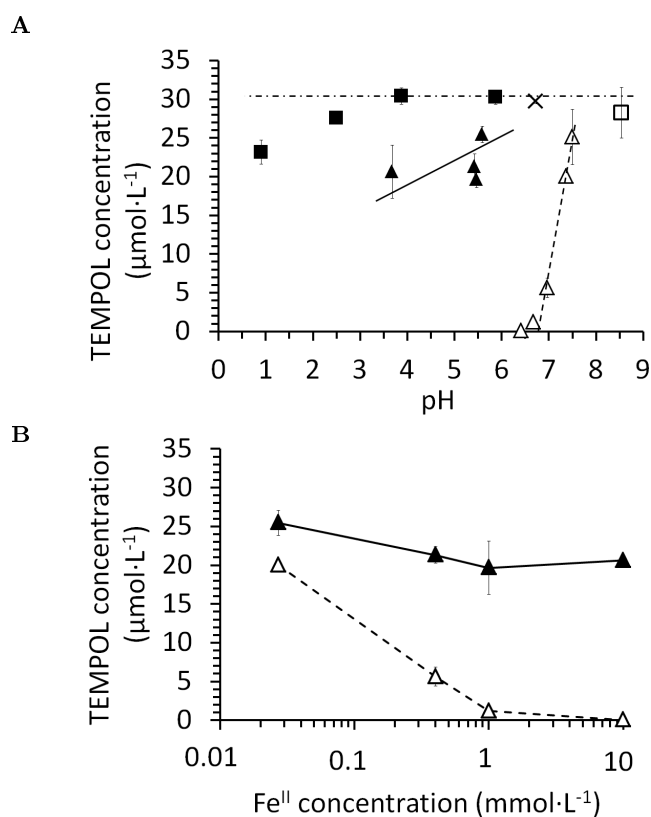
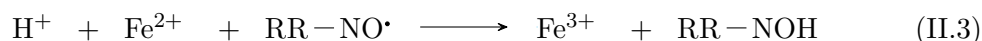


FIG. II.17 – Evolutions of TEMPOL radicals concentrations with pH (A) and initial  $\text{Fe}^{\text{II}}$  concentrations (B). Values at 30 min were considered after mixing TEMPOL solution with water (cross), sulphuric acid (full square), sodium hydroxide (empty square) or  $\text{Fe}2\text{-M}_z$  samples solutions without (full triangle, protocol 3) or with (empty triangle, protocol 4) formate.

cols 3 and 4 (TAB. II.1). As already observed in section II.3.2, the absence (protocol 3) or presence (protocol 4) of formate in the analyzed solution resulted in different pH ranges, being either 3.7-5.6 (without formate, FIG. II.17A, full triangles) or 6.4-7.5 (with formate, FIG. II.17B, empty triangles). Even if such pH changes are not expected to have, by themselves, any effect on TEMPOL concentration (seen above to be stable over a large pH range), TEMPOL concentration decreased from  $30 \mu\text{mol} \cdot \text{L}^{-1}$  to  $20 \mu\text{mol} \cdot \text{L}^{-1}$  upon  $\text{Fe}^{\text{II}}$  concentration increase from  $0 \text{ mmol} \cdot \text{L}^{-1}$  to  $1 \text{ mmol} \cdot \text{L}^{-1}$  in Fe2-M<sub>z</sub> (FIG. II.17, full triangles), and the decrease was significantly enhanced in presence of formate, till complete TEMPOL disappearance at the highest  $\text{Fe}^{\text{II}}$  concentrations (FIG. II.17, empty triangles). Even if scavenging of TEMPOL (a radical) by formate (a scavenger) is expected to provoke some signal decay (see above, FIG. II.4A), this sole explanation is insufficient to explain the observed signal decreases, since formate concentration was the same ( $4 \text{ mol} \cdot \text{L}^{-1}$ ), whatever the Fe2-M<sub>z</sub> solution. Hence, the strong signal decay at high iron loadings must predominantly result from  $\text{Fe}^{\text{II}}$  presence, more precisely from TEMPOL decomposition into non-radical species facilitated by iron II. Especially, this decomposition could be related to TEMPOL (RR-NO $\cdot$ ) reduction to hydroxylamine (see eq. II.3), nitroxides being indeed prone to reduction by electron donors such as  $\text{Fe}^{\text{II}}$  [156].



To support this proposal, it is worth recalling that TEMPOL has a reduction potential of 0.585 V at pH 7 [157], whereas, iron complexes have an oxidation potential around 0 V at this pH ( $\text{Fe}^{\text{II}}/\text{Fe}^{\text{III}}_{\text{oxide-hydroxide}}$  couple, for instance) [158, 159]. Hence, the reduction of TEMPOL to hydroxylamine by  $\text{Fe}^{\text{II}}$  is thermodynamically possible.

Interestingly, a similar reaction involving a reduction by  $\text{Fe}^{\text{II}}$  of  $\text{DMPO-CO}_2^-$  adducts into a non-radical hydroxylamine product could stand as well, possibly explaining the adduct disappearance at high iron loading seen in FIG. II.14.

### Tests with TEMPOL.

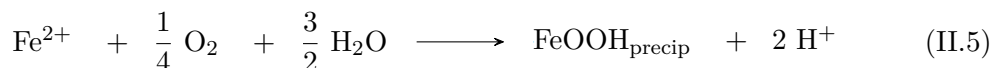
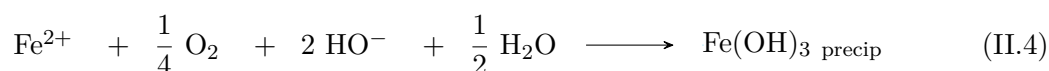
Tests with TEMPOL have evidenced the impact of pH was negligible on a large range of pH, while  $\text{Fe}^{\text{II}}$  had a major impact on radical concentration, more probably due to its reduction into an hydroxylamine. This could also be the case for the  $\text{DMPO-CO}_2^-$  adduct at high iron concentrations, thus preventing the comparison between samples at high iron concentrations.

### II.3.6 Roles of oxidation processes and of iron(II) in radicals production

From above data, completed by bibliographic ones, a close relationship is found to exist between  $\text{Fe}^{\text{II}}$  oxidation and formation of  $\text{DMPO-CO}_2^-$  adducts. As a recall, the various arguments in this direction are the following;  $\text{DMPO-CO}_2^-$  formation i) is strongly correlated to the presence of  $\text{Fe}^{\text{II}}$  in the analyzed solution; ii) is also oxygen dependent (II.3.2), in line with previous reports on  $\text{Fe}^{2+}$  solutions [148], which suggests that oxidation processes play an important role as well. Also in agreement with a previous work [131] that showed a lower ESR signal was obtained for  $\text{Fe}^{\text{II}}$  sulfate solutions prepared in distilled water compared to those containing a phosphate buffer (known to enhance  $\text{Fe}^{\text{II}}$  oxidation); iii) is also related to “close to neutral” pH conditions (see sections II.3.2 and II.3.4) and this corresponds to a pH range where  $\text{Fe}^{2+}$  is easily oxidized to  $\text{Fe}^{3+}$ .

An additional argument in favor of the close relationship between  $\text{Fe}^{\text{II}}$  oxidation and formation of  $\text{DMPO} - \text{CO}_2^{\cdot-}$  lays in the data obtained with gallic acid. Although the latter is often considered as an antioxidant (possibly limiting the formation of radical species [115]), it is, as many other hydroquinones [160, 161], a powerful  $\text{Fe}^{3+}$  reductant [34, 45] that efficiently converts  $\text{Fe}^{3+}$  to  $\text{Fe}^{2+}$ . Because further reduction of  $\text{Fe}^{\text{II}}$  to  $\text{Fe}^0$  is thermodynamically not possible [45],  $\text{Fe}^{2+}$  can only be re-oxidized to  $\text{Fe}^{3+}$ , giving rise to a redox  $\text{Fe}^{2+}/\text{Fe}^{3+}$  cycling forming new radical species (and consequently new adducts). This could explain i) the ESR signal that is double in Ink-M<sub>2.1</sub> (with gallic acid) compared to Fe2-M<sub>2.1</sub>, in spite of identical initial  $\text{Fe}^{\text{II}}$  concentrations and ii) the higher  $\text{Fe}^{\text{II}}$  amounts detected in the Ink-L<sub>7</sub> and Ink-L<sub>21</sub> solutions compared to the Fe2-L<sub>7</sub> and Fe2-L<sub>21</sub> ones (TAB. II.3).

On a mechanistic point of view, the oxidation of  $\text{Fe}^{2+}$  in the pH range 5-7 is known to lead to precipitation of  $\text{Fe}^{\text{III}}$  oxy-hydroxides according to EQ.II.4 [162] and to the chemically equivalent more recent version of it (EQ.II.5):



From both reactions, the kinetics of  $\text{Fe}^{\text{II}}$  oxidation is expected to increase with the concentration of dissolved oxygen, with pH, and with the  $\text{Fe}^{\text{II}}$  concentration (see appendix D), which is exactly what is observed in our solutions samples at  $\text{Fe}^{2+}$  concentrations below  $1 \text{ mmol} \cdot \text{L}^{-1}$ .

### II.3.7 ROS involved in the DMPO-formate adduct formation and impact on cellulose depolymerization

With respect to the comprehension of the precise nature of the ROS involved in the formation of  $\text{DMPO} - \text{CO}_2^{\cdot-}$  adducts, their precise nature remains difficult to assess since the measurements involved an intermediary (not specific) target molecule. A determinant impact of iron oxidation mechanisms was clearly assessed, implying oxygen reduction and subsequent formation of intermediate reactive oxygen species such as superoxide ( $\text{O}_2^{\cdot-}$ ), hydroperoxyl ( $\text{HO}_2^{\cdot}$ ), hydrogen peroxide ( $\text{H}_2\text{O}_2$ ) and hydroxyl radicals ( $\text{HO}^{\cdot}$ ). These latter, often put forward as the main cause of cellulose degradation by iron gall inks [64, 141, 65] were definitively not evidenced (or remained at very low level) in our experiments.

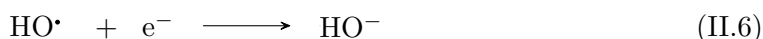
The non-detection of  $\text{DMPO} - \text{OH}^{\cdot}$  adducts may at first be accounted to the fact that cellulose attack by possible  $\text{HO}^{\cdot}$  (see chapter I) may compete  $\text{DMPO} - \text{OH}^{\cdot}$  formation. Indeed, considering first order reactions and using published rate constants [99], comparable rates can be estimated for glucose hydrogen abstraction ( $1.2 \cdot 10^8 \cdot [\text{HO}^{\cdot}]$ ) and DMPO trapping ( $1.1 \cdot 10^8 \cdot [\text{HO}^{\cdot}]$ ). In contrast, the rate of  $\text{DMPO} - \text{CO}_2^{\cdot-}$  formation ( $2.5 \cdot 10^9 \cdot [\text{HO}^{\cdot}]$ ) is largely higher, therefore  $\text{DMPO} - \text{CO}_2^{\cdot-}$  adducts could be formed at a rate fast enough to make hydroxyl radicals detectable. This scenario does not stand since similar results were obtained on X-P<sub>y</sub> (paper solutions) and X-L<sub>y</sub> (leached solutions) samples giving evidence that the presence (or not) of paper did not strongly impact adducts formation.

Another explanation would be to consider that  $\text{DMPO} - \text{OH}^{\cdot}$  were formed but immediately quenched by  $\text{Fe}^{2+}$  ions as already proposed by Li et al. [163]. Nevertheless, this scenario appear doubtful as well when considering the results of TPA hydroxylation

experiments. Indeed, even if TPA and DMPO experiments remains difficult to compare (because of the different experimental methodologies), it has been shown experimentally that the TPA hydroxylation method is several order of magnitude more sensitive than the DMPO ESR method in phosphate buffer[164]. This is also what was observed in our tests: taking as reference the cumulative amount of hydroxyl radicals detected by TPA hydroxylation on Fe<sup>2+</sup> impregnated papers, a value below 8 nmol · g<sup>-1</sup> is obtained after 50 days of ageing (FIG. II.11). Then, supposing that HO• trapping occurs linearly with time, it implies that less than 0.6 pmol · g<sup>-1</sup> and 7 pmol · g<sup>-1</sup> of hydroxyl radicals were trapped per gram of paper during five minutes and one hour, respectively (mean durations for DMPO – OH• and DMPO – CO<sub>2</sub><sup>-</sup> analyses, respectively). Both amounts are much below the limit of detection of DMPO trapping technique (50 nmol · g<sup>-1</sup>). In view of these very low level of HO•, such radical could not explain, on its own, the levels of the DMPO – CO<sub>2</sub><sup>-</sup> adduct detected by ESR (around 150 nmol · g<sup>-1</sup>). The DMPO – CO<sub>2</sub><sup>-</sup> adduct formation that should therefore arise mostly from other species.

Since none of above two explanations seems valid, other hypotheses have to be considered. The third one could involve the participation of iron intermediates in which iron oxidation number is above 3 (oxo- peroxy-, hydroperoxy-compounds) [122, 165]. These highly reactive non-radical intermediates are sometimes believed to be involved in the pathway of Fe<sup>II</sup> oxidation. As they were never directly detected in iron oxidation mechanisms, their existence remains controversial. This latter is mainly accounted to ESR studies [131, 148] in which superoxide radicals, hydroxyl radicals and hydrogen peroxide were researched but not evidenced.

A last and more convincing scenario can be put forward in which HO• formed during oxygen reduction would be preferentially reduced to hydronium ions (EQ. II.6):



The standard potential of this reaction increases from 2.3 to 2.7 V versus normal hydrogen electrode (NHE) when pH decreases from 7 to 0 [166]. As the standard potential of Fe<sup>II</sup>/Fe<sup>III</sup> remains largely below 2, Fe<sup>II</sup> appears as a good electron donor for HO• reduction through EQ. II.7:



Interestingly, the acidity of the medium clearly favors this reaction, thus limiting the HO• occurrence in iron bearing acidic medium. This last scenario implies that the DMPO – CO<sub>2</sub><sup>-</sup> adducts formation cannot be attributed to HO• but to other ROS that cannot be seen with DMPO alone. Superoxide or hydroperoxyl radicals (the acidic form of superoxide) are good candidates. Their formation is usually considered as limiting steps for oxygen reduction since standard potential of O<sub>2</sub>/O<sub>2</sub><sup>-</sup> is negative (-0.35 V vs NHE) [98]. The occurrence of these radicals is consistent with published data [167] on the  $\frac{\text{Fe}^{\text{II}}}{\text{O}_2}$  system with POBN spin trapping in combination with different target molecules (dimethyl sulfoxide (DMSO), ethanol, glucose): a significant ESR signal of corresponding adducts was observed, which largely decreased upon addition of superoxide dismutase, an enzyme that catalyzes superoxide radical dismutation.

### II.3.8 Does hydroxyl radicals have an impact on cellulose depolymerization?

The last question that remains to be answered is that of the potential contribution of  $\text{HO}\cdot$  on cellulose degradation in acidic medium in which acid-catalyzed hydrolysis is also known to occur. From FIG.II.12B, it is clear that cellulose chain scissions were more numerous in inked papers than in Fe<sup>2+</sup> impregnated ones. Within the same period of ageing, no  $\text{HO}\cdot$  radicals were detected on inked papers while a weak occurrence of  $\text{HO}\cdot$  was evidenced on Fe<sup>2+</sup> impregnated ones (FIG.II.11). These two observations tend to demonstrate that  $\text{HO}\cdot$  radicals do not play any role in cellulose depolymerization. Thus, formed  $\text{HO}\cdot$  (if present) would not react with cellulose, but preferentially with the ink constituents, especially Fe<sup>II</sup> ions through EQ.II.7 that is probably the dominant pathway of  $\text{HO}\cdot$  extinction in Fe<sup>II</sup> impregnated papers. The extinction of the HTPA signal on inked papers could then be accounted to gallic acid that has anti-oxidant properties in Fenton like reactions [115, 168, 169]. It is also a strong reducer [34] of Fe<sup>III</sup> leading to regeneration of Fe<sup>II</sup> that in turn reacts with  $\text{HO}\cdot$  through EQ.II.7. Similar mechanisms of  $\text{HO}\cdot$  consumption probably prevails for DMPO hydroxylation assay, explaining the absence of DMPO –  $\text{OH}\cdot$  adducts while DMPO –  $\text{CO}_2^{\cdot-}$  is detected in relation to other ROS.

## II.4 Conclusion

This study investigated the use of ESR combined with DMPO spin trapping to identify Reactive Oxygen Species produced in the “iron gall ink – paper” system. Paper samples were immersed in DMPO solutions that were analyzed by ESR. No hydroxyl radicals were evidenced. Conversely, the use of formate as intermediate target molecule led to the detection of an intense signal of DMPO –  $\text{CO}_2^{\cdot-}$  adducts. Complementary measurements were performed on several types of solutions (including TEMPOL), additionally using the TPA hydroxylation assay when necessary, as the method is highly sensitive. This step-by-step approach highlighted several points:

- First, the detected ESR signals can not be attributed to phenomena occurring on the paper sheet itself. They are rather correlated to processes involving iron species leached out of the paper, which concentration decreased with ageing time;
- Second, the DMPO spin-trap became inefficient at high iron loads, because of the formation of hydroxylamine as competing reaction.
- Third, the DMPO –  $\text{CO}_2^{\cdot-}$  radicals detected in paper-solution samples (Ink-P) are linked to the oxidation of leached Fe(II) species that can occur at a pH of 6 imposed by formate;
- Fourth, ROS are clearly involved in the formation of the DMPO –  $\text{CO}_2^{\cdot-}$  radicals. Yet, these species are not hydroxyl radicals, but more probably superoxide ( $\text{O}_2^{\cdot-}$ ) or hydroperoxyl ( $\text{HO}_2^{\cdot}$ ) although metal-oxo species cannot be totally ruled out;
- Fifth, the DMPO –  $\text{OH}\cdot$  adduct was not formed due to the amount of leached iron that leads to both acidification of the solution and electron donation. These two characteristics made the reduction of  $\text{HO}\cdot$  radicals (EQ. II.6 and II.7) a predominant pathway compared to DMPO spin-trapping;

- Last but not least, the amount of HO• radicals detected by TPA hydroxylation is not correlated to cellulose chain scissions, indicating that HO• radical oxidation is not the main mechanism of cellulose depolymerization.

Although hydroxyl radicals do not seem to play a role in paper degradation by themselves, the ability of ink/iron sulfate solutions to produce an harmful ROS could be at the origin of the bond breaking in cellulose. In order to investigate more in details the mechanisms involved, a study dedicated to the kinetics of depolymerisation of inked paper, never undertaken to our knowledge, will be presented in the next chapter, together with complementary measurements done on a model molecule, which is cellulose building block: cellobiose.

# Chapter III

## Glycosidic bond scission

This chapter deals with the scission of the glycosidic bond, which is at the origin of the depolymerization process of cellulose. The chapter will be divided in three sections. My own contribution lays mainly in the two last sections since the work presented on the first section was already in an advanced stage at the time of my arrival into the laboratory. The first section focuses on the depolymerization of model inked paper samples, which have the specificity to degrade at room temperature, thus offering a way to study the validity of the Arrhenius law at ambient temperature. The other sections deal with the degradation of a model molecule, cellobiose, that is the smallest repeating unit constituting cellulose, being therefore easier to study than cellulose because it can be analyzed with a larger range of techniques. Indeed studying paper degradation is difficult due to complexity and heterogeneity of this high molecular weight material and to the fact that there are few techniques that allow following both the depolymerization and the degradation products at a molecular level. Although the choice of cellobiose could provide only a partial understanding of degradation processes involved in such a complex material as paper, it appeared appropriate to clarify the combination of parameters inducing glycosidic bond scission in the case of iron induced depolymerization. In light of the observations made on paper samples in chapter II, iron, oxygen and pH will be the three parameters investigated in this new chapter that will analyze their respective role with respect to cellobiose decomposition. Preliminary tests were first performed on solid systems, trying to impregnate cellobiose with iron sulfate. Because of its high ability to crystallize, the solid system rapidly appeared inappropriate, as will be discussed in section III.2. We therefore switched to solution systems in which a strong interaction between cellobiose and iron components could be achieved.

### III.1 Depolymerisation of inked papers: a kinetic study

On a general point of view, paper degradation (i.e. cellulose depolymerization) is monitored by the loss in degree of polymerization ( $DP$ ). Different techniques can be used to evaluate the  $DP$ , such as viscosimetry or size exclusion chromatography [170]. In this section, only viscosimetry will be developed.

#### III.1.1 Evaluation of the degree of polymerization ( $DP$ ) by viscosimetry

Ostwald viscosimeter is often used for the viscosimetry measurements. This is a glass capillary tube of U shape. Two horizontal marks on the capillary define a particular known

volume. The measure of time for the sample solution to flow between those two marks allows viscosity  $[\eta]$  determination using volumic mass of the sample  $\rho$  and viscosimeter constant  $c$ :

$$\delta t = \frac{c \cdot [\eta]}{\rho} \quad (\text{III.1})$$

The limiting viscosity number  $[\eta]$  can be converted to  $DP_v$  values using the Mark-Houwink-Sakurada equation :[171]

$$DP_v^\alpha = K'[\eta] \quad (\text{III.2})$$

with  $\alpha = 0.85$  and  $K' = 1.1$  for cupri-ethylene-diamine as solvent. Following directly the evolution of  $DP_v$  allows paper ageing monitoring and comparison between samples.

### III.1.2 Ekenstam model and Arrhenius law

When studying alteration mechanisms the first problem to face is to reproduce them within a reasonable timescale. Artificial ageing combining high temperature, high humidity and/or high illumination conditions are often needed to boost the degradation assuming that these strong conditions do not promote different degradation pathways than those occurring in real storage environments. It is then necessary to extrapolate artificial ageing behaviors to more realistic conditions using different mathematical models.

The cellulose degree of polymerization is a good indicator of paper condition. Monitoring this parameter upon artificial ageing enables to determine the rate constant  $k'$  of chain scissions using the Ekenstam model, which is adequate to model the depolymerisation of linear polymers assuming that the bond breaking rate is constant (EQ. III.3) :

$$\frac{1}{DP_n(t)} - \frac{1}{DP_n(0)} = k' \cdot t \quad (\text{III.3})$$

in which

$t$ , the ageing time (s);

$DP_n(t)$ , the number-average degree of polymerisation at  $t$ ;

$DP_n(0)$ , the number-average degree of polymerisation before ageing.

$DP_n$  can be converted to  $DP_v$ , which represents the viscosity-average degree of polymerisation, using the following relation involving the  $\Gamma$  mathematical function (tabulated values) and the  $\alpha$  coefficient of the Mark-Houwink-Sakurada equation EQ. III.2[77]:

$$\frac{DP_v}{DP_n} = [(1 + \alpha)\Gamma(1 + \alpha)]^{\frac{1}{\alpha}} \quad (\text{III.4})$$

This gives a proportionality constant close from 2 (evaluated to 1.9308 for the cupri-ethylene-diamine system).

The EQ. III.3 becomes

$$\frac{1}{DP_v(t)} - \frac{1}{DP_v(0)} = k \cdot t \quad (\text{III.5})$$

in which

$t$ , the ageing time (s);

$DP_v(t)$ , the viscosity-average degree of polymerisation at  $t$ ;

$DP_v(0)$ , the viscosity-average degree of polymerisation before ageing.

$DP_v$  is obtained from viscosimetry measurements.

The rate constant  $k'$ , and consequently  $k$  (expressed in  $s^{-1}$ ) depends on temperature (Arrhenius law):

$$k = A \cdot \exp \frac{-E}{R \cdot T} \quad (\text{III.6})$$

With:

$A$ , the frequency factor

$E$ , the activation energy ( $J \cdot mol^{-1}$ );

$T$ , the temperature (K);

$R$ , the Boltzman constant ( $8.314 J \cdot K^{-1} \cdot mol^{-1}$ ).

In the case of a multiple reaction system (which is most probably the case of paper),  $A$  becomes  $A_a$ : the apparent frequency factor and  $E$  becomes  $E_a$ : the apparent activation energy which is an average weighted by the rates of each reaction [70]. The determination of the activation energy of the chemical reactions at the origin of the glycosidic bond scission can be obtained from the experimental data using the two formulas (EQ. III.5 and III.6).

Several studies have been done on pulps, papers or crystalline cellulose to determine activation energy values from ageing experiments. Most of the studies have attributed cellulose depolymerisation to acid hydrolysis because rate constants raised with increasing relative humidity and decreasing the pH values. Activation energies of hydrolysis degradation mechanism are always higher (around  $97 kJ \cdot mol^{-1}$  to  $113 kJ \cdot mol^{-1}$ ) than those attributed to oxidation phenomena (around  $75 kJ \cdot mol^{-1}$  to  $93 kJ \cdot mol^{-1}$ ) (TAB. III.1). Rychlý et al.[176] reported that oxidation could be made of two processes, one faster with a smaller activation energy and another one slower with a higher activation energy (TAB. III.1).

The great majority of kinetic studies performed on cellulosic systems involved oxygen, but not iron. Yet, it has been shown in chapter II that iron can participate to both hydrolysis and oxidation mechanisms. The present kinetic study, the details of which can be found in Appendix H, was also performed to get some additional knowledge on the respective involvements of hydrolysis and oxidation in the degradation pathway of cellulose in presence of iron.

### III.1.3 Inked paper model: conditions of experiments

In order to study the kinetics of paper depolymerisation, experiments were carried out using Whatman papers impregnated with model solutions as those described in section II.2.1. The degradation was monitored with viscosimetry measurements to follow depolymerization and with a zero-span tensile tester (measuring the tensile strength of fibers) to evaluate loss of mechanical properties, as detailed in the paper presented in appendix H. It was shown in a previous study [111] performed on similar samples that the degradation was measurable at ambient temperature and this measurement was considered to evaluate the validity of Arrhenius law's extrapolation at ambient temperature. The degradation was otherwise monitored at different increasing temperatures up to  $90^\circ C$  to measure rate constants, which were in a second run used to determine activation energies.

Sample	Technique	Temperature and humidity	$E_a$ (kJ · mol <sup>-1</sup> )	Mechanism interpretation	Source
Bleached softwood pulps pH 4 to 5	viscosimetry	60 °C to 100 °C; 75 % RH	104-113	acid hydrolysis	[70]
Bleached kraft pulps	viscosimetry	23 °C; 50 % RH	109	acid hydrolysis	[71]
Bleached softwood pulps pH 5	viscosimetry	65 °C to 90 °C	103-106	acid hydrolysis	[172]
Whatman n° 1 paper	viscosimetry	50 °C to 90 °C; 30 % to 80 % RH	97	acid hydrolysis	[173]
Softwood cellulose paper	viscosimetry	60 °C to 100 °C; 60 °C to 70 °C	78 133	oxidation non negligeable above 80 °C	[174, 175]
Paper, Bleached Sulphate Softwood Pulp, no size	viscosimetry	60 °C to 220 °C; 0 % HR 60 °C to 90 °C; 65 % HR	93 126	mixed conclusions	[73]
Paper, Bleached Soft Wood Kraft, Alum sized, pH 5.7, aged in glass tubes	Zero-span viscosimetry	70 °C to 90 °C; 56 % to 60 % RH	113 108		[72]
Whatman paper	Chimi- luminescence	50 °C to 240 °C; 0 % RH	84 (fast) 110(slow)	2 oxidation processes	[176]
Cotton cellulose linters, ageing in air	viscosimetry	150 °C to 190 °C; 0 % RH	88	oxidation (formation of hydroperoxides)	[97]
Cotton cellulose linters, ageing under N <sub>2</sub>	viscosimetry	150 °C to 190 °C; 0 % RH	113	pyrolysis	[97]
Cellobiose H <sub>2</sub> SO <sub>4</sub> solution	glucose formation	25 °C to 80 °C; solution	110	hydrolysis	[76]
Cellobiose Fenton system	glucose formation	25 °C to 80 °C; solution	55	Fenton oxidation	[76]

TAB. III.1 – *Activation energies from several published data. Values from experiments obtained on cellobiose solutions are added for comparison with the values obtained for other cellulosic solids.*

### III.1.4 Main outcomes of the kinetic study paper model

From above experimental measurements, it was possible to linearly interpolate  $\ln(k)$  versus  $(RT)^{-1}$  between 20 °C and 90 °C, thus assessing the reliability of the Arrhenius law for iron gall inks (IGI) induced chain scissions in all this range of studied temperatures (FIG. III.1), and confirming in turn the possibility to extrapolate artificial ageing results to natural ageing conditions. This is a crucial point for scientists involved in the chemical aspects of paper degradation. This result should, however, be considered with great care by paper conservators and curators as the samples were designed to reproduce the chemical reactions occurring during paper decay by IGI but are not relevant to test the initial step of degradation occurring on original manuscripts, i.e. the migration of iron within the paper sheet because of humidity. A second outcome of the present study lies in the fact that similar activation energy values were found for DP (FIG. III.1A) and Zero Span testing strength (FIG. III.1B) measurements (approx. 97 kJ · mol<sup>-1</sup>). These two parameters are quite complementary: DP measurements are highly sensitive to the very beginning of depolymerization while Zero Span testing is more appropriate for advanced stage of degradation. Finding similar values of activation energy with these two techniques suggests that the depolymerization pathways remain similar all along paper ageing. A third outcome lies i) in the value found for depolymerization activation energy (97 kJ · mol<sup>-1</sup>) that is relatively close but inferior to the value measured on naturally aged

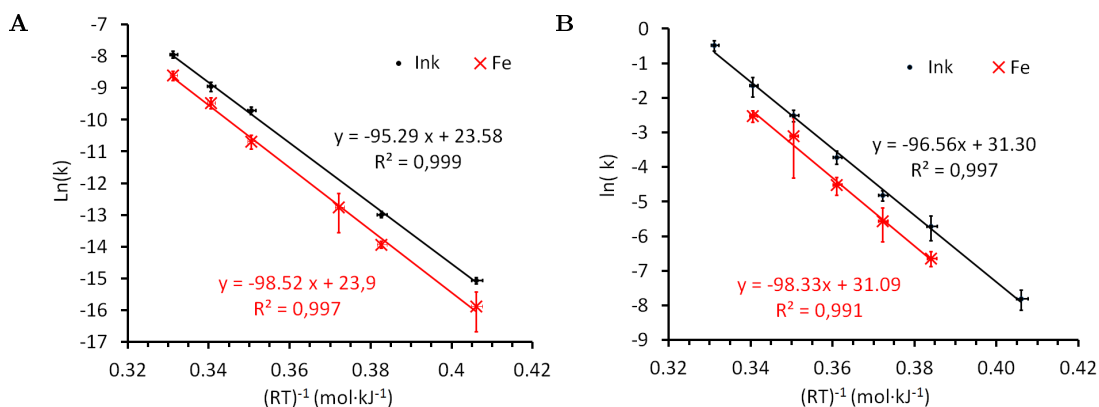


FIG. III.1 – Arrhenius plot of (A) DP measurements and (B) zero-span measurements. Samples of paper impregnated with Ink are represented with black filled circle and those impregnated with Fe2 with red cross.

lignin-free acidic papers ( $109 \text{ kJ} \cdot \text{mol}^{-1}$ ) [71] and ii) in the reaction rates of IGI impregnated papers that are 1–2 orders of magnitude above those of lignin-free acidic papers (at  $50 \text{ }^\circ\text{C}$  for example, a value of  $k = 4.18 \cdot 10^{-5} \text{ h}^{-1}$  was found for inked papers and a value around  $1.67 \cdot 10^{-6} \text{ h}^{-1}$  was reported for bleached kraft papers [71]). These observations would not be in line with the superimposition of two independent pathways and rather suggest a dominant acidic hydrolytic process of which the energy barrier is reduced by the presence of oxygen and iron.

## III.2 Degradation of cellobiose in solid state

### III.2.1 Bibliographic recalls

Paper is a complex cellulosic matrix with a particular structure that does not allow the use of broad range of analytical tools. To investigate the mechanisms at the origin of glycosidic bond cleavage, cellobiose, the cellulose building block, was chosen as model compound.

Some works on cellobiose degradation have already been carried out to study different reactions, such as acid hydrolysis and oxidation. Yet no published data was found on the degradation of cellobiose in presence of iron. Interestingly, another sugar, methyl4-O-ethyl- $\beta$ -D-glucopyranoside, has been studied as model compound in Fenton type reaction systems involving hydrogen peroxide and iron(II) [110]. The influence of pH and oxygen on the formation of carbonyl and carboxyl functions has been also investigated carrying out reactions two hours at room temperature. It was shown that:

- carbonyl groups are formed at C<sub>2</sub>, C<sub>3</sub>, C<sub>6</sub> and carboxyl groups at C<sub>1</sub> and C<sub>6</sub>;
- the initial pH has a determining influence on degradation which was important between 2.1 and 4.7 and almost absent between 6.3 or 10.9. These observations are consistent with what is known about the optimal pH of Fenton reaction (3 to 5) [118];
- oxygen inhibites the degradation and osidic bond cleavage. This last observation seems at first contradictory with the fact that oxidation mechanisms are dominant in Fenton type systems. It can however be supported by the fact that oxygen is able to generate hydroperoxyl radicals (that can compete with hydroxyl radicals).

Therefore the authors suggested that the presence of oxygen promotes a higher contribution of hydroperoxyl than hydroxyl radicals on the degradation.

On cellobiose, we did not find any work on glycosidic bond cleavage in presence of iron or Fenton reagents. Yet, the effect of hydroxyl radicals (produced by  $\gamma$  irradiation) on cellobiose was studied by Schuchmann and Sonntag[102], who showed that the presence of oxygen decreased the glycosidic bond cleavage induced by hydroxyl radicals in the disaccharide cellobiose.

Other degradation studies are available, dealing with oxidation in alkaline medium [177, 178, 179], with alkaline hydrolysis [180, 181, 182] and with acid hydrolysis [183, 75]. Regarding oxidation in mild alkaline medium, Löwendahl, Petersson, and Samuelson [178] noticed that the  $\beta$ -elimination and the conversion of the aldehyde end into carboxylic acid happens faster than the oxygen attack on glucose (degradation product). Degradation of cellobiose was also studied during heterogeneous catalytic oxidation [184, 185], with especially solid acid catalysts in green conditions (mild temperatures: 50 –80°C) [186], or in less milder (150 –160°C, 20-80 bar) [187, 188].

Since we wanted to study the influence of various parameters (iron, pH, oxygen) on the degradation of a simpler model than cellulose (cellobiose) and since this had, to our knowledge, never been reported, preliminary tests were first performed on solid state cellobiose, monitoring its degradation by infrared spectroscopy. The rest of the experiments were carried in solution, as will be detailed in section III.3.

## III.2.2 Experimental aspects

### a Sample preparation

Solid state samples were prepared by first dissolving 1 g of D(+)-cellobiose powder (99.0 %, Sigma-aldrich, Fe:  $\leq 5$  ppm) in 10 mL of model solutions. These solutions contained iron sulfate ( $118.1 \text{ mmol} \cdot \text{L}^{-1}$ ), eventually in combination with gallic acid (at  $44.9 \text{ mmol} \cdot \text{L}^{-1}$  or  $1.0 \text{ mmol} \cdot \text{L}^{-1}$ )(TAB. III.2). They were stirred during 3 h, then freeze-dried for 48 h with the apparatus Cryos-55 (Cryotec) in order to recover solid samples that were then aged into an oven. Two ageing procedures were considered: 50 °C during 15 days and 80 °C during 7 days.

### b Infrared spectroscopy

By giving information on the vibrations present in molecules, infrared spectroscopy is useful to study a wide range of compounds, especially carbohydrates. It has been already used to study cellulose oxidation upon ageing of paper [84, 189, 86].

In the present work, the degradation of cellobiose was monitored with a Nicolet 6700 spectrometer (Thermo scientific) using the single reflection ATR accessory, equipped with

Sample	Concentrations ( $\text{mmol} \cdot \text{L}^{-1}$ )		pH impregnation solution
	Iron(II)	Gallic acid	
Pwd_Fe2	118.1	–	3.5
Pwd_Fe2_Ink_ratio2.6	118.1	44.9	2.7
Pwd_Fe2_Ink_ratio118	118.1	1.0	3.0

TAB. III.2 – Description of cellobiose solid samples preparation.

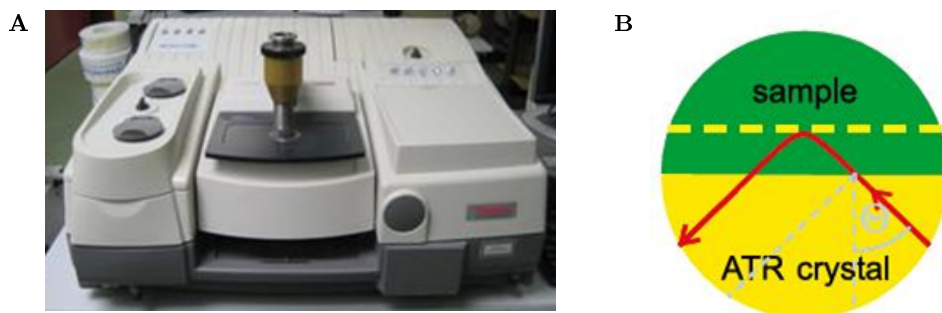


FIG. III.2 – Attenuated total reflectance FTIR spectroscopy: (A) NICOLET 6700 FTIR spectrometer (Thermo Scientific) equipped with a diamond ATR module and (B) ATR principle.

a diamond crystal (FIG. III.2 A). During measurement, the sample is pressed on the diamond crystal, then the infrared incident light goes through the crystal and is reflected on the sample (FIG. III.2B). This internal reflectance creates an evanescent wave that penetrates only a few  $\mu\text{m}$  into the sample (from  $0.5\ \mu\text{m}$  to  $5\ \mu\text{m}$ ), making ATR a surface analysis. The main advantage of this technique lies in the fact that no sample preparation is needed (no inclusion in KBr). IR spectra were collected within the range  $500\ \text{cm}^{-1}$  to  $4000\ \text{cm}^{-1}$ , with a resolution of  $4\ \text{cm}^{-1}$  and averaging 128 scans.

### c X-ray powder diffraction (XRD)

For each measurement, the powder sample was ground and deposited on a plexiglass sample holder in a manner as to have an homogeneous deposit and a smooth flat surface to obtain isotropic diffraction and avoid a shift of the peak position in the diffraction pattern. XRD were acquired with a Bruker Advanced D8 equipped with a copper source emitting with a wavelength of  $\lambda_{k\alpha 1} = 1.5406 \cdot 10^{-10}\ \text{m}$  and  $\lambda_{k\alpha 2} = 1.5443 \cdot 10^{-10}\ \text{m}$ . X-ray diffraction patterns were measured using the following parameters: tension of acceleration, 40 kV; current, 40 mA;  $2\theta$  values ranging from  $8^\circ$  to  $80^\circ$ ; step,  $0.020^\circ$  and step time, 0.94 s. Data were processed using the *FullProf suite* software.

The crystallinity degree (C.D) was obtained from a given area of the amorphous region ( $A_{amorph}$ , corresponding to the area of the baseline below the diffraction peaks) and the area of the crystalline region ( $A_{crist}$ , corresponding to the area of the diffraction peaks) by the following formula:

$$C.D. = \frac{A_{crist}}{A_{crist} + A_{amorph}} \quad (\text{III.7})$$

### III.2.3 Results

These preliminary tests carried out on solid impregnated cellobiose samples did not lead to any noticeable modification of infrared signatures during artificial ageing protocols (during 15 days at  $50\ ^\circ\text{C}$  or during 7 days at  $80\ ^\circ\text{C}$ ), as illustrated on FIG. III.3. In first approach, the main bands characteristic of carbohydrates are clearly visible on the FTIR spectra, namely:

- O-H stretching vibrations of hydroxyl groups between  $3700\ \text{cm}^{-1}$  and  $3000\ \text{cm}^{-1}$ , that is more or less defined depending on the water content of the sample (more details about attribution of hydroxyls groups of cellobiose can be found on the work of Xie et al. [190]);

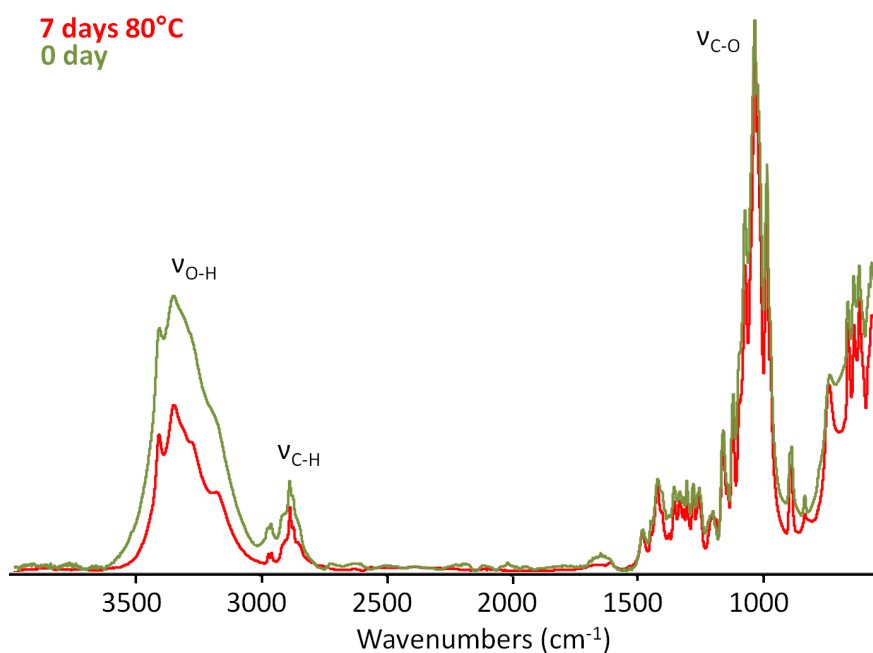


FIG. III.3 – Infrared spectra of *Pwd\_Fe2\_Ink\_ratio2.6* sample before (green spectrum) and after (red spectrum) ageing one week at 80 °C.

- C-H stretching vibrations of aliphatic groups between 2950 cm<sup>-1</sup> and 2800 cm<sup>-1</sup>;
- C-C-H deformations vibrations between 1500 cm<sup>-1</sup> and 1400 cm<sup>-1</sup>;
- (C)O-H deformation vibration of hydroxyl groups between 1300 cm<sup>-1</sup> and 1200 cm<sup>-1</sup>;
- C-O stretching vibrations between 1160 cm<sup>-1</sup> and 975 cm<sup>-1</sup>, with glycosidic bond elongation bands reported to be at 1163 cm<sup>-1</sup>, 1145 cm<sup>-1</sup>, 989 cm<sup>-1</sup>, 975 cm<sup>-1</sup>[191].

However, the ageing at 80 °C did not provoke a clear effect. The main change is toward the hydration: the sample aged one week at 80 °C (FIG. III.3, red spectrum) is less hydrated than the one before ageing (FIG. III.3, green spectrum).

The fact that no degradation occurred at 80 °C was particularly puzzling because it was previously observed on model papers that depolymerization at 80 °C was perceptible with DP measurements within a few hours only [192]. Therefore, we could have also expected that, after 7 days of ageing, the degradation of cellobiose would be detected on FTIR spectra but this was not the case. This point finds an explanation in the fact that cellobiose, in its solid state, has a high ability to form crystals. Sugars are often used as bulking agents of pharmaceuticals, and freeze drying techniques are generally applied to prevent them from crystallization and thus obtain amorphous matrices [193, 194]. Yet freeze drying is not always 100 % efficient to obtain amorphous samples, as attested by a study performed on the sucrose disaccharide [195]. Moreover, hydration has been shown to have an impact on crystallinity of freeze-dried saccharides samples [196]. FIG. III.4 A illustrates the evolution of the crystallinity of a cellobiose freeze-dried sample left one week under 50 % relative humidity. On our cellobiose samples, elimination of water and preventing re-hydration after lyophilisation was tested according to the protocol of Heljo et al. [196] that was claimed to be highly efficient against combined rehydration and recrystallization, which consist in placing water dissolved samples in desiccators for one week directly after freeze-drying. These measures induced a decrease of crystallinity,

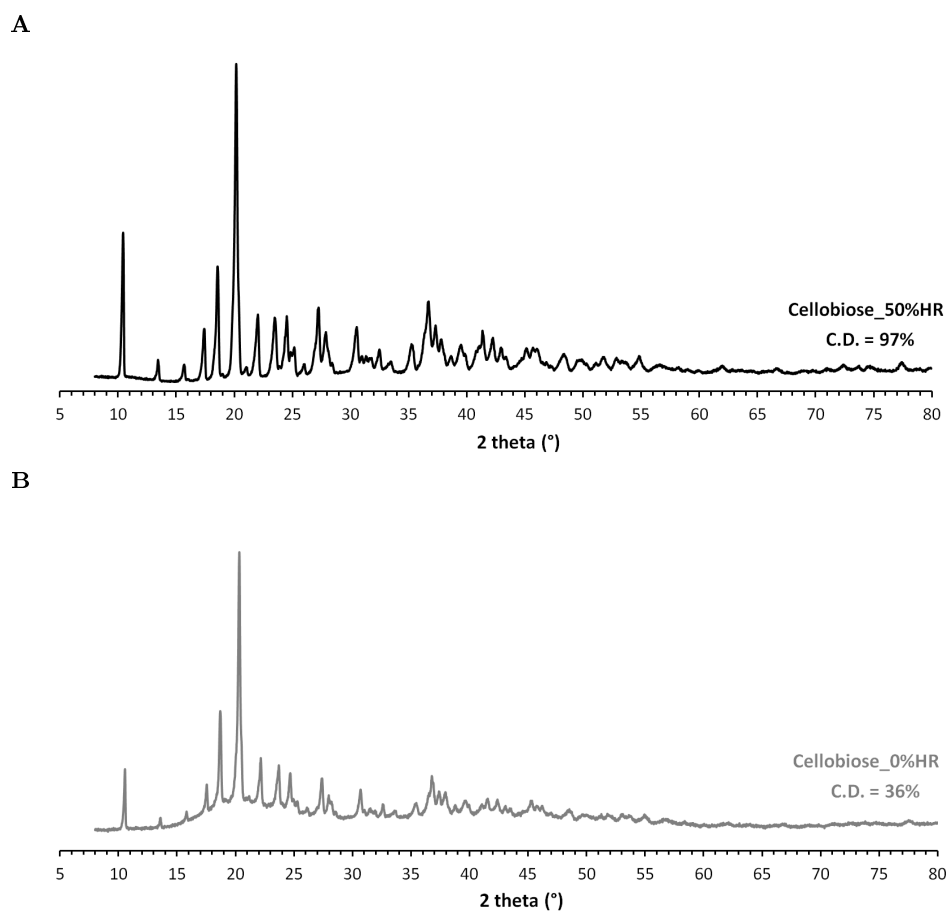


FIG. III.4 – X-rays powder diffraction of cellobiose sample freeze-dried and kept one week under: (A) 50 % relative humidity or (B) 0 % relative humidity in  $P_2O_5$  with the protocol [196].

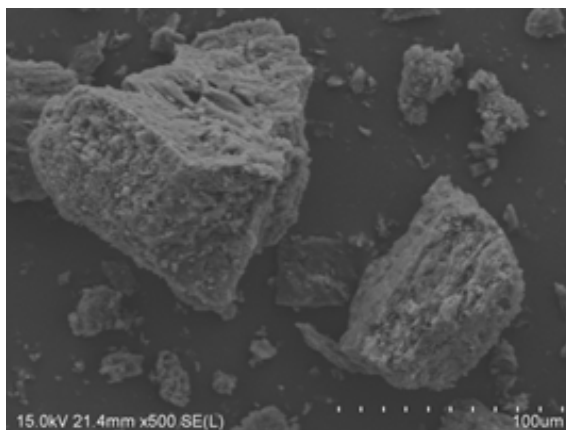


FIG. III.5 – SEM observation of *Pwd\_Fe2\_Ink\_ratio3* after ageing.

but were insufficient to obtain a fully amorphous matrix: the crystallinity, evaluated with the software Fullprof Suite, remained close to 36 % (FIG. III.4B). We also came to the conclusion that the crystallization of our samples jeopardized chemical interaction of cellobiose with iron and oxygen due to the rather big size of the crystals (of the order of some mm) and to their low porosity limiting the contact with atmospheric humidity and air (FIG. III.5). Solid state systems therefore did not appear to be the most appropriate ones to study the glycosidic bond cleavage induced by iron and oxygen. Therefore we decided to pursue our investigations on solution systems.

### III.3 Degradation of cellobiose in solution

The monitoring of the cellobiose degradation in solution (and of related glucose formation due to bond scission) was done using capillary electrophoresis. This investigation was together with complementary measurements that were done to monitor: i) pH evolutions in the solution media; ii) infrared spectroscopic changes, especially with respect to oxidized functions; iii) UV-vis spectroscopic responses to follow iron oxidation; iv) formation followed by mass spectrometry of glucose decomposition products with or without iron.

#### III.3.1 Experimental factorial design

In view of the several parameters to be changed in the experiments (mainly pH, iron nature and content, and presence or not of oxygen), we chose in this part to carry out the study with the help of a factorial experiment approach. Indeed, in classical experiments, the objective is often to individually follow each type of experimental conditions. By contrast, in a factorial experiment the objective is generally to evaluate how combinations of different types of experimental conditions impact the global response of the system in order to maximize or minimize it. This allows identifying the parameters having most important impact.

##### a Experimental domain

Ideally, we wanted to study the impact of different factors on cellobiose degradation: oxygen, pH, iron(II) and iron(III). As those factors are not independent from each others, these four parameters are not compatible with a factorial experimental design. A different approach was used to get independent factors: oxygen content, total iron (i.e. iron(II)

initially introduced) and pH (fixed with the addition of a base or an acid). Ageing being carried out during several weeks, we limited ourselves to two levels for each factors: with oxygen or with argon, with or without iron and under midly or highly acidic conditions (TAB. III.3).

N°	Factor	Coding	
		1	-1
$X_1$	Atmosphere	O <sub>2</sub>	Ar
$X_2$	Iron	Fe	no Fe
$X_3$	pH	3.6	1.6

TAB. III.3 – Coding of the three factors studied.

### b Experimental conditions: trials matrix

Because there are three factors and each factor has two levels, this is a  $2 \times 2 \times 2$ , or  $2^3$ , factorial design. This design will have  $2^3=8$  different experimental conditions. TAB. III.4 represents all the combination to be tested. The experimental domain will be a cube with data points at each corner.

Trial N°	$X_1$	$X_2$	$X_3$	Atmosphere	Iron	pH
1	-1	-1	-1	Ar	no Fe	1.6
2	1	-1	-1	O <sub>2</sub>	no Fe	1.6
3	-1	1	-1	Ar	Fe	1.6
4	1	1	-1	O <sub>2</sub>	Fe	1.6
5	-1	-1	1	Ar	no Fe	3.6
6	1	-1	1	O <sub>2</sub>	no Fe	3.6
7	-1	1	1	Ar	Fe	3.6
8	1	1	1	O <sub>2</sub>	Fe	3.6

TAB. III.4 – Trial matrix. Fe stands for total iron, Ar for argon bubbling and O<sub>2</sub> for oxygen bubbling.

### c Matrix of the model

For three variables  $X_1$ ,  $X_2$  and  $X_3$ , the first order model of the experimental response  $Y$  is:

$$Y = a_0 + a_1X_1 + a_2X_2 + a_3X_3 + a_{1,2}X_1X_2 + a_{1,3}X_1X_3 + a_{2,3}X_2X_3 + a_{1,2,3}X_1X_2X_3 \quad (\text{III.8})$$

with

$a_0$ , the response at the center of the experimental domain (an average of all responses);

$a_1$ ,  $a_2$  and  $a_3$ , the effect of each factor;

$a_{1,2}$ ,  $a_{1,3}$ ,  $a_{2,3}$  and  $a_{1,2,3}$ , a measure of the interaction between factors.

The higher is the value of  $a_x$ , the higher is the impact of the factor for  $x = 1$  to 3 or the interaction for  $x = (1,2); (1,3); (2,3); (1,2,3)$ . The matrix of the model  $X$  is given in TAB.

III.5, along with  $Y$ : matrix of experimental responses and  $A$  vector of  $a_x$  coefficients, which is obtained using the following formula

$$A = ({}^tX \cdot X)^{-1} \cdot {}^tX \cdot Y \quad (\text{III.9})$$

With  ${}^tX$  the transpose of the matrix  $X$ .

Trial N°	$I$	$X_1$	$X_2$	$X_3$	$X_1X_2$	$X_1X_3$	$X_2X_3$	$X_1X_2X_3$	$Y$	$A$
1	1	-1	-1	-1	1	1	1	-1	$y_1$	$a_0$
2	1	1	-1	-1	-1	-1	1	1	$y_2$	$a_1$
3	1	-1	1	-1	-1	1	-1	1	$y_3$	$a_2$
4	1	1	1	-1	1	-1	-1	-1	$y_4$	$a_3$
5	1	-1	-1	1	1	-1	-1	1	$y_5$	$a_{1,2}$
6	1	1	-1	1	-1	1	-1	-1	$y_6$	$a_{1,3}$
7	1	-1	1	1	-1	-1	1	-1	$y_7$	$a_{2,3}$
8	1	1	1	1	1	1	1	1	$y_8$	$a_{1,2,3}$

TAB. III.5 – Matrix of the model ( $X$ ), vector of the response  $Y$  and vector  $A$  of the  $a_x$  coefficients.

### III.3.2 Sample preparation

Samples were prepared by dissolving, in a round bottom flask, 3 g of D(+)-cellobiose (99.0 % Sigma Aldrich, Fe  $\leq$  5 ppm) in 34 mL of one of the aqueous solutions depicted in TAB. III.4 and III.6. Samples names are hereafter described as  $X\_pH\_gas$  where  $X$  stands for the ingredient initially present in solution that is supposed to interact with cellobiose (Fe2 for ferrous sulphate, Fe3 for ferric sulphate, Ink for a mixture of gallic acid and iron(II) sulphate and  $H_2SO_4$  for sulfuric acid), followed by the pH of the solution after one day of ageing and the gas used for flowding (argon or oxygen). A first set of samples was prepared according to the factorial experimental plan defined here above (TAB. III.4 and TAB. III.6). It was usefully completed by three additional samples depicted in TAB. III.7: a blank sample prepared with pure water and designed to check that cellobiose does not undergo thermal degradation (sample Water\_ $O_2$ ); a Fe(III) based sample, prepared with iron(III) sulphate (sample Fe3\_pH1.6\_ $O_2$ ), and a sample combining iron(II) sulphate and gallic acid (sample Ink\_pH2\_ $O_2$ ). The concentration of iron in solution was chosen so as to obtain a ratio  $n_{iron}/n_{cellobiose}$  of 0.16 which would correspond, on original manuscripts, to an iron concentration in paper of 26 mg  $\cdot$  g $^{-1}$  (or approx.  $2 \cdot 10^{18}$  atomes  $\cdot$  cm $^{-2}$  assuming a paper grammage close to 70 g  $\cdot$  m $^{-2}$ ). This concentration is relatively high but remains realistic with respect of the values found on original manuscripts [197].

Ferrous iron solutions (Fe2) were made from iron(II) sulfate heptahydrate (Sigma, 99.0 %) and ferric iron solutions (Fe3) from iron(III) sulfate pentahydrate (Accros organics, 99.0 %). Ink was prepared with a combination of iron(II) sulfate and gallic acid with a molar ratio of 3 identical as the one chosen before (chapter II section II.2.1). The experimental set-up consisted in a reflux apparatus with a triple necks round bottom flask, which allowed gas bubbling into the solution (FIG. III.6). Anoxia was obtained with argon bubbling using water that was deaerated during at least one hour prior solution preparation (factor Ar). Oxygen bubbling was used to reach oxygen saturation (factor  $O_2$ ). Solutions were stirred until complete dissolution of cellobiose then heated to a temperature of 80 °C

Sample	Concentrations <sup>a</sup> (mmol · L <sup>-1</sup> )		pH	Atmosphere
	Iron	H <sub>2</sub> SO <sub>4</sub>		
Fe2_pH1.6_O <sub>2</sub>	41.9	–	1.6	O <sub>2</sub>
Fe2_pH1.6_Ar		25		Ar
Fe2_pH3.6_O <sub>2</sub> <sup>b</sup>	41.9	–	3.6	O <sub>2</sub>
Fe2_pH3.6_Ar				Ar
H <sub>2</sub> SO <sub>4</sub> _pH1.6_O <sub>2</sub>	–	25	1.6	O <sub>2</sub>
H <sub>2</sub> SO <sub>4</sub> _pH1.6_Ar				Ar
H <sub>2</sub> SO <sub>4</sub> _pH3.6_O <sub>2</sub>	–	0.32	3.6	O <sub>2</sub>
H <sub>2</sub> SO <sub>4</sub> _pH3.6_Ar				Ar

<sup>a</sup> Final concentration in the flask. Cellobiose concentration was 258.8 mmol · L<sup>-1</sup>.

<sup>b</sup> For this sample, the pH was maintained above 3 with NaOH 0.1 mol · L<sup>-1</sup> addition along ageing.

TAB. III.6 – Description of samples for cellobiose degradation prepared according to the trial matrix.

Sample	Fe Concentrations <sup>a</sup> (mmol · L <sup>-1</sup> )	pH	Atmosphere
Fe3_pH1.6_O <sub>2</sub>	41.9	1.6	O <sub>2</sub>
Ink_pH2_O <sub>2</sub>	41.9	2	
Water_O <sub>2</sub>	–	6.8	

<sup>a</sup> Final concentration in the flask. Cellobiose concentration was 258.8 mmol · L<sup>-1</sup>.

TAB. III.7 – Additional samples.

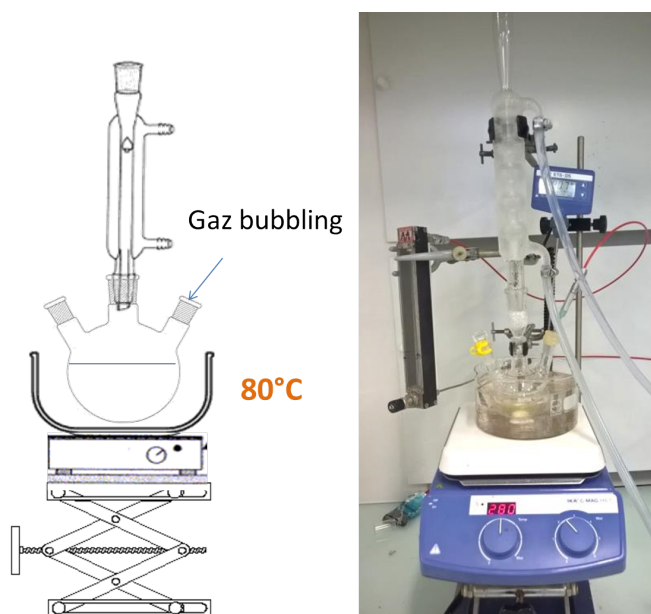


FIG. III.6 – Experimental set-up for cellobiose degradation study.

chosen to accelerate the degradation. This temperature was regulated by use of a silicon oil bath heated at 90 °C and equipped with a probe that was constantly adjusting the temperature to the desired value. Solutions were kept during ten days under continuous stirring and gas bubbling at a flow rate of 25 mL · min<sup>-1</sup>. Milli-Q water was added from time to time to replace water lost by evaporation. Two samples were systematically taken at 0, 1, 3, 7 and 10 days:

- the first was cooled down to ambient temperature in a ice-water bath then used for pH measurements and iron quantification;
- the second was frozen at -20 °C and kept apart until analysis by capillary electrophoresis, infrared spectroscopy and/or mass spectrometry measurements.

### III.3.3 Analytical techniques

#### a Capillary electrophoresis

To follow the evolution of carbohydrates (cellobiose and glucose) concentrations in the round bottom flask, capillary electrophoresis with a PDA was used following earlier works [198, 199, 200]. Complementary measurements were done to assess the presence of low organic acids using the method of Dupont et al.[200]. This section sums up the general principle of capillary electrophoresis in general, and next the method used for the analysis of carbohydrates and organic acids in particular.

#### b Principle of capillary electrophoresis [201]

Electrophoresis is a separation technique based on the mobility of charged molecules under an applied electric field. Separation occurs if the molecules have a different mobility through the fluid. This mobility is dependant on the size and on the charge of the analyte at a given pH. Capillary electrophoresis uses narrow capillaries to conduct the separation (typically of 20 µm to 75 µm internal diameter). This allows efficient heat dissipation and application of high voltage, which increases the speed of the separation in comparison to gel electrophoresis.

In the experimental conditions, the capillary is charged negatively and a mobile positively charged layer is formed in the solution and drives globally the liquid phase to the cathode, this phenomenon is called an electro-osmotic flux (EOF). All the molecules

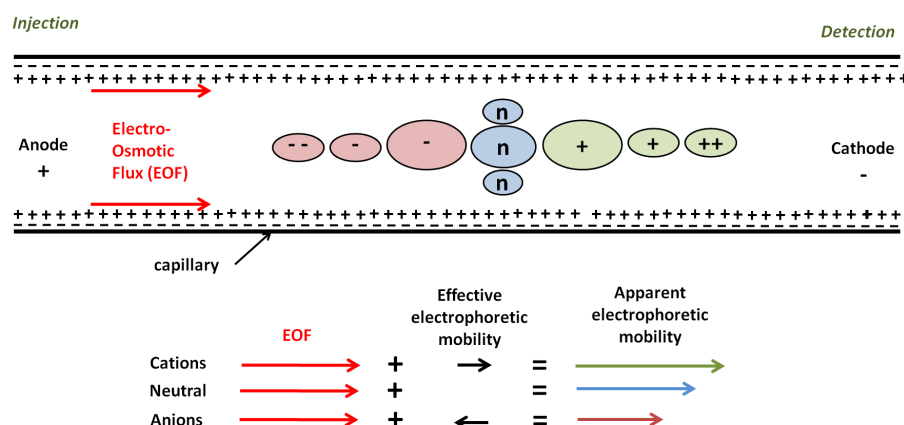


FIG. III.7 – Capillary electrophoresis principle.

(ionic and neutral) are affected by this flux. However, ions are attracted to the cathode (for cations) and to the anode (for anions), which increases or decreases their apparent electrophoretic mobility (as illustrated in FIG. III.7). Under this conditions, cations with the higher charge/mass ratio move first, followed by cations with lower charge/mass ratio, then neutral compounds and finally anions. The ions charge/mass ratio can be modified by adjusting the pH of the buffer (which affects their ionisation and also their mobility).

The capillary is mounted in a cartridge flowed by a specific cooling liquid. Two sample trays (inlet and outlet) move relatively to the capillary in an automated way. During separation, both capillary extremities and electrodes are immersed in the two buffer vials (inlet and outlet). When voltage is applied, the molecules migrate through the capillary from one end to the other and are detected by UV spectroscopy through the detection window.

### c Protocol for carbohydrates analysis

To analyze carbohydrates with capillary electrophoresis, a derivatization reaction is required as preliminary step (FIG. III.8A). This consists in grafting an UV-absorbant molecule 4-aminobenzoic acid ethyl ester, also called benzocaine (ABEE) (Sigma) to the sugar. This step aims at increasing the sugar detection. The ABEE reagent solution consists in ABEE ( $100 \text{ mg} \cdot \text{mL}^{-1}$ ) and acetic acid (99.6 %, Carlo Erba Reagents) ( $100 \text{ mg} \cdot \text{mL}^{-1}$ ) dissolved in MeOH. In conical bottom vials, 10 mg of sodium cyanoborohydride (95 %, Aldrich) is added to 1 mL of the ABEE reagent solution and then mixed with 1 mL of the diluted carbohydrate solution (sample diluted by a factor  $51^1$ ). After heating for 1 h at  $80 \text{ }^\circ\text{C}$ , the unreacted ABEE is precipitated by adding 3 mL of borate

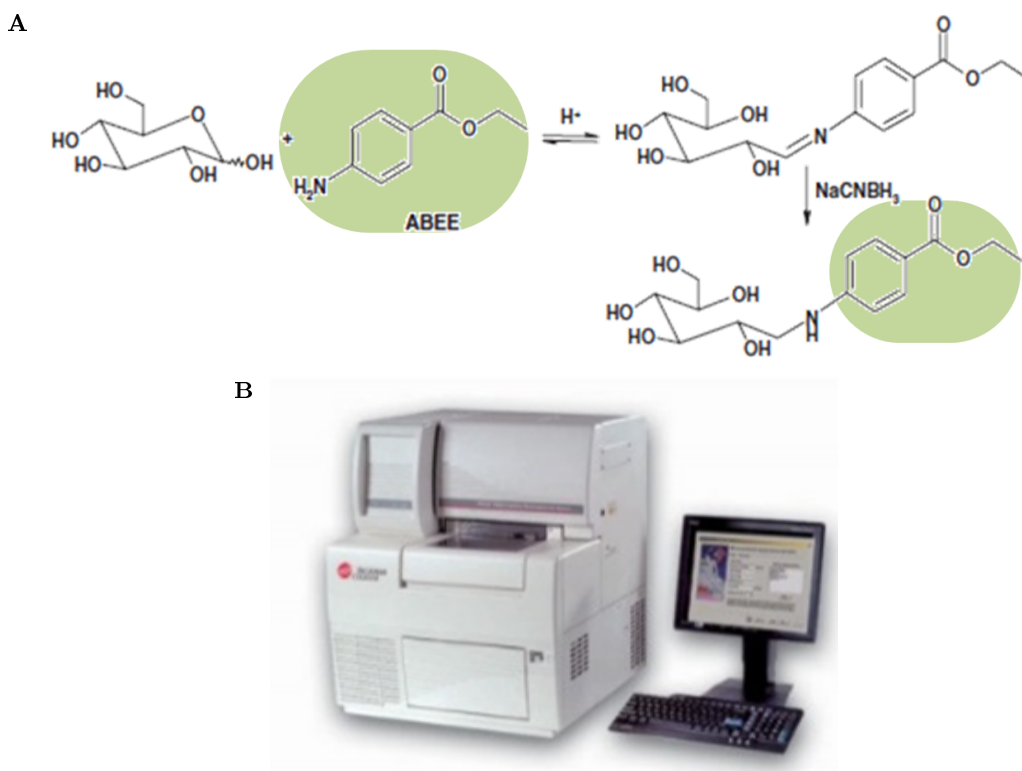


FIG. III.8 – Steps of the protocol for sugar analysis: (A) derivatization of the sugar, (B) then analysis on the P/ACE™ MDQ instrument from Beckman Coulter.

<sup>1</sup>194  $\mu\text{L}$  of the sample diluted by water into a 10 mL flask

buffer ( $450 \text{ mmol} \cdot \text{L}^{-1}$ , pH 8.6) which was prepared by dissolving boric acid (99.79 %, Fisher Chemicals) in milli-Q water and adjusting pH with sodium hydroxide  $1 \text{ mol} \cdot \text{L}^{-1}$  (Fisher Chemicals). Vials were vortexed and cooled at room temperature. The precipitate was removed by filtration with a chromafil filter ( $0.20 \text{ } \mu\text{m}$  PTFE, Macherey-Nagel).

A capillary electrophoresis P/ACE™ MDQ (Beckman Coulter) equipped with a photodiode array detector PDA was used to detect derivatized sugars (FIG. III.8B). The system operation, data acquisition, calibration, and quantitation were performed using the 32 Karat 5.0 software (Beckman Coulter). The derivatized sugars in the sample were identified according to their migration time  $t_m$  compared to model compounds. Direct UV detection at 305 nm of the pre-derivatised carbohydrates was used with a bandwidth of 30 nm (reference 400 nm). Data collection rate was set to 4 Hz. A bare fused silica capillary with  $20 \text{ } \mu\text{m}$  internal diameter (Beckman Coulter) was cut to a total length of 48.5 cm (40 cm effective length). The capillary was rinsed by flushing 1 min with NaOH at  $0.1 \text{ mol} \cdot \text{L}^{-1}$  followed by 1.5 min with deionised water. It was then conditioned for 3 min with the running buffer, a borate buffer  $450 \text{ mmol} \cdot \text{L}^{-1}$ , pH 9.94, prepared with boric acid and NaOH ( $1 \text{ mol} \cdot \text{L}^{-1}$ ). The injection was made in hydrodynamic mode by applying a pressure of 0.5 psi for 20 s. The separation voltage was 28 kV applied to the anodic end, and the resulting current was 17  $\mu\text{A}$ . The run temperature was fixed to  $20 \text{ }^\circ\text{C}$ . After the analysis the capillary was rinsed for 2 min with deionised water.

Sugars concentrations in diluted solutions were determined with the calibration curve established with standards solutions (Appendix I). Concentrations in the round bottom flask were then deduced. Normalized cellobiose concentration ( $C_t$ ), cellobiose conversion ( $X_t$ ) and glucose yield ( $R_t$ ) were evaluated for each time  $t$  with the  $n_t^y$  number of moles of  $y$  at  $t$  by using the following formulas:

$$C_t = \frac{n_t^{cell}}{n_0^{cell}} \quad (\text{III.10}) \quad X_t = 1 - C_t \quad (\text{III.11}) \quad R_t = \frac{n_t^{gluc}}{2 \cdot n_0^{cell}} \quad (\text{III.12})$$

It is worth noting that the carbohydrates concentrations are obtained at one precise time and result from the sum the quantity that is formed and the one that disappears. They are not cumulative measurements.

#### d Protocol for organic acid analysis

The presence of small organic acids in the solution samples was researched by capillary electrophoresis, with the same instrument as for carbohydrates analysis, yet using a different protocol already defined by Dupont et al.[200]. Indirect UV detection at 350 nm was used with the reference wavelength at 200 nm and a bandwidth of 20 nm. Data collection rate was set to 4 Hz. A bare fused silica capillary with  $75 \text{ } \mu\text{m}$  internal diameter (ID) (Beckman Coulter) was cut to a total length of 62 cm. Prior to injection the capillary was rinsed by flushing 1 min with NaOH  $0.1 \text{ mol} \cdot \text{L}^{-1}$  followed by 1.5 min with deionised water. It was then conditioned for 1 min with the running buffer. The buffer was prepared with 2,6-pyridinedicarboxylic acid (PDAc) (99 %, Aldrich) at  $5 \text{ mmol} \cdot \text{L}^{-1}$  as background electrolyte and Cetyltrimethylammonium bromide (CTAB) (Aldrich) at  $0.5 \text{ mmol} \cdot \text{L}^{-1}$ , pH 5.6 (adjusted with NaOH  $1 \text{ mol} \cdot \text{L}^{-1}$ ). The injection was made in hydrodynamic mode

by applying a pressure of 0.7 psi for 4.5 s. A separation voltage of  $-25$  kV was applied to the anodic end. The run temperature was fixed to  $25$  °C. After each analysis the capillary was rinsed for 2 min with deionised water.

#### e Infrared spectroscopy

For infrared spectroscopic measurements, the solution samples were freeze-dried for 48 h with the apparatus Cryos-55 (Cryotec). The resulting powder samples were ground in an agate mortar then analyzed by ATR-FTIR spectrometry using the apparatus and protocol already depicted in section III.2.2b. The spectra were normalized with respect to the  $2900\text{ cm}^{-1}$  peak height corresponding to C-H elongation (to serve as internal standard for semi-quantitative measurements, and to correct for an eventual difference of pressure applied to the sample). To follow the evolution of oxidation, the signal between  $1550\text{ cm}^{-1}$  and  $1850\text{ cm}^{-1}$ , that mainly corresponds to the presence of carbonyl and carboxyl groups, was deconvoluted in a series of Gaussian distributions using the *Omnice* software.

#### f Iron quantification by UV-vis spectroscopy

In order to monitor iron speciation during the experiment, UV-vis spectroscopy was used and measurements were performed on a UNICAM UV/Vis Spectrometer. The same protocol as the one described in section II was used (see details in appendix C).

#### g Mass spectrometry

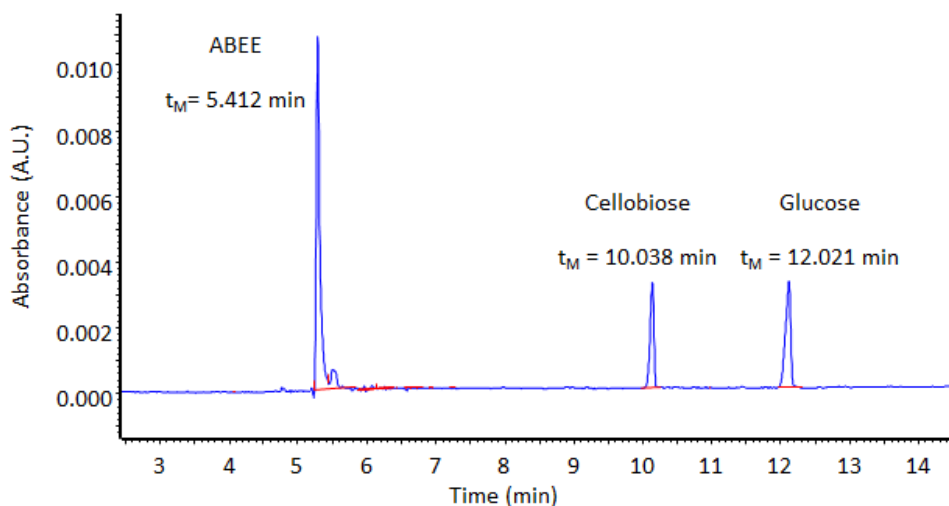
A few mass spectrometry measurements were attempted to investigate samples exposed to sulfuric acid and iron(II) sulphate (samples  $\text{H}_2\text{SO}_4_{\text{pH}1.6_{\text{O}_2}}$  and  $\text{Fe}2_{\text{pH}1.6_{\text{O}_2}}$ , see TAB. 1.6 ) in order to detect some differences in composition that could be attributed to oxidative degradation. Electrospray mass spectra were acquired using a Q-STAR instrument (ESI-qQ-TOF) from AB-Sciex. Since no prior separation was done, the whole sample mass distribution was analyzed by direct injection. Both positive and negative ion modes were tested. Full scan mass spectra were acquired from  $m/z$  50 to 1000. Samples solutions were diluted by 1000 in milli-Q water and  $2\text{ }\mu\text{L}$  were injected with a mixture of methanol/acidified water (formic acid) 60:40 at a flow of  $40\text{ }\mu\text{L}\cdot\text{min}^{-1}$ .

### III.3.4 Influence of pH, iron and oxygen on cellobiose conversion into glucose

Before using capillary electrophoresis to analyse our samples, it was necessary to check that the presence of iron/ink was not an issue for quantitative measurements since iron has a high ability to form precipitates that may block small capillaries. Non-degraded samples with and without iron/ink were analyzed and similar concentrations were obtained, meaning that filtration and precipitation steps of exceeding ABEE with borate buffer were sufficient to remove most of iron.

In presence of both iron(II) and oxygen a partial conversion of cellobiose to glucose was achieved at  $80$  °C, as attested by the detection of two peaks on the electropherogram (FIG. III.9). These scissions are not due to pure thermal effect as no conversion was observed on the  $\text{Water}_{\text{O}_2}$  sample, even after 10 days of ageing. They are clearly attributable to low pH values and/or presence of iron and oxygen.

The influence of different parameters (pH, presence of iron and/or oxygen) on cellobiose degradation has been tested. For all experiments carried out at pH 3.6, no degradation

FIG. III.9 – Electropherogram of derivatized  $Fe_2\_pH1.6\_O_2$  sample at 3 day of ageing.

Sample	pH decrease at 1 d	Fe oxidation	mixture color	presence of precipitate	Products		formation of C=O
					glucose	≠	
$Fe_2\_pH1.6\_O_2$	✓	✓	orange	✓	✓	✓	✓
$Fe_2\_pH1.6\_Ar$			transparent		✓		
$Fe_2\_pH3.6\_O_2$	✓*	✓	orange/brown	✓			
$Fe_2\_pH3.6\_Ar$			transparent				
$H_2SO_4\_pH1.6\_O_2$			transparent		✓		
$H_2SO_4\_pH1.6\_Ar$			transparent		✓		
$H_2SO_4\_pH3.6\_O_2$			transparent				
$H_2SO_4\_pH3.6\_Ar$			transparent				
$Fe_3\_pH1.6\_O_2$			orange	✓	✓	✓	✓
$Ink\_pH2\_O_2$	✓	✓	dark blue/ dark brown	✓	✓	✓	✓

\* a slight decrease of pH was noticed between the addition of sodium hydroxide.

TAB. III.8 – Changes observed during ageing of cellobiose samples.

of cellobiose occurred even when iron and oxygen were present ( $Fe_2\_pH3.6\_O_2$  sample, grey plain line, FIG. III.10, TAB. III.8). The stability of cellobiose at pH 3.6 was clearly unexpected since depolymerization of ink impregnated papers of similar pH values was perceptible at ambient temperature [111]. This apparent contradiction directly questions the meaning of pH measurements on paper that are in fact performed on aqueous extracts. They correspond to an average response of released acidic compounds. If these compounds are not uniformly distributed within paper fibers, local pH values may undergo great variations. This is probably why, at “pH 3.6”, glycosidic bond cleavage occur on inked papers but not on cellobiose in homogeneous medium.

Conversely, a clear cellobiose degradation was observed for all experiments carried out at pH 1.6 (FIG. III.11). It is however not similar for all types of samples. The  $H_2SO_4\_pH1.6\_Ar$  sample was used as a reference sample for acid hydrolysis (low pH, no iron, no oxygen). On this sample, the sum of glucose yield and normalized cellobiose concentration reaches 100 % recovery, meaning that cellobiose is converted into exclusively glucose. This behavior is consistent with pure acid hydrolysis (FIG. III.11A). On sample

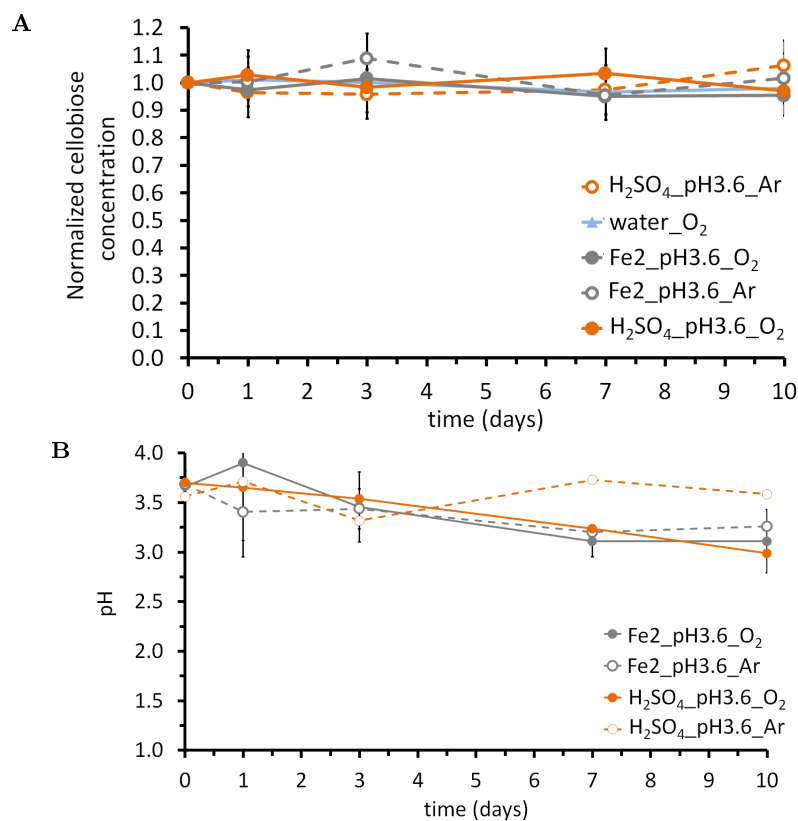


FIG. III.10 – Monitoring of (A) cellobiose concentration and (B) pH in samples solutions at pH3.6. Orange curves represent sulfuric acid mixture with (plain lines) or without (dotted lines) oxygen. Grey curves represent iron (II) sulfate mixture with (plain lines) or without (dotted lines) oxygen.

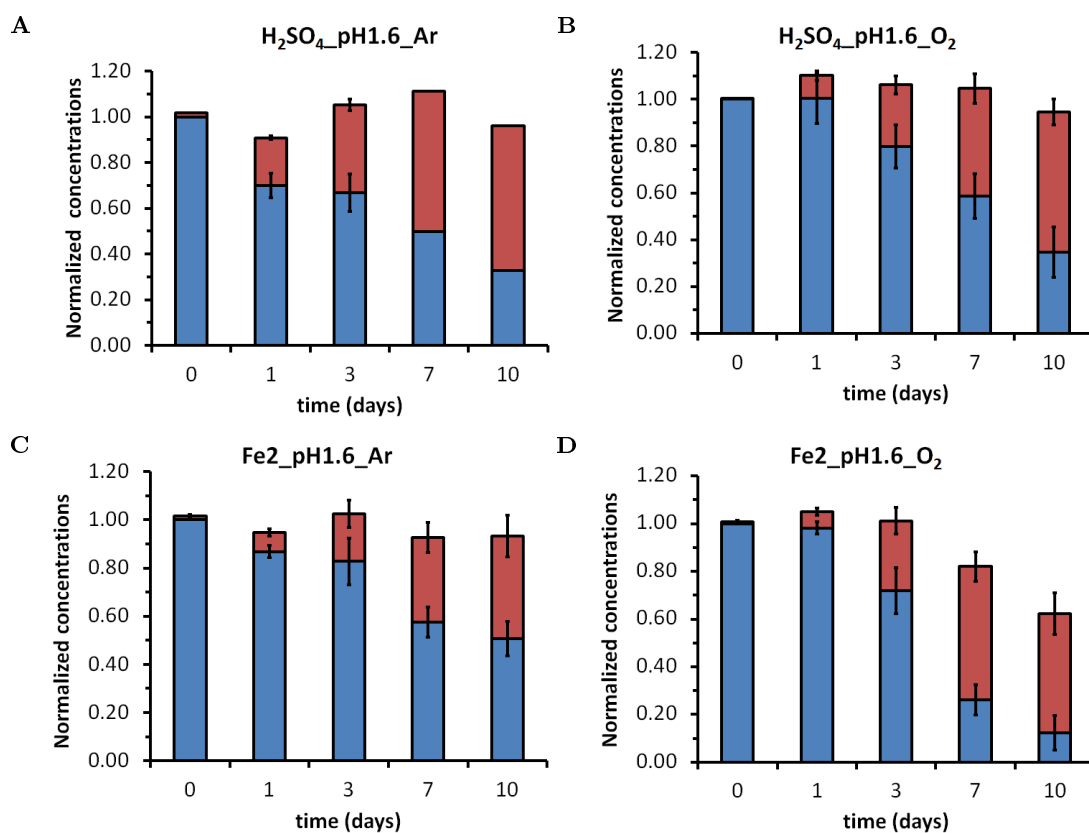


FIG. III.11 – Normalized cellobiose concentration (in blue) and glucose yield (in red) measured by capillary electrophoresis in samples at pH 1.6. Monitoring of (A) H<sub>2</sub>SO<sub>4</sub>\_pH1.6\_Ar, (B) H<sub>2</sub>SO<sub>4</sub>\_pH1.6\_O<sub>2</sub>, (C) Fe2\_pH1.6\_Ar and (D) Fe2\_pH1.6\_O<sub>2</sub> samples.

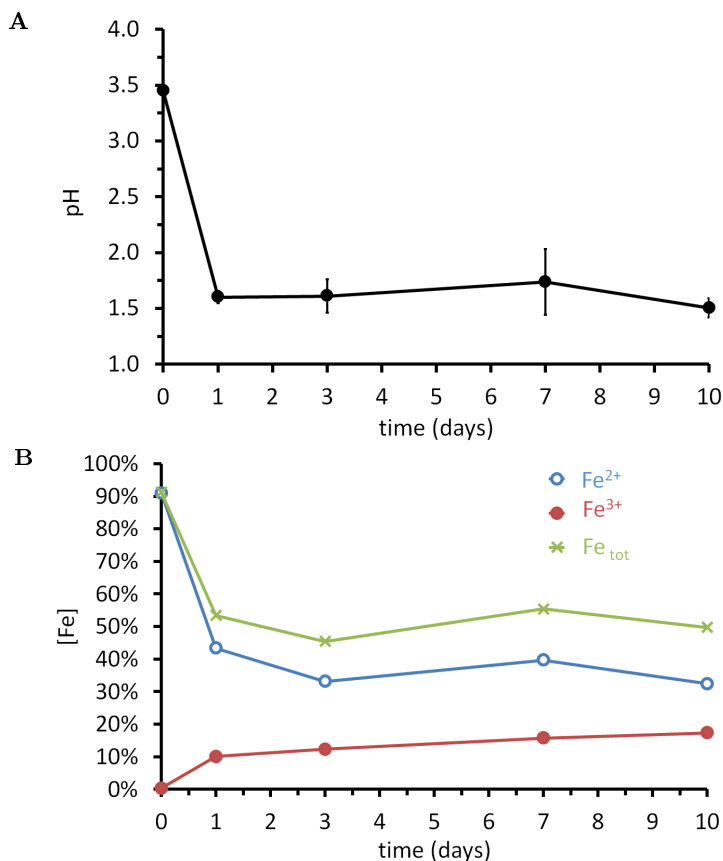


FIG. III.12 – Evolution of (A) pH and (B) iron concentrations in the  $Fe_2\_pH1.6\_O_2$  sample versus ageing time. Soluble iron(II) and iron(III) are monitored by UV-vis spectroscopy. Concentrations are normalized with respect to initial amount of iron.

$H_2SO_4\_pH1.6\_O_2$  for which oxygen is additionally present, the evolutions of normalized cellobiose concentration and glucose yield remain the same within error bars as what occurs without oxygen (FIG. III.11A and B). Therefore, the presence of oxygen did not induce oxidation at a perceptible level and the conversion of cellobiose exclusively followed an acid hydrolysis pathway. Similar considerations prevail for the  $Fe_2\_pH1.6\_Ar$  sample (FIG. III.11C), showing that, in absence of oxygen, the degradation of Fe(II) bearing samples is attributable to pure acidic hydrolysis.

However, a different behavior is observed on the  $Fe_2\_pH1.6\_O_2$  sample, for which oxygen and iron are simultaneously present (FIG. III.11D). During the first three days of ageing, cellobiose is exclusively converted into glucose (100 % recovery) and in same proportions than for above mentioned samples. Afterwards, the sum of glucose yield and normalized cellobiose concentration significantly decreases, suggesting either i) degradation of cellobiose into other products or ii) degradation of glucose into other products. Since glucose is the first degradation product of cellobiose, the latter point (ii) appears more likely. This by-product formation was not evidenced for the sample  $H_2SO_4, pH1.6, O_2$ , which is in agreement with Kwon et al.[76], who showed that cellobiose hydrolysis is easier than glucose degradation in dilute acid hydrolysis.

It is worth noting that the pH of Fe(II) bearing samples was not stable when oxygen is present. Immediately after solution preparation, the pH of  $Fe_2\_pH1.6\_O_2$  sample was 3.6. It rapidly decreased during the first day down to a value of 1.6 then remained stable (FIG. III.12). This behavior matches that of Fe(II) concentration which decreased from  $41.9 \text{ mmol} \cdot \text{L}^{-1}$  to  $18.8 \text{ mmol} \cdot \text{L}^{-1}$  (i.e. 60 % of soluble iron(II) was oxidized) within

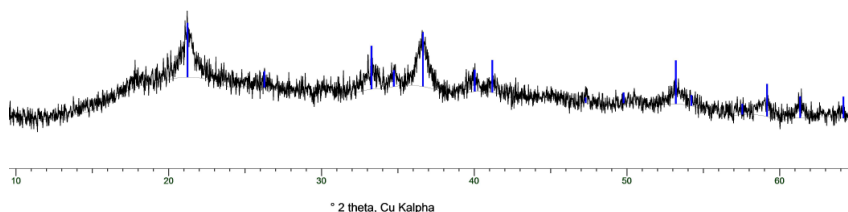


FIG. III.13 – XRD pattern of yellow precipitate formed during cellobiose  $Fe2\_pH1.6\_O_2$  (black curve) and peaks of reference compound goethite (blue lines).

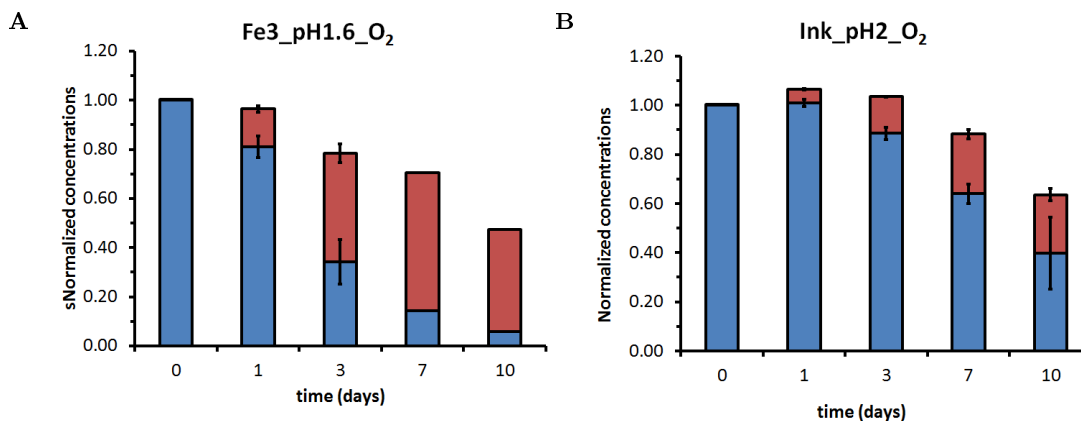


FIG. III.14 – Monitoring of cellobiose concentration (in blue) and glucose yield (in red) in (A)  $Fe3\_pH1.6\_O_2$  and (B)  $Ink\_pH2\_O_2$  samples.

the first day of ageing (FIG. III.12 B). In the same timeframe, Fe(III) concentration in the solution increased from 0 to  $4.21 \text{ mmol} \cdot \text{L}^{-1}$  and we observed formation of an orange iron oxide hydroxide precipitate identified as goethite by XRD (FIG. III.13, TAB. III.8). All these evolutions are related to oxidation of Fe(II) to Fe(III) and precipitation of this latter, which can be summarized with EQ. III.13 .



On the  $Fe2\_pH1.6\_O_2$  sample, after three days of ageing, the sum of glucose yield and normalized cellobiose concentration does not reach anymore 100 % recovery, but decreases down to approximately 60 %. This decrease is not related to an evolution of pH, or of concentration in Fe(II) or Fe(III) because all these parameters remain constant after three days (FIG. III.12). It is however for sure related to the simultaneous presence of iron and oxygen because it was also observed on  $Fe3\_pH1.6\_O_2$  and  $Ink\_pH2\_O_2$  samples (FIG. III.14). Also the combination of oxygen and iron (whichever the iron type) enhances other reactions than glycosidic bond scission. Interestingly, some proportion of Fe(II) is formed during ageing of the Fe(III) based sample ( $Fe3\_pH1.6\_O_2$ ), meaning that the solution contains a strong enough reducer (FIG. III.15B). Finally it is observed that the degradation of sample  $Ink\_pH2\_O_2$  is slower than the degradation of  $Fe3\_pH1.6\_O_2$  and  $Fe2\_pH1.6\_O_2$  samples (FIG. III.14 B, III.14A and III.11D). This is probably due to the pH of the solution which is initially 2.6, and decreases to 2 during ageing. These slightly higher pH values decrease the reaction rate of acid hydrolysis.

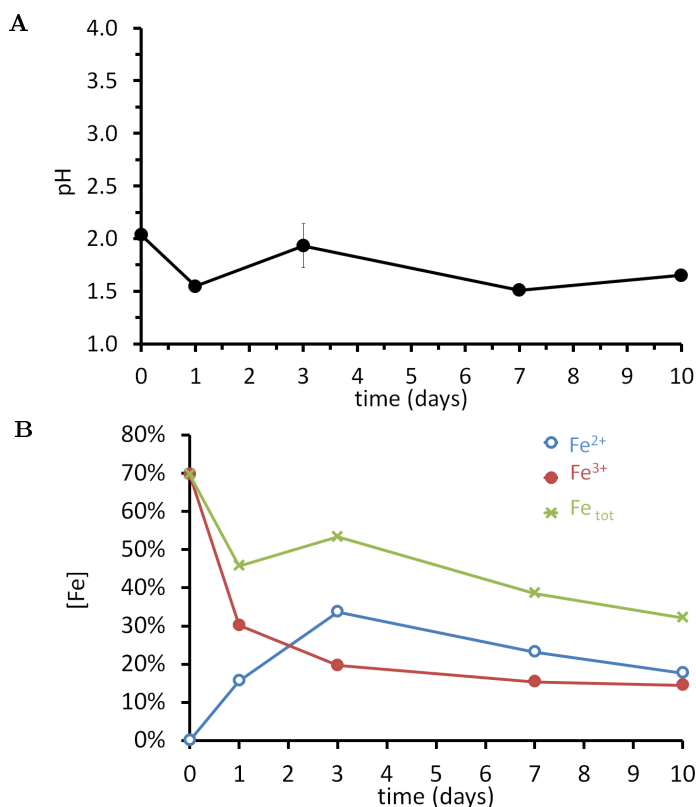


FIG. III.15 – Evolution of (A) pH and (B) iron concentrations of  $Fe_3\_pH1.6\_O_2$  sample versus ageing time. Soluble iron(II) and iron(III) are monitored by UV-vis spectroscopy. Concentrations are normalized with respect of initial amount of iron.



### Parameters influencing cellobiose degradation.

The study of cellobiose degradation in solution shows that pH is the parameter that has the most important impact: when pH is fixed at a value of 3.6, no modification is observed whatever the other parameters (presence of iron and/or oxygen). When it is fixed at a value of 1.6, cellobiose conversion is observed on all samples, meaning that acid hydrolysis is the main pathway of glycosidic bond cleavage. When iron and oxygen are simultaneously present additional reactions take place consuming glucose and/or cellobiose. These reactions are linked to redox reactions involving iron and oxygen, but requiring low pH as well.

### III.3.5 Investigation of degradation products

Investigation of the by-products formed in the  $Fe_2\_pH1.6\_O_2$  sample was done by infrared spectroscopy and mass spectrometry.

#### a Infrared spectroscopy

ATR-FTIR spectroscopy was used to investigate the nature of the by-products formed during ageing. The characteristics bands of carbohydrates are clearly visible as previously described for solid state samples. First analysis of sulfuric acid samples ( $H_2SO_4\_pH1.6\_O_2$ ) evidenced minor changes during ageing (FIG.III.16). They mostly involve the band at  $1641\text{ cm}^{-1}$ , attributed to water remaining after the freeze-drying process. This band increases with ageing, meaning that hydration is easier. Moreover a small shoulder appears

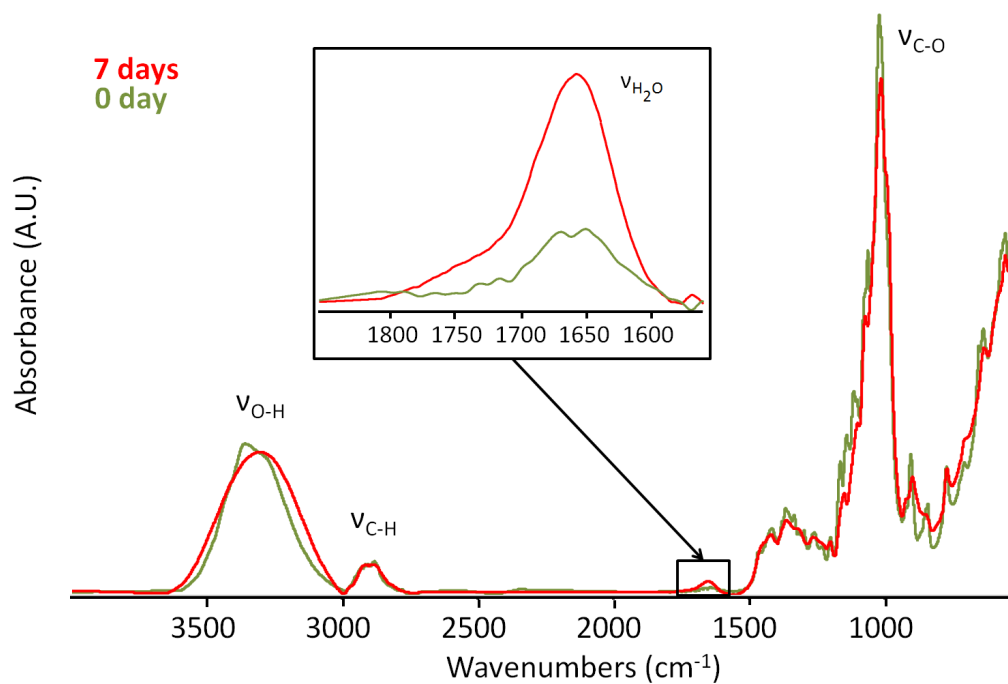


FIG. III.16 – ATR-IRTF spectra of  $\text{H}_2\text{SO}_4$ \_pH1.6\_ $\text{O}_2$  before ageing (green curve) and after seven days of ageing (red curve).

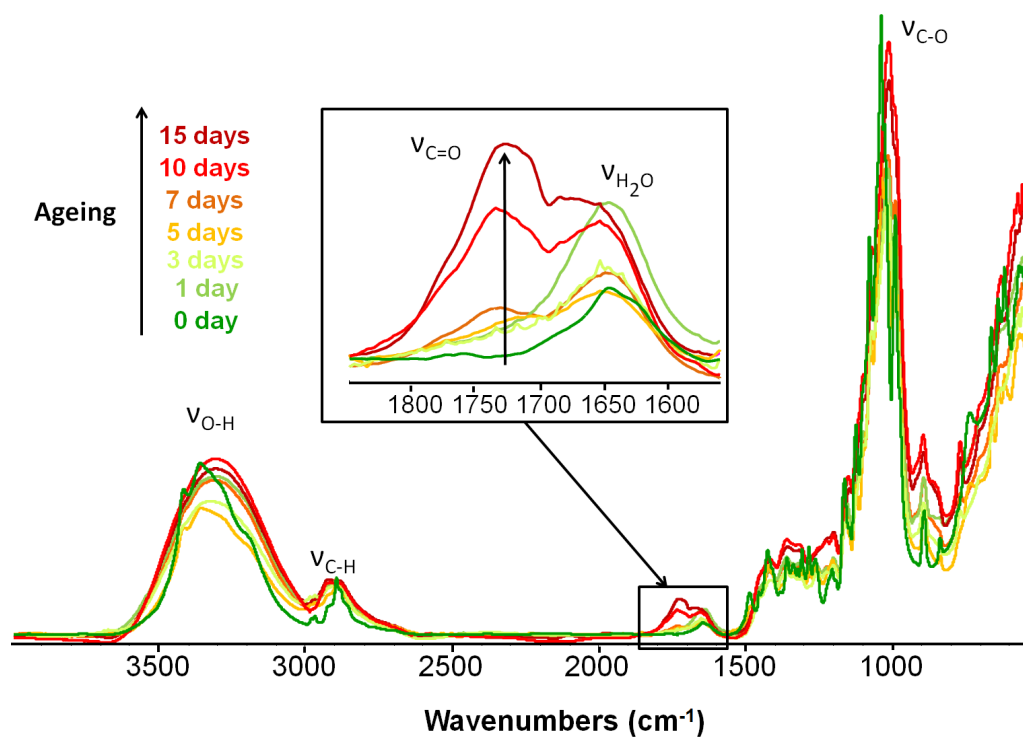


FIG. III.17 – ATR-FTIR spectra obtained during the ageing of  $\text{Fe}_2$ \_pH1.6\_ $\text{O}_2$  sample, going from 0 day (green curve) to 15 days (red curve).

near  $1750\text{ cm}^{-1}$  (FIG.III.16) that might be correlated to osidic bond cleavage, increasing the number of reducing end groups (aldehydes of the open-ring sugars). Indeed emergence of a weak absorption band at  $1718\text{ cm}^{-1}$  has already been attributed to formation of C=O on open-ring sugars present in freeze-dried solutions that underwent epimerisation: terminal aldehydes in case of aldose and ketones in the case of ketose [202].

With the iron containing Fe2\_pH1.6\_O<sub>2</sub> sample, the FT-IR spectra are less defined after 10 days of ageing but no substantial spectral evolution is detected in the fingerprint regions of cellobiose (FIG. III.17). Conversely, significant modifications are noticed in the region between  $1850\text{ cm}^{-1}$  to  $1650\text{ cm}^{-1}$  characteristic of water adsorption and the C=O stretching (FIG. III.17). The deconvolution of the signal in a series of Lorentzian-Gaussian distributions highlighted several contributions (FIG. III.18).

Absorptions at  $1621\text{ cm}^{-1}$ ,  $1641\text{ cm}^{-1}$  and  $1682\text{ cm}^{-1}$ , attributed to O-H bending vibration modes of adsorbed water [203, 204] were initially present. Conversely, the four other bands are appearing with ageing:

- the two bands at  $1729\text{ cm}^{-1}$  and  $1775\text{ cm}^{-1}$  are assigned to the C=O stretching mode of different functional groups (aldehyde, ketone, carboxylic acids, lactones. . . [205]). On paper, the band at  $1729\text{ cm}^{-1}$  has been attributed to mainly carboxyl groups [189](the participation of aldehyde end groups being negligible). More generally on carbohydrates, carboxylic acids absorb in the range  $1730\text{ cm}^{-1}$  to  $1740\text{ cm}^{-1}$ , ketone or aldehyde end groups of open-ring sugars around  $1718\text{ cm}^{-1}$ , lactones between  $1760\text{ cm}^{-1}$  and  $1726\text{ cm}^{-1}$  (for aldono-1,5-lactone) and  $1790\text{ cm}^{-1}$  and  $1765\text{ cm}^{-1}$  (for aldono-1,4-lactone) and ester between  $1748\text{ cm}^{-1}$  and  $1724\text{ cm}^{-1}$  (for example  $1727\text{ cm}^{-1}$  on cellobiose octoacetate);
- the bands at  $1705\text{ cm}^{-1}$  and  $1662\text{ cm}^{-1}$  were not fully interpreted but interestingly match values calculated for formation of two carboxylic acid functions on cellopentose [189]. They are also compatible with aldehyde end group formation and water respectively.

Furthermore, there is a systematic increase with time of the absorption bands at  $1729\text{ cm}^{-1}$  and  $1775\text{ cm}^{-1}$  (see FIG.III.17 and III.18C) while the other bands seem more or less constant. This attests of C=O formation during ageing. These groups could appear through oxidation mechanisms of cellobiose or glucose. They could as well result from decomposition of glucose that is prone to isomerization to fructose and then dehydrate under acidic condition (FIG.III.19). This forms HMF, humin and possibly levulinic acid and formic acid through hydrolysis [76]. All these new molecules bear C=O groups that might also account for the increase of absorption bands at  $1729\text{ cm}^{-1}$  and  $1775\text{ cm}^{-1}$ .

## b Organic acid investigation

To get a better insight in the formation of the small molecules mentioned above (FIG.III.19), the Fe2\_pH1.6\_O<sub>2</sub> solution was analyzed by capillary electrophoresis after 10 days of ageing to investigate the presence of low molecular organic acid. The electropherogram (FIG. III.20) shows some positive peaks corresponding to organic acids and negative peaks attributed to other UV absorbant molecules. Formic acid and acetic acid were identified in our sample aged ten days by comparison with standard sample prepared with sodium formate and sodium acetate (Aldrich), consistent with glucose decomposition in low molecular organic acids.

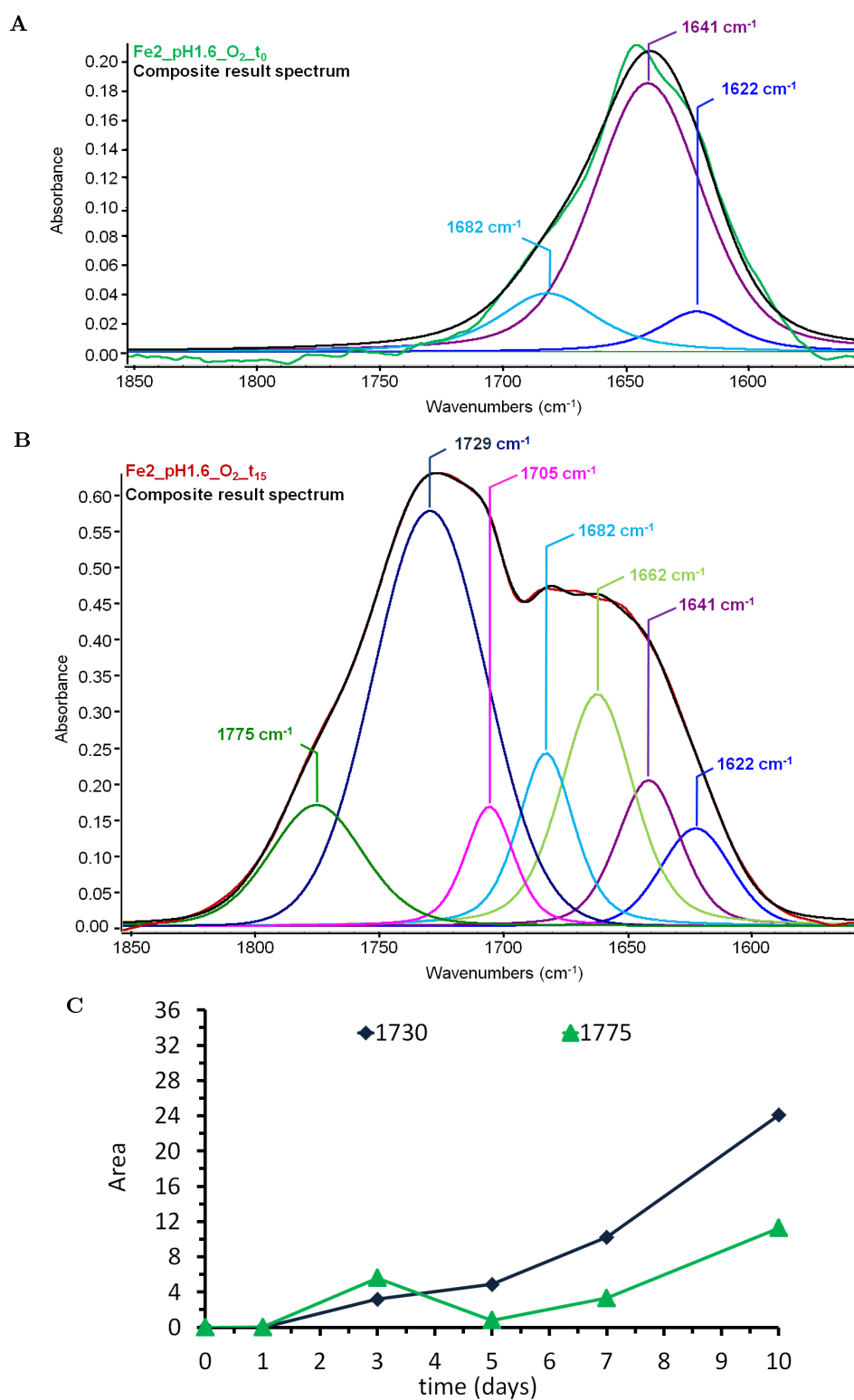


FIG. III.18 – Deconvolution of the infrared spectra of the Fe2\_pH1.6\_O2 sample in component peaks (A) before and (B) after 15 days of ageing and (C) follow-up of absorption peaks at 1729 cm<sup>-1</sup> and 1775 cm<sup>-1</sup>.

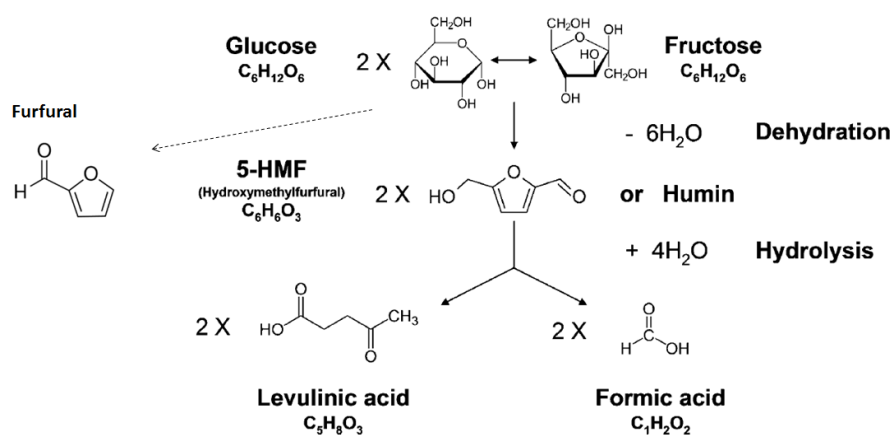


FIG. III.19 – Molecules formation from degradation pathways of glucose in acidic medium [76].

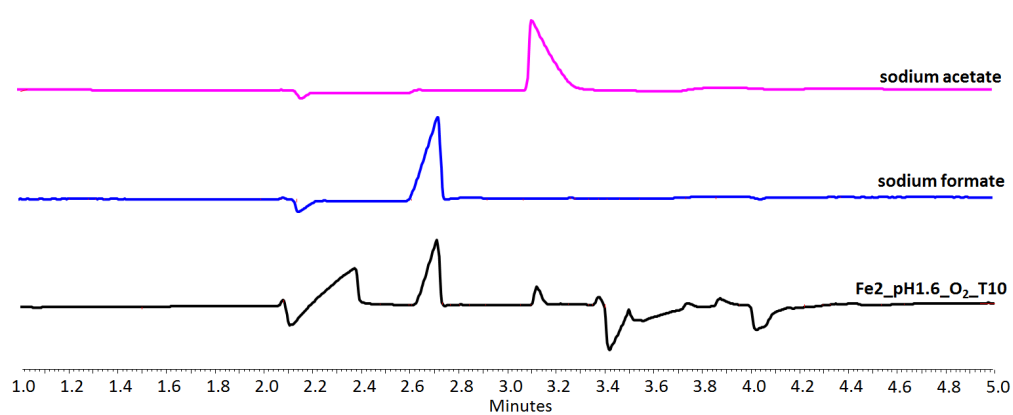


FIG. III.20 – Analysis of organic acids in Fe2\_pH1.6\_O2 by capillary electrophoresis.

Positive mode		Negative mode	
m/z	adducts	m/z	adducts
685	$[2M + H]^+$ cellobiose dimer	683	$[2M - H]^-$ cellobiose dimer
365	$[M + Na]^+$ cellobiose	387	$[M + HCOO]^-$ cellobiose
360	$[M + NH_4]^+$ cellobiose ammoniac pollution		
343	$[M + H]^+$ cellobiose	341	$[M - H]^-$ cellobiose
325	$[M + H - H_2O]^+$ cellobiose		
289	?		
281	?		
265	?		
207	?	212	?
203	$[M + Na]^+$ glucose		
198	$[M + NH_4]^+$ glucose ammoniac pollution		
190	?	188	?
181	$[M + H]^+$ glucose	179	$[M - H]^-$ glucose
163	$[M + H - H_2O]^+$ glucose		
149	$[M + Na]^+$ 5-HMF		
145	$[M + H - 2H_2O]^+$ glucose		
142	?		
127	$[M + H]^+$ 5-HMF	96	$HSO_4^-$

TABLE III.9 – Main peaks found on mass spectra of Fe2\_pH1.6\_O2 and H2SO4\_pH1.6\_O2 samples

### c Mass spectrometry

Mass spectrometry was attempted as a complementary tool to investigate formed by-products despite the fact that sugars are prone to dehydration after ionisation in positive mode [206].

A particular attention was put on differences between solutions with iron(II) sulfate and those with sulfuric acid. Mass spectra of Fe2\_pH1.6\_O2 and H2SO4\_pH1.6\_O2 samples were recorded after 7 days of ageing (FIG.III.21). No obvious difference was noticed between the two spectra: the observed peaks in both samples have the same  $\frac{m}{z}$  value. Major peaks observed are those of cellobiose adducts and glucose adducts (FIG.III.9). Masses (at 127 and 149) that could correspond to hydromethylfurfural adducts have been detected. They could suggest decomposition of glucose. However these peaks are very small, present in both samples (sulfuric acid and iron sulfate) and thus cannot explain the differences observed on FT-IR spectra. No mass corresponding to carbonylated cellobiose or glucose was evidenced meaning that major formation of carboxyl or carbonyl groups on cellobiose and glucose pyranose rings should be excluded. The similarity of mass spectra suggests that the formation of oxidized functions observed in infrared spectroscopy near  $1700\text{ cm}^{-1}$  does not correspond to the formation of a major oxidized compound. It more likely results from the contributions of C=O groups present in several minor compounds difficult to highlight when glucose and cellobiose are major components. This difficulty might be overcome by using a separative technique (for example HPLC) prior mass spectrometry to remove the contribution of glucose and cellobiose on the mass spectra.

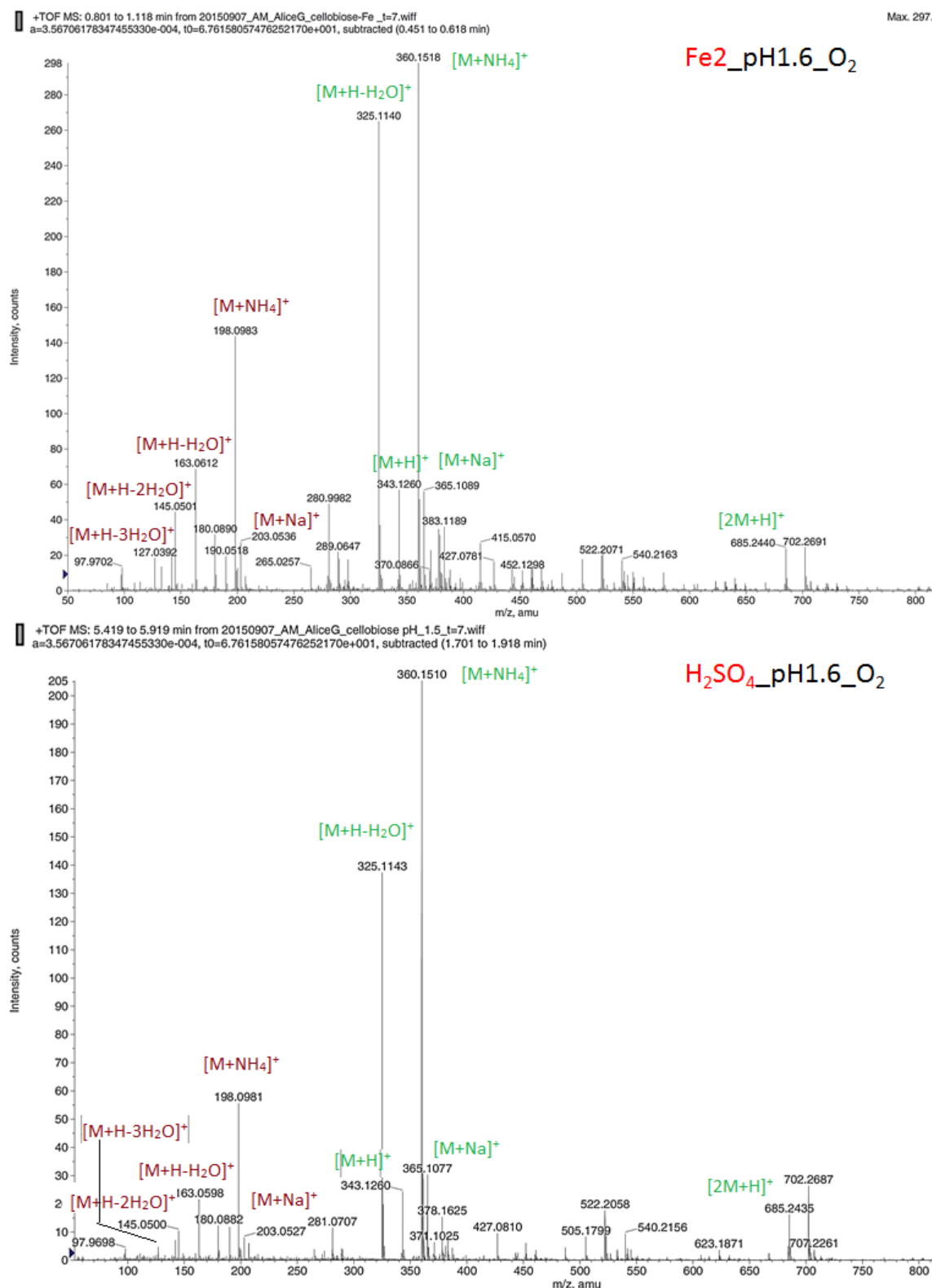


FIG. III.21 – Mass spectra obtained in positive ion mode of  $\text{Fe}_2\text{_pH1.6\_O}_2$  (top) and  $\text{H}_2\text{SO}_4\text{_pH1.6\_O}_2$  samples (bottom) after seven days of ageing. In green are represented adducts of cellobiose and in red adducts of glucose.

 **The case of iron(II) sulfate mixture with oxygen at pH 1.6.**

During the first three days of the ageing, hydrolysis is predominant, in link with the iron oxidation that acidifies the medium and leads to iron oxide hydroxide formation. After seven days of ageing, other products than glucose are produced, as shown by capillary electrophoresis and infrared spectroscopy, which attested the formation of C=O groups, coming predominantly from oxidation or dehydration. Formic acid and acetic acid were detected as well in this sample, but due to their volatility, they are doubtfully responsible for the observed infrared bands as the samples were freeze-dried prior FT-IR spectroscopy measurement.

### III.3.6 Analysis of the results with experimental design

Regarding the experimental design, the parameter having the biggest impact on the response can be determined. In our case, the response matrix  $Y$  gathers the measurements of cellobiose concentrations measured by capillary electrophoresis. Ten days of ageing were chosen to evaluate the most decisive parameter and the combination of conditions which maximize cellobiose conversion (i.e. gives a minimal cellobiose concentration) (TAB. III.10A).

Trial N°	$C_{10}$	Factors	Value
1	0.33	$a_0$	0.66
2	0.35	$a_1$	-0.07
3	0.51	$a_2$	-0.01
4	0.12	$a_3$	0.34
5	1.06	$a_{1,2}$	-0.05
6	0.97	$a_{1,3}$	0.03
7	1.02	$a_{2,3}$	0.00
8	0.95	$a_{1,2,3}$	0.05

TAB. III.10 – (A) Response matrix of normalized cellobiose concentration at 10 days and (B) factors of the first order model for minimal [cellobiose].

The factors reported in TAB. III.10B were obtained with the experimental matrix TAB. III.5. The most important factors  $X$  are those with the significant  $a_x$  coefficients. In order to assess this latter, the standard deviation had to be determined with a repetition test. The conditions of the trial 4 have been chosen since they allow a minimal concentration of cellobiose (maximal conversion). A average value of 0.12 ( $\pm 0.07$ ) was found. We can conclude that only the coefficient  $a_0$  and  $a_3$  are significant meaning i) that only the  $X_3$  factor, i. e. pH, is significant and ii) that there are no interactions between the factors.

## III.4 Conclusion

In the first part of this chapter, the scission of the cellulose chain in model paper samples was followed by viscosity measurements and zero-span mechanical testing. Inked paper samples were prepared in such a way as to undergo a fast depolymerisation even at ambient temperature. During the first phase of the degradation, the Ekenstam model was used to determine the rate constant of chain scissions. The degradation of our ink impregnated

model papers was much faster than that of acidic papers (rate constants of 1–2 orders of magnitude above). The rate constants were then used to calculate activation energies using Arrhenius law. It was shown that this law could be extrapolated at ambient temperature. Resulting activation energies were close to those of lignin-free acidic papers. All these observations are consistent with a dominant acidic hydrolytic process of which the energy barrier is reduced by the presence of oxygen and iron.

In order to further investigate the degradation mechanism, cellobiose was chosen as a simpler model molecule to study the key parameter leading to osidic bond scissions. To this end, the degradation of cellobiose solutions was also monitored by capillary electrophoresis in presence of iron sulphate or sulfuric acid, with or without oxygen, and at different pH values (3.6 and 1.6). This approach showed that pH is the major parameter governing cellobiose conversion to glucose, the presence of iron and oxygen being of secondary importance with respect to chain scissions. Iron and oxygen are however not entirely de-correlated to pH considerations since the combination of ferrous iron and oxygen leads to the formation of iron oxide-hydroxide (goethite) and to the release of protons which acidify the medium and favors acid hydrolysis. In addition, the presence of iron leads to other side-products in comparison to pure sulfuric acid solutions. Formation of these products is linked to a strong increase in number of C=O groups that comes from formation of carboxylic acids and ketones. This is probably due to the fact that oxidation of glucose is enhanced in presence of iron at low pH. The presence of formic and acetic acids in solution was also evidenced by capillary electrophoresis. However, attributing to these acids the increase of C=O groups observed by FTIR appears unlikely since formic and acetic acids are both highly volatile and probably do not remain in the sample after the freeze-drying process.

The two approaches developed on model inked papers samples and cellobiose solutions lead to a similar conclusion that hydrolysis (promoted by oxidation and precipitation of ferrous compounds) is the predominant pathway of chain scissions. However the low pH at which the scissions are observed for cellobiose (pH 1.6) is largely below what is commonly found on paper aqueous extracts (pH 3-4). This directly questions the meaning of pH measurements performed on aqueous extracts. As they correspond to an average of leached acidic species, they might largely underestimate local pH values.

We also found useful to pursue our work by exploring the repartition of iron, and more particularly iron(II), in paper fibers. As paper fibers diameter is close to a tenth micrometers, a nano-scale technique, such as Scanning Transmission X-ray Spectroscopy seemed promising for this purpose. It moreover allows mapping the speciation of several elements, such as carbon, nitrogen, iron, etc. In the next chapter, we will investigate the possibilities offered by this technique to map the repartition of several ink ingredients in paper fibers.

## Chapter IV

# The distribution of ink components in paper fibers

### IV.1 Introduction

The degradation of paper by iron gall inks is not only governed by the chemical reactions inducing osidic bond cleavage of cellulose chain, but also by the penetration of the ink (and iron) within the paper sheet. This last aspect is in the scope of this chapter.

Paper fibers are initially highly permeable to water. The paper making process includes sizing, an operation that corresponds to the impregnation of paper with an adhesive (size), such as gelatin, which makes it less permeable to water and thus suitable for writing (see part I.1.5). Consequently, the size is a key parameter in the ability of iron gall ink to migrate (or not) in the paper during the writing. Moreover the size interacts chemically with the ink: it has been shown that the paper of original manuscripts is often more permeable to water on the verso of the ink line than on blank areas, attesting that the size is altered by iron gall inks [49].

As it was illustrated in part I.1.4, water transport in paper results from different processes which include not only pores and capillaries within the sheet but also migration, absorption and diffusion within the paper fibers [207] (which diameters ranges from 5  $\mu\text{m}$  to 20  $\mu\text{m}$ ). This is why it is important not only to study the distribution of size and ink at the micro scale (to study penetration in the paper sheet), but also at the nano scale (to study penetration in fibers).

Regarding the ink distribution into paper at the macro scale, several studies looked into the penetration depth of modern inks with several techniques, such as optical microscopy using algorithms to analyze color distribution on paper cross-sections [208, 209], confocal laser scanning microscopy [210], scanning electron microscopy (SEM) [211], X-ray microtomography and laser ablation [212]. Regarding more particularly iron gall inks, particule-induced X-ray emission (PIXE) has been used to investigate the penetration of metallic ink components (Fe, Zn, Cu) into unsized paper section through measurements of concentrations profiles with a spatial resolution of 1.5  $\mu\text{m} \times 1.5 \mu\text{m}$  [213]. This resolution is clearly insufficient to map elemental distribution in a fiber of 10  $\mu\text{m}$  diameter.

X-ray absorption near edge structure (XANES) spectroscopy at iron K-edge has been largely used at a micro/macroscale on iron gall inks to quantify the respective amounts of iron II and iron III, which is of a keen interest for understanding the behaviour of iron in both historical inks [214, 215, 216, 217] and model inks [216, 111]. Rouchon et al. [111] have

studied both the evolution versus ageing of iron valence and cellulose depolymerisation on model samples. Although XANES spectroscopy gives information on the elemental speciation at specific location in the sample, no information on the spatial distribution is obtained.

Scanning transmission X-ray microscopy (STXM), which reaches a resolution of 30 nm, offers promising perspectives because it combines elemental mapping and XANES measurements at a nanoscale. Previous measurements have been done with STXM to study the ink penetration at the scale of a paper fiber using mapping and XANES spectroscopy at Fe L- and C K- edges [155]. These preliminary tests highlighted migrations of Fe(II) and precipitation of Fe(III) gallates in the inner part of unsized fibers and clearly established the feasibility of the STXM technique to map the speciation of C and Fe on cross-sections of a single fiber.

Before the 19<sup>th</sup> century, paper was mainly sized with gelatin (see chapter I). As ink penetration within paper sheets and paper fibers strongly depends on the size, it is also important to measure the distribution of gelatin within the paper. Moreover, gelatin is currently used in paper conservation workshops for re-sizing purpose (on fragile papers or on papers that have undergone a washing treatment). In northern European countries, it is largely used for local mending of manuscripts and it is often put forward that an application of gelatin can delay iron gall ink corrosion [219].

Several studies have attempted to investigate the gelatin distribution at the macro scale. For instance, Hummert, Henniges, and Potthast [220] have used fluorescence microscopy to map it inside paper after labelling with a fluorescent marker. This study showed that the distribution depends on the application mode (spray or immersion) and on the paper used (rag or whatman). In another study, infrared spectroscopy, which is undeniably one of the most used characterization technique in chemistry, has been applied on cross-section of a resin embedded paper sheet to study gelatin distribution [218] (FIG.IV.1). The picture of a sample impregnated with gelatin at 3 % is shown on FIG. IV.1A with infrared maps at three different wavelengths ( $1060\text{ cm}^{-1}$ ,  $1660\text{ cm}^{-1}$  and  $1715\text{ cm}^{-1}$ ) that are specific of cellulose, gelatin and resin respectively (FIG. IV.1B). The absorbance profile at  $1660\text{ cm}^{-1}$  points out that gelatin is more concentrated at the surface

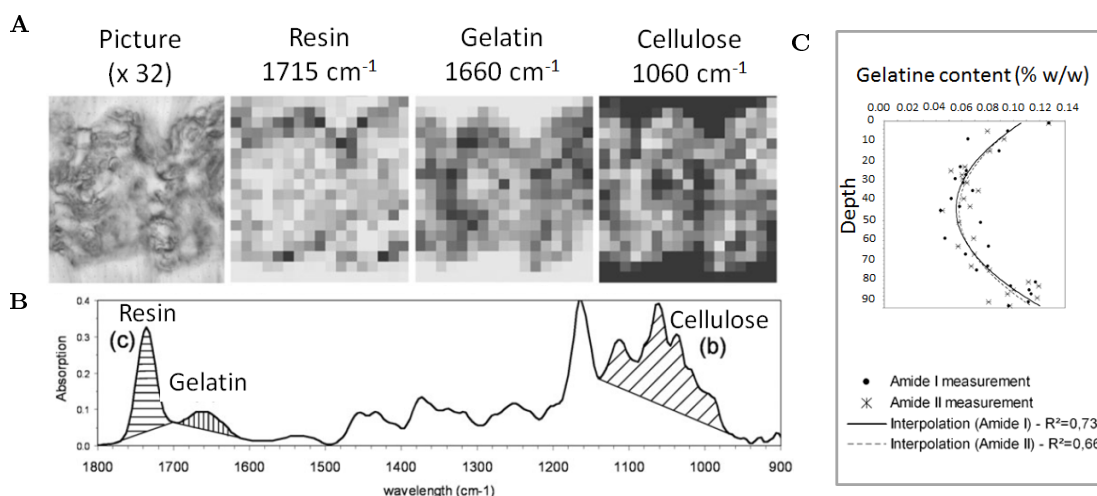


FIG. IV.1 – Picture and infrared microscopy maps of the cross-section of a paper impregnated with gelatin and embedded in a resin: (A) Infrared mapping of resin, gelatin and cellulose (one pixel= $10\text{ }\mu\text{m}\times 10\text{ }\mu\text{m}$ , dark regions correspond to high absorption); (B) Characteristic infrared spectrum; (C) gelatine concentration profile [218].

of the paper than in the inner part (FIG. IV.1C). However with an imaging technique like infrared microscopy, resolution is limited to 5  $\mu\text{m}$  to 10  $\mu\text{m}$  which is not precise enough for mapping an individual fiber. This limitation is clearly seen on FIG. IV.1, where pixels are too large to distinguish paper fibers. Nowadays higher spatial resolutions (of the order of 20 nm) can be reached with the innovative technique of atomic force microscopy (AFM)-infrared (IR) that couples AFM and IR spectroscopy.

All these considerations led us to consider both AFM coupled with IR spectroscopy (AFM-IR) and synchrotron-based STXM spectroscopy for investigating ink and gelatin distributions at a nano-scale within a paper fiber. Thus, these two techniques were applied in this chapter to study the physical and chemical interactions between gelatin, iron gall inks and cellulose in paper fiber cross-sections. The aim was: 1) to better understand the way ink components distribute themselves inside a fiber; 2) to assess the impact of gelatin size on their penetration; 3) to investigate the impact of a gelatin application on inked areas during conservation treatments.

This chapter will present successively: 1) the choice of the samples and their preparation involving two cutting techniques: ultramicrotomy and focussed ion beam (FIB); 2) the AFM-IR and STXM principles; 3) the analysis of the reference samples and the methodological development for the whole sample batch analysis; 4) the results regarding gelatin and ink penetration at a nano-scale.

## IV.2 Material

### IV.2.1 Preparation of fiber samples

Different types of fibers samples were prepared by successive impregnations with gelatin and/or a combination of ink main ingredients (gallic acid and/or iron(II) sulfate), according to procedures detailed below. The selection of fiber type, gelatin and ink will be presented, along with the preliminary tests carried out to determine impregnation durations.

A paper pulp made from linen rag by the Moulin du Verger Papermill (Fig. IV.2) according to a traditional process similar to those used in the 18<sup>th</sup> century, has been chosen as model. A paper was made with this pulp and is hereafter referred to as *Verger*. It contains no additive (no sizing agent, no fillers, no optical brightener). Single fibers were extracted from the *Verger* paper with tweezers under a binocular magnifier by moisturing the paper with distilled water. They were let to dry for one hour on a glass slide before



FIG. IV.2 – *Moulin du Verger Papermill* [221].

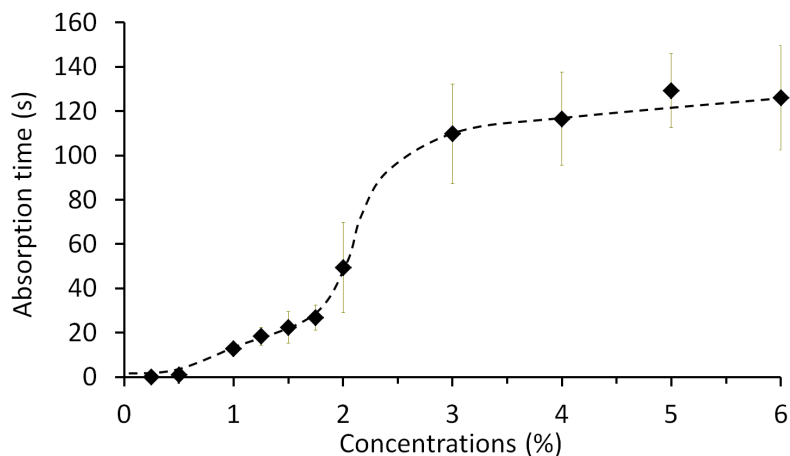


FIG. IV.3 – Water adsorption properties of Whatman paper sized with gelatin solution of different concentrations. The absorption time corresponds to the time necessary for a  $0.1 \mu\text{L}$  drop of water to be absorbed by the paper [49].

being impregnated with gelatin and/or different ink ingredients.

Different types of gelatin exist depending on their origin (fish or cattle). They have different sizing properties. In this study, a gelatin of photographic grade with good sizing properties was chosen: GELITA®. This is a type B gelatin with a gel strength of 269 g Bloom produced by Kind and Knox (batch number: 073603, date: 19.04.2011) from alkali treated cattle bones. This gelatin is often used for conservation purposes and will be hereafter referred to as *gel*.

Gelatin impregnation was performed in a way similar to the one used in a previous study [218]: the fibers were impregnated for 1 min in a gelatin aqueous solution, which was stirred and heated to  $50 \text{ }^\circ\text{C}$  in a water bath to keep it in an homogenous liquid state. Gelatin was used at two different concentrations: 1.5 % and 4 %, weight for weight. The choice of these two concentrations is motivated by two aspects:

i) these concentrations are among the range 1 % to 5 % commonly used by conservators for resizing or lining; ii) these two concentrations have a different impact on the paper size. It was indeed observed that gelatin prepared at 1.5 % has poor sizing properties on Whatman papers. Indeed, as illustrated on FIG. IV.3, the time of water absorption by the paper is very short, meaning that it remains water permeable and is unsuitable for writing. Conversely, when 4 % *gel* solution is used, the Whatman paper becomes much less permeable, being then suitable for writing. These two different behaviours may not only be related to the amount of gelatin deposited in the paper, but also to the distribution of gelatin in the fibers. Indeed, a 1.5 % *gel* solution is significantly more fluid than a 4 % *gel* solution. Gelatin might then penetrate more deeply in the inner part a fiber and account for a higher affinity of paper surface toward water.

Fe<sup>2+</sup>-, Ac- and Ink-model solutions were prepared as presented in part II.2.1 at a concentration of  $40 \text{ g} \cdot \text{L}^{-1}$  for iron(II) sulfate, heptahydrate and  $9 \text{ g} \cdot \text{L}^{-1}$  for gallic acid. The ink, hereafter referred to as *ink<sub>R</sub>*, was prepared three days before use. Details on the sample preparation and on samples names are summed up in TAB.IV.1. In the sample name, the order  $a + b$  indicates that solution  $a$  was applied before solution  $b$ . On sample *ink<sub>R</sub> + gel*, for which the ink impregnation was done prior gelatin deposition, gelatin was sprayed directly on the inked fibers in an attempt to avoid the dissolution of the ink components. Ink impregnation was additionally tested after gelatin impregnation. Therefore,

	Name	Impregnation solutions			Powder	
		Gelatin	Ink			Gum Arabic (40 g · L <sup>-1</sup> )
		Concentration (w:w)	Age	Fe <sup>2+</sup> 40 g · L <sup>-1</sup> , Ac 9 g · L <sup>-1</sup>		
Samples	gel <sub>1.5</sub> fiber	1.5 %				
	gel <sub>4</sub> fiber	4 %				
	ink <sub>R</sub> fiber		3 d	✓		
	gel <sub>4</sub> +ink <sub>R</sub> fiber	4 %	3 d	✓		
	ink <sub>R</sub> +gel <sub>4</sub> fiber*	4 %	3 d	✓		
	79/7 fiber	unkn.				
Model compounds	raw fiber					
	<i>Avicel</i>				Avicel PH-101 powder	
	Fe <sub>2</sub> _ref				Fe <sup>II</sup> Cl <sub>2</sub> powder	
	Fe <sub>3</sub> _ref				Fe <sup>III</sup> Cl <sub>3</sub> powder	
	Ac_ref				Gallic acid powder	
	IGI_ppt_ref				precipitate from ink centrifugation	
	Gel_ref	4 %				
	ink <sub>O</sub> +gum drop		4 yr	✓	✓	

\* Gelatin was sprayed above the sample.

TAB. IV.1 – Description of fibers samples and model compounds. Except powders, all samples are cut in thin cross-sections.

the time that is appropriate for inking the fibers without removing gelatin had to be estimated. This was done on a macro scale with *Verger* paper sheets impregnated with 4 % *gel*. Papers were let to dry for one day before immersion in water for different durations ranging from 15 s to 60 s, and then let to dry another day. Afterwards the size quality was evaluated by measuring the time necessary for the penetration of 0.1 μL drop of water into the paper. It was visually assessed according to a protocol previously described [49]. Similar penetration times were measured for all samples (FIG. IV.4) meaning that the water immersion step had, at a macro scale, no substantial impact on the paper size. This suggests that phenomena only concern a minor proportion of gelatin and that fibers can be inked by immersion after gelatin impregnation without substantial removal of gelatin. Moreover it was difficult to obtain colored fibers after only one bath into ink solution (probably because of low precipitate concentration), hence it was decided to duplicate immersions of 15 s into the ink, letting dry the fiber in the meantime.

In addition, a paper dating from the 14<sup>th</sup> century was chosen to probe the penetration of gelatin and this for two reasons: i) this paper, referred to as *79/7*, still contains a significant amount of size, as attested by conventional attenuated total reflectance (ATR)-Fourier transform (FT)IR analysis [222]; ii) the fibers that composed this paper are rather large (cross-section of approximately 27 μm), strong and easy to handle, which is expected to facilitate the realization of cross-sections.

## IV.2.2 Preparation of model compounds for STXM

Several model compounds were chosen as references for XANES analyses:

- iron(II) chloride and iron(III) chloride spectra given by J. Wang (CLS) were used

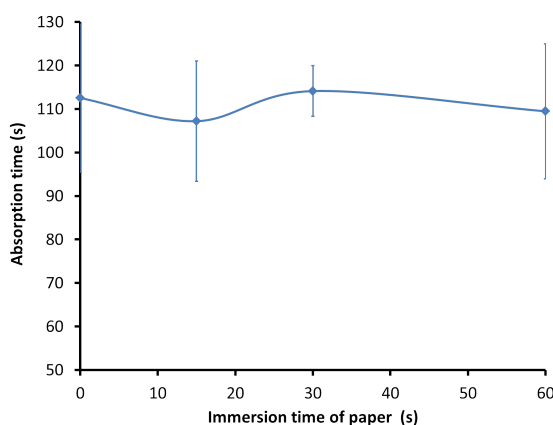


FIG. IV.4 – Evaluation of water absorption time of Brejoux papers impregnated with 4 % gelatin K and washed different duration in a water bath.

for the determination of the iron valence (Fe L-edge), because the iron sulphates compounds initially considered revealed themselves inappropriate due to the oxidation they had undergone;

- the C K-edge signature of cellulose was measured on two model compounds: firstly on a FIB foil extracted from a raw fiber (TAB. IV.1) and secondly on  $\alpha$  crystalline cellulose (Avicel PH-101, hereafter referred to as *Avicel*). This latter was put in suspension in ethanol and a drop was deposited on a transmission electron microscopy (TEM) copper grid with carbon mesh;
- the gelatin C K-edge signature was obtained on a FIB foil which presented excess of gelatin that was not in contact with the fiber (gel\_ref);
- gallic acid model compound (Ac\_ref) was obtained by the deposition of a saturated ethanolic gallic acid solution on a TEM grid with carbon mesh.
- iron gall ink precipitate hereafter referred to as IGI\_ppt\_ref) was also prepared in addition to gallic acid because this latter is probably chemically transformed during precipitation with iron and it appeared necessary to identify the C K-edge signature specific of the precipitate. IGI\_ppt\_ref was obtained by centrifugation of a solution containing iron(II) sulfate, heptahydrate and gallic acid with a molar ratio of 1:1. It was finely ground, put in suspension in ethanol and then deposited on a TEM grid with carbon mesh;
- finally, in order to check the stability of iron under the beam, it was necessary to find a model compound that is rich in iron(III) (the main impact of the beam is reduction) and also contains a high proportion of organic matter such as polysaccharides. A complete ink, prepared with gallic acid, iron(II) sulfate and gum Arabic, was found appropriate. Before being dried, the ink was naturally aged for one year, which has allowed oxidation of iron(II) to iron(III) and formation of the iron gall ink precipitate. A FIB foil (hereafter referred to as Ink<sub>O+</sub> gum drop, see TAB. IV.1) was drilled in a drop of this ink that was deposited on a silicium wafer. It shows a uniform distribution of iron(III) in a matrix of gum that is a co-polymer of several sugars such as arabinose, glucose and rhamnose.

### IV.2.3 Ultra-thin cross-sections preparation

AFM-IR analysis can ideally be performed on samples that are 100 nm to 400 nm thick, while STXM requires maximum 100 nm thick cross-sections. To prepare such thin cross-section, ultramicrotomy was first considered since it is easily accessible and not expensive. It has been used on resin embedded samples to prepare cross-section of paper sheets [218] and of single fibers [223]. However, the polymeric resins induced undesired signatures that compromise infrared spectroscopy [218] and STXM measurements [223], especially when carbon-containing species are considered. This is why thin cross-sections obtained without embedding into a resin were desired in our study.

Obtention of fiber cross-sections without resin inclusion was attempted by Jérémy Henin with LEICA EM UC6 ultramicrotome at IPANEMA laboratory (European research platform on ancient materials), Saclay (FIG. IV.5), with the following protocol. First the fiber is placed between two small plastic pieces that are glued on one edge to stick to each other (FIG. IV.6A). The whole sample (plastic sandwich and fiber) is then mounted in a flat jaw. Then a razor blade (LEICA 818 high profile microtome blade) is used to cut the sample extremity into a pyramidal shape, in order to minimize the amount of plastic to cut (FIG. IV.6B). The pyramidal sample is then fixed to the mobile arm and cut with a diamond dry-ultracryomicrotomy knife (FIG. IV.6C). After cutting, the cross-sections are laying on the diamond knife. They are then transfered from the knife to the ZnSe support needed for the AFM-IR measurements with an eyelash (FIG. IV.6D). This methodology appeared both laborious and time consuming. It was indeed difficult to separate the fiber cross-sections from the plastic remains and to transfer them from the knife to the ZnSe support without damaging the cross-sections. Yet, despite these difficulties, some samples from 200 nm to 400 nm could be prepared for AFM-IR analysis.

FIB was considered as an alternative to obtain cross-sections without mechanical damage, although it is much more expensive. Its feasibility for preparing 100 nm thick fiber cross-sections has been already demonstrated [155], and thus, without embedding the sample into a resin. Foils were prepared by David Troadec at IEMN (Institut d'Electronique, de Microelectronique et de Nanotechnologies, Lille) with a FEI STRATA DB 235 (FIG. IV.7). For this milling, fibers are deposited on Si wafers and remain attached with electrostatic forces (FIG. IV.8A). Before extracting a foil, a metal (Pt) is deposited by Ion Beam Induced deposition on the sample to protect it during milling (FIG. IV.8B ). Then, the gallium ions beam used for cutting is focussed next to the platine deposit to remove the matter from both part of the foil. The cross-section is thinned down to 100 nm and the sample is then tilted, allowing final cutting of the foil and removal of the sample (FIG. IV.8D ). The foil is then fixed on a post of a FIB lift-out grid having two wide posts



FIG. IV.5 – Ultramicrotome LEICA EM UC6 of IPANEMA, Saclay.

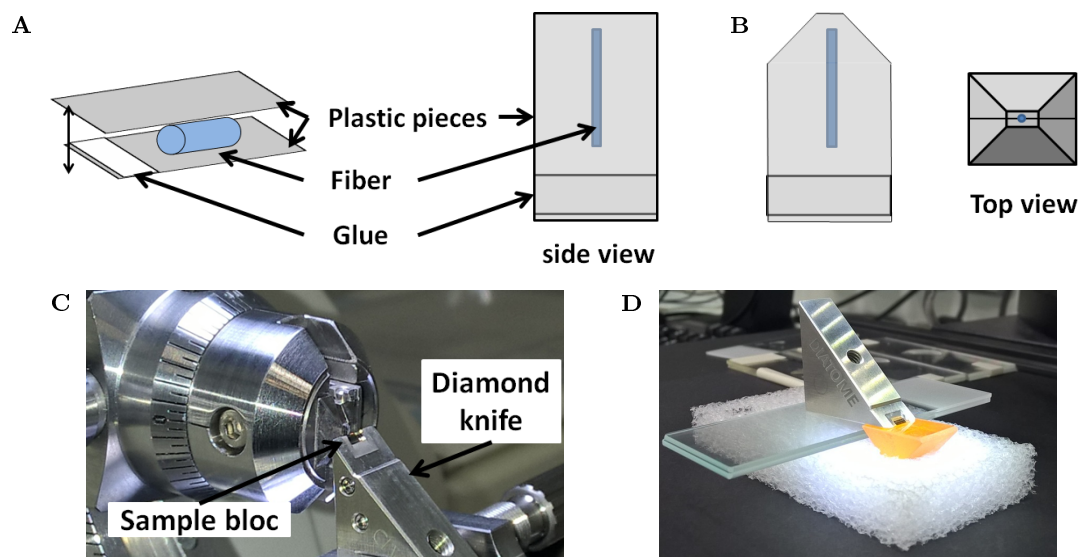


FIG. IV.6 – Protocol of fiber preparation for ultramicrotomy cross-section process: (A) preparation of the sample bloc; (B) cutting of the sample bloc; (C) thin cross-sections cutting with a diamond knife; (D) Cross-section deposit onto an ZnSe prism.

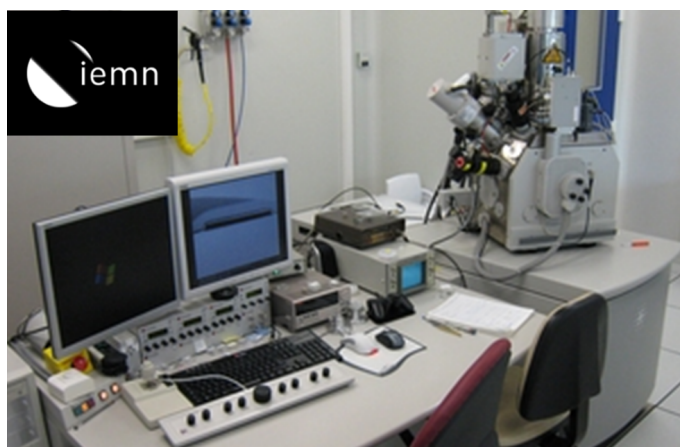


FIG. IV.7 – FIB of the Institut d'Electronique, de Microelectronique et de Nanotechnologies, Lille.

in V-shaped (FIG. IV.8E). These grids were used for STXM experiments during which correct positioning of the sample in the X-ray beam was done with the help of the A to C marks on the copper lift-out grid.

#### IV.2.4 Diversity and quality of cross-sections.

From a general point of view, paper fiber cross-sections show some similarities with cross-sections of a plant fibers. These latter are composed of several walls and a central lumen, a tubular structure conveying sap when the plant is alive (FIG. IV.9). When the plant is dead and dry, the lumen is replaced by a void. On rag paper fibers, the external walls are often partly removed or damaged, because i) rags used for paper making are often worn out and ii) the paper making process provokes fibrillation.

The fibers extracted from the *Verger* paper show a great variety of aspects, not only dealing with their size (diameters in the range from 15  $\mu\text{m}$  to 35  $\mu\text{m}$ ), but also with their condition. This is clearly illustrated on FIG. IV.10, that shows fibres in a rather good condition (green arrows) and others that are defibrillated and flattened (red arrows). This is not surprising since this paper was made from linen rag which implies aged fibers

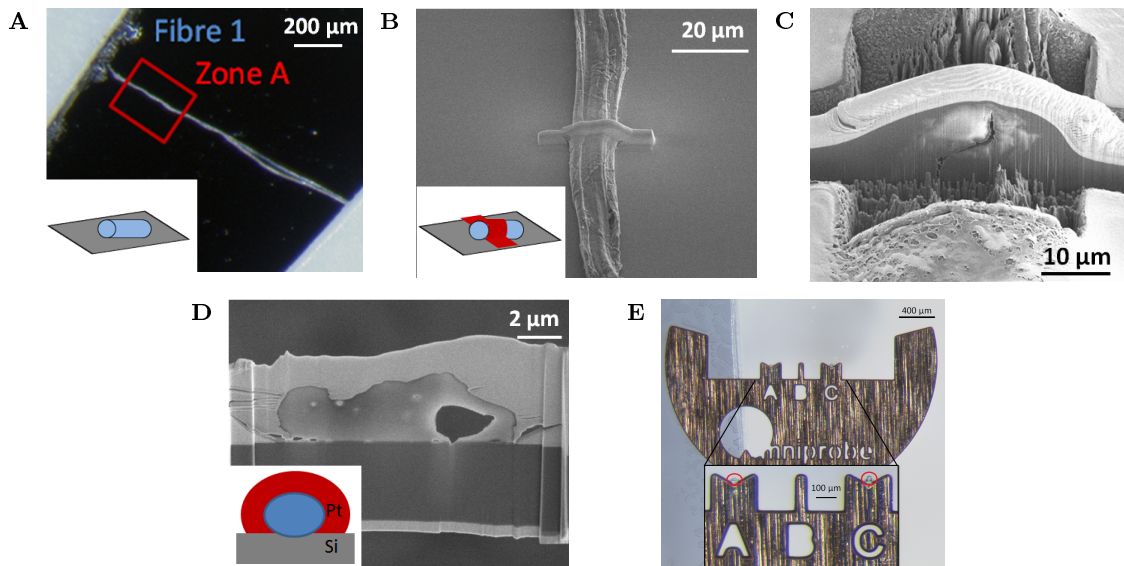


FIG. IV.8 – Protocol of fiber preparation and FIB cross-section process: (A) deposit of the fiber on a silicium wafer; (B) platinum deposit on the fiber; (C) FIB cutting of the cross-section with trenches on each side of the foil; (D) Raw fiber cross-section obtained by FIB. (E) FIB foils on the two wide posts in V-shaped of the lift-out grid, on which letters A to C serve as marks to locate the sample. Red circles highlight two FIB foils.

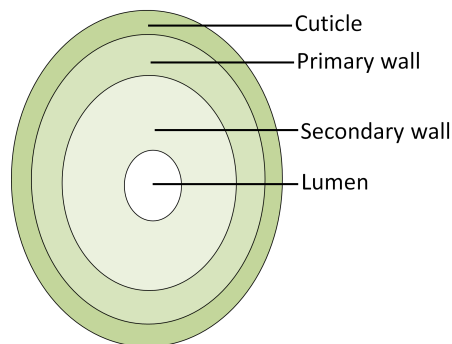


FIG. IV.9 – Structure of a fiber cross-section.

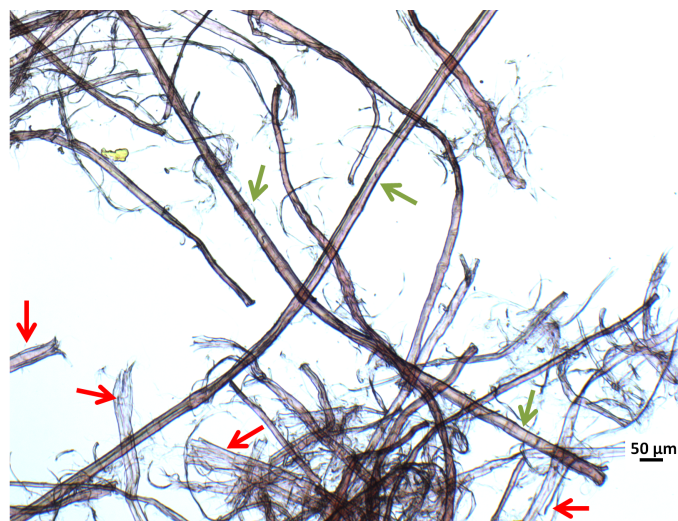


FIG. IV.10 – Observation of Verger paper fibers with an optical microscope, showing fibers in good condition (green arrows) and defibrilated fibers (red arrows).

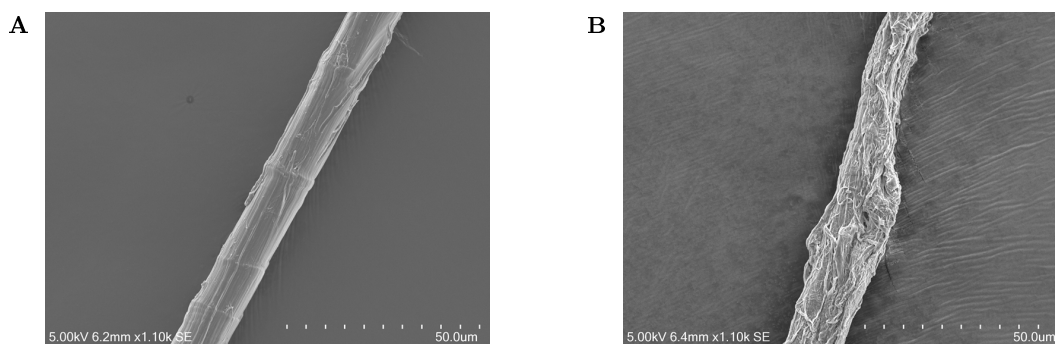


FIG. IV.11 – SEM image of a well preserved fiber (A) and of a defibrillated fiber (B) extracted from Verger paper.

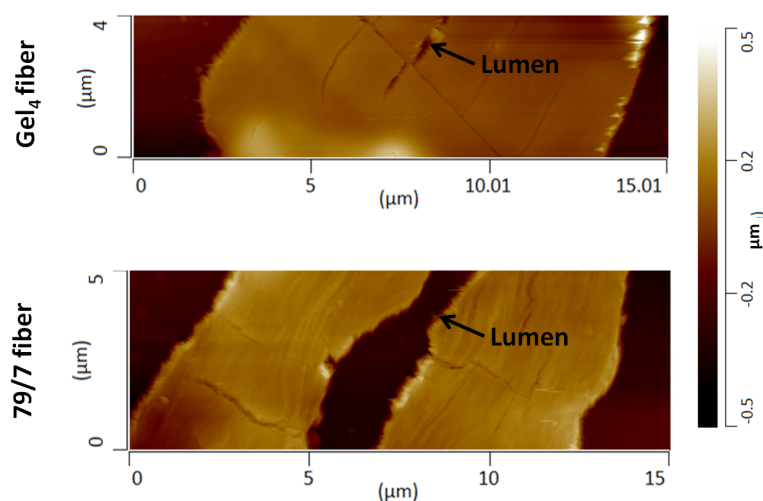


FIG. IV.12 – AFM topography images of the cross-sections of a  $gel_4$  fiber and of a 79/9 fiber obtained by ultramicrotomy.

that were milled again during paper making. However, a lumen is seen with optical microscopy on most fibers, and other features typical of linen fibers, such as transversal walls, are observed on certain fibers. The difference between damaged fibers (defibrillated fibers) and well preserved ones (with parallel strands and transversal walls) is also clearly revealed by SEM images (FIG. IV.11A and IV.11B).

This heterogeneity between fibers led to an heterogeneity of cross-sections. FIG. IV.12 illustrates cross-sections obtained for the  $gel_4$  fiber and 79/9 fiber. These two fibers show a central crack corresponding to the lumen but also other cracks which are often circular, suggesting some alteration of cellular walls. This is probably due to the cutting which applies a mechanical stress on the fiber. Besides, the edges of the fibers are difficult to image.

Regarding FIB foils (FIG. IV.13), the protective layer of the metal (Pt) is clearly visible around the fibers and the darker layer at the bottom of the images corresponds to the silicium wafer on which fibers were deposited. On some fibers (FIG. IV.13, fibers 1, 3, 4 and 6), the cutting provoked lace-like structures, leading to holes and cracks. The FIG. IV.13 also shows the variety of cross-sections shapes: rounds, ovoid or very flat. Some of them (FIG. IV.13, fibers 4 and 6) show a central crack, attributed to the lumen. Yet this latter is not visible on all cross-sections.

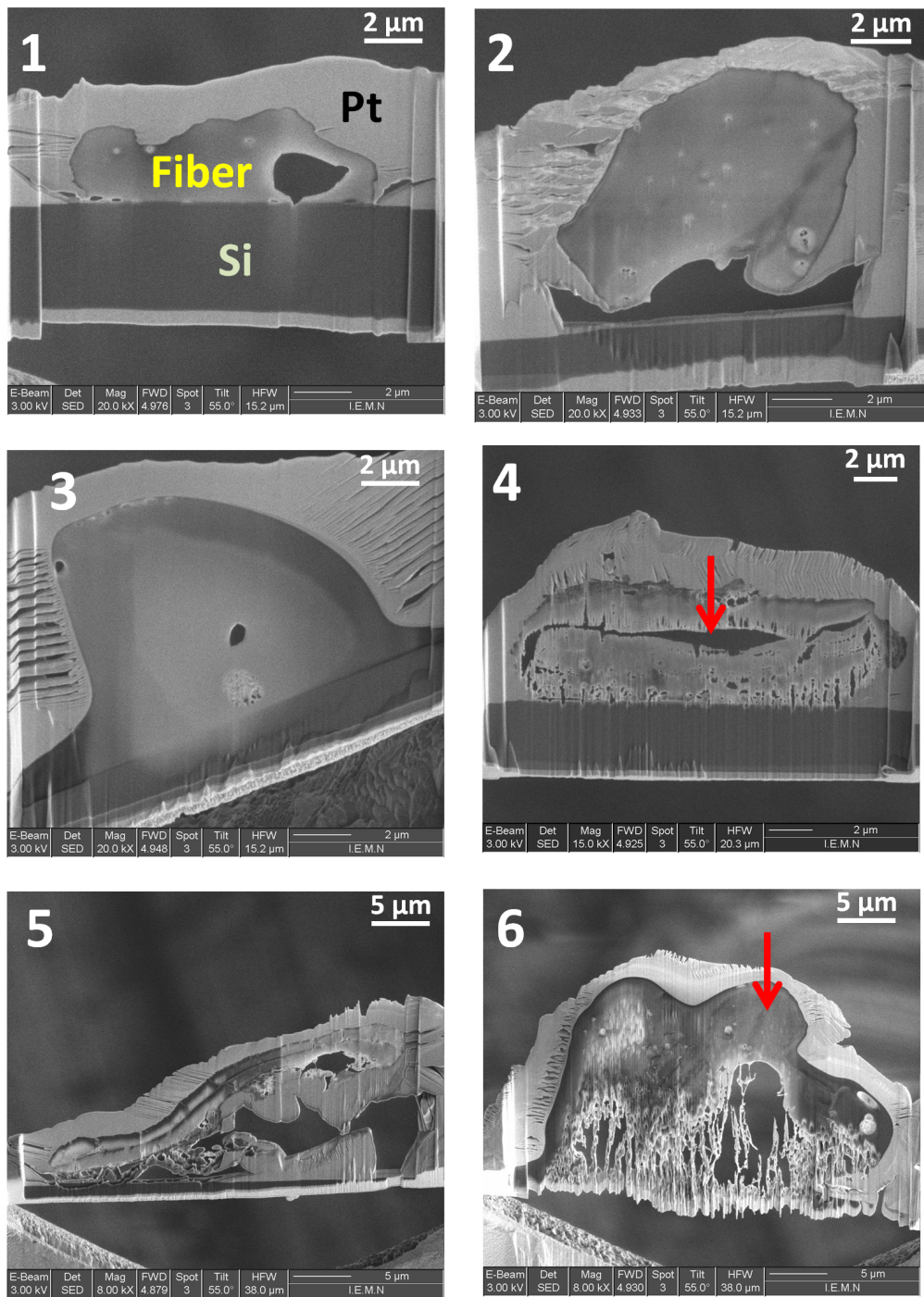


FIG. IV.13 – FIB foils of fiber cross-sections.

1) raw fiber; 2)  $gel_4$  fiber; 3)  $gel_{1.5}$  fiber; 4)  $gel_4 + ink_R$  fiber; 5)  $ink_R$  fiber; 6)  $ink_R + gel_4$  fiber. Nomenclature and concentrations are the same of the ones described in TAB. IV.2.2. Red arrows show lumen.

## IV.3 Analytical techniques

### IV.3.1 Atomic force microscopy coupled with infrared spectroscopy

The nano-infrared spectroscopy (AFM-IR) is based on the coupling of atomic force microscopy and of infrared spectroscopy. The laboratoire de Chimie-Physique de Paris-sud in which the measurements were done is a pioneer of this technique which principle relies on photo-thermal induced resonance [224]. In this technique, a sharp AFM probe, also called ‘tip’ (located at the end of the cantilever (FIG. IV.14)), is brought into contact with the sample which is mounted on a ZnSe prism (FIG. IV.14). The tip movement is controlled by a piezo stage allowing scanning of the sample in a raster pattern, and a quantity (for exemple sample height) is measured during this movement at discrete locations (pixels). The cantilever position and oscillation signal is recorded by reflecting a visible laser on the top surface of the cantilever and measuring its position with the four-quadrant detector of the AFM. The cantilever is part of a closed-loop feedback system. In this contact mode, the force on the tip is repulsive. By maintaining a constant cantilever deflection (using the feedback loops) the force between the probe and the sample remains constant and an image of the surface is obtained.

Regarding the coupling with infrared spectroscopy, this is done in a bottom-up configuration, in which a pulsed tunable laser is used to excite the sample from below (total internal reflection) (FIG. IV.14). When the sample absorbs radiation, a localized heating is produced, leading to rapid thermal expansion of the sample. Since the AFM tip is in contact with the sample, this expansion is transmitted to the AFM cantilever that oscillates. A characteristic ringdown is produced during the decay of the induced oscillations, as shown in FIG. IV.14. Extraction of the amplitudes and frequencies of these oscillations can be done by Fourier transform. Local absorption spectra are obtained by plotting the amplitudes of the cantilever oscillation as a function of the source wavelength. It is worth to note that the oscillation frequencies of the ringdown are related to the mechanical stiffness of the sample.

On a practical point of view, since AFM is used, huge height differences should be avoided because they could damage the tip and thus compromise image recording. The samples should also be in good contact with the prism, thin (100 nm to 400 nm) and flat.

With this technique, chemical mappings and spectra are obtained from two different measurements. Chemical maps are recorded at one wavelength, with a simultaneous to-

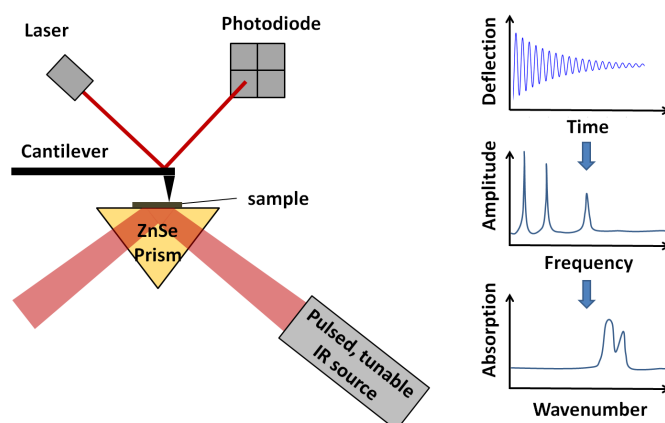


FIG. IV.14 – Description of the AFM-IR technique.

pography measurement by the AFM tip. Mapping at several wavelengths can be achieved by repeating the scan at each wavelength on the same sample region. However, no mapping is done within the whole wavelengths range of a spectrum to avoid excessive measurement duration. Hence, recording an infrared spectrum in the whole wavelength range is only possible at a specific location (point) selected on the AFM topography image.

### IV.3.2 Scanning transmission X-ray microscopy (STXM)

STXM is a synchrotron based microscopy technique, which allows imaging the X-ray absorption of the sample. The measurements presented in this thesis were done at the Canadian Light Source facility (CLS, Saskatoon, Canada) (FIG.IV.15A) on SM 10ID-1 Beamline (FIG.IV.15B).

#### a Synchrotron light and STXM

A synchrotron is a cyclic electron accelerator. Synchrotron light starts by electrons production with an electron gun. After that, electrons are accelerated in a linear accelerator (LINAC) to reach a speed close to light speed. Then, they go through a booster (acceleration ring) which increases their energy from 1.5 GeV to 2.9 GeV (enough to produce synchrotron light from infrared to hard X-ray) before being injected in a storage ring. The storage ring diameter is of several meters wide. Synchrotron light (photons) is produced when the electron stream is bend by magnets in the storage ring. This light is emitted tangentially to the storage ring and goes through different machines (in particular, a monochromator) to the beamline end, where the experimental station is located. This monochromator allows filtration of the energy of the light between 200 eV to 2000 eV (soft X-rays) in our case. It thus allows high spectral resolution (0.1 eV for STXM).

In the conditions of our experiments, the beam is focused on the sample with a Fresnel zone plate (FIG. IV.16A and B). Only the first order of the diffracted beam is selected with an order sorting aperture (OSA). The sample is scanned in x and y directions and the transmitted intensity is detected on an X-rays sensitive detector. The microscope chamber is evacuated to 100 mtorr after sample insertion and back-filled with He to avoid heating. A width of approximately 100 nm should not be exceeded for the sample to be transparent to X-rays at the C-K edge energy. This requires a particular preparation based on FIB milling, as described in section IV.2.1.

#### b X-ray absorption

When X-rays go through the sample, one part of them is absorbed by the matter. During energy scanning, an increase in the absorption of the sample (edge) is observed when the incident beam energy matches the transition energy of an atom inner shell electron to the

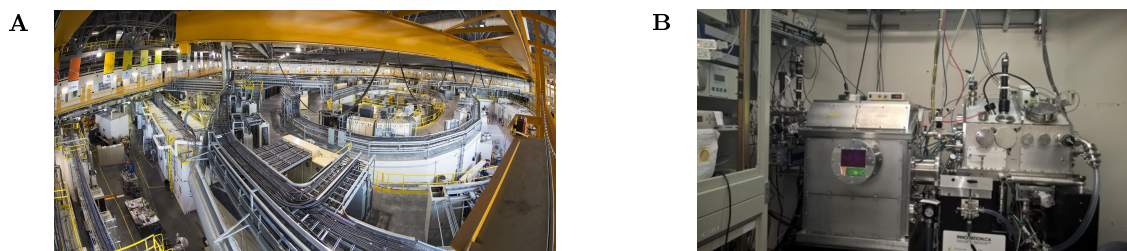


FIG. IV.15 – Pictures of (A) the CLS experimental floor [225] and of (B) the SM beamline.

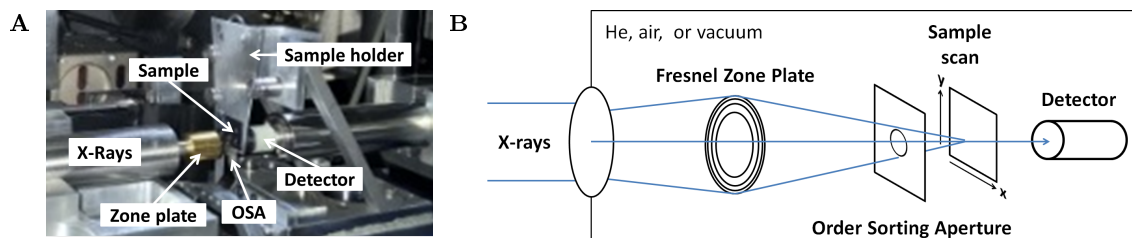


FIG. IV.16 – (A) Picture and (B) scheme of the STXM experimental setup showing the position of the sample and of the focusing and detecting tools in the SM end station.

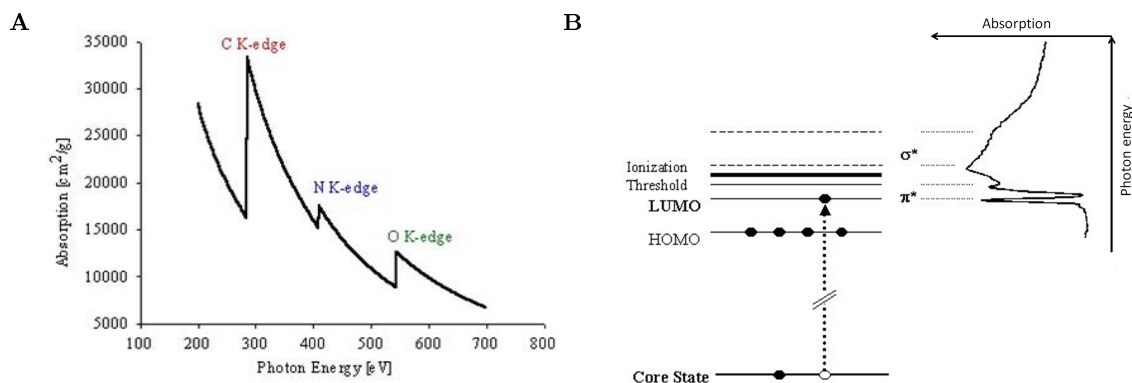


FIG. IV.17 – (A) XANES absorption edges of typical organic compounds and (B) electronic transitions at the origin of the spectrum.

continuum. These transitions are specific of the element: C K-edge ( $\sim 300$  eV), N K-edge ( $\sim 400$  eV), O K-edge ( $\sim 520$  eV), Fe L-edge ( $\sim 700$  eV)... (FIG. IV.17A). The absorbance  $A$  (also named  $O.D.$ ) is linked to the incident ( $I_0$ ) and transmitted ( $I_t$ ) intensities. It is additionally expressed as a function of  $\mu$ , the linear absorption coefficient and  $x$ , the thickness of the sample (equation (IV.1)).

$$O.D. = A(E) = -\ln\left(\frac{I_t}{I_0}\right) = \mu(E) \times x \quad (\text{IV.1})$$

Near the edge, the absorption profile  $A(E)$  is dependant on the elemental speciation and gives information on the chemical groups in which the element is involved. The absorption fine structure is measured, taking advantage of the high spectral resolution (0.1 eV) of the synchrotron light. It corresponds to electron transitions from intern orbitals to vacant orbitals of higher energy (FIG. IV.17B). TAB. IV.2 gives an overview of the main electronic transitions and corresponding energies, as well as the chemical groups accounted for the transitions. For iron,  $L_{2,3}$  edges correspond to transitions  $2p^6 3d^n \rightarrow 2p^5 3d^{n+1}$  and also give information about the redox state of the element.

### c Chemical mapping and XANES spectrum extraction from STXM data stacks

STXM is a microscope: it allows mapping of a sample at a given X-ray energy on a nano scale (spatial resolution around 30 nm) in a short time. Images are first converted to optical density (absorbance) using equation (IV.1). Comparison of images recorded at different energies drives information on the distribution of the elements and on their speciation. In the example shown FIG. IV.18, two energies have been chosen, 286.7 eV and

Edge	Energy (eV)	Electronic transition	Chemical groups	References
<b>C (K)</b>	284.3 - 284.8	$1s \rightarrow \pi^*$	quinones-benzoquinones	[226, 227, 228, 229]
	284.9 - 285.5	$1s \rightarrow \pi^*$	aromatics/ olefines(C=C)	[226, 227, 228, 229, 230, 231, 232, 233, 234]
	286.1 - 286.7	$1s \rightarrow \pi^*$	ketones-pyridines-phenols	[227, 228, 229]
	287 - 287.3	$1s \rightarrow \pi^*$	ketones-phenols	[227, 228, 229, 230, 232, 233, 234]
	287.7-288	$1s \rightarrow 3p/\sigma^*$	aliphatics-CH <sub>3</sub> ,CH <sub>2</sub> ,CH	[231, 228, 229, 232]
	288.2	$1s \rightarrow \pi^*$	Amides-Peptides $NH_2 - C = O$	[231, 229, 234, 235, 236]
	288.3 - 288.7	$1s \rightarrow \pi^*$	Carboxylique	[231, 229, 227, 232, 236]
	289	$1s \rightarrow \pi^*$	aldehydes	[230]
	289.3 - 289.5	$1s \rightarrow 3p/\sigma^*$	Alcohols-ether	[226, 231, 227, 232, 228]
	290	$1s \rightarrow 4p$	Aliphatic-CH <sub>3</sub> ,CH <sub>2</sub>	[230]
	290.6	$1s \rightarrow 4p/\sigma^*$	Aliphatic	[231]
	291.5	$1s \rightarrow 4p$	graphite exciton	[237]
	292.5 - 292.8	$1s \rightarrow 4p$	aromatics C-C	[237, 231, 229]
296.5	$1s \rightarrow 4p$	aliphatics C-C	[231, 229]	
<b>N (K)</b>	401.3 - 402.7	$1s \rightarrow 3p/p^*$	amide	[236]
<b>Fe (L)</b>	707.8 - 708.0	$2p^6 3d^n \rightarrow 2p^5 3d^{n+1}$	major pic in Fe(II)-compounds	[238, 239, 240]
	709.8 - 710	$2p^6 3d^n \rightarrow 2p^5 3d^{n+1}$	major pic in Fe(III)-compounds	[238, 239, 240]

TAB. IV.2 – Main energy values at C (K), N (K) and Fe (L) edges.

288.3 eV which are specific of cellulose and gelatin respectively. Brighter areas represent regions of high absorption and darker areas regions with low absorption. On these two images, we can observe a clear difference of absorption between upper and lower parts. Assuming an homogeneous thickness within the analysed region of the sample, gelatin concentration is higher than cellulose in the upper part, and conversely.

In order to differentiate more precisely the speciations of C, N, and Fe, it is necessary to collect a stack. From a practical point of view, a stack corresponds to the record of a serie of maps scanning the energy with small steps (Fig. IV.18). The stack is then a 3D data recording of the absorption (x: x scanning direction, y: y scanning direction, z: energy). In this thesis, stacks were recorded from 700 eV to 720 eV for the Fe L-edge, 395 eV to 435 eV for the N K-edge and 270 eV to 325 eV for the C K-edge. The detail of the stacks parameters are presented in appendix K. Once stack recording is completed, XANES spectra with good resolution can be obtained by choosing a region of interest in the image and reconstructing the spectrum along all studied energies, using a dedicated software (see below). This allows a more precise interpretation of the elemental speciation. In the example shown on FIG. IV.18, the spectra obtained from the upper layer and the bottom layer of the analyzed zone, are respectively typical of gelatin and of cellulose, by comparison to reference spectra, which will be presented in section IV.4.1. From these spectra, we can conclude that gelatin and cellulose form two separate layers.

#### d STXM data stacks treatment

The treatment of the stacks images was done using the *aXis2000* software (Analysis of X-ray microscopy Images and Spectra)[241]. The treatment consisted in:

- *an alignment* of images using the *Zimba* macro to correct the eventual shifts;

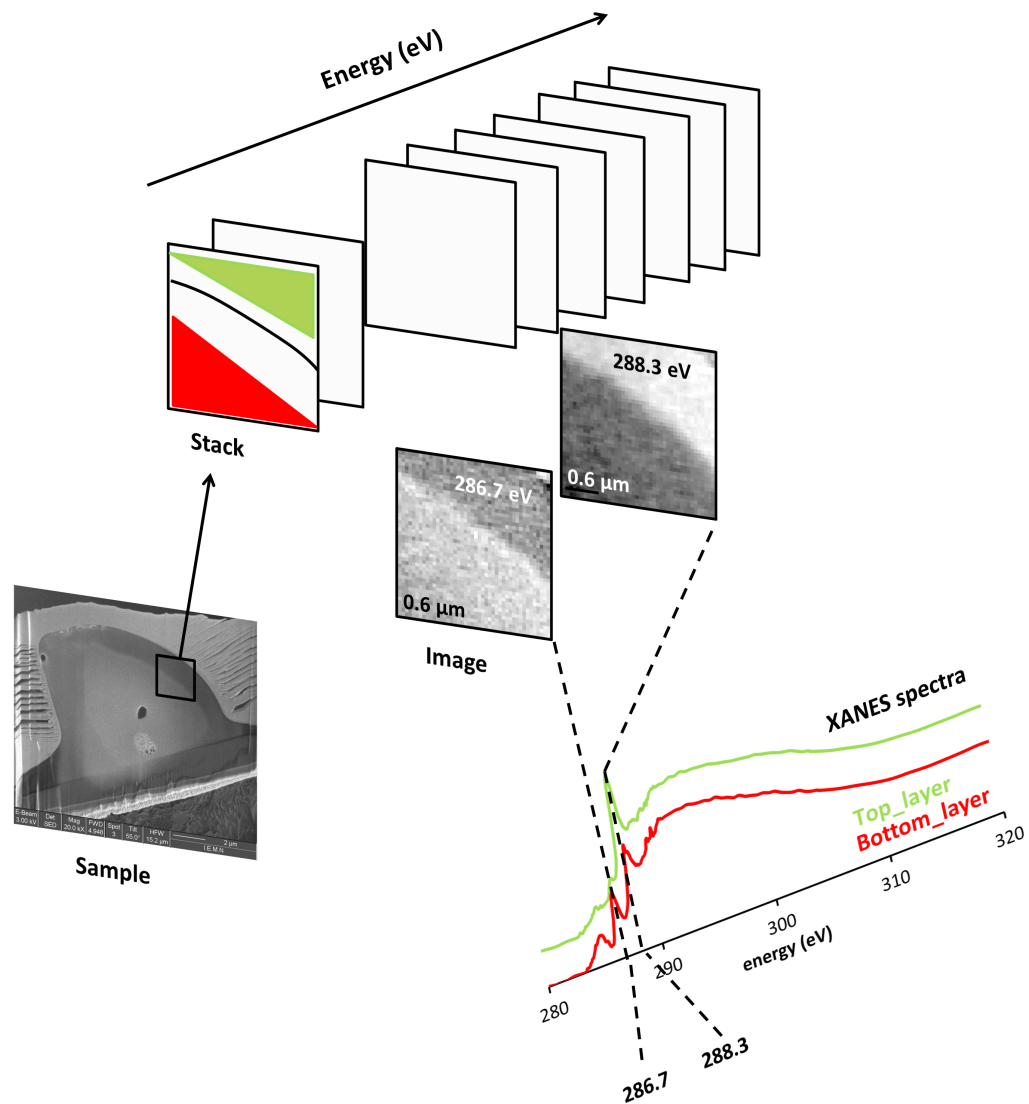


FIG. IV.18 – Scheme of a STXM stack recorded at the C K-edge on an enlarged region (black square) of a fiber cross-section (SEM sample image). Maps of the enlarged zone are recorded while scanning in energy. The green and red spectra correspond to data extracted from all the maps in the green and red regions, respectively.

- *a normalization* of the stack with incident intensity by using the spectra extracted from a region without sample and recorded with the same parameters; this allows to convert images in *O.D.*. After this treatment, the extraction of XANES spectra could be done in the different regions of interest;
- *a subtraction* of the images at characteristic energies by the image before the edge was done to enhance the visualization of component distribution;
- *a stack fit* to obtain component maps. This option performs a linear regression analysis (linear least squares fit) of the spectrum at each pixel to a sum of (1 to 8) user-defined model spectra and a constant. The option can also be used to visualize the distribution of a phase within the stack by using spectra extracted from the stack, instead of spectra of model compounds. Before drawing any conclusion of the stack fit, it is important to check the significance of those component maps. Examination of the residual stack allows to highlight region of poor fitting of the data, which may result from a missing chemical component. In addition, a curve fit can be done on the spectrum extracted from the region of the stack with high residual component to check the quality of the fit.
- *an red green blue (RGB) treatment* to map the distribution of reference compounds using colors. Indeed the stack fit produces component maps in greyscale as result (as many as the defined model spectra). To explore the spatial correlations of components, it is useful to merge any 3 of the component maps into a single color-coded composition map.

For the spectra comparison, an additional normalization to carbon or iron quantities and determination of spectral peak positions have been done using the Athena software package [242, 243]. C-K edge spectra were shifted in energy by 0.2 eV. This was done to recalibrate our spectra, based on the comparison of our gallic acid reference spectrum with published spectra of gallic acid [244] for which the peak of C=C  $1s \rightarrow \pi^*$  transition was located at 285.1 eV. After the shift, peaks were corresponding to literature data. It was then applied to all our spectra recorded at the C-K edge.

## IV.4 Model compounds analysis and protocol optimization

### IV.4.1 XANES signatures of model compounds

In order to be able to attribute XANES signatures in the fiber samples, model compounds have to be analyzed beforehand. Analysis at the C K-edge were first performed on the chosen model compounds (section IV.2.2 and TAB. IV.1) of cellulose, gelatin and ink components: gallic acid and iron gall ink precipitate (FIG. IV.19 and IV.20). The C K-edge spectra of the two cellulose model compounds vary in terms of relative intensities of the absorption peaks. These variations may find several explanations:

- The *Avicel* product is considered as pure crystalline cellulose. The spectrum (FIG. IV.19) exhibits a peak at 286.7 eV, which could be attributed to vinyl keton [245, 246] and may correspond to cellulose degradation during X-ray exposure. The main peak characteristic of cellulose, is present at 289.4 eV and correspond to  $1s \rightarrow \pi^*$  transition of aliphatic C-OH [247, 232]. A second cellulose characteristic peak, associated with

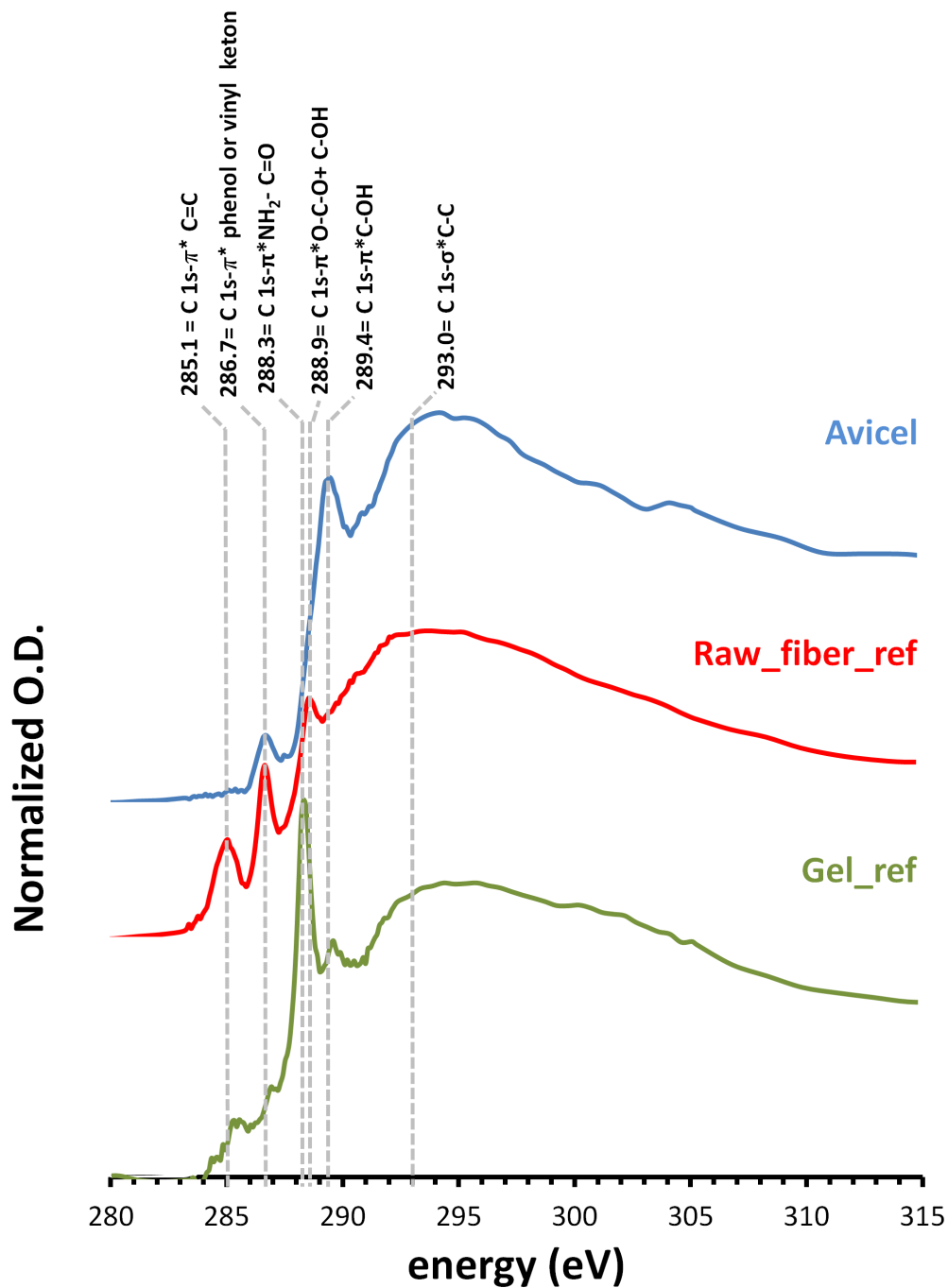


FIG. IV.19 – C K-edge spectra of cellulose and gelatin model compounds.

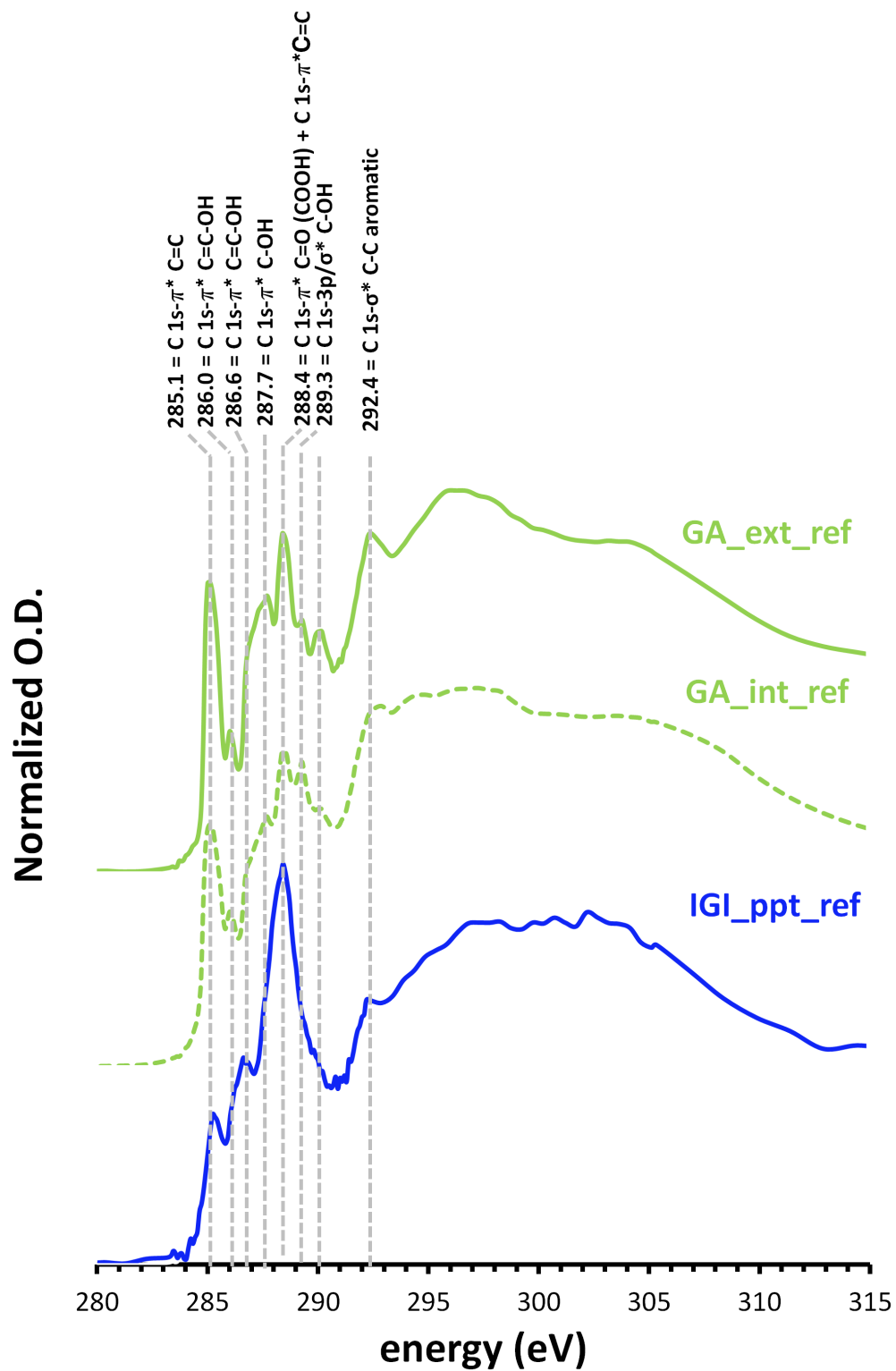


FIG. IV.20 – C K-edge spectra of ink components.

aliphatic C-H, is reported in literature at 290.8 eV but was not observed on our measurement;

- On the spectrum of the raw fiber, the main peak of *Avicel* at 289.4 eV is not observed. Instead three peaks are present at 285.1 eV, 286.7 eV, that 288.9 eV and were already reported in the literature [155]. The peak at 288.9 eV could be attributed to alcohol and ether, but is slightly shifted in comparison to the usual range reported in TAB. IV.2 (its energy is closer to carbonyl group). This peak is probably present in the *Avicel* spectrum, but is embedded in the main 289.4 eV peak and thus hardly noticeable as a shoulder. The two other peaks at 285.1 eV and 286.7 eV are representative of aromatic carbons and of oxygen substituted aromatic carbons. They could be attributed to the fact that raw linen fibers contain a few percent of lignin (aromatic polyphenols)[247]. They could additionally be due to some degradation occurring in the fiber during FIB milling or X-ray exposure. Cody[246] has reported changes in C-XANES spectra of oak's cell walls: loss of alcohol groups (289.5 eV), growth of peaks of enol (286.6 eV) and potential ketone at 288.5 eV. Although no changes have been observed at 285 eV by Cody et al.[248], Karunakaran et al.[247] indicates that radiation damage can be monitored in cellulose by following the increase of aromatics and keto-enol regions at 285 eV and 286.6 eV.

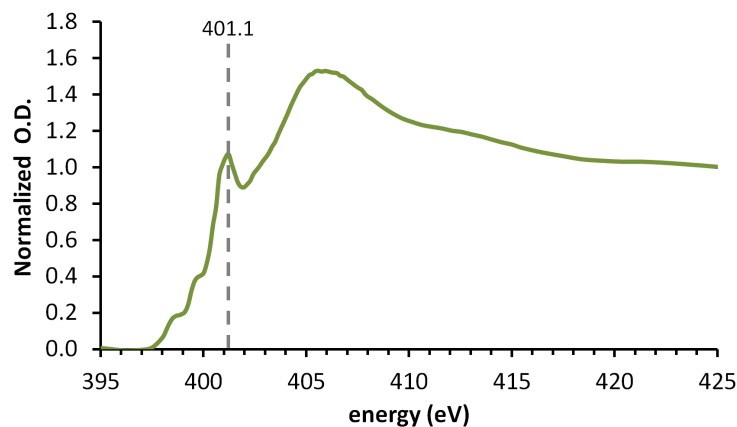
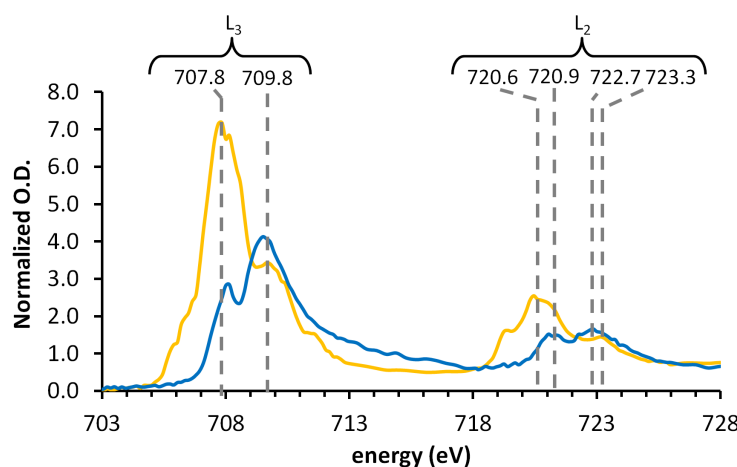
Although not well understood, the substantial differences observed between the *Avicel* and *raw fiber* spectra, did not limit STXM analysis. In this chapter, since all fibers have been cut using FIB, it was consistent to take the spectrum of the *raw fiber* as model to locate cellulose rich area.

The gelatin spectrum (FIG. IV.19) shows a main peak at 288.3 eV which is attributed to the  $1s \rightarrow \pi^*$  transition of the amide group. The peak at 289.6 eV could be attributed to alcohol function. The large band at 294.4 eV corresponds to aliphatic carbons.

Regarding gallic acid, two slightly different signatures (intensity ratio) are seen depending on the region selected: at the edge of a grain (GA\_ext\_ref) or inside a grain (GA\_int\_ref). The spectrum obtained on the edge is similar to previously published data [244] and our peaks attribution was therefore done mainly following these previously published data (see [244], TAB. IV.2 and FIG. IV.20);

The spectrum of the ink precipitate (FIG. IV.20) presents most of the peaks of gallic acid: 285.1 eV, corresponding to the transition of aromatic carbons C=C; 286.0 eV and 286.6 eV, attributed to aromatic C connected to hydroxyl group C=C-OH; 288.4 eV, assigned to carboxylic group and to a lesser extent to transition of the aromatic ring; 292.4 eV, characteristic of aromatic C-C. However, in the IGI\_ppt\_ref sample, the peak at 288.4 eV is enhanced in comparison to the other peaks and larger than in GA\_ext\_ref. This suggests modifications in the environment of the carboxylic acid groups which is coherent with precipitate formation (iron chelation in precipitate is done via phenolic hydroxyls groups and the carboxylic acid group [40]).

Besides the information obtained at the C K-edge, measurements at the N K-edge and at the Fe L-edges give additional clues to map the distribution of gelatin or iron respectively. At the N K-edge, gelatin presents one main peak at 401.1 eV corresponding to an amide, as illustrated on the spectrum extracted from the FIB foil (FIG. IV.21. At the Fe L-edge, Fe2\_ref and Fe3\_ref present two main peaks at 707.8 eV and 709.8 eV (for Fe L<sub>3</sub> edge) and between 720.6 eV and 723.3 eV (for Fe L<sub>2</sub> edge) (FIG. IV.22). The peaks intensities differ and, in principle, quantification of the amount of iron(II) and iron(III)

FIG. IV.21 – *N K-edge spectrum of gelatin.*FIG. IV.22 – *Fe L-edge spectra of iron(II) and iron(III) references, in yellow and blue, respectively.*

can be done as illustrated on silicates by Bourdelle et al.[240].

**XANES as a tool to differentiate fiber, gelatin and ink components.**  
 Cellulose, gelatin and ink components have different C K-edge XANES spectra. Consequently, XANES spectroscopy at the C K-edge provides a way to map their distribution in the fiber samples by choosing appropriate energies, specific to the component. Analysis at the N K- and Fe L-edges provides complementary information on the distribution of gelatin and ink or free iron.

#### IV.4.2 Influence of X-ray beam on iron oxidation state

XANES spectroscopy is a powerful tool but it also presents some limitations: Wilke et al. [217] and Kanngießner et al. [215] mentioned that the X-ray beam can influence the oxidation state of iron gall inks. Indeed, a reduction of iron(III) to iron(II) has been observed under the beam during their experiments. This phenomenon of iron photoreduction has been observed on several materials at the K-edge (for example on biological samples [249, 250] or pigments [251]) and at the L-edge [252]. Consequently, parameters for the optimal analysis of our samples had to be determined.

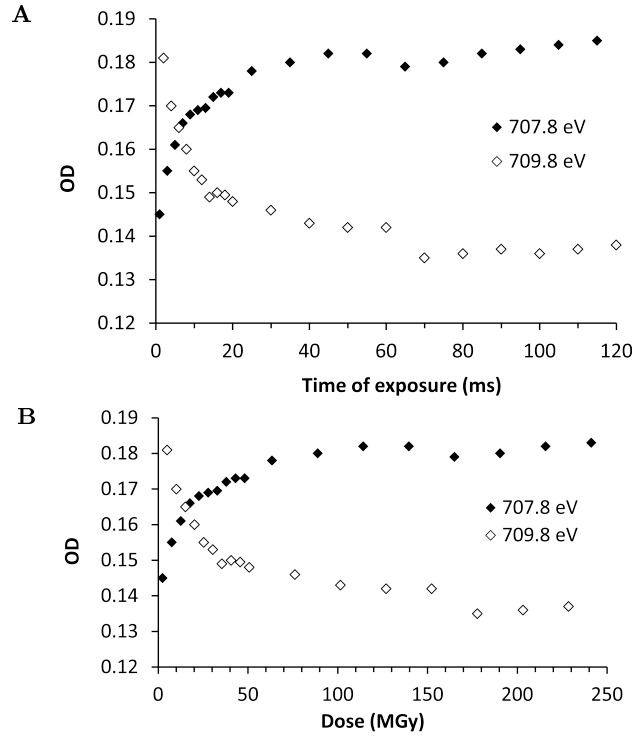


FIG. IV.23 – Iron reduction test on “*ink<sub>O</sub>+gum drop*”: evolution of OD with (A) the time of exposure and (B) with the dose.

To research optimum parameters for stack recording, we performed irradiation at ambient temperature on the FIB foil obtained with the sample “*ink<sub>O</sub>+gum drop*”, which is a mixture of ink and polysaccharides, and is thus, a good model for the “*ink + cellulose*” system. The sample was mapped several times to estimate the rate at which the XANES spectrum is changed (if it occurs) and to choose the optimum parameters for stack recording. The maps were recorded at the two energies typical of iron L<sub>2</sub> edges maximal absorption, i.e. 707.8 eV and 709.8 eV, corresponding mainly to iron(II) and iron(III) contributions respectively (see spectra of ref. samples in this range in FIG.IV.22). For each map, the dwell time was 1 ms for each pixel, consistent with the acquisition parameters defined in appendix K. The recording of successive maps logically increased the exposure time  $t$  of the sample to X-ray radiation. It was therefore necessary to take into account this parameter and to evaluate the corresponding absorbed radiation doses  $D$  (i.e. total amount of deposited energy per mass of material, expressed in Gy ( $\text{J} \cdot \text{kg}^{-1}$ )) which was done using the EQ. IV.2:

$$D = \frac{F \cdot E \cdot t}{m} \quad (\text{IV.2})$$

with:

$F$ , the absorbed flux (Hz): number of photons absorbed per second;

$E$ , the photon energy (J);

$t$ , the exposure time (s);

$m$ , the mass of the irradiated volume (kg).

Since soft X-ray spectro-microscopy applied on thin samples obeys the Beer-Lambert law, the absorbed flux  $F$  can be derived from the incident flux ( $I_0$ ) and from the  $O.D.$

of the material at the energy of exposure (see details in appendix K), leading to the estimation of the dose  $D$ .

On FIG.IV.23, the decay of the  $O.D.$  at 709.8 eV versus time (or dose) is correlated to an increase of the  $O.D.$  at 707.8 eV, meaning that photoreduction occurred on the “ink<sub>O</sub>+gum drop” sample. This was expected knowing that iron gall inks were previously shown to be sensitive to Fe K-edge X-rays [215, 215]) and that transition metal studies at L-edges induced generally more radiation damage in comparison to K-edge studies [252].

The critical dose (or lifedose) is the dose that attenuates (or increments) a specific spectroscopic feature by 63 % [252]. For this sample material, the critical dose was then evaluated to 125 MGy (see details in appendix K). It is worth noting that this value is a rough estimation due to a poor fitting of the data. However it gives a sense of how radiation sensitive the sample is. This value is of the same order than the value reported for prussian blue, another photosensitive iron component, which has an half-dose of 54 MGy [252](dose that modifies a specific spectroscopic feature by 50 %).

These preliminary testing shows that, on this test sample, iron is substantially sensitive to beam induced reduction. This point seriously compromised proper quantification of Fe(II)/Fe(III) ratios. However, qualitative analysis of Fe(II) and Fe(III) rich areas remained possible. For this purpose, acquisition parameters (see appendix K) were defined in an attempt to make compromise between photoreduction, damage and spectrum resolution. With these parameters, 15 pts were recorded before reaching the Fe(II) specific edge (i.e. points taken between the starting energy and 707.8 eV) and 25 pts before reaching the Fe(III) specific edge (i.e.points taken between the starting energy and 709.8 eV). This means that the sample was already irradiated for approximately 15 ms and 25 ms, respectively, when Fe(II) and Fe(III) specific edges were recorded. Considering in first approximation that damage is not energy dependent in the energy range of the spectrum, it can be concluded with FIG. IV.23 that these irradiation durations provoked a change in  $O.D.$  of 15 % to 20 % with respect of initial  $O.D.$  values. These changes remain compatible with a qualitative STXM approach consisting in identifying Fe(II) and Fe(III) rich areas.

### Methodology and impact on iron speciation.

To take into account the high sensitivity of iron under the beam, a specific protocol was defined with parameters reported in appendix K (TAB. K.4). The whole sample was first mapped with low spatial resolution at Fe L-edges energies of 700 eV, 707.8 eV, 709.8 eV, and 730 eV so as to locate Fe(II) and Fe(III) rich areas that deserve a closer investigation. Full Fe L-edges stacks were then recorded in the thus identified enlarged areas with high spatial resolution to allow extraction of XANES spectra. Then energy was shifted to the C K- and/or N K-edges for complementary recording in the same areas. This enabled identification of regions of interest while limiting sample irradiation at the Fe L-edges. It makes it possible to map on the same area the distribution of Fe(II), Fe(III), cellulose, gelatin and iron gall ink compounds.

This methodology may be improved by working at a lower temperature so as to limit secondary radiation effects, also change in element speciation. Greater doses may then be withstood by the sample before the same extent of global damage is reached [253, 254]. This option could be explored in a further study, but was not available on the beamline at the time of the experiments.

## IV.5 Components penetration into fibers

The investigation of gelatin and/or ink penetration within the paper fiber has been carried out mainly on modern samples described in IV.1. The penetration of gelatin into the fibers was investigated both with AFM-IR and STXM whereas the ink distribution was evaluated only with STXM. The impact of the gelatin size of the fiber on the ink components distribution was also analyzed. In addition, the effect of a gelatin spray on an inked fiber was assessed. Due to limited beamline time, only one cross-section of each sample was analyzed during this thesis. Consequently, all the conclusions are drawn based on the examination of one region of the sample, which homogeneity may not be the same all along the fiber (and within). Future experiments are planned to double-check those conclusions.

### IV.5.1 Gelatin penetration into fibers

#### a AFM-IR analysis

Preliminary tests were conducted with nano-infrared spectroscopy on both the model *gel<sub>4</sub> fiber* and the 79/7 fiber. The cross-sections were prepared by ultramicrotomy as described in part IV.2.3.

For each sample, a smaller region was chosen near a flat edge to map the sample. The *gel<sub>4</sub> fiber* was mapped at two wavelengths  $1068\text{ cm}^{-1}$  (specific of cellulose) and  $1532\text{ cm}^{-1}$  (specific of the amide II group of gelatin), as illustrated on FIG. IV.24. Although it is less intense, the amide II band was preferred to the amide I band ( $1639\text{ cm}^{-1}$ ) because this latter may overlap the band of absorbed water usually located near  $1640\text{ cm}^{-1}$ .

For the *gel<sub>4</sub> fiber*, AFM mapping shows that the surface of the sample is uniform. Also the cellulose response at  $1068\text{ cm}^{-1}$  is expected to be uniform. On the infrared map recorded at  $1068\text{ cm}^{-1}$ , this is not the case: a region appears red in the right bottom corner while the rest of the map appears green. This green (weaker) signal probably corresponds to a poorer adherence of the sample on the ZnSe crystal. The contact seems nevertheless sufficient to record spectra from the edge of the fiber toward the center (colored squares on FIG. IV.24). These IR spectra were normalized with respect to the absorbance at  $1068\text{ cm}^{-1}$  to visualize more easily if there is a change in the height ratio of the two bands of interest. On this sample, no band was present at  $1532\text{ cm}^{-1}$ , meaning that there was no significant amount of gelatin in the paper. Also the band observed at  $1660\text{ cm}^{-1}$  did not correspond to an amide signature, but more probably to water absorption.

On the 79/7 fiber (FIG. IV.25), maps were done at  $1068\text{ cm}^{-1}$  (specific of cellulose) and  $1660\text{ cm}^{-1}$  (specific of the amide I group of gelatin) because the signal was expected to be clearly present in view of previous ATR measurements made on the paper sample. However, the IR signal was weak and no profile was evidenced on the maps, probably because of a poor adhesion of the sample to the crystal. Yet, some spectra were recorded in the inner part of the fiber (FIG. IV.25), showing a band at  $1532\text{ cm}^{-1}$  compatible with the presence of gelatin in the fiber.

During these preliminary tests, we came to the conclusion that ultramicrotomy preparation presented serious limitations. It first appeared time-consuming. Second, the major difficulty was to obtain flat and thin cross-sections in good adherence with the crystal. Third, a lot of cross-sections had to be cut to collect a few ones apparently in good contact with the crystal, but none of them was in fact correct enough when being analyzed by AFM-IR analysis. Fourth, this method can also not be used as a routine

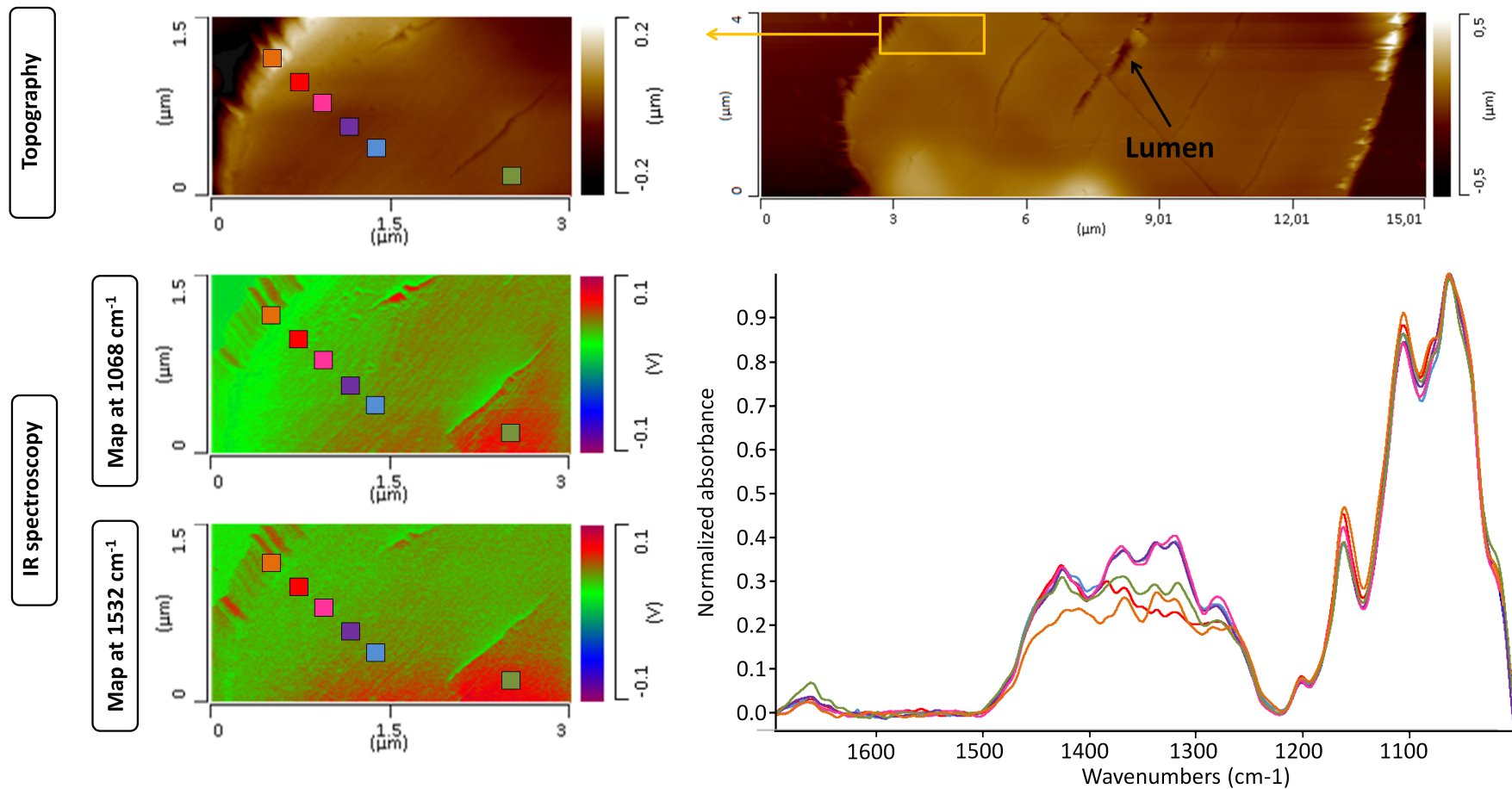


FIG. IV.24 – Topography and IR measurements of  $gel_4$  fiber. Mapping were recorded with the following parameters: 0.1 Hz AFM scan frequency, 16 points, 5 % laser power at  $1068\text{ cm}^{-1}$  and 20 % laser power at  $1532\text{ cm}^{-1}$ . Red and green areas represent regions of high and low absorbance, respectively.

The presented spectra were recorded with: 5 % laser power and 256 points.

Spectra are the average of three spectra taken at each location.

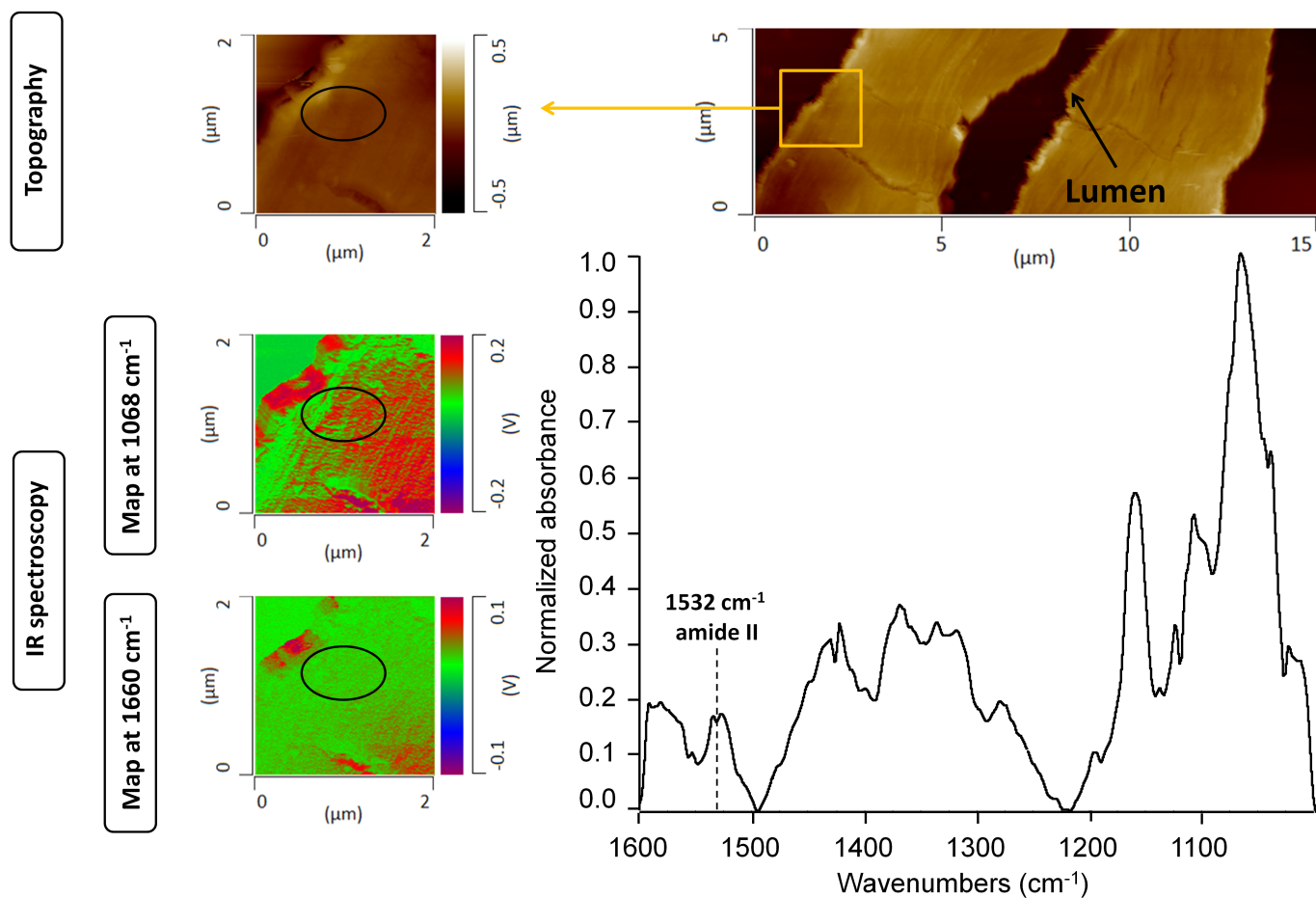


FIG. IV.25 – Topography and IR measurements of 79/7 fiber. Mapping were recorded with the following parameters: 0.1 Hz AFM scan frequency; 16 points; 5 % laser power at  $1068\text{ cm}^{-1}$  and 20 % laser power at  $1660\text{ cm}^{-1}$ . Red and green area represent regions of high and low absorbance, respectively. The presented spectrum was recorded with 5 % laser power in the range  $1000 - 1500\text{ cm}^{-1}$ , 20 % laser power in the range  $1500 - 1600\text{ cm}^{-1}$  and 256 points. The spectrum is the average of three spectra taken inside the circle.

technique. Moreover, the gelatin layer could possibly be lost during the cutting if it stays as an outside layer. Finally, imaging the edge remains an issue with AFM, because of our samples thickness, which creates a difference of height higher than what the technique is designed to follow. For all these reasons we decided not to pursue the studies with this cutting methodology but to rather turn our efforts towards FIB cutting even if this technique is more expensive than microtomy, complex and time consuming as well.

In this work, the analysis of FIB foils with AFM-IR was not attempted. However, it would be interesting to try it in future experiments with another more adapted equipment (with an infrared excitation of the sample from above), which would solve the problem faced during our experiments for which perfect contact between the sample and the support was mandatory.

## b STXM analysis at C and N K-edges

With STXM, due to the synchrotron limited access, we chose in the first shifts to analyze only the modern mock-up samples described in TAB. IV.1. For gelatin distribution analysis, a small region next to the edge of the fiber was selected. Then stacks were recorded with parameters mentioned in appendix K. Maps were extracted from these stacks at the energies that gave the best contrast in order to observe the distribution of the different organic components. FIG. IV.26 shows the images obtained on the *gel*<sub>1.5</sub> and *gel*<sub>4</sub> fibers at the two energies, 286.6 eV and 288.2 eV, which matches to one of the maxima of cellulose's C K-edge XANES spectrum and to one of gelatin's spectrum, respectively (see reference spectra on FIG. IV.19). Regions that are brighter at the first energy are also darker at the second one (FIG. IV.26). This suggests that gelatin does not penetrate much in the fiber but forms a coating around the fiber.

To go further, spectra were extracted from these two regions (FIG. IV.27). They do not correspond to a mixed signature of cellulose and gelatin references but instead are similar to the signatures of individual model compounds. This means again that gelatin does not significantly penetrate the fibers.

Another illustration of this point can be found with gelatin and cellulose on RGB component maps, obtained with the "stack fit" option of the Axis 2000 software (FIG. IV.26). It gives a colorful estimation of the proportions of each constituents in each pixel. On FIG. IV.26, a clear separation of gelatin (green) and cellulose (red)-rich areas is observed, confirming that gelatin does not significantly penetrate the fiber.

At the N K-edge (FIG. IV.28), the spectrum of the top layer for the *gel*<sub>1.5</sub> fiber is similar to the *gel\_ref* spectrum, in contrast to the bottom layer extracted spectrum which shows only noise. This is consistent with a gelatin coating and confirms the previous observation at the C edge.

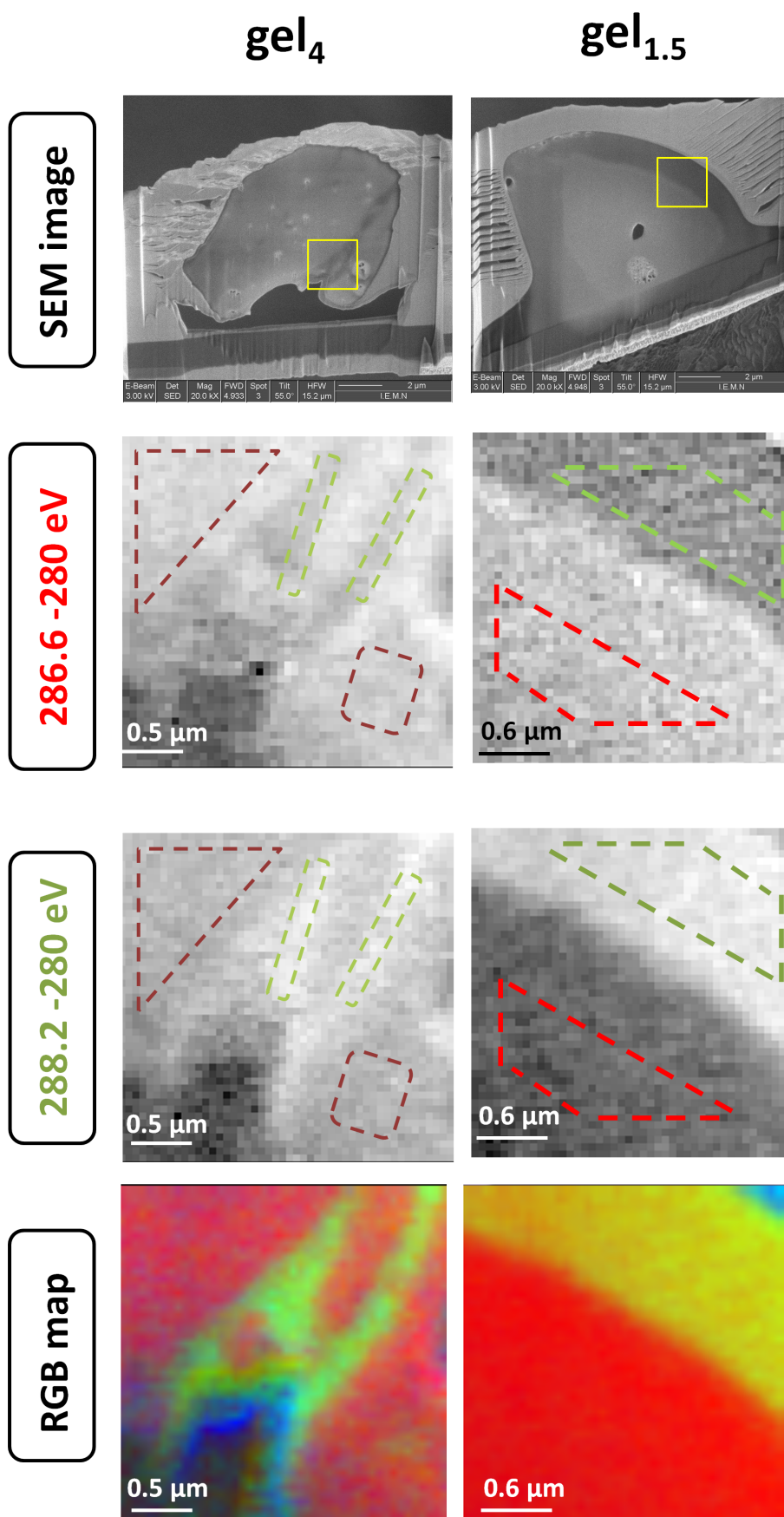


FIG. IV.26 –  $C$  K-edge STXM mapping of  $gel_{1.5}$  and  $gel_4$  fibers, enlarged area of analysis (yellow squares, top images) and regions of spectra extraction (dashed zones). Related  $C$  K-edge RGB compositionnal maps obtained from comparison with gelatin and raw fiber reference spectra. Red represents cellulose (region with spectra matching mostly raw fiber reference spectra) and green gelatin (region with spectra matching mostly gelatin reference spectra). Blue represents region of the metal coating and also regions where residual components of the fit is high.

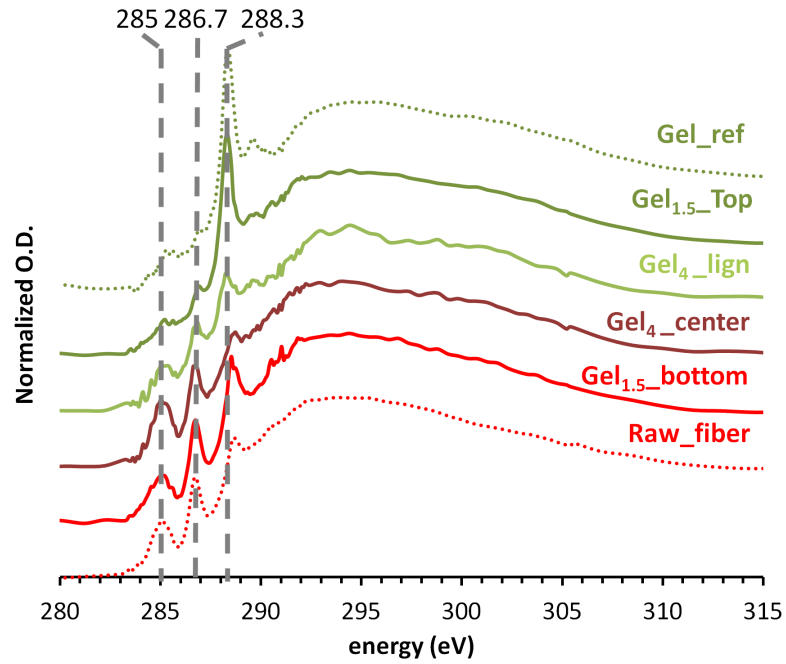


FIG. IV.27 – Spectra obtained from selected regions of gel<sub>1.5</sub> and gel<sub>4</sub> fibers and comparison with reference spectra of gelatin and raw fiber. The colours of the spectra correspond to those of the regions chosen for spectra extraction (dashed zones in FIG. IV.26).

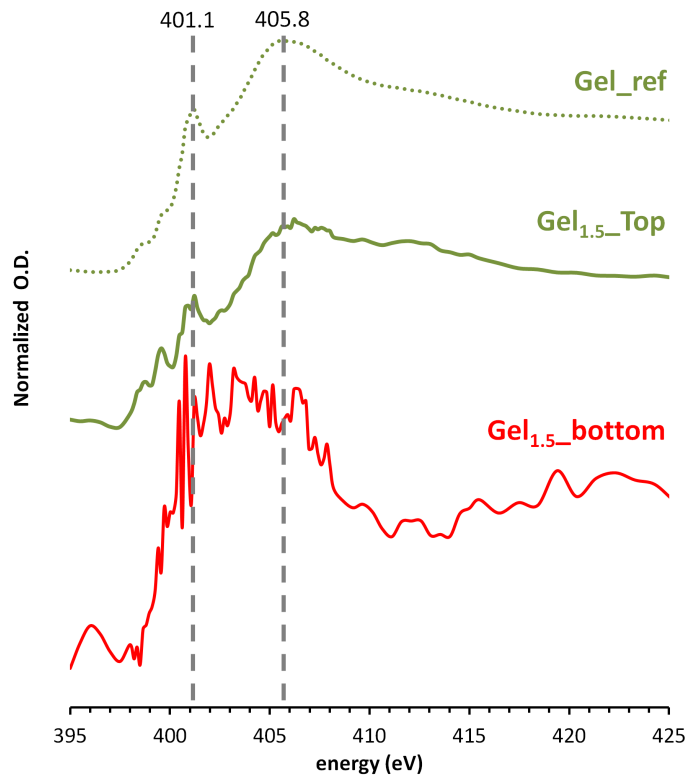


FIG. IV.28 – N K-edge extracted spectra from gel<sub>1.5</sub> fibers. The colours of the spectra correspond to those of the regions chosen for spectra extraction (dashed zones in FIG. IV.26).

### Nano-IR and STXM for gelatin impregnated fibers

AFM-IR was investigated for mapping at a nanoscale gelatin distribution in paper fibers. To avoid signal overlapping, samples were not resin embedded which raised several difficulties in the preparation of their cross sections dealing mostly with mechanical damages. A few cross sections only could be obtained by ultramicrotomy and their infrared mapping was not conclusive probably because of insufficient adherence to the substrate. Spot analyses were attempted: on the *gel<sub>4</sub> fiber*, no gelatin signature was evidenced meaning that it does not significantly penetrate the fiber. On one ancient fiber (79/7) some gelatin signal was detected but since mapping was not conclusive, it does not necessarily attest of gelatin penetration in the fiber. It could as well be due to some contamination deposited by the diamond knife. STXM imaging of FIB cross sections proved to be much more powerful (at least in the frame of this study) for mapping gelatin distribution at the C and N K-edges. On *gel<sub>4</sub> fiber* and *gel<sub>1.5</sub> fiber* samples, gelatin coats the fiber but does not penetrate in it, consistent with AFM-IR observations.

## IV.5.2 Ink penetration into unsized fibers

The ink penetration in the fiber was investigated on the “ink<sub>R</sub> fiber”. With SEM imaging (FIG.IV.29), it can be seen that the fiber presents a particular structure : it is very large (approx. 30 μm), flat and seems to be composed of two walls 1 μm to 2 μm wide. These features are consistent with those of the most fibrillated fibers (FIG.IV.10, red arrows) and suggest squashing during paper making. Interpretation of the separation between the two walls (FIG.IV.29, dotted line) remains delicate : it could be due to a former lumen, or to a crack that appeared between the inner and outer walls of the former fiber (meaning that this latter was entirely opened during paper milling).

On Fe L-edge maps (FIG.IV.29), iron appears in bright around the fiber (as an ink layer), but also inside the fiber along cracks. Outside the fiber, mainly one region is brighter on the map at 709.8 eV minus 707.8 eV, suggesting a predominance of iron(III) probably due to precipitate formation. Inside the fiber, bright spots are also seen along cracks, but consist mainly in iron(II), as attested by the map at 707.8 eV minus 700.0 eV.

On enlarged regions of the “ink<sub>R</sub> fiber” (FIG.IV.30, yellow squares on top images), stack fits were performed using *Axis2000* software to get an RGB map showing the distribution of iron(II) and iron(III) based on a comparison with the reference compounds spectra. This approach confirmed predominance of iron(III) outside the fiber (FIG.IV.30, map on the left), consistent with the deposition of some precipitate. This deposit apart, the surface of the fiber is covered relatively homogeneously by a thin Fe(II) rich layer that also follows cracks in the inner part of the fiber (FIG. IV.30, maps on the right). Many of these cracks are oriented perpendicular to the walls, and it is believed that they were formed during paper milling. Bright Fe-rich spots, approx. 200 nm wide are also observed along the cracks. On the RGB picture, they appear yellow (color chosen for Fe(II)), suggesting that they are predominantly composed of Fe(II). This point should be taken with great care as a relatively high residual component was obtained with stack fit (poor fit of the data, which may be due to the different nature of the iron salts) (FIG. IV.31).

Extraction of Fe L-edge spectra from different regions of interest (FIG. IV.32), showed that iron is not only distributed along cracks but also penetrates the fiber walls in which

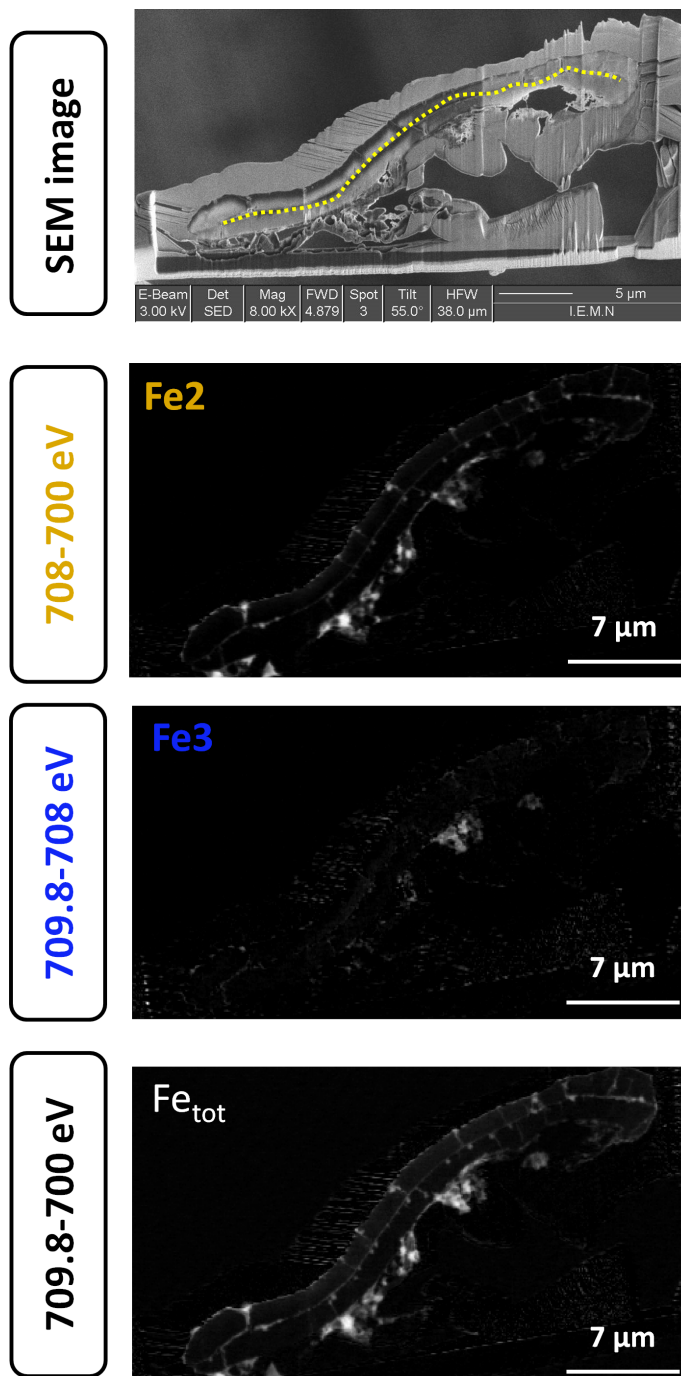


FIG. IV.29 – Iron penetration in  $ink_R$  fiber. Top image correspond to SEM image of the cross-section. The three other images are Fe L-edge STXM mappings of iron distributions: iron(II), iron(III) and total iron, respectively from top to bottom.

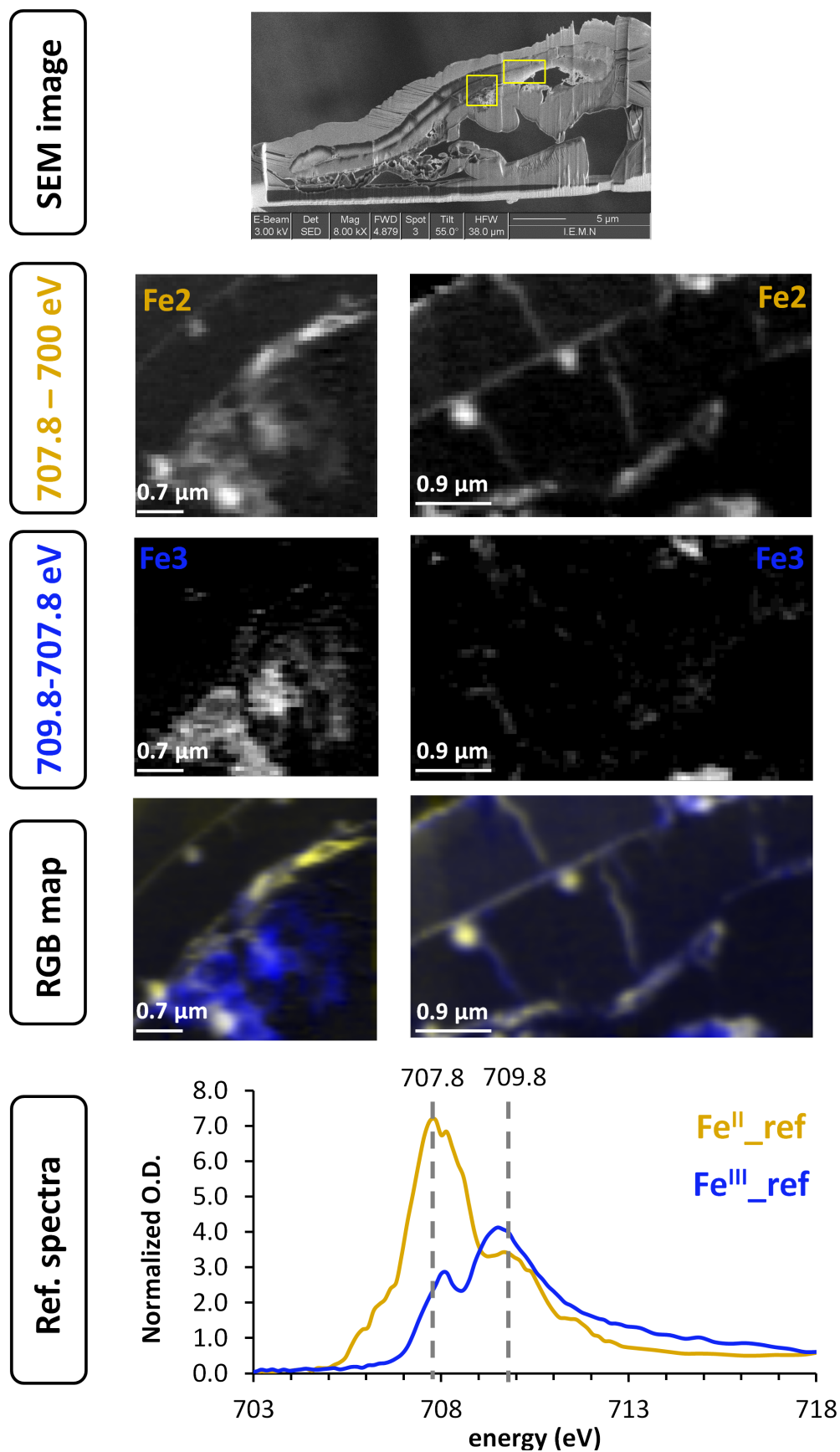


FIG. IV.30 – Iron distribution in  $ink_R$  fiber. In blue, are represented regions matching the iron(III) reference and in yellow, regions matching the iron(II) reference.

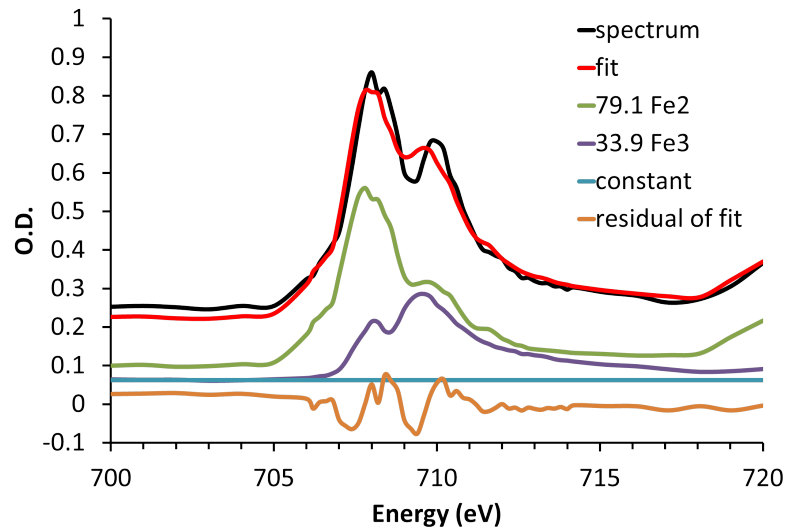


FIG. IV.31 – Fit of the spectrum extracted from an iron dot using the linear regression analysis of the Axis2000 software as done for the entire stack with the stack fit option.

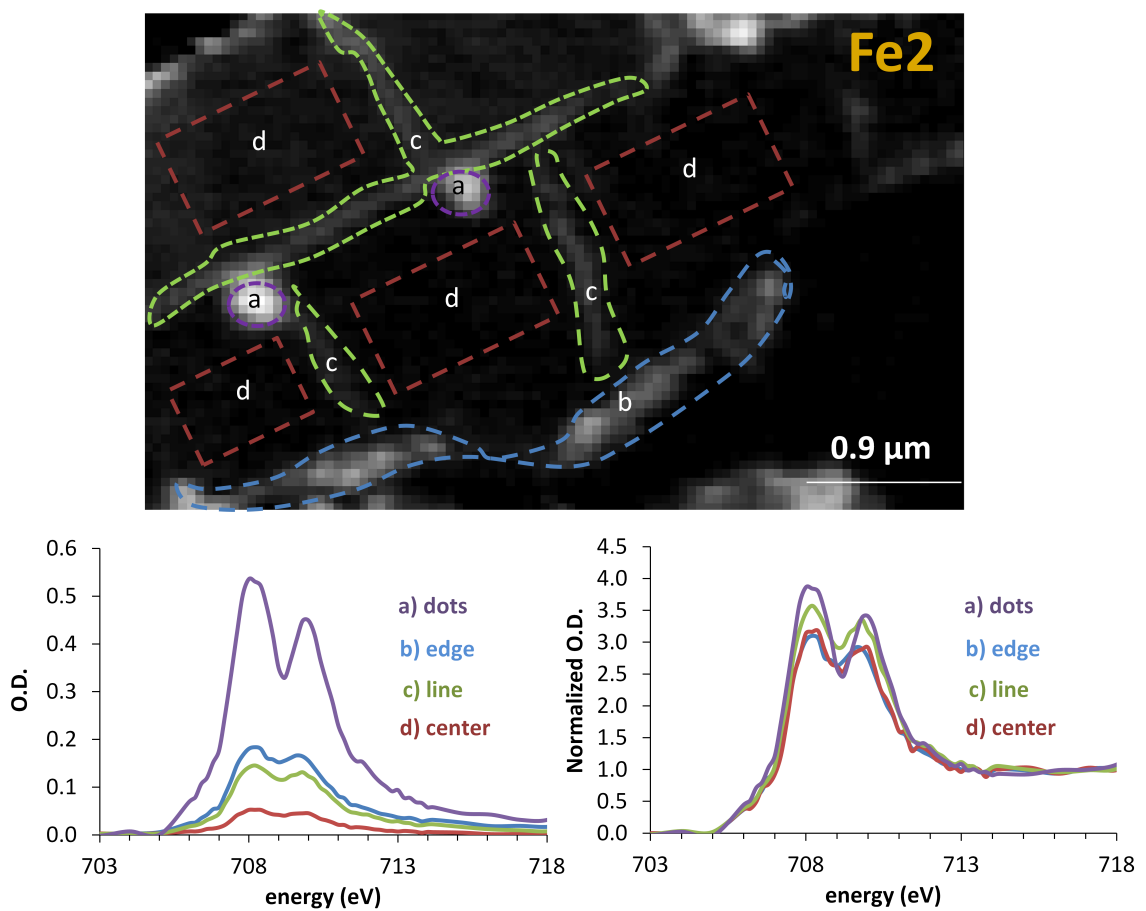


FIG. IV.32 – Spectra extracted from inked-fiber Fe L-edge stacks (dashed areas). The spectra colors correspond to those of the dashed areas. On the left are represented raw spectra and on the right normalized spectra.

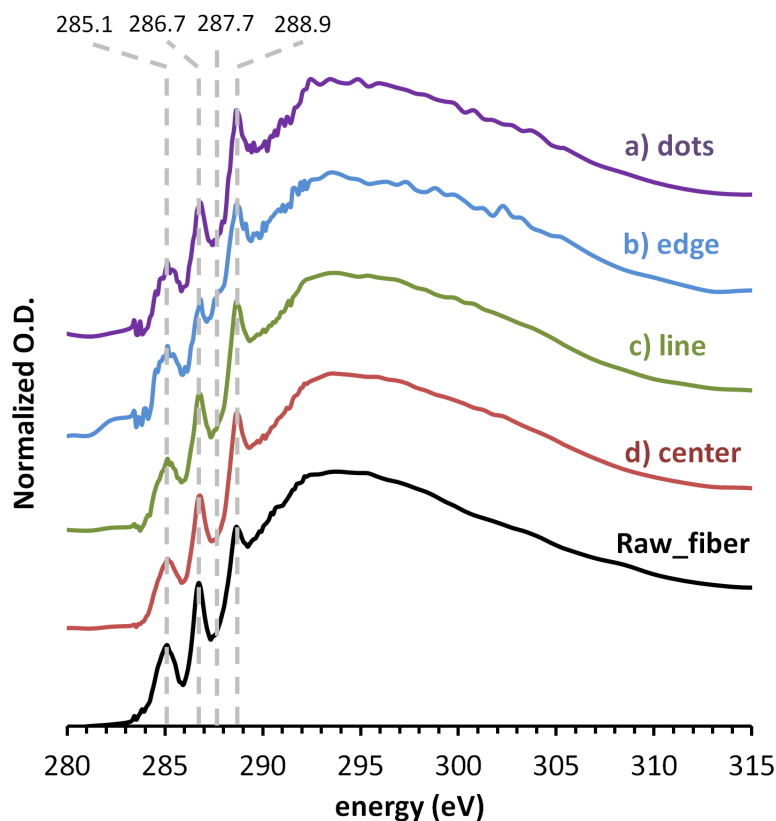


FIG. IV.33 – Spectra obtained on  $ink_R$  fiber at C K-edge. The spectra colors correspond to those of the dashed areas of FIG. IV.32.

it is present at very low concentration (FIG. IV.32, spectrum d). Although the spectra significantly differ in intensity (FIG. IV.32), they have a similar shape that corresponds to a mixture of Fe(II) (major component) and Fe(III) (FIG. IV.31).

In order to identify more precisely iron compounds, C K-edge spectra were extracted from areas a to d of FIG. IV.32. Spectra from region a, c and d presented only the signature of cellulose raw fiber (FIG. IV.33) suggesting that iron is either bound to cellulose or present as an inorganic compound (sulfate or hydroxide). A shoulder at 287.7 eV is noticed on the spectrum extracted from region b. This could come from gallic acid but the signature is weak and hidden by cellulose. Indeed, the ink was aged 3 days only before use, which means the ink solution still contained some proportion of gallic acid when impregnation was done. In addition, the small amount of precipitate formed in the ink, is probably present in too small concentrations to be detected.

#### STXM on ink impregnated fibers

Fe(III)-rich compounds were identified at the surface of the fiber. They probably correspond to IGI precipitate. Iron was also present in the inner part of the fiber as a mixture of Fe(II) and Fe(III). It is heterogeneously distributed, with high concentrations along cracks and low concentrations in the walls. It might correspond to iron sulfates, iron oxide hydroxide or iron bound to cellulose as no signature of gallic acid or iron gall ink could be detected by C K-edge analysis.

### IV.5.3 Ink penetration into sized fibers

STXM was also used to investigate the effect of gelatin on ink and iron penetration on the  $gel_4+ink_R$  fiber (FIG. IV.34). This fiber presented a rather classical linen fiber shape (ovoid) with a central hole probably corresponding to the lumen. The SEM image shows some damage due to the milling process (holes where the FIB section is too thin). Fe L-edge maps highlight regions containing iron which are mostly located outside the fiber suggesting some coating with an ink layer.

STXM observations were then focused on an area where the coating seemed partially detached (FIG. IV.35 and IV.36). The Fe L-edge mapping confirmed that iron remains mainly outside the fiber with an uneven Fe(II)/Fe(III) distribution. Only small amounts of iron(II) penetrate a little at the edge of the fiber. C K-edge analyses were first expected to discriminate all organic components. Yet they mainly evidenced cellulose and gallic acid distributions. The presence of gelatin was not highlighted which might be accounted by two points:

- gelatin may have been released into the ink during sample preparation. Duration of impregnation was chosen according to macroscopic observations and a single fiber

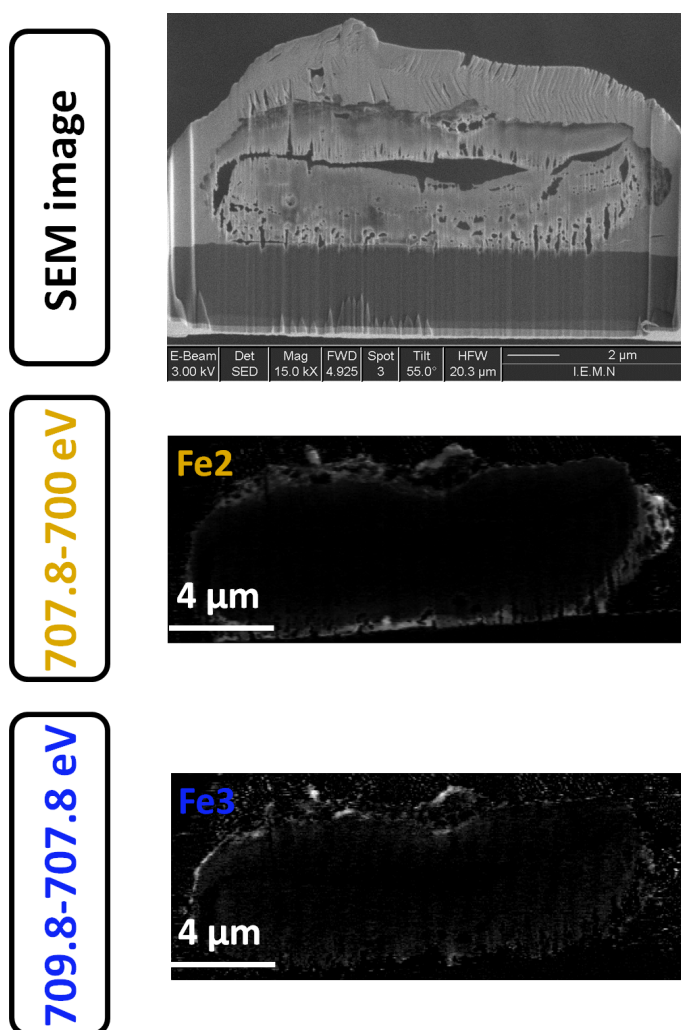


FIG. IV.34 – Images of  $gel_4+ink_R$  fiber. Top image correspond to SEM image of the cross-section. The two other images are Fe L-edge STXM mappings of iron distributions: iron(II) and iron(III), respectively from top to bottom.

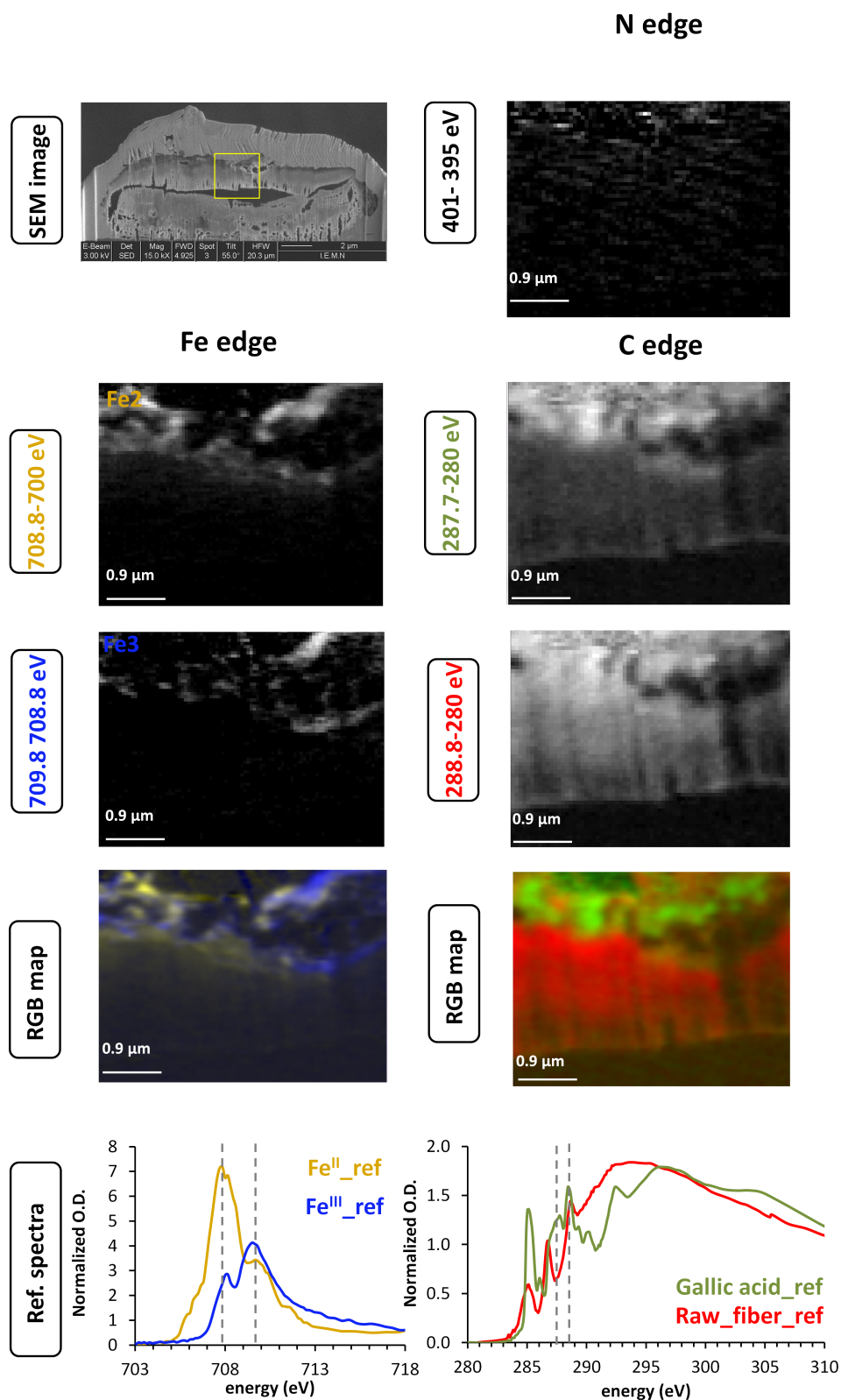


FIG. IV.35 – Comparison of Fe and C edges maps of an enlarged area of  $gel_A + ink_R$  fiber and repartition of ink ingredients. On the RGB compositionnal maps, regions in blue and in yellow are rich in iron(III) and iron(II), respectively. Red and green areas represent regions matching cellulose and gallic acid references, respectively. No signal is detected at the N K-edge.

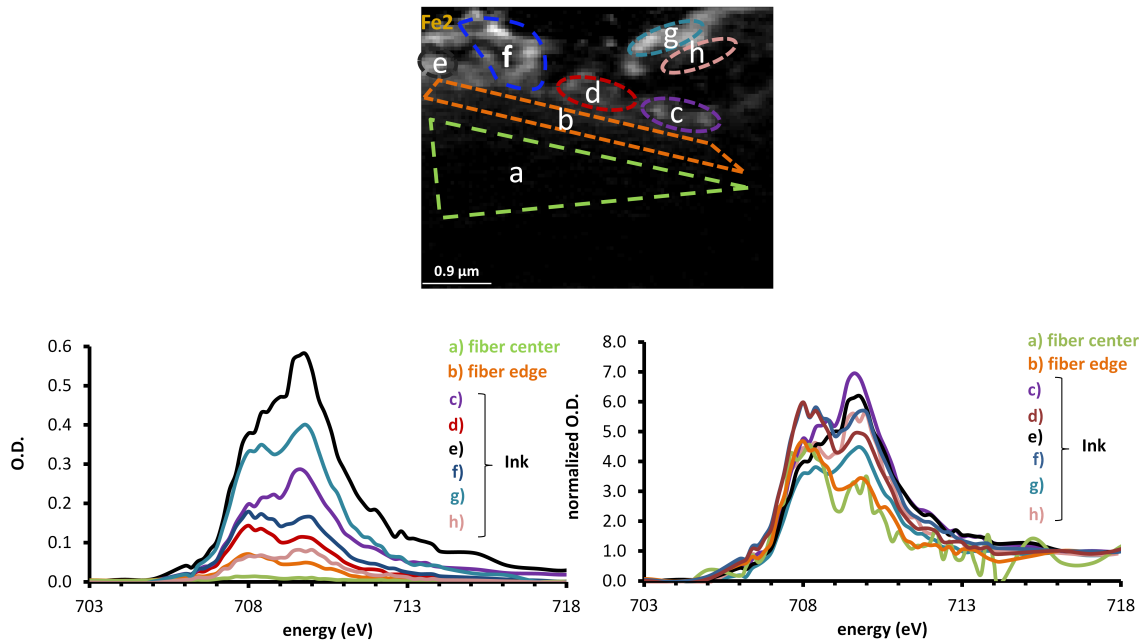


FIG. IV.36 – Comparison of Fe L-edge spectra recorded in different regions of the  $gel_4 + ink_R$  fiber. The spectra colors correspond to those of the dashed areas. On the left are represented raw spectra and on the right normalized spectra.

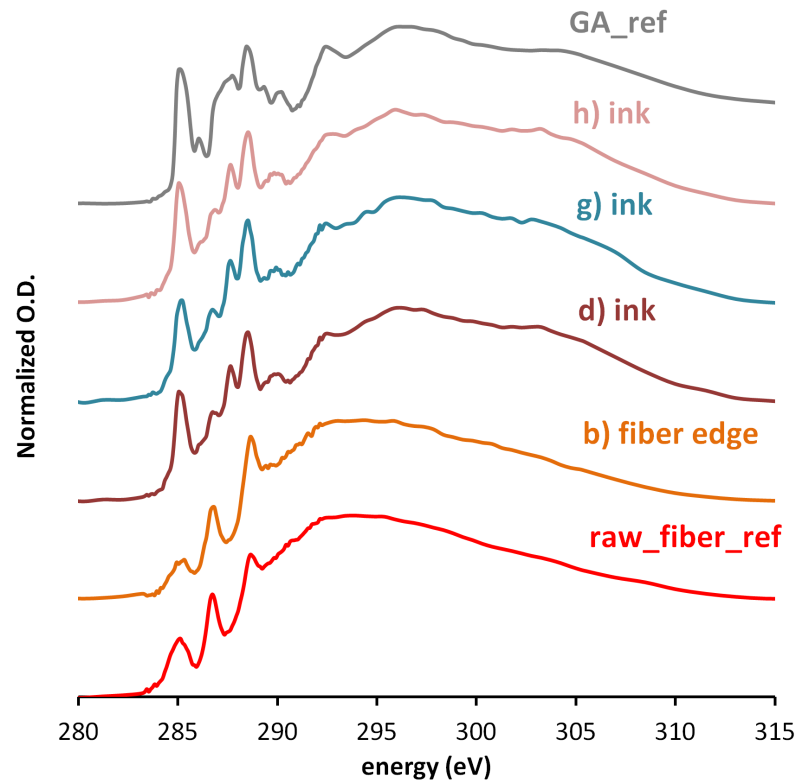


FIG. IV.37 – Comparison of C K-edges spectra recorded in different regions of the  $gel_4 + ink_R$  fiber. The spectra colors correspond to those of the dashed areas of FIG. IV.36.

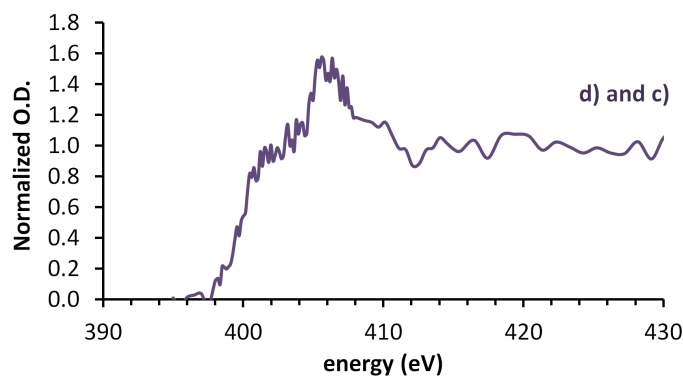


FIG. IV.38 – *N K-edge spectrum extracted from inked regions c and d in an enlarged area of the  $gel_A + ink_R$  fiber (see FIG. IV.36).*

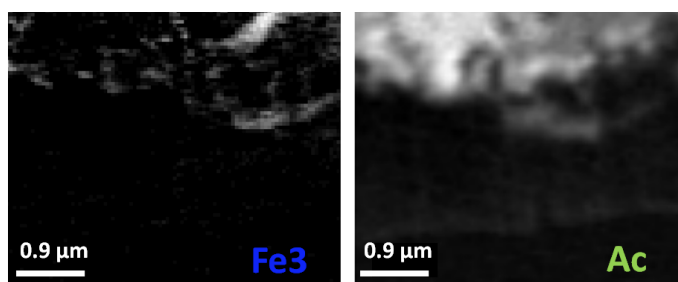


FIG. IV.39 – *Comparison of  $Fe(III)$  and gallic acid distribution on the enlarged area of  $gel_A + ink_R$  fiber.*

may behave differently; N K-edge analysis supports this hypothesis as no significant concentration of nitrogen was found on the whole sample (FIG. IV.38);

- the gelatin specific feature at 288.4 eV overlaps the signatures of other components, meaning that gelatin may easily go unnoticed if it is a minor component.

This latter point also prevails for the iron gall ink precipitate which signature was not detected: if it is present in minor quantity, its specific signature at 288.4 eV could easily be mixed up with other signatures.

Several stack fits of the data were attempted considering different available model spectra. The most conclusive, shown on FIG. IV.35 (RGB map) corresponds to a clear discrimination between cellulose and gallic acid, meaning that this latter does not penetrate the fiber but remains instead at the surface. It is not necessarily associated with iron(III) rich areas: on FIG. IV.39, the bright areas of the gallic acid component map are not always correlated with bright areas of  $Fe(III)$  distribution map. At the edge of the fiber, a small penetration of iron(II) is seen on a depth of approx.  $0.5 \mu m$  (FIG. IV.36, area b). It corresponds to a maximum *O.D.* of 0.07, a value close to 0.05 that was measured in the inner part of the *Ink<sub>R</sub>* fiber (see part IV.5.2 and FIG. IV.40, orange and red curves).

These two values are much higher than the maximum *O.D.* found in the inner part of the *gel + ink<sub>R</sub>* sample (FIG. IV.36, area a and FIG. IV.40, green curve), meaning that the former presence of gelatin significantly prevented migration of iron in the fiber.

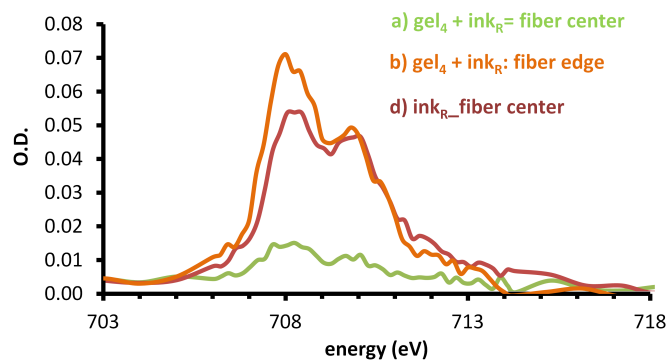


FIG. IV.40 – Comparison of Fe K-edge spectra on the  $ink_R$  fiber and  $gel_4 + ink_R$  fiber.



### Effect of gelatin size on ink distribution

Surprisingly, gelatin was not evidenced at the C and N K-edges on the  $gel + ink_R$  sample. This could be due to its dissociation from the fiber in the ink impregnation solution, and also to a heterogeneous distribution of gelatin along the fiber. However the gelatin size seemed to have significantly limited gallic acid and iron migration inside the fiber. It also may have influenced the ink chemistry as no iron gall ink precipitate was detected. Organic matter signatures suggested a pure cellulose fiber coated with a gallic acid rich deposit presenting an heterogeneous distribution in iron(II) and iron(III). Although, ink has been prepared three days before impregnation to ensure enough precipitate formation, no iron gall ink precipitate was detected. This fact may be accounted firstly by an heterogeneous distribution around the fiber and secondly by the fact that gelatin is known to bind iron [255, 256, 257] which could efficiently compete precipitation with gallic acid.

#### IV.5.4 The impact of a gelatin top layer on ink distribution

A previous study has shown that spraying gelatin on an inked paper can slow down the depolymerisation process [258]. The  $ink_R + gel_4$  fiber was prepared to investigate possible interactions between ink and gelatin. It is of interest for conservation purposes, as gelatin is often applied on inked areas during conservation treatments.

In the SEM image of the  $ink_R + gel_4$  fiber cross-section, three fibers can be distinguished (FIG. IV.41, numbers 1 to 3). Even if the lower part of the foil was damaged by the FIB milling, the upper part was appropriate for STXM analysis. Mapping at different edges allowed a quick differentiation of components: gelatin is highlighted at energies 401 eV (N K-edge) and 288.3 eV (C K-edge) while cellulose is mainly responsive at 286.7 eV (C K-edge). Maps recorded at these three energies clearly evidenced that gelatin does not penetrate the cellulosic fiber (FIG. IV.41) consistent with what was observed on  $gel$  fibers (section IV.5.1b). Interestingly, gelatin seems to fill in the lumen of fiber 2 probably because this fiber was initially opened on one end, allowing gelatin solution to migrate in the lumen along the fiber axis. The small cellulose rich area situated between fiber 1 and fiber 2 probably corresponds to some fibrillated cellulosic matter partially detached from its original fiber. Maps recorded at the Fe L-edge show that the gelatin rich areas contain more iron than the inner part of the fibers. They also evidence gelatin embedded bright spots that are rich in iron.

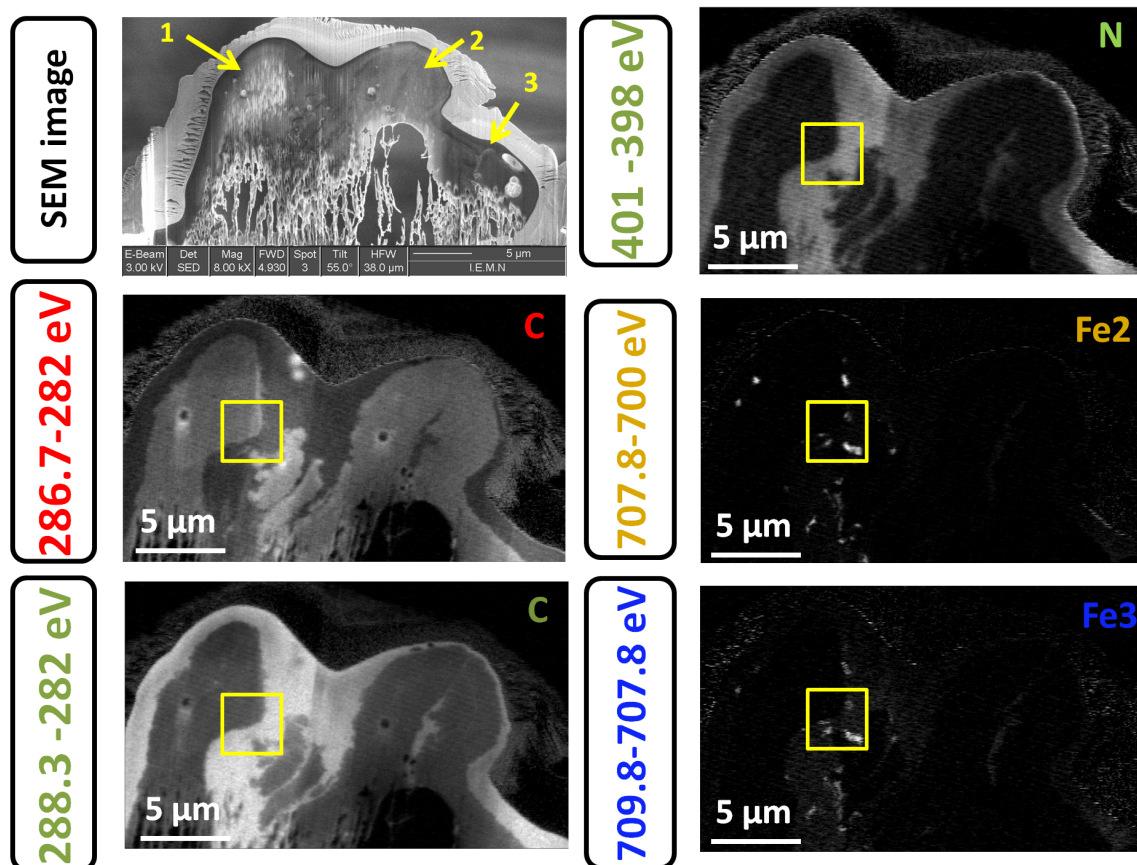


FIG. IV.41 – Comparison of  $N$ ,  $C$  and  $Fe$  K-edges maps on  $ink_R + gel_4$  fiber.

A small region including the main features as those mentioned above (cellulose, gelatin, bright iron spots) was chosen for complete stack recording (FIG. IV.42 and IV.43). No iron was detected in the inner part of the fiber (FIG. IV.43, area a) whereas some iron was present in the gelatin coating, mostly as iron(III) (FIG. IV.43, area a). Iron rich spots were assigned to a combination of iron(III) and iron(II) (FIG. IV.43, area b). Besides, the  $C$  K-edge signature of these spots is consistent with a combination of gelatin and presence of iron gall ink precipitate (FIG. IV.44). A stack fit treatment of the data was performed at the  $C$  K-edge with extracted spectra (from three regions: fiber center, between fibers and dots) shows the repartition of the three phases (FIG. IV.44). Apart from the lower part of the map, no high residual component is observed suggesting only three major components. Another stack fit with available model spectra of the raw fiber, gelatin and iron gall ink precipitate showed the same repartition (FIG. IV.42, RGB map) and confirmed the presence of iron gall ink precipitate. Unlike what was observed on the  $gel_4 + ink_R$  fiber, no gallic acid was evidenced on the  $ink_R + gel_4$  fiber. Complete consumption of gallic acid in the precipitate formation is relatively unlikely. The non-detection of gallic acid more probably means that this component is not localized on specific spots but instead diluted in cellulose or gelatin and thus remains under the limit of detection.

The non-detection of iron in the inner part of the fiber was completely unexpected since small concentrations of iron were detected in the inner part of previously analyzed fibers ( $ink_R$  and  $gel_4 + ink_R$ ), mainly corresponding to a mixture of iron(II) and iron(III). On the  $ink_R + gel_4$  fiber, gelatin was sprayed after ink impregnation and, iron gall ink

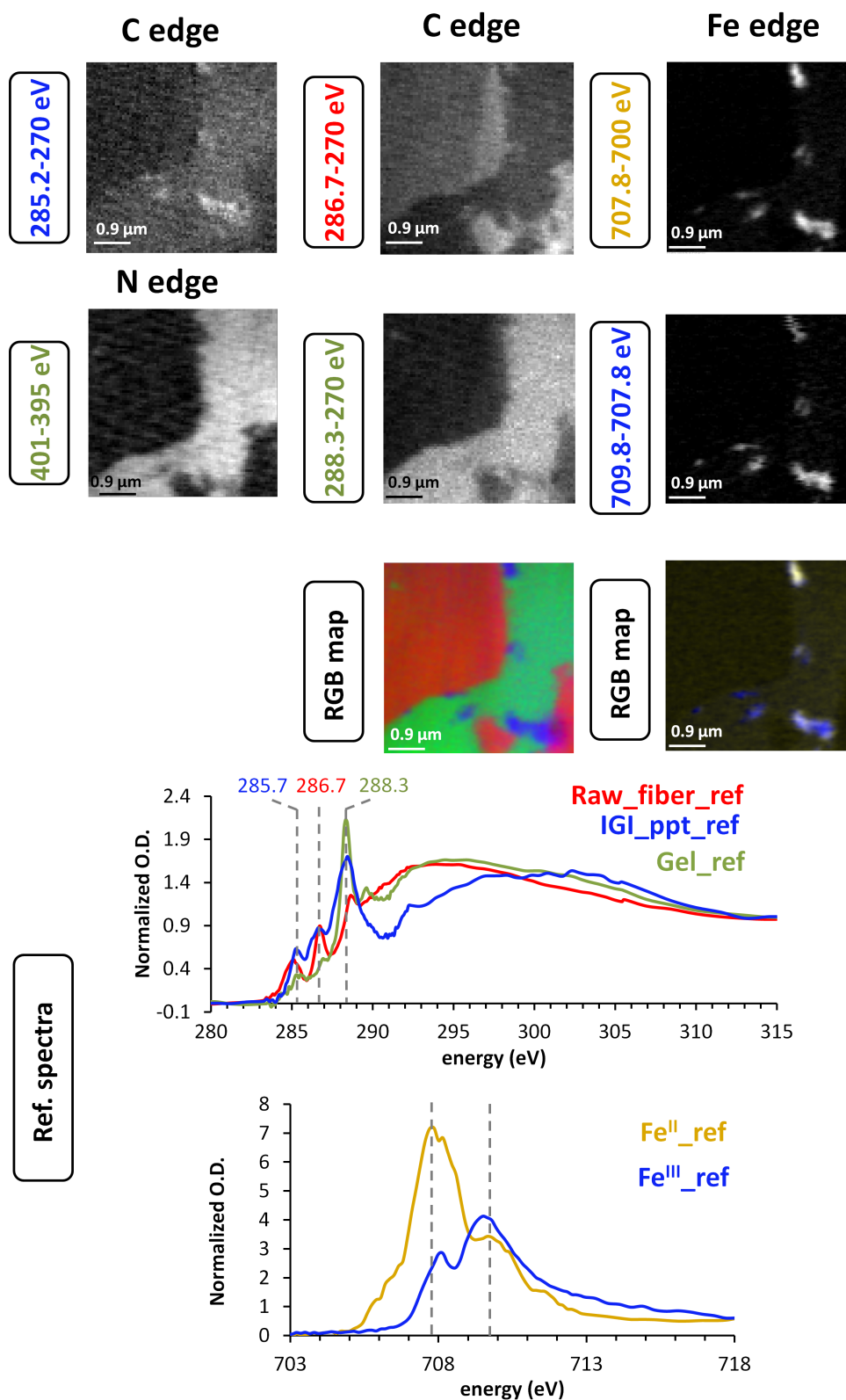


FIG. IV.42 – Comparison of *N*, *C* and *Fe* *K*-edges maps on *ink<sub>R</sub>* + *gel<sub>4</sub>* fiber. Gelatin is represented in green and located in the central part of the image. Cellulose is shown in red and the iron gall ink precipitate in blue.

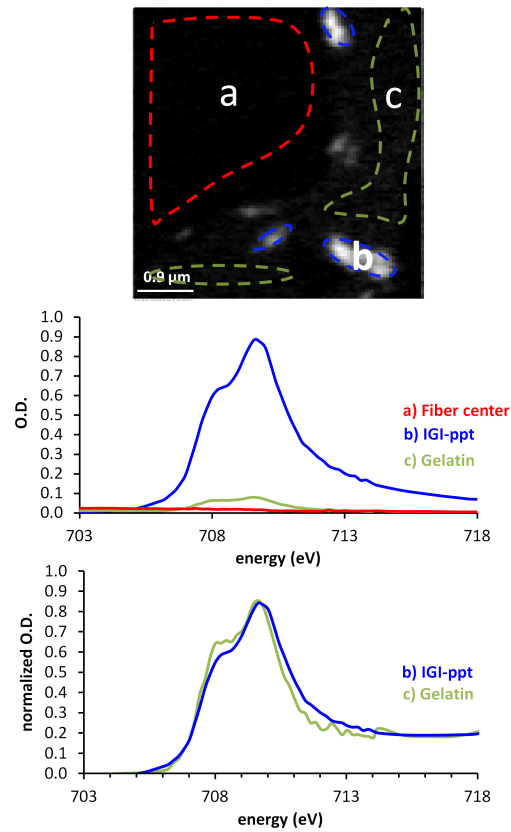


FIG. IV.43 – Comparison of Fe L-edge spectra extracted from the dashed areas on  $ink_R + gel_4$  fiber. The spectra colors correspond to those of the dashed areas.

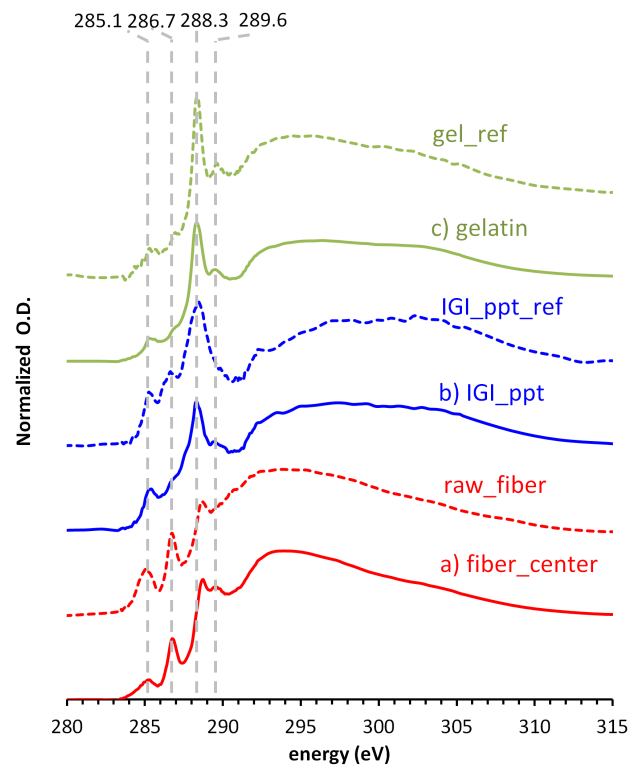


FIG. IV.44 – Comparison of C K-edge spectra on  $ink_R + gel_4$  fiber. The spectra colors correspond to those of the dashed areas of FIG. IV.43.

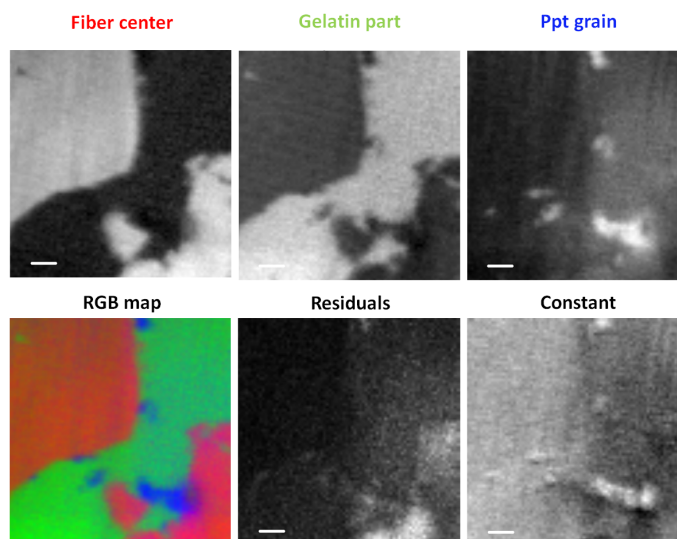


FIG. IV.45 – Component maps of  $ink_R + gel_4$  fiber obtained with a stack fit at C K-edge using extracted spectra.

precipitate apart, iron is distributed relatively homogeneously in the gelatin coating as iron(III) mainly. These observations suggest iron migration occurs during humidification: iron that is not involved in the IGI precipitate is indeed known to be highly water soluble [51, 259]. During gelatin spraying, gelatin remains outside the fiber, but water migrates inside, thus allowing dissolution and migration of iron. The high predominance of iron(III) in gelatin suggests occurrence of oxidation reactions occurring during the migration or fixation on gelatin. This is consistent with the ability of gelatin to chelate iron ([255, 260, 219, 257]). These chelation mechanisms may have favored iron migration by entropic effect thus lowering iron concentration in the inner part of the fiber below the limit of detection.



#### Effect of a gelatin spray on ink impregnated fibers

STXM analysis of  $ink_R + gel_4$  fiber evidenced a clear distribution of gelatin layer outside the cellulosic fiber. Although no gelatin was detected inside the fiber, it has an impact on iron distribution. Indeed, some iron(III) clusters are present in the gelatin around the fiber and present C K-edge signatures that could match iron gall ink precipitate. Apart from these clusters, iron is also present in the gelatin, consistent with its iron chelation abilities. However, inside the fiber no iron is noticed although no size was done prior inking. Gelatin spray could have favoured the iron migration outside the fiber. This behaviour could explain the former observations at a macro-scale on inked paper on which a slower depolymerization was observed after gelatin application [258].

## IV.6 Conclusion

At a macro-scale the size quality of a paper directly impacts its water permeability. Therefore a paper that is well sized will be more resistant to ink penetration and also less subjected to iron gall ink corrosion. However, there is little understanding about the parameters that make a size work while another does not. To this respect, the size distribution in the paper, and more specifically in fibers, is a key point that was in the focus of

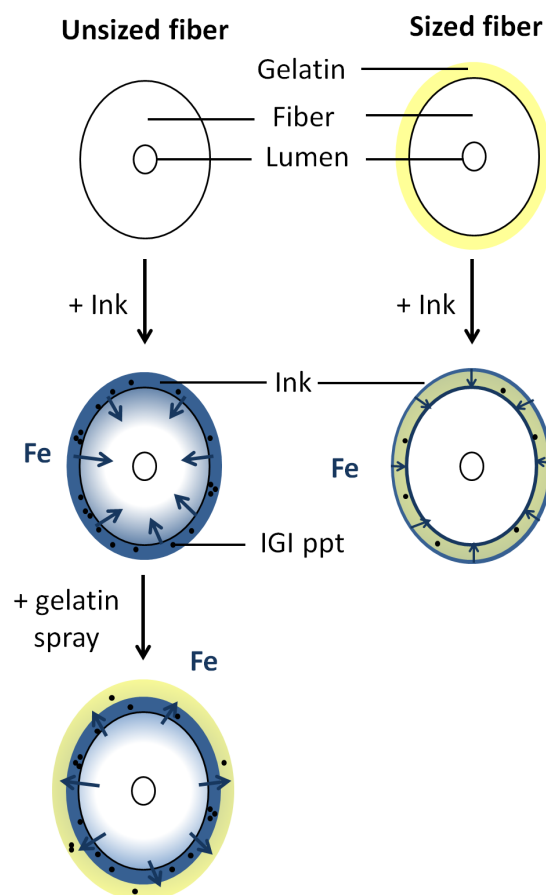


FIG. IV.46 – Scheme of fiber cross-section, and its behaviour upon ink impregnation depending on the fiber type (sized or unsized). Effect of gelatin application on the diffusion of iron in an inked fiber.

this chapter. The aim of this study was therefore to investigate at a nano-scale the distribution of gelatin and ink components in a paper fiber. For this purpose, two techniques of sample cross-section preparation (ultramicrotomy and FIB) were investigated along with two imaging techniques (AFM-IR and STXM). Preparing cross sections by ultramicrotomy without embedding the sample in a polymeric resin turned out to be damaging for the samples. In addition, samples were in this case not perfectly flat and this resulted in a non-uniform adhesion to the AFM-IR crystal, which compromised the interpretation of the measurements. Using this cutting technique was finally not conclusive.

FIB milling was successfully chosen as another option to prepare samples for STXM analysis. This technique proved to be effective to study the distribution of gelatin and the migration of ink components into a fiber. XANES spectroscopy at the C K-edges made it possible to map the distribution of cellulose, gelatin, gallic acid and ink precipitate on the prepared cross sections. Complementary measurements were performed at the N K-edge to confirm distribution of gelatin, and at the Fe L-edge to map iron distribution and speciation. The photo-reduction of iron under the beam was measured and in some way, managed, but speciation of iron(II) and iron(III) remained qualitative. The use of a cryo-system to cool down the sample could be attempted in a further study to limit this photo-reduction. Although preventing damage using low temperature is not always assured, as was shown by Beetz and Jacobsen [261] on PMMA samples. Besides, the distribution of gelatin or other components was sometimes difficult to assess due to their weak concentration.

The FIG. 1 sums up our observations. When the fiber was not sized (FIG. 1, left middle scheme), the ink mostly formed an outside layer including some iron clusters. The exact nature of these clusters could not be assessed because they did not show a specific C K-edge signature. They might correspond to iron sulfate. More interestingly, some iron (most probably free iron II) was able to penetrate inside the fiber. It was homogeneously distributed at low concentration inside the fiber, but spots of high concentration in iron were also found along cracks. This distribution of iron probably promotes low pH values inside the fiber and causes acid hydrolysis, along with some oxidation. On sized fibers, gelatin was found to stay around the fiber and no trace of it was evidenced inside the fiber (FIG. 1, right top scheme). When the fiber is additionally inked (FIG. 1, right middle scheme), no gelatin was anymore detected on the cross section most probably because most of it was detached in the ink bath during impregnation. The remaining gelatin is probably too diluted in the ink (iron sulfate/gallic acid mixture) layer to be detected. Although gelatin was not evidenced, iron penetrates much less inside the fiber. This could come from a chelation with gelatin that slows down its penetration inside the fiber. Indeed gelatin bears carboxylate groups which can interact with iron(II) and iron(III). Besides, while spraying gelatin on an inked fiber (FIG. 1, left bottom scheme), the iron concentration inside the fiber was much reduced which is coherent with a slower degradation of cellulose previously observed on paper samples [219, 258]. Some hypothesis has been proposed to explain this behavior but they require further confirmations. All these conclusions are drawn based on examination of one cross-section per sample type. To go further, it would be interesting to duplicate some of the cross sections since fibers are expected to show some heterogeneity. It would be also interesting to work at the S K-Edge to estimate possible migrations of sulfate in the fibers.

Studying other samples would be useful as well to answer many other questions : How is the distribution of iron/ink components on an ancient sample? Is it similar to what was observed on our freshly prepared model samples? Do the ink components penetrate differently if they are used in combination (as ink) or alone? How does the age of the ink influence the ink components distribution inside a fiber? Does the gelatin spray have the same effect on an old ink? This will imply preparing cross-sections of ancient inked fibers before or after gelatin impregnation, of a fiber impregnated with gallic acid or iron sulfate only, etc.. Some of those samples are already prepared but have not been analyzed yet due to limited beam time allocation. Whatever the questions that still remain open, this study clearly establishes the fact that iron has the capacity to deeply penetrate in paper fibers, while gelatin cannot and remains at the surface.



# Conclusion

The iron gall inks being both acidic and rich in iron, two main mechanisms, acid-catalyzed hydrolysis and radical oxidation, are currently proposed in literature to explain the depolymerisation of papers. Among radicals, hydroxyl ones are often put forward as responsible for the degradation due to Fenton reaction. Although their impact has been demonstrated in alkaline media, their occurrence in acidic conditions is still questionable. In this thesis, three complementary approaches have been developed in order to clarify the mechanisms at stake in the case of iron gall ink corrosion.

Previous experiments [111] highlighted that the combination of both iron(II) and oxygen is a key parameter inducing depolymerisation, suggesting that cellulose oxidation is not negligible. This was next confirmed by a measurement showing in aged inked papers carbonyl groups due to oxidation (Appendix IV.6). These previous results led us to investigate the reactive oxygen species possibly involved in paper depolymerisation by radical oxidation.

A particular attention was focused on their identification by electron spin resonance spectroscopy and high performance liquid chromatography. The first technique was used both in solid and liquid states. The direct analysis with solid state ESR of paper samples impregnated with ink or iron(II) sulfate did not show the presence of organic radicals. Only paramagnetic iron(III) was observed, in pseudo-octahedral (hydrated complex) or rhombic environment, attributable to complexes of iron(III) with carboxylic and hydroxylic cellulose groups. This could favor the degradation of cellulose in their surroundings. ESR in liquid state was carried out with spin-traps (particularly DMPO) put in contact with paper samples in a solution. No hydroxyl radicals, nor superoxyl or hydroperoxyl radicals were detected with the spin-trap alone. However other experiments with an added target molecule (formate) led to a significant ESR signal, which could arise from the sum of different species. According to complementary tests, this signal was due iron(II) ions in solution leached by the paper and depended on iron(II) concentration and oxygen. It did not arise from hydroxyl radicals as demonstrated by HPLC-TPA method that revealed their presence, but at a very low concentration, and only in the case of iron sulfate paper samples.

A significant amount of ROS different from hydroxyl radicals being formed in the ink/iron sulfate solutions, they could be at the origin of bond breaking. In order to investigate more in details the possible mechanisms involved, kinetics of depolymerisation of inked paper was studied. To our knowledge, this had never been undertaken. Viscosity and zero-span measurements were done at different temperatures and activation energies were estimated. The rate constants measured on inked impregnated papers were one or two orders of magnitude higher than those measured on acidic blank (iron free) paper. Yet the activation energies were close from the values proposed in the literature for acid hydroly-

sis although slightly below. This suggested a predominant acid hydrolysis mechanism with a small catalytic effect of iron. This study was completed by tests on a model molecule, cellobiose, to explore the effect of iron presence, pH and oxygen. The degradation was monitored by capillary electrophoresis and infrared spectroscopy. The key parameter for glycosidic scission was found to be pH. For this system, the impact of iron and oxygen is indirect since iron oxidation leads to an acidification that provokes the osidic scission (glucose production). Compared to sulphuric acid, iron sulfate induced the formation of other by-products bearing C=O functions, probably due to glucose degradation.

The low pH (1.5) reached in the presence of both iron and oxygen during cellobiose degradation experiments was far away from pH (3-4) of iron-impregnated papers determined by water extraction. This led us to envisage that iron enriched spots could exist in the fibers and generate localized acidity. This hypothesis of an inhomogeneous iron distribution in the paper was investigated by scanning transmission X-ray microscopy (STXM). The distribution of the ink components and gelatin in FIB cross-sections of rag paper fibers were studied, together with the effect of gelatin size on iron penetration. The use of another technique, namely AFM-IR carried out on microtomy cross-sections, was also attempted to study gelatin distribution, but rapidly abandoned because samples preparation was too tricky. For an unsized fiber, iron was found to penetrate inside the fiber while the penetration was reduced in the case of gelatin sized fibers. In unsized fibers, iron also forms small clusters along existing cracks that could give some explanation for low local pH values. These observations are consistent with a predominant acid hydrolysis mechanism that is initiated locally through iron oxidation. Cellulose oxidation also occurs and it could favor the attachment of iron to the fibers. However, it remains a secondary mechanism.

As a whole, the STXM technique proved to be highly effective for mapping elemental speciation inside fibers at the nanoscale, thus giving a deep insight in the physical behavior of the ink when it is put in contact with paper fibers. The distribution of gelatin, gallic acid, iron(II) and iron(III) gave key information to understand the physical and chemical mechanism of iron gall ink corrosion. In the near future, scanning at the S K-edge is foreseen so as to better understand the role of sulfates that may favor the transport of protons via the formation of hydrogenosulfate ions.

# Appendices



# Appendix A

## Carbonyl content analysis

;

**Universität für Bodenkultur Wien**  
University of Natural Resources and Applied Life Sciences, Vienna



Ao. Univ. Prof. Dr. Antje Potthast  
Dr. nat.techn. Dipl. Rest. Ute Henniges  
Department für Chemie  
Abteilung für Organische Chemie  
Muthgasse 18  
A-1190 Wien  
antje.potthast@boku.ac.at  
phone:0043-1-36006-6071  
fax: 0043-1-36006-6059

## REPORT

### DETERMINATION OF CARBONYL GROUPS IN PULPS BY CCOA<sup>1-3</sup>

Name: Véronique Rouchon  
Company: Muséum National d'Histoire Naturelle  
Department: Centre de Recherche sur la Conservation des Collections (CRCC)  
Address: 36 rue Saint Hilaire, 75005 Paris  
Phone: +33 1 40 79 53 03  
Fax:

Sample in: 03.06.2009  
Sample out:

The following samples were analysed:

Sample ID	Treatment	Aging	Mw kg/mol	Mn kg/mol	Mz kg/mol	PDI Mw/Mn
WM_Ref	none	none	533	372	739	1.45
267_N2	Fe(II)sulphate	1 day	496	356	650	1.80
268_N2	Fe(II)sulphate + gallic acid	1 day	351	229	491	1.93
241_N2	Fe(II)sulphate	120 days	443	285	690	1.44
242_N2	Fe(II)sulphate + gallic acid	120 days	250	168	358	1.48
267_O2	Fe(II)sulphate	1 day	474	329	669	1.40
268_O2	Fe(II)sulphate + gallic acid	1 day	339	234	465	1.54
241_O2	Fe(II)sulphate	120 days	243	135	407	1.56
242_O2	Fe(II)sulphate + gallic acid	120 days	71	37	112	1.43

Table 1: Overview of molecular weight data.



Sample ID	Treatment	Aging	C=O [ $\mu\text{mol/g}$ ]	REG [ $\mu\text{mol/g}$ ]	C=O – REG [ $\mu\text{mol/g}$ ]	Interpretation
WM_Ref	none	none	1.6	2.7	-1.1	no oxidation
267_N2	Fe(II)sulphate	1 day	2.6	2.8	-0.2	no oxidation
268_N2	Fe(II)sulphate + gallic acid	1 day	3.9	4.4	-0.5	no oxidation
241_N2	Fe(II)sulphate	120 days	3.3	3.5	-0.2	no oxidation
242_N2	Fe(II)sulphate + gallic acid	120 days	9.3	5.9	3.4	some oxidation
267_O2	Fe(II)sulphate	1 day	3.0	3.0	0.0	no oxidation
268_O2	Fe(II)sulphate + gallic acid	1 day	5.4	4.3	1.1	some oxidation
241_O2	Fe(II)sulphate	120 days	10.0	7.4	2.6	some oxidation
242_O2	Fe(II)sulphate + gallic acid	120 days	44.6	27.1	17.5	oxidation

Table 2. Overview of carbonyl group data.

## Results

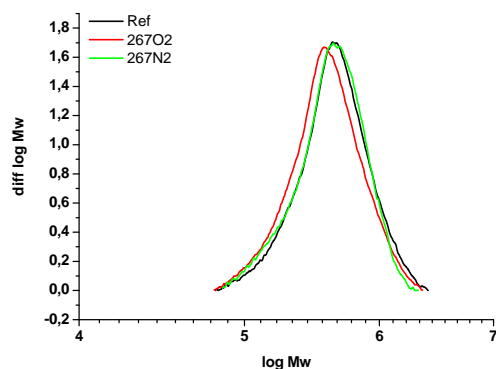


Figure 1: Differential molecular weight distribution of the samples with iron(II)sulphate solution (1 day of aging). There is a small but significant degradation when the iron(II)sulphate sample was stored in oxygen containing atmosphere, while no change compared to the reference has occurred on paper stored under nitrogen.

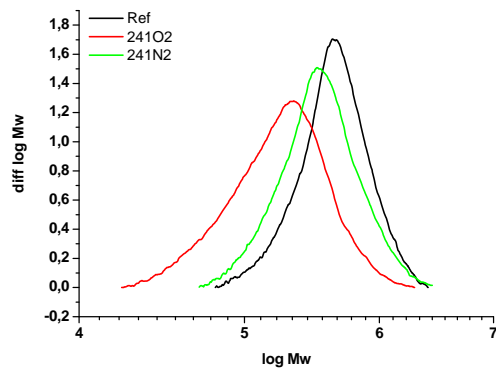


Figure 2: Differential molecular weight distribution of the samples with iron(II)sulphate solution (120 days of aging). The iron(II)sulphate will cause degradation in both cases, with and without oxygen. However, the cellulose degradation is by far more pronounced in the oxygen containing atmosphere.

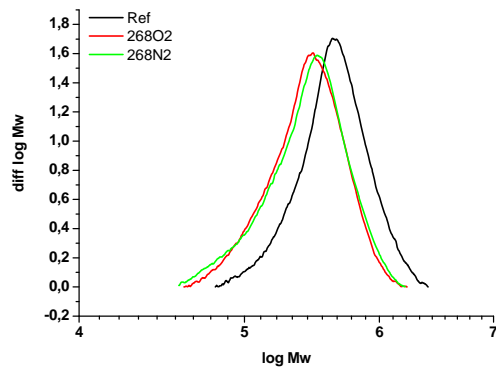


Figure 3: Differential molecular weight distribution of the samples with a mixture of iron(II)sulphate and gallic acid solution (one day of aging). Both samples, with and without oxygen, suffer from a very rapid cellulose degradation. There is no difference between the two sample modifications at this stage of the experiment.

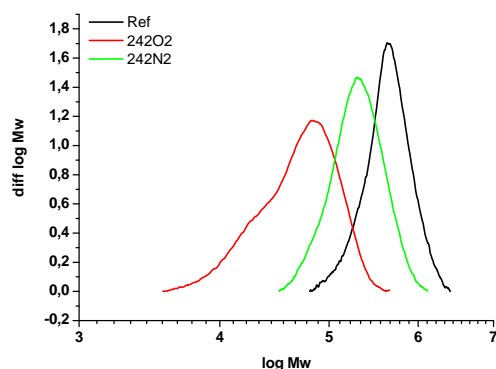


Figure 4: Differential molecular weight distribution of the samples with a mixture of iron(II)sulphate and gallic acid solution (120 days of aging). While the cellulose degradation in the oxygen-free atmosphere only slowly proceeds in the course of aging, the sample that was allowed to be in contact with oxygen suffers from severe cellulose degradation. A shoulder starts to develop in the low molecular weight region of the sample stored in oxygen atmosphere.

### Summary

The molecular weight distributions show clearly that an oxygen-free environment prevents cellulose from degradation in terms of chain scission and oxidation. When the samples were stored under nitrogen hardly any oxidation occurs. Combining iron(II)sulphate and gallic acid, however, leads to significant chain scission and even some oxidation despite of the oxygen-free storage and aging.

When the contact of oxygen is allowed the degradation of the cellulose is very pronounced in both cases, chain scission and development of carbonyl groups. Especially the aging of cellulose in contact with iron(II)sulphate and gallic acid leads to a severe chain scission accompanied with strong oxidation of the cellulose.

The combination of iron(II)sulphate and gallic acid has an immediate effect on the cellulose that can be detected even after one single day of storage regardless of with or without oxygen.



Please do not hesitate to contact us for further information.

With kind regards

---

A. Potthast  
U. Henniges

**References:**

- [1] J. Röhring, A. Potthast, T. Rosenau, T. Lange, G. Ebner, H. Sixta, P. Kosma, *Biomacromolecules* **2002**, *3*, 959-968. A novel method for the determination of carbonyl groups in celluloses by fluorescence labeling. 1. Method development.
- [2] J. Röhring, A. Potthast, T. Rosenau, T. Lange, A. Borgards, H. Sixta, P. Kosma, *Biomacromolecules* **2002**, *3*, 969-975. A novel method for the determination of carbonyl groups in celluloses by fluorescence labeling. 2. Validation and application.
- [3] A. Potthast, J. Röhring, T. Rosenau, A. Borgards, H. Sixta, P. Kosma, *Biomacromolecules* **2003**, *4*, 743-749. A novel method for the determination of carbonyl groups in celluloses by fluorescence labeling. 3. Monitoring oxidative processes.



# Appendix B

## ESR spectroscopy

### B.1 ESR principle

As for all spectroscopic techniques, energy exchange between radiation and matter happens only if there are interactions between the electromagnetic field and the matter elementary entity, and if the photon energy equal the energy difference between two spin levels.

When these conditions are fulfilled, interactions lead to transitions associated to an energy absorption which can be detected and measured. A spectrum is composed of absorption bands containing informations about the samples: its shape reflects energy levels transitions and gives information about the nature and configuration of the compounds; the intensity is proportionnal to the concentrations in the sample in liquid state (when the power has been well chosen).

ESR is based on the interaction of paramagnetic entities with the magnetic component of the electromagnetic field. Those paramagnetic entities can be atoms or molecules having unpaired electrons such as free radicals or complex of transition ions.

When a paramagnetic specie has an energy without any magnetic field, the magnetic moment ( $\mu$ ) is given by:

$$\mu = -g\beta S \quad (\text{B.1})$$

With  $\beta$  a constant called Bohr magneton ( $9.2741 \cdot 10^{-24} \text{ J} \cdot \text{T}^{-1}$ ),  $g$  factor, a positive number which is characteristic of the paramagnetic specie and  $S$  the angular momentum respecting:

$$S^2 = S \cdot (S + 1) \quad (\text{B.2})$$

$S$  is called the spin of the paramagnetic specie although it is not always determined by angular momentum of electron spin.

When a paramagnetic specie is put in a magnetic field, the interaction energy is given by:

$$H = -\mu \cdot B = g\beta S \cdot B \quad (\text{B.3})$$

Which gives by projection onto z axis:

$$H = g\beta B S_z \quad (\text{B.4})$$

in which  $S_z$  is the projection of  $S$  on z axis can take one of these  $(2S + 1)$  values. Since  $S_z$  is quantified,  $H$  is quantified.

Interaction between a magnetic moment and a magnetic field produces a splitting of

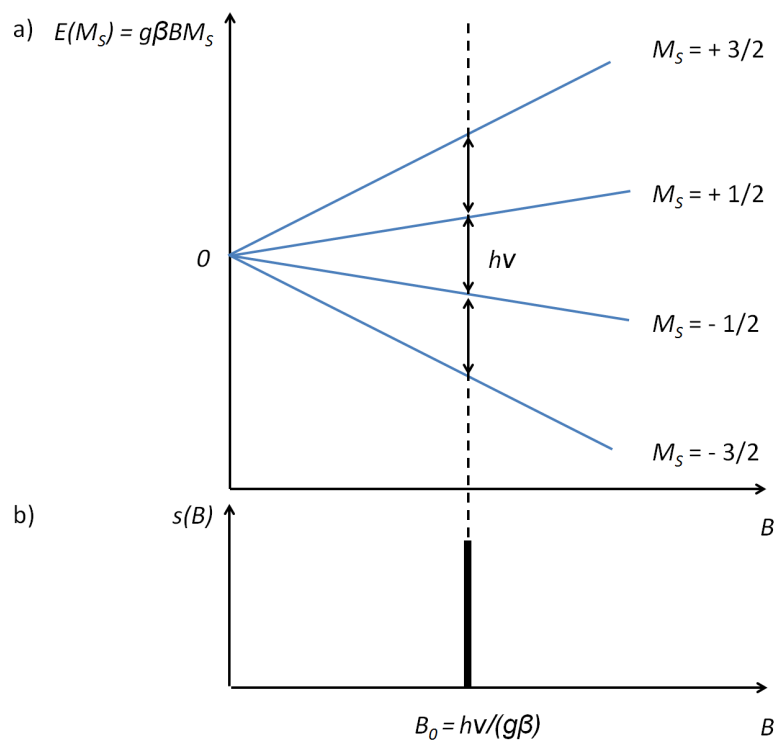


FIG. B.1 – a) Splitting of energy levels of a paramagnetic specie with  $S = \frac{3}{2}$  and evolution with  $B$  magnetic field. b) Formation of an absorption signal at the field of resonance  $B_0$ . Adapted from [262].

the energies levels (Zeeman effect) centered on the level of energy of the paramagnetic specie without a magnetic field (FIG. B.1).

$$E(M_S) = g\beta BM_S \quad (\text{B.5})$$

When another electromagnetic radiation of  $\nu$  frequency is applied on the sample, transition between two adjacent levels can be observed if photons energy matches the difference of energy between the levels. In ESR experiment, due to technical reasons, the frequency  $\nu$  (in the microwave domain (GHz)) stays constant and the  $B$  value is changed. The application of the electromagnetic radiation of  $\nu$  frequency lead to the absorption giving one resonance band at  $B_0$  value (resonance field).

## B.2 Hyperfine coupling

In the previous section, an example of the interaction of a paramagnetic specie of spin  $S$  and moment  $\mu$  with a magnetic field  $B$  was given. The resulting spectrum was a unique line centered on  $B_0$ . Hopefully, real spectra give more information on the structure due, for example, to the hyperfine coupling of the electron with the magnetic moment of nuclei. For free radicals, the unpaired electron is in an orbital delocalized on several atoms and it can interact with several paramagnetic nuclei ( $^1\text{H}$ ,  $^{13}\text{C}$ ,  $^{14}\text{N}$ ,  $^{19}\text{F}$  or  $^{31}\text{P}$ ).

In liquid state, molecules such as nitroxides take quickly all possible orientations. This is called the isotropic state. All the parameters are average values. The interaction

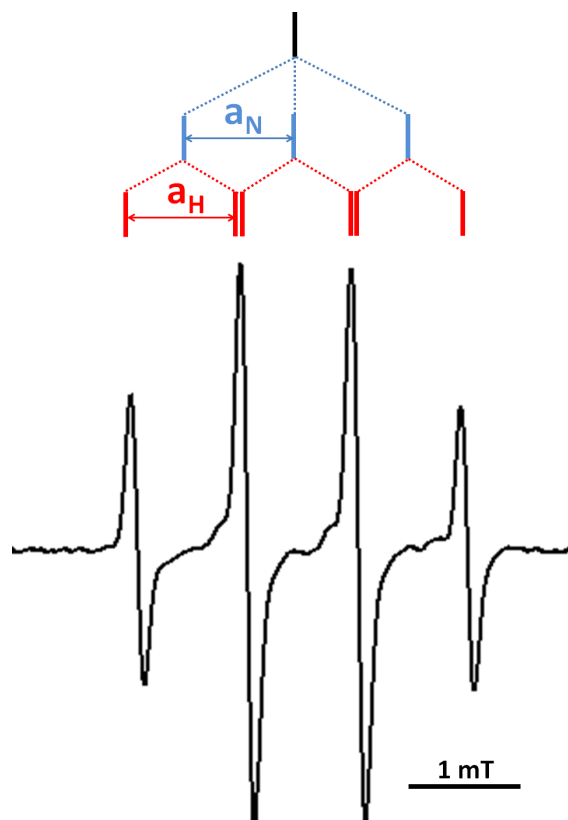


FIG. B.2 – Spectrum of the DMPO – OH<sup>•</sup> adduct due to hyperfine coupling leading to lines splitting.

between unpaired electrons and a nucleus of spin  $I$  is also isotropic and expressed as:

$$H_{\text{hyperfine}} = AS \cdot I + g\beta S \cdot B \quad (\text{B.6})$$

with  $A$  the hyperfine constant (MHz). With spin-trapping, another parameter,  $a$ , is favored to measure the distance between hyperfine lines:

$$a = \frac{A_{\text{iso}}}{g_{\text{iso}} \cdot \beta} \quad (\text{B.7})$$

$a$  is expressed in gauss (G) or milli tesla (mT).  $g_{\text{iso}}$  is determined by measuring the field in the center of the spectrum. For nitroxides spin-traps, this value is around 2.006 and gives few information about the radicals structure. If we take the example of a nitroxide spin-trap, such as DMPO, it gives a four line spectrum of (1:2:2:1) intensities with hydroxyl radicals (FIG. B.2). This is due to the coupling of the nitroxide radical with the neighbour nitrogen atom (3 lines of same intensity) and to the coupling with the hydrogen atom in  $\beta$  of the nitrogen which divides each lines in two. Since the coupling constants are almost equal, we do not observe a six lines spectrum of same intensities but a four lines spectrum due to the superimposition of the central lines. For the DMPO – CO<sub>2</sub><sup>-</sup> adduct, six lines of same intensity are observed (FIG. II.9) due to different coupling constants.

### B.3 Spin-trapping artefacts

Although spin-trapping is a really usefull technique, some caution should be taken when attributting the signal observed to a radical. Indeed, other reactions than spin-trapping

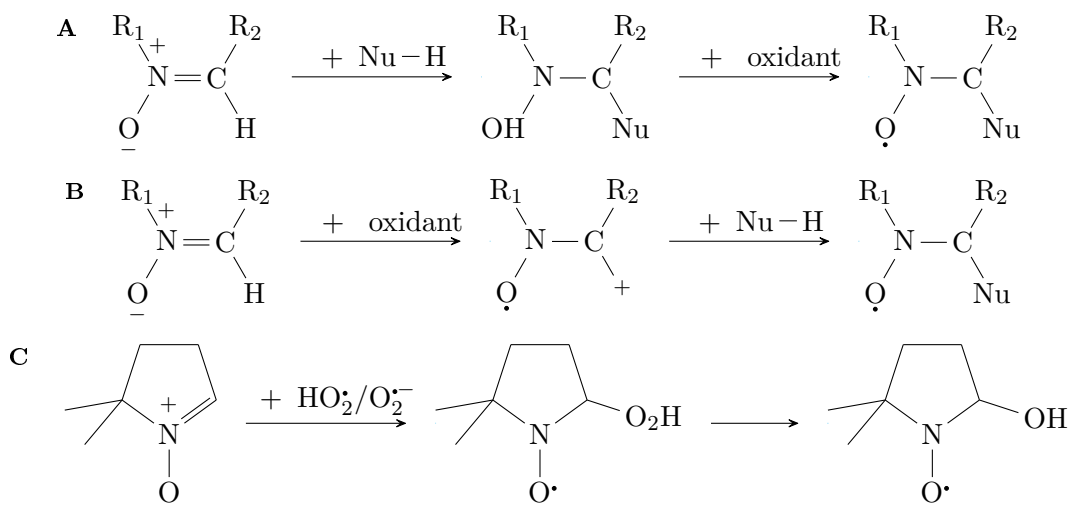


FIG. B.3 – Main artefact reactions with spin-trapping: (A) Forrester-Hepburn mechanism, (B) inversed spin-trapping and (C) DMPO adduct decomposition after superoxide trapping.

can lead to the formation of paramagnetic adducts without any radicals involved [263]:

- The Forrester-Hepburn mechanism (FIG. B.3A) consists in the addition of a nucleophile on the spin-trap to form an hydroxylamine, followed by its oxidation. This reaction can be favored in aqueous medium especially in presence of metallic ions which can activate the nitron function by complexation. This is one of the artefact that can lead to  $\text{DMPO-OH}\cdot$  by water addition, without hydroxyl radicals trapping.
- The inversed spin-trapping (FIG. B.3B) is another artefact leading to adducts formation without spin-trapping. This reaction is an oxidation of the spin-trap followed by a nucleophile attack of the formed carbocation. It can happen when strong oxidants or UV radiation are used.
- The DMPO spin trap forms with superoxide anion or hydroperoxyl radicals an adduct that will decompose into  $\text{DMPO-OH}\cdot$  (FIG. B.3C).

## B.4 Complementary tests to investigate hydroxyl radicals

### B.4.1 Tests using POBN

As presented in chapter II,  $\text{HO}\cdot$  were not detected in our ESR experiments. In order to ensure absence of artefacts, complementary experiments were performed. The first idea we tried to attest the presence of hydroxyl radicals was to use the POBN spin-trap and its decomposition into other spin-trap (MNP) upon reaction with hydroxyl radicals (FIG. B.4). Indeed, by adding a target molecule such as methanol, MNP could react with the  $\text{HO-CH}_2$  radical formed in the medium and give an adduct with a different signature than  $\text{POBN-CH}_2\text{OH}\cdot$ .

Prior to this attempt on our samples, experiments were conducted with Fenton system to test the feasibility. With such system, the  $\text{POBN-OH}\cdot$  adduct, although known to be unstable, should be detected. This adduct was indeed formed (FIG. B.5) but decomposed rapidly, as attested by the decrease of the signal during the same acquisition (blue spectrum), and by its almost full disappearance after one and two sweeps (red and green

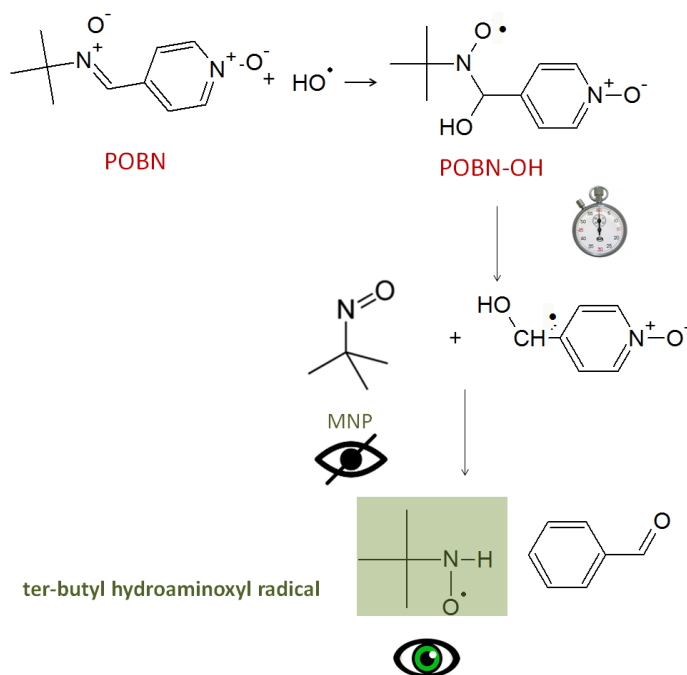


FIG. B.4 – Scheme of decomposition reaction of  $\text{POBN-OH}^\bullet$  adduct leading to formation of MNP spin-trap, which could also decompose into tert-butyl hydroaminoxyl radical.

spectra). In addition, another small signal is visible (black triangles) which could be attributed to tert-butyl hydroaminoxyl radical. This radical formation was already observed by Janzen, Kotake, and Randall D. [264] during decrease of  $\text{PBN-OH}^\bullet$ . Consequently

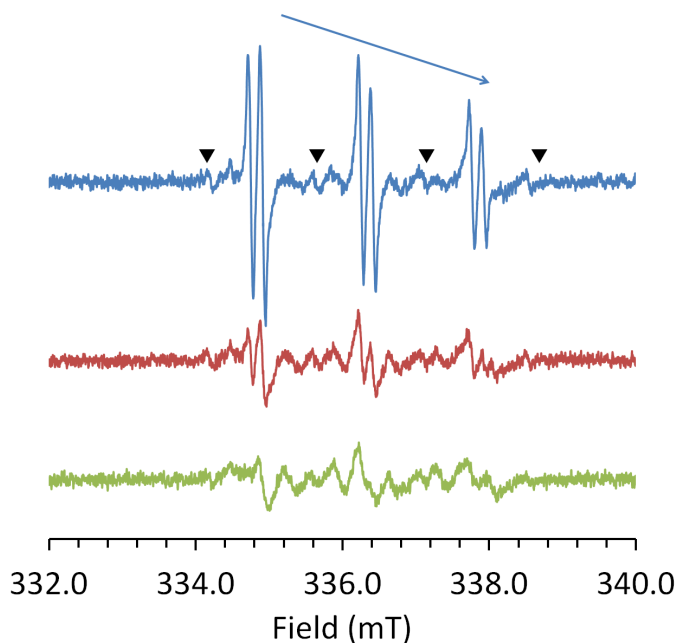


FIG. B.5 – Spectra of  $\text{POBN-OH}^\bullet$  after 2 min mixing with  $\text{H}_2\text{O}_2$ .

if hydroxyl radicals were present at high enough concentration, the  $\text{POBN-OH}^\bullet$  adduct would be present.

By adding the methanol, no signal characteristic from the  $\text{MNP-CH}_2\text{OH}^\bullet$  was noticed. Only the signal from  $\text{POBN-CH}_2\text{OH}^\bullet$ . Therefore, this test could not reveal hydroxyl radicals presence in the conditions of our experiments (i.e. without hydrogen peroxide).

### B.4.2 Investigation of DMPO hydroxylamine formation without scavenger

The second test carried out was based on the assumption that DMPO–OH• adducts could form but be rapidly decomposed into hydroxylamine, and thus not be detected. In order to test this hypothesis, mixtures of DMPO with or without iron were analysed by mass spectrometry. No differences were observed between the blank and the mixture of DMPO with iron. In particular, no peak was observed at  $m/z = 132$ , a mass that could correspond to hydroxylamine hydrogen adduct. However, a tiny peak was noticed at  $(m/z) = 154$  which could correspond to the sodium adduct, but it was also present in the blank. This suggests no hydroxylamine formation due to iron presence.

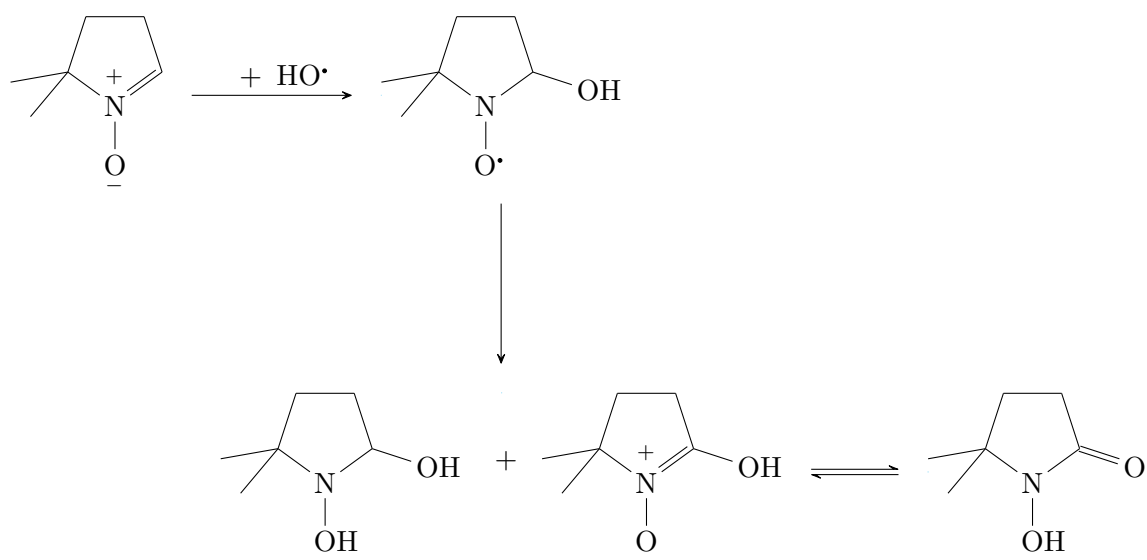


FIG. B.6 – Decomposition of DMPO·OH• adducts in hydroxylamine (left) and nitron (right).

# Appendix C

## Iron dosage by UV-vis spectroscopy

In this appendix are presented first a literature review of the main techniques used for iron dosage by UV-vis spectroscopy, then the two protocols chosen and their calibration curve.

### C.1 State of the art

Numerous methods exist to quantify iron in solution. TAB. C.1 and C.2 sum up some of them specific for iron(II) or iron(III), respectively. From the chelates presented in TAB. C.1, 2,2-bipyridine was chosen because this method is highly sensitive and it gives a stable complex without interfering with iron(III). Regarding iron(III) dosage, potassium thiocyanate was chosen because of its low detection limits. Although, there are a lot of interferences possible, they are well established and those ions are not present in our samples.

Reactant	pKa	Color	Stability constante	Solvant	Medium	pH	$\lambda_{max}$ (nm)	Molar extinction coefficient ( $L \cdot mol^{-1} \cdot cm^{-1}$ )	Interferences	Comments	Sources
Orthophenanthroline	4,96	Pink	21,48	Water	Acid, aqueous	4 à 4,5	510	$11.100 \cdot 10^3$	Fe III , Cu, Ni II, Co II, Mn, Ru, Zn	i interferences from Iron(III), trapping needed ii fluoride utilisation iii errors possible on the measurement due to ferric o-phen reduction to ferrous o-phen. iv measurements in dark	[265, 144]
Bathophenanthroline		Red	Ethanol	Complex extraction with hexanol	water-sodium acetate-ethanol	4	535	$22.350 \cdot 10^3$	Fe(III)	i more sensitive than orthophenanthroline method ii insoluble in water iii complexe extraction required	[266]
Ferrozine	3,13	Magenta	15,86	Water			562	$27.900 \cdot 10^3$	Fe(III)	i sensitive ii interferences with Iron(III)	[144, 267, 268]
2,2-bipyridine	4,33	Red	17-18.8	Water		pH 3 to 8	522	$27.900 \cdot 10^3$		i sensitive ii stable complexe	[144, 145]
2',3,4',5,7-pentahydroxyflavone (Morin)	8,04 (water)			ethanol	aqueous	3.8-4	415	$6.85 \cdot 10^4$	reaction highly selective with appropriate masking (use of EDTA for Iron(III) )	i sensitive ii moderately selective	[269]

TAB. C.1 – Main quantification techniques of iron(II) described in literature

Reactant	pKa	Color	Stability constante	Solvent	Medium	pH	$\lambda_{max}$ (nm)	Molar extinction coefficient ( $L \cdot mol^{-1} \cdot cm^{-1}$ )	Linearity domain ( $mg \cdot L^{-1}$ )	Detection limite ( $\mu g \cdot L^{-1}$ )	Interferences	Comments	Sources
Leuco xylene cyanole		Blue	N.D.	–	Acetate buffer	H <sub>2</sub> SO <sub>4</sub> , 2.8–4.4	615	$5.6 \cdot 10^4$	0.15–0.9	50	Not studied but assumed high	i pH dependant ii Interference not studied iii Detection limit not studied	[270]
Acide squarique	1.5 et 3.5	Violet	41	Ammonium squarate	Phtalate buffer	2.7	515	$3.95 \cdot 10^3$	0.5–20	30	not very selective	i pH dependant ii less sensitive iii adequate to few samples iv high detection limit	[271]
Sulfosalycilic acid	2,6	Violet	14,05	water		3-4.5	500		0.09–9	30	Cu	i pH dependant ii allows also total iron dosage in alkaline medium iii high detection limit	[272]
Thyocyanate		Bloodish red	2,3 (1:1)	water	acid, aqueous	Acid 1-3	480	$2.1 \cdot 10^4$	0–5,6	20	NO <sub>2</sub> , S <sub>2</sub> O <sub>3</sub> <sup>2-</sup> , C <sub>2</sub> O <sub>4</sub> <sup>2-</sup> , HPO <sub>4</sub> <sup>2-</sup> , Co <sup>2+</sup> , Cu <sup>2+</sup> , H <sub>2</sub> PO <sub>4</sub> <sup>2-</sup>	i high excendant needed to drive the equilibrium e ii instable coloration, fast measurements (less than 30 min) iii pH dependant	[146, 273, 147]

TAB. C.2 – Main quantification techniques of iron(III) described in litterature.

## C.2 Iron(II) quantification in solution

2,2-Bipyridine was chosen as a specific reactant for iron(II), which forms a pink complex 1:3 (Fe:bipyridine) and absorbs predominantly around 520 nm to 530 nm. The stability constant of this complex is between 17 and 19 according to published data. Bipyridine pKa is 4.33 according to Thompson and Mottola [144], therefore a phosphate buffer (25 mmol · L<sup>-1</sup>) was used to reach pH 6 and thus stay in the predominance domain of bipyridine under its alkaline form.

The 2,2-bipyridine reactant solution was prepared at 3.72 mmol · L<sup>-1</sup> in the phosphate buffer. Iron(II) calibration curve (FIG. C.2) was done in the range 1.00 · 10<sup>-5</sup> mol · L<sup>-1</sup> to 1.00 · 10<sup>-4</sup> mol · L<sup>-1</sup> using standard iron(II) sulfate (Fe(II)SO<sub>4</sub>, 7H<sub>2</sub>O) solutions prepared by dilution of a mother solution (FIG. C.1). All measurements were done at a wavelength of 523 nm, which corresponds to the maximum of the absorbance of the UV-visible spectrum.

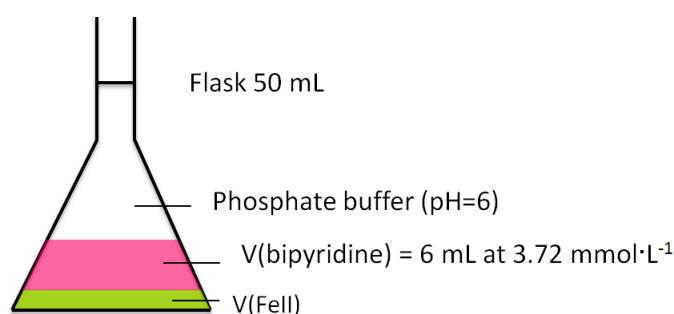


FIG. C.1 – Flask for iron(II) quantification.

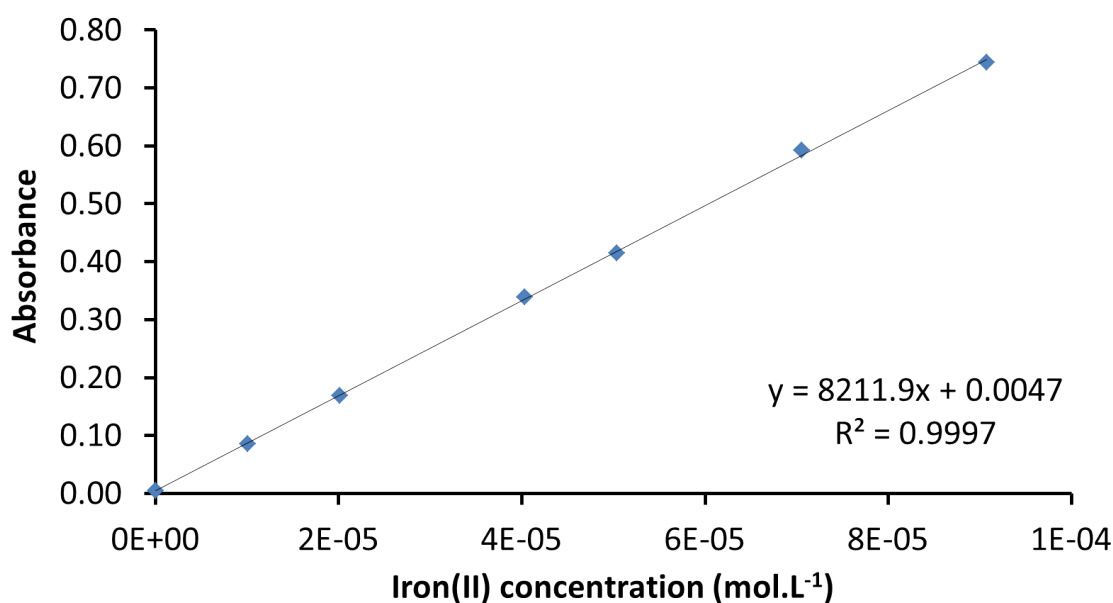
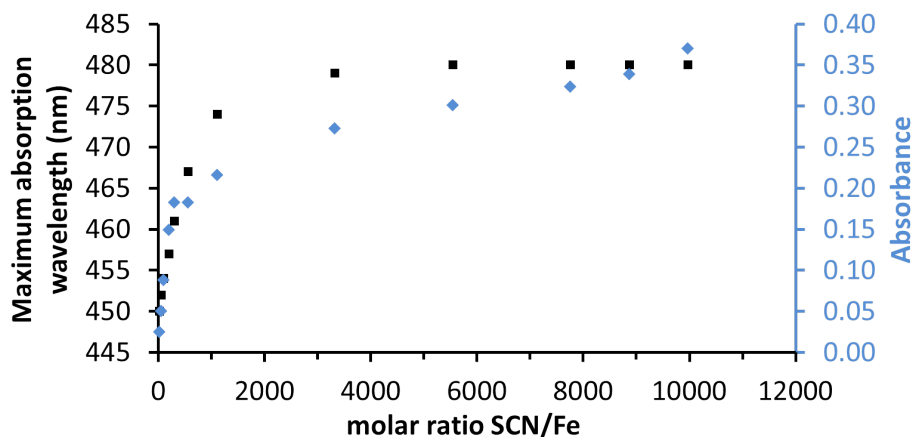


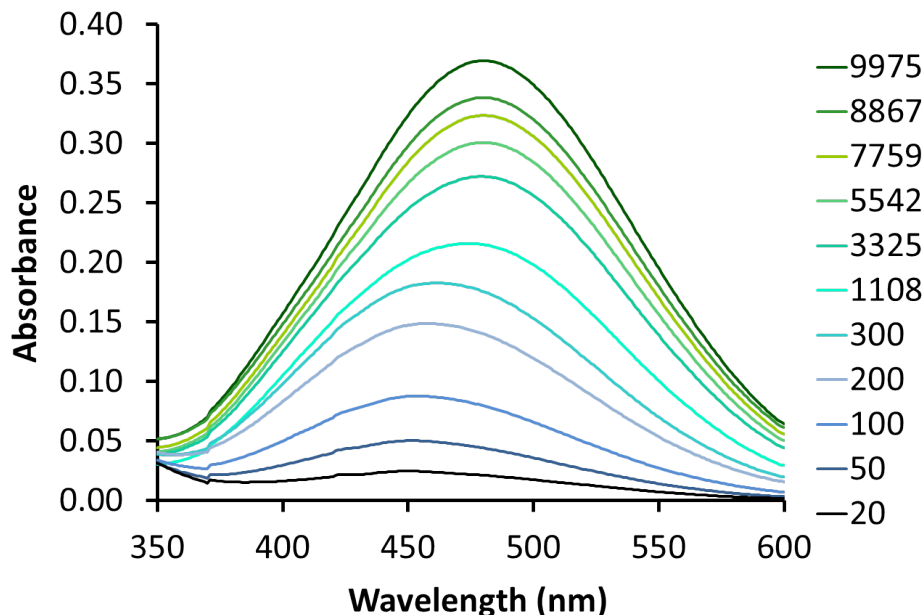
FIG. C.2 – Calibration curve for iron(II) quantification.

### C.3 Iron(III) quantification

Thiocyanate was chosen as chelating agent for iron(III). It gives the iron(III)-SCN complex, which has a maximal absorption wavelength ranging from 460 nm to 480 nm depending on experimental conditions chosen, namely on the excess of  $\text{SCN}^-$  used. Moreover, the molar extinction coefficient can change according to used reactants ( $\text{SCN}^-$  excess, acid type... ). For the same concentration of iron(III), various amount of  $\text{SCN}^-$  were tested in order to chose the most adequate. The results showed that the use of an  $\text{SCN}^-$  amount allowing a  $\text{SCN}^- / \text{Fe}^{\text{III}}$  ratio of at least 3325 is required to have a stable wavelength around 479 nm–480 nm (FIG. C.3a and C.3b).



A – Evolution of the maximum absorption wavelength (black curve) and of the absorbance (blue curve) versus the excess of  $\text{SCN}^-$  used.



B – Visible absorbance spectra obtained for various  $\text{SCN}^-/\text{Iron(III)}$  ratio. Colors represent various  $\text{SCN}^-/\text{Iron(III)}$  molar ratio (from 20 to 9974).

FIG. C.3 – Monitoring of spectra evolution with various molar  $\text{SCN}^-/\text{Iron(III)}$  ratio.

The iron(III) dosage were carried out as follows. A  $1.5 \text{ mol} \cdot \text{L}^{-1}$  potassium thiocyanate solution and a  $10^{-2} \text{ mol} \cdot \text{L}^{-1}$   $\text{H}_2\text{SO}_4$  solution were prepared in milli-Q water. Iron(III) cCalibration curve (FIG. C.5) was done in a range of  $1.00 \cdot 10^{-5} \text{ mol} \cdot \text{L}^{-1}$  to  $1.00 \cdot 10^{-4} \text{ mol} \cdot \text{L}^{-1}$  with iron(III) standard solutions prepared from a mother solution of

FeCl<sub>3</sub> (FIG. C.4). Measurements were done at 479 nm.

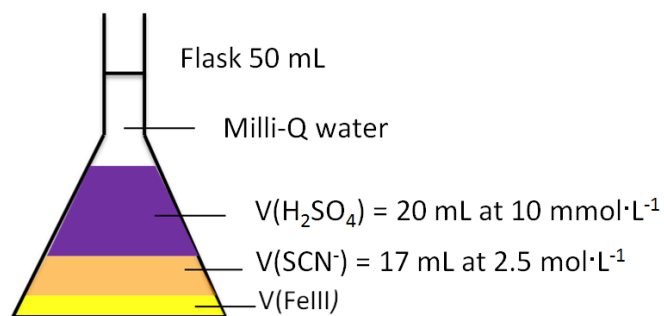


FIG. C.4 – *Flask for iron(III) quantification.*

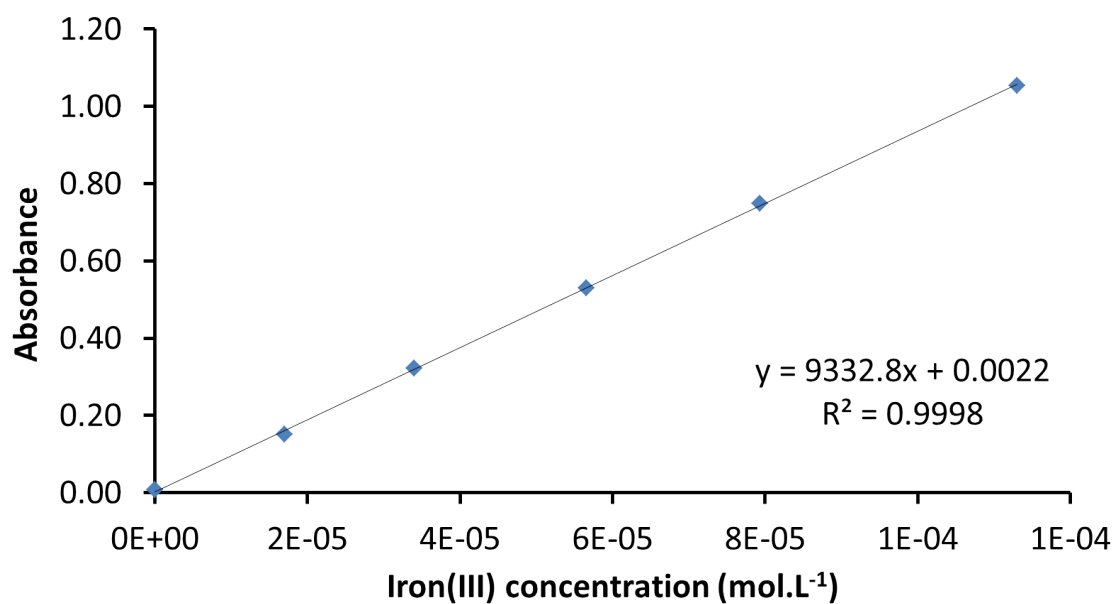


FIG. C.5 – *Calibration curve for Iron(III) quantification.*

# Appendix D

## Iron chemistry in solution

### D.1 Pourbaix diagram

Pourbaix diagrams allow to predict the direction of oxido-reduction reactions and to estimate quickly the influence of pH on the stability of the different species based on thermodynamic considerations. They illustrate the regions of potential and pH where species are prevailing. FIG. D.1 shows the distribution of iron main species for an iron total concentration of  $1 \cdot 10^{-2} \text{ mol} \cdot \text{L}^{-1}$ . The iron(II) predominance domain is clearly separated from the one of oxygen (above the  $E_b$  red lines). Consequently, iron(II) solution are expected to oxidize spontaneously and especially as the pH is high (since the potential difference between the two couples increases with pH).

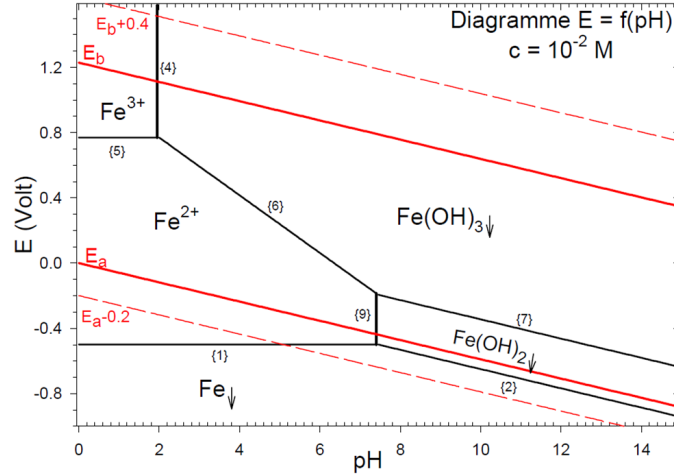


FIG. D.1 – Pourbaix diagram of iron species  $1 \cdot 10^{-2} \text{ mol} \cdot \text{L}^{-1}$ .

### D.2 Iron(II) oxidation

Several works studied iron auto-oxidation. The kinetics of iron oxidation depends on pH. Indeed kinetics of the auto-oxidation reaction of ferrous ions has been described by Stumm and Lee[162] as Eq. D.1 and implies a second order regarding hydroxyl ions concentration.

$$-\frac{d[\text{Fe}^{2+}]}{dt} = k \cdot [\text{Fe}^{2+}] \cdot [\text{HO}^-]^2 \cdot p_{\text{O}_2} \quad (\text{D.1})$$

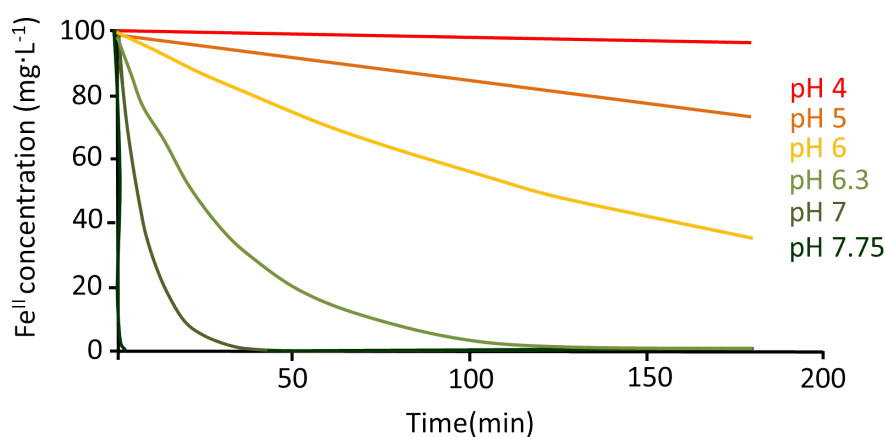


FIG. D.2 – Impact of pH on the oxidation kinetic of total iron(II) species in infinite dilution (adapted from [274]).

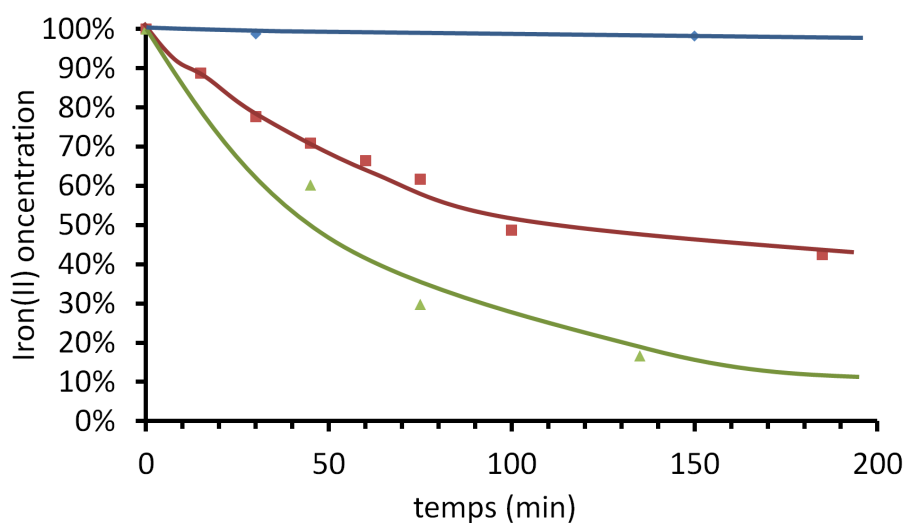


FIG. D.3 – Impact of the medium on the oxidation kinetic of iron(II) sulfate solution at  $1 \text{ mmol} \cdot \text{L}^{-1}$ . Blue, red and green curves represent water,  $(4 \text{ mol} \cdot \text{L}^{-1})$  formate solution and phosphate buffer, respectively.

A study from Barak Morgan[274] has estimated the kinetics of the oxidation of total soluble iron in solution at infinite dilution in water: at pH 4, the oxidation reaction is very slow and at neutral pH oxidation is almost immediate (FIG. D.2).

Indeed, the pH is not the only factor playing a role in the oxidation. Different kinetics have been reported depending on the anions in the medium. Iron oxidation has a first order kinetic regarding ferrous iron concentration with phosphate anions, and a second order in presence of sulfate ions [275]. In addition, our own tests showed that at the same pH 6.8, the phosphate buffer (FIG. D.3, green curve) increases clearly the oxidation of iron(II) in comparison to formate solution ( $4 \text{ mol} \cdot \text{L}^{-1}$ ) (FIG. D.3, red curve). The higher concentration, the faster the oxidation as illustrated by FIG.D.4.

Iron oxidation often increases with chelation of ferrous iron by compounds with oxygen donor atoms, due to their greater affinity for ferric iron [275]. Chelation also shift the ferric/ferrous iron potential.

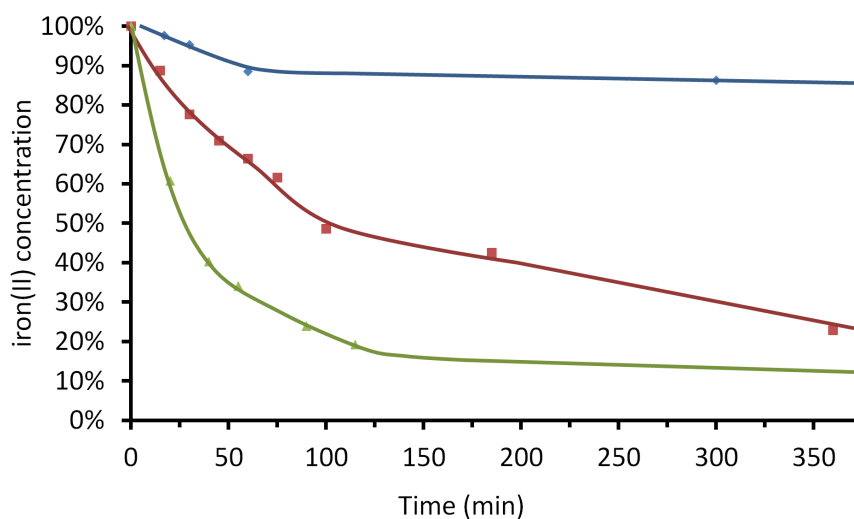


FIG. D.4 – Effect of the iron concentration on iron oxidation in  $4 \text{ mol} \cdot \text{L}^{-1}$  formate solution. Blue, red and green curves represent iron sulfate solution at  $10 \text{ mmol} \cdot \text{L}^{-1}$ ,  $1 \text{ mmol} \cdot \text{L}^{-1}$  and  $0.1 \text{ mmol} \cdot \text{L}^{-1}$ , respectively.



# Appendix E

## HPLC-TPP method

The method with TPP (Triphenylphosphine) is a method used for dosage of peroxides due to their specific reaction with TPP E.1. This method has been used in the laboratory to quantify peroxides on paper samples during their ageing [107].

### E.1 Calibration

The calibration curve of TPPO (FIG. E.2) was obtained by preparing a stock solution of TPPO at  $150 \mu\text{mol} \cdot \text{L}^{-1}$  that was next used to prepare standard solutions were prepared within a concentration range of  $1 \mu\text{mol} \cdot \text{L}^{-1}$  to  $100 \mu\text{mol} \cdot \text{L}^{-1}$  by dilution in methanol.

The conditions used for HPLC analysis were the following: C18 column  $2.1 \text{ m} \times 10 \text{ m}$  with particles diameter of  $5 \mu\text{m}$ . The flow was  $0.3 \text{ mL} \cdot \text{min}^{-1}$ , the pressure was 150 bar. The mobile phase was composed of a mixture of methanol and water in gradient mode:  $T_0 = \text{CH}_3\text{OH}$  (20 %) and  $\text{H}_2\text{O}$  (80 %) ;  $T_{5 \text{ min}} = \text{CH}_3\text{OH}$  (100 %). The column temperature was  $25 \text{ }^\circ\text{C}$  and the injection volume  $10 \mu\text{L}$ . Detection was done with DAD detectors at 224 nm (TPPO) and 262 nm (TPP).

### E.2 Test of ink component interferences

Preliminary tests were performed on inked paper samples aged 1.2 days and 43 days and on iron containing solutions.

A solution of TPP at  $150 \mu\text{mol} \cdot \text{L}^{-1}$  was prepared in methanol and heated at  $75 \text{ }^\circ\text{C}$  during 5 min to dissolve the TPP. When this protocol was used on paper samples, 1.2 mL of TPP solution was poured onto 40 mg of paper cut in tiny pieces. This mixture was kept under magnetic stirring for 2 h in order to react with peroxides. The iron solutions were also prepared at the same concentration as the iron expected to be leached in solution by the paper ( $5 \text{ mmol} \cdot \text{L}^{-1}$ ). The protocol was the following: 0.6 mL of TPP solution at

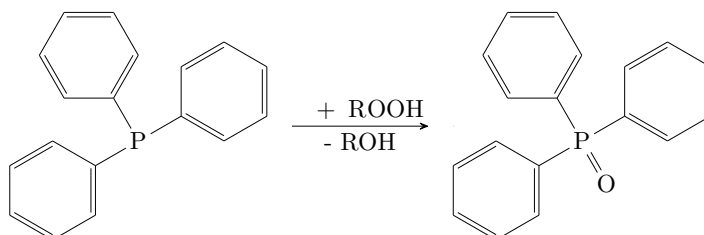


FIG. E.1 – Reaction of Triphenylphosphine (TPP) with peroxides.

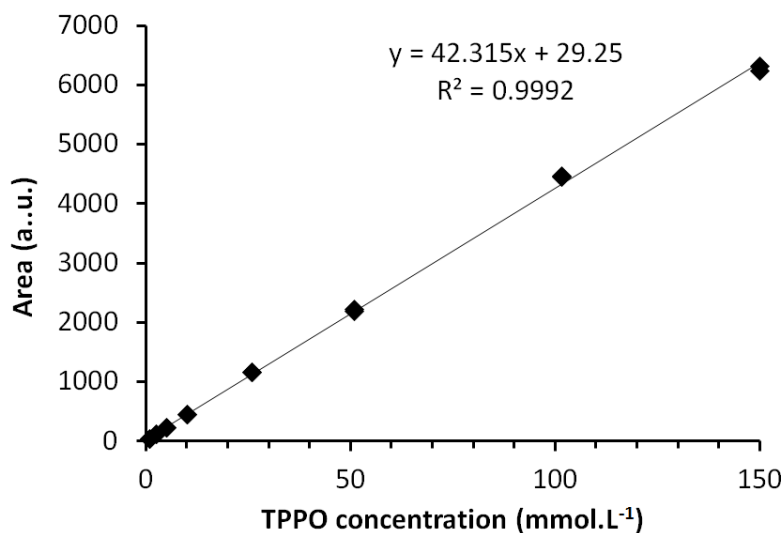


FIG. E.2 – Calibration curve for TPPO quantification.

Sample	Atmosphere	Oxygen content	Iron	Iron salt	Solvent	[TPPO]
inked paper aged 1.2 d	Room	20 %	ink	Fe <sup>II</sup> SO <sub>4</sub>	MeOH	20.9
inked paper aged 43 d			ink	Fe <sup>II</sup> SO <sub>4</sub>	MeOH	3.7
Fe <sup>II</sup> SO <sub>4</sub> _water_O <sub>2</sub>			Fe(II)	Fe <sup>II</sup> SO <sub>4</sub>	water	1.5
Fe <sup>III</sup> Cl <sub>3</sub> _O <sub>2</sub>			Fe(III)	Fe <sup>III</sup> Cl <sub>3</sub>	MeOH	23.9
(Fe <sup>III</sup> ) <sub>2</sub> (SO <sub>4</sub> ) <sub>3</sub> _O <sub>2</sub>			Fe(III)	(Fe <sup>III</sup> ) <sub>2</sub> (SO <sub>4</sub> ) <sub>3</sub>	water	11.5
Fe <sup>III</sup> Cl <sub>3</sub> _N <sub>2</sub>	Glove box	0 %	Fe(III)	Fe <sup>III</sup> Cl <sub>3</sub>	MeOH	4.6

TAB. E.1 – Description of samples preparation for cellobiose degradation.

300  $\mu\text{mol} \cdot \text{L}^{-1}$  and 0.6 mL of iron solution at 10  $\text{mmol} \cdot \text{L}^{-1}$  were mixed and the mixture was let 2 h under stirring. The effect of iron type, solvent and oxygen was investigated.

Iron solutions led to the formation of TPPO without any peroxides. Thus, iron interacts with the TPP probe. This could be due to iron(III) which can oxidize TPP in presence of oxygen. The ability of iron(III) to oxidize TPP has already been reported at high temperature and in solvent and led to the formation of an iron chloride phosphine oxide complex. However no free TPPO was observed [276]. In addition, oxidation of TPP by phthalocyanine compounds has also been reported [277].

## Appendix F

### HTPA calibration by HPLC

The HTPA stock solution was prepared at  $250 \mu\text{mol} \cdot \text{L}^{-1}$  in a buffer consisting in a mixture of 70 %  $\text{KH}_2\text{PO}_4$ ,  $50 \text{ mmol} \cdot \text{L}^{-1}$ , pH 3.2 (adjusted with phosphoric acid  $1 \text{ mol} \cdot \text{L}^{-1}$ ) and 30 % methanol. Standard solutions were then prepared by dilution to concentration ranging from  $25 \text{ nmol} \cdot \text{L}^{-1}$  to  $500 \text{ nmol} \cdot \text{L}^{-1}$  to do a calibration (FIG. F.1).

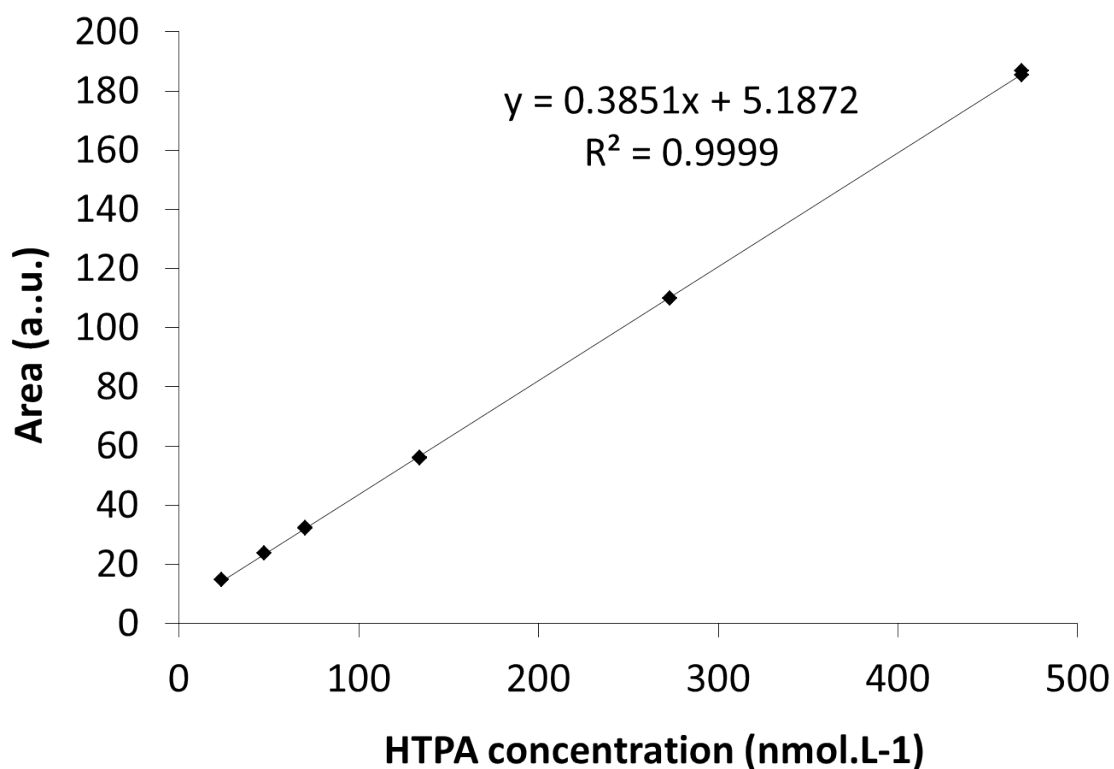


FIG. F.1 – Calibration curve for HTPA quantification.



# Appendix G

## SECM

This part of the experiments was done at Université Paris Diderot Paris 7 in the ITODYS laboratory with Jean-Marc Noël. The idea was to produce hydroxyl radicals by electrochemistry and to study the damage they create to a substrate with different conditions of pH using scanning electron microscope (SECM). First we wanted to test with a known substrate a graphite carbon electrode grafted with an aryldiazonium salt, which has been used in previous work and demonstrate the feasibility. Then, once the best conditions for the substrate degradation found, the purpose was to study the degradation of another substrate, either with carbohydrates grafted on a diazonium or with a paper fiber.

### G.1 Principle of scanning elctro-chemical microscopy

#### G.1.1 Substrate and ultra micro electrode preparation

##### a Obtention of the test organic substrate

The test substrate was obtained by electrochemical reduction grafting. An aryldiazonium salt was dissolved in a solvent and reduced at a graphite carbon electrode: a radical is then formed and  $N_2$  gas is produced. The radical being produced in the vicinity of the carbon electrode, a bond is formed with the substrate. Different diazonium salts were tested but the most commonly used was the benzenediazonium ( $10 \text{ mmol} \cdot \text{L}^{-1}$ ) in acetonitrile. Once formed, only a mechanical polishing of the surface can remove the grafted layer from the carbon substrate.

##### b Ultra micro electrode preparation

For SECM experiments, a ultra micro electrode (UME) is used. The diameter is typically of  $25 \mu\text{m}$ . The electrodes used for these experiments were gold electrodes. They were made by inserting a gold wire into a capillary glass tube. The UME was created by fusing the capillary and stretching it. Platinum wires were inserted by the other end of the capillary to make the junction with the gold wire. The end of the electrode (gold side) was polished until having a round electrode of the desired diameter. With this UME, cyclic voltametry or amperometry can then be done, as with a classical electrode.

Voltametry is a technique in which the current is recorded while sweeping the potential at a constant rate. Cyclic voltametry involves an inversion of the scan of the potentials, the example of a cyclic voltamogram is illustrated in FIG.G.1. This allows to observe the redox species in the medium through their oxidation and reduction curves. Chronoamperometry

allows to follow the evolution of the current with time while applying a potential at the electrode.

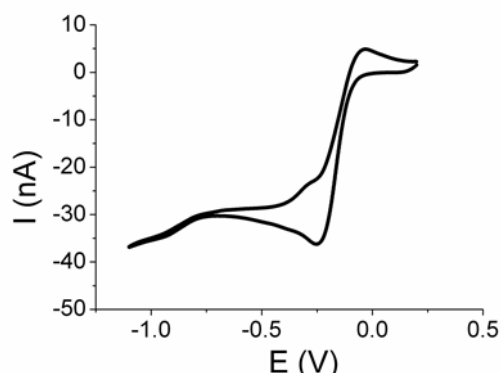


FIG. G.1 – *Cyclic voltametry of  $\text{Fe}^{\text{III}}\text{Cl}_3$  at  $1 \text{ mmol} \cdot \text{L}^{-1}$ ,  $\text{HCl}$   $100 \text{ mmol} \cdot \text{L}^{-1}$ .*

### G.1.2 Principle of the experiment

The SECM was used in feedback mode. The experiment is typically done in four steps: i) an approach of the surface (approach curve); ii) a drawback from the surface contact of  $10 \mu\text{m}$ ; iii) a reduction of oxygen at the electrode (pulsed chronoamperometry); iv) a drawback and an approach curve after the reduction. The approach curves are carried out in a solution containing an electroactive couple (as for exemple, ferri/ferrocyanide couple, or ferrocene/ferricenium cation). The oxygen reduction step was carried out in an acidified aqueous solution of iron salts with oxygen bubbling.

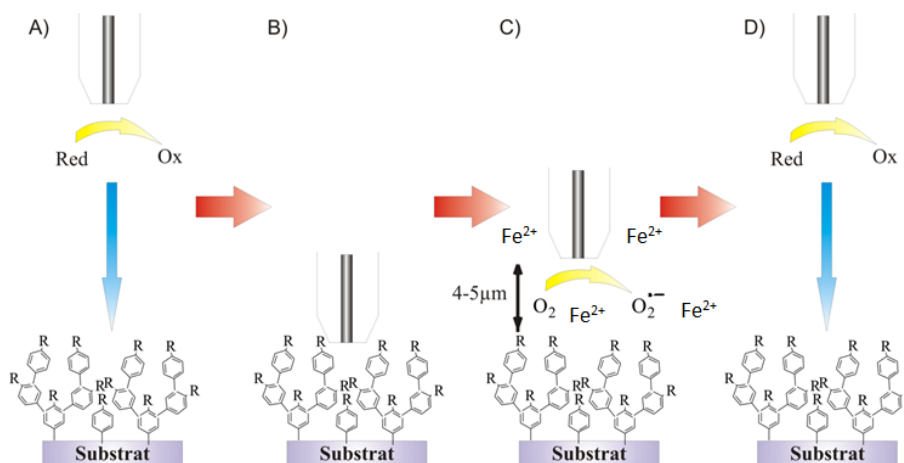


FIG. G.2 – *Principle of the experiments carried out with SECM.*

#### a Approach curves

The approach curve allows obtaining information on the surface state and also to know the position of the electrode regarding the surface. A constant voltage (corresponding to the couple, in this test it was ferrocene methanol) is applied to the electrode (chronoamperometry). When the electrode is far from the surface, the current is only limited by diffusion of the electroactive species to the electrode and corresponds to the stationary current.

When the electrode is moved down toward the surface (on Z axis) slowly, the current changes depending on the distance between the surface and the electrode. An approach curve is then obtained (after data normalization to stationary current). The shape of the approach curve depends on the nature of the substrate. When the substrate is non-conductive, the more we approach the surface, the slower is the exchange of electrons. Species diffusion is harder and the current decreases. On the contrary, if the substrate is conductive, species can be regenerated at the surface: the current will then increase at the vicinity of the surface.

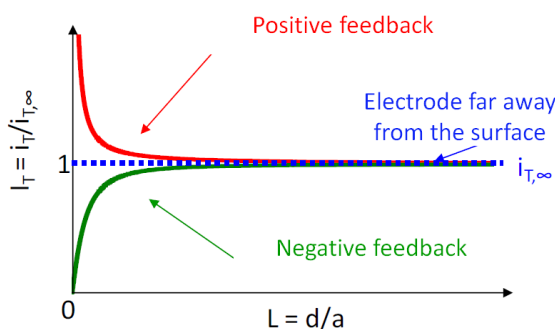


FIG. G.3 – Typical approach curves obtained with a conductive (red) or non conductive (green) surface [278].

## b Reduction

The reduction step lead to the production of hydroxyl radicals near the surface. In the case of oxygen, reduction step produces the superoxyl radicals, which in presence of iron(II) and protons produces hydroxyl radicals. In the case of the Fenton reaction, hydrogen peroxyde is introduced in the solution along with iron(III). The reduction of iron(III) into iron(II) povokes the fenton reaction leading to hydroxyl radicals. This latter is faster than production of hydroxyl radicals from oxygen reduction.

## G.2 Test of degradation of a oragnic layer by localized formation of hydroxyl radicals

Different parameters were tested for the conditions of degradation and substrate layer preparation (TAB. G.1). However, the results with oxygen reduction were not always reproducible: for some experiments, almost no changes occured (FIG. G.4 A, negative feedback) in the approach curve and in other cases, the degradation of the organic layer was very effective (FIG. G.4 B, positive feedback after reduction) and even similar to the one obtained in Fenton system (FIG. G.5).

The comparison between the different conditions of pH was consequently impossible. These discrepancies between the results may be attributed to differences in the diazonium layers, which can be too thick. Some trials of degradation of a fiber were nevertheless attempted.

Parameters	Nature and range
Iron oxidation state	Fe II ( $5 \text{ mmol} \cdot \text{L}^{-1}$ to $200 \text{ mmol} \cdot \text{L}^{-1}$ )
	Fe III ( $3 \text{ mmol} \cdot \text{L}^{-1}$ to $100 \text{ mmol} \cdot \text{L}^{-1}$ )
Acidity	HCl ( $10 \text{ mmol} \cdot \text{L}^{-1}$ to $100 \text{ mmol} \cdot \text{L}^{-1}$ )
Fenton reaction	$\text{H}_2\text{O}_2 + \text{Fe III}$
Diazonium type	benzenediazonium
	$\text{N}_2^+ - \text{ph} - \text{COOH}$
	p-phenylene diamine + Na NO <sub>2</sub> (in situ preparation)

TAB. G.1 – Description of samples preparation for cellobiose degradation.

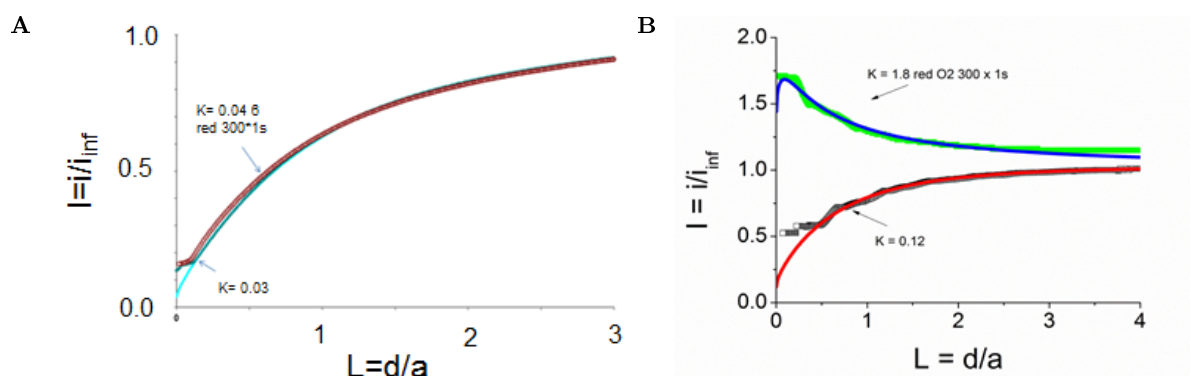
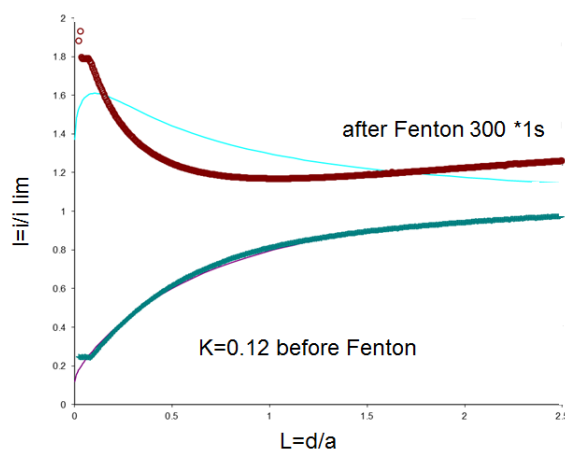


FIG. G.4 – Approach curve obtained before and after oxygen reduction (300 pulses of one second) in a solution of Fe(II) 50 mL, and HCl 100 mL).

FIG. G.5 – Approach curve obtained before and after iron(III) reduction in a Fenton system ( $\text{H}_2\text{O}_2$   $1 \text{ L}^{-1}$ , Fe(III) 100 mL, and HCl 100 mL).

### G.3 Test of degradation of a fiber by localized formation of hydroxyl radicals

Unique fibers were extracted from the *Verger* paper and fixed from both ends on a transparent conductive substrate with an adhesive. This substrate was then fixed between a plexiglass layer and a cell (in which the solution can be poured). This system was then fixed on a reverse optical microscope, which allowed to have both optical visualisation of

the sample (from bottom) and SECM above the substrate.

In order to avoid damaging the fiber surface, approach curve was done on the fiber, but rather on the substrate next to the fiber. The electrode was then withdrawn to be at a distance of 10  $\mu\text{m}$  of the fiber and was moved above the fiber with microscopy observation.

Both Fenton system and "iron +  $\text{O}_2$ " acidified solutions were tested. Several reduction experiments were done. After that fibers were rinsed with water several times to observe the eventual damage with optical microscopy and . An example of the observations made on one fiber after the Fenton reaction had been carried out is shown in FIG.G.6. A small alteration may have occurred: the fiber has a different color in the region of analysis and in SEM, an alteration of a size compatible with electrode size is noticeable although this is not clear, if it is due to the experiment or to the previous state of the fiber. Note that SEM was not done before the SECM analysis to avoid electron damage. Other fibers were analyzed with the "iron +  $\text{O}_2$ " system and the results were inconclusive.

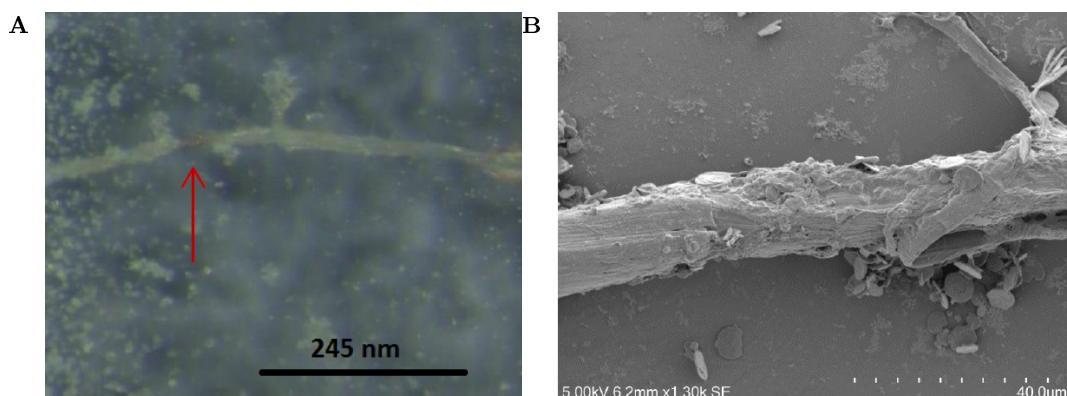


FIG. G.6 – Observations of one fiber after 20 reductions in a Fenton system. The red arrow show the region of analysis in (A) optical microscopy and (B) SEM.



# Appendix H

## Paper depolymerisation: a kinetic study

Appl. Phys. A (2016) 122:773  
DOI 10.1007/s00339-016-0307-1

Applied Physics A  
Materials Science & Processing



### Application of Arrhenius law to DP and zero-span tensile strength measurements taken on iron gall ink impregnated papers: relevance of artificial ageing protocols

Véronique Rouchon<sup>1</sup> · Oulfa Belhadj<sup>1</sup> · Maroussia Duranton<sup>1</sup> · Alice Gimat<sup>1,2</sup> · Pascale Massiani<sup>2</sup>

Received: 23 July 2015 / Accepted: 24 July 2016 / Published online: 30 July 2016  
© Springer-Verlag Berlin Heidelberg 2016

**Abstract** Iron gall inks (IGI) were largely used for writing until the nineteenth century. Under certain circumstances, they provoke a substantial degradation of their cellulosic support. It was shown in a previous works that combination of oxygen and iron largely impacts cellulose chain breaking occurring in acidic conditions (pH 3–4). The present study aims to study the kinetic of this degradation. It assesses the validity of Arrhenius law between 20 and 90 °C taking advantage of the fast depolymerization of IGI impregnated papers at room temperature and using two complementary tools: DP measurements and zero-span tensile strength. The first one is sensitive enough to measure degradation at its very beginning, while the second is more appropriate for advanced stage of degradation. Similar activation energies ( $97 \pm 2 \text{ kJ mol}^{-1}$ ) were found via DP and zero-span measurements, and reaction rates of IGI impregnated papers were 1–2 orders of magnitude above available data related to lignin-free acidic papers. These observations suggest a dominant hydrolytic mechanism that involves directly or indirectly oxygen and iron.

### 1 Introduction

Iron gall inks (IGI) have been extensively used in Western countries for writing and to a lesser extent for drawing. They are made of gall nut extracts rich in gallic acid. When mixed with iron(II) sulphate, these extracts turn instantly towards a dark colour, characteristic of an iron(III)/tannin precipitate. Gum Arabic is added as a binder to create a suspension of the particles that are formed in this manner and thus make the ink more suitable for writing.

IGI have been the scope of many studies [1] because they may, under certain conditions, damage paper, causing browning and loss of mechanical properties such as tensile strength and flexibility. However, the chemistry of these inks still remains poorly understood, mainly because of the high reactivity of iron that allows many interactions with surrounding components: precipitation with gallic acid [2–4], chelation with polysaccharides [5], redox reactions with gallic acid [6], oxidation induced by atmospheric oxygen, etc. All these reactions may compete with each other. Moreover, as most of original recipes correspond to a large excess of iron compared with gallic acid [7], the iron gall ink precipitate formation is most probably not the dominant reaction involving iron.

Paper degradation is usually attributed to the superimposition of acid or alkaline-catalysed hydrolysis and oxidation mechanisms. It inspired many kinetic studies in which depolymerization is quantified by the decline of average number of monomer per macromolecule, also called degree of polymerization, and hereafter referred to as DP. The Ekenstam approach is generally considered in order to model the decrease in DP(*t*) versus time at a given temperature [8]:

$$1/DP(t) - 1/DP_0 = kt \quad (1)$$

✉ Véronique Rouchon  
rouchon@mnhn.fr

<sup>1</sup> Sorbonne Universités, Centre de Recherche sur la Conservation (CRC, USR 3224), Muséum national d'Histoire naturelle, Ministère de la Culture et de la Communication, CNRS, CP21, 36 rue Geoffroy-Saint-Hilaire, 75005 Paris, France

<sup>2</sup> Sorbonne Universités, UPMC Univ Paris 06, CNRS UMR 7197, Laboratoire de Réactivité de Surface, 4 place Jussieu, 75005 Paris, France

where  $t$  represents the time,  $DP_0$  the initial DP value (at  $t = 0$ ) and  $k$  the degradation rate.

This approach was recently refined to model advanced stages of degradation [9], but it remains largely reliable on linear polymers in the early stage of degradation. By measuring the degradation rates at different temperatures, the activation energy of cellulose depolymerization ( $E_a$ ) is obtained through the Arrhenius law:

$$k(T) = A e^{-E_a/RT} \quad (2)$$

Thus, most kinetic studies involve activation energy measurements [10]. However, many of them consider ageing temperature above 90 °C [11, 12] or very low pH values (pH < 1) [13]. These extreme conditions may provoke additional degradation mechanisms than those occurring during natural ageing of paper. Lower temperatures in the range 60–100 °C and milder acidic conditions (pH 3–5) were used by Zou et al. [14] and Begin et al. [15], and in such case, the activation energies were between 103 and 118 kJ mol<sup>-1</sup> depending on the paper and on the way of ageing (Table 1).

The loss of DP also provokes a loss of mechanical properties, a second aspect in which paper conservators and curators have a major interest. Therefore, Arrhenius plots were additionally drawn with data related to mechanical properties applying mathematical treatments similar to that of Eq. (1), yet replacing  $(DP)^{-1}$  by the measured quantity [16] (Eq. 3a) or by the inverse of the measured quantity [17] (Eq. 3b):

$$M(t) - M_0 = kt \quad (3a)$$

$$1/M(t) - 1/M_0 = -kt \quad (3b)$$

In these equations,  $M(t)$  stands for the measured quantity and strongly depends on the type of mechanical testing to be considered. There is a priori no strong evidence regarding which of Eqs. (3a) or (3b) is physically the most relevant to model the evolution of  $M(t)$ . This might explain why a large range of activation energy values was found (between 92 and 165 kJ mol<sup>-1</sup>) depending on the chosen papers, mechanical tests and data treatment [16, 17].

All these studies find a direct application in the estimation of lifetime expectancies for collection management purposes (see, for instance, recommendations from the Commission on Preservation and Access [18] or from the British Standard Institute [19]). This presupposes extrapolating Arrhenius plots obtained at high temperature (accelerated ageing) to room temperature (natural ageing). These extrapolations, crucial for the reliability of the models, are based on the assumption that no change in the degradation mechanism takes place between low and high temperature. Moreover, since Arrhenius law is exponential, small experimental errors in  $E_a$  values at high temperature

induce through extrapolation at room temperature huge uncertainties in lifetime expectancies. In addition, paper depolymerization being very slow below 50 °C, few experimental evidence of the extrapolation validity exists, thus questioning the reliability of accelerated ageing protocols. Up to now, the only quantitative comparison of accelerated and natural ageing was drawn by Zou et al. [20] who had access in the 90 s to paper pulps that were already analysed in the 70 s and kept meanwhile in relatively constant humidity and temperature conditions. They found a good correlation with the prediction of their kinetic model considering an  $E_a$  value of 109 kJ mol<sup>-1</sup>.

From a chemical point of view, a consensus has been reached on the fact that acid-catalysed hydrolysis is the main pathway of acidic paper degradation below 100 °C [10, 21, 22] while oxidation prevails over 100 °C. Surprisingly, the great majority of kinetic studies rely on experiments performed in aerated conditions. Also, if a degradation pathway is driven by both oxygen and low pH values, it would naturally be interpreted as acid-catalysed hydrolyses. It is nevertheless considered that the predominant degradation route in dark at mild environmental conditions is that of hydrolysis and potential oxidation mechanism could play merely a synergistic role. These general considerations largely prevail on iron-free papers, but in case of iron gall ink impregnated papers, the dominant mechanism of degradation remains questionable because (i) there is no exhaustive kinetic study dealing with iron-containing papers and (ii) the rich chemistry of iron may allow alternative pathways.

The acidity of the ink is evidently a damaging factor. It has been shown that the paper nearby the ink line has often a low pH value [23] which implies acid-catalysed hydrolysis reactions. In addition to that, an oxidative degradation pathway is often suggested in the case of IGI manuscripts. It is related to the presence of iron(II) that promotes highly reactive hydroxyl radicals formation through Fenton reactions [24]. The predominance of this oxidative mechanism was evidenced on deacidified IGI impregnated papers [25] (pH 6.5–8). Its occurrence at lower pH values was not highlighted and thus remains questionable.

In a previous work, using anoxic and aerated ageing conditions, we showed that the combination of oxygen and iron was a key factor for cellulose chain breaking occurring in acidic conditions (pH 3–4) [26]. Therefore, paper degradation induced by IGI would be predominantly driven by oxidative mechanisms involving iron or cellulose. Nevertheless, additional knowledge on this aspect is still required, and this will be part of the questions raised in the present work.

Another relevant information gained from our above-mentioned work [26] lies in the fact that cellulose depolymerization was sufficiently fast to be measured at

**Table 1** Selection of some activation energy values related to paper degradation

Author	Tested material	HR	T (°C)	$E_a$ (kJ mol <sup>-1</sup> )	Data considered
This work	Whatman paper impregnated with Fe	50 %	23–90	98.6 ± 2.5	DP (Ekenstam)
			40–80	96.6 ± 2.4	Zero-span
	Whatman paper impregnated with Fe + Ac	50 %	23–90	95.3 ± 1.7	DP (Ekenstam)
				23–90	98.3 ± 3.1
Daruwalla et al. [13]	Cotton cellulose in HCl, 1 N	100 %	30–50	95.4	DP (early stage)
				123.8	DP (advanced stage)
	Regenerated cellulose in HCl, 1 N	100 %	30–50	95.0	DP (early stage)
				113.8	DP (advanced stage)
	Cotton cellulose in H <sub>2</sub> SO <sub>4</sub> , 0.1 N	100 %	30–50	87.0	DP (early stage)
				113.8	DP (advanced stage)
Regenerated cellulose in HCl, 1 N	100 %	30–50	91.2	DP (early stage)	
			114.6	DP (advanced stage)	
Zou et al. [14]	Bleached softwood bisulphite pulp, pH 4.8	75 %	60–100	104 ± 3	DP (Ekenstam)
				111 ± 4	
				103 ± 5	
Zou et al. [20]	Bleached kraft pulps	50 %	23 °C	109	DP (Ekenstam)
Begin et al. [15]	100 % Softwood bleached ChemiThermoMechanical pulp, pH 5	65–72 %	65–90	103	DP (free sheet)
				114	DP (Stack)
				106	DP (free sheet)
Shahani et al. [16]	Paper, 100 % bleached northern softwood kraft paper, alum sized, pH 5.7, aged in glass tubes	56–60 %	70–90	113	Zero-span
				108	DP
				83.7	CI (early stage)
Rychly et al. [35]	Whatman paper	0 %	40–220	93 ± 2	DP (Ekenstam)
Kocar et al. [21]	Paper, bleached sulphate softwood pulp, no size	0 %	60–220	93 ± 2	DP (Ekenstam)
				65 %	60–90
Shafizadeh et al. [11]	Cotton cellulose linters, ageing in air	0 %	150–190	88	DP (Ekenstam)
				113	DP (Ekenstam)
				110	CI (advanced stage)
Kwon et al. [43]	Cellobiose in H <sub>2</sub> SO <sub>4</sub> solution	Solution	25–80	110 ± 7	Glucose formation
				118 ± 8	Cellobiose hydrolysis
	Cellobiose in a Fenton reaction system	Solution	25–80	55 ± 1	Glucose formation

This selection focusses on ageing conditions relatively close to those used in this study and/or on data that are found relevant to the discussion. CI Chemiluminescence intensity

room temperature. This point is quite unusual as most kinetic studies on paper degradation involve artificial ageing protocols using relatively high temperatures [10].

Based on this previous knowledge, the present study aims to evaluate the relevance of Arrhenius law extrapolations taking advantage of the fast depolymerization of IGI impregnated papers (measurable at room temperature) and using two complementary tools: DP measurements and zero-span tensile strength. The first one is sensitive enough to measure degradation at its very beginning, while the second is more appropriate for advanced stage of degradation.

## 2 Experimental section

### 2.1 Sample preparation

Pure laboratory products were used: monohydrate gallic acid (398225, Aldrich) and heptahydrate iron(II) sulphate (215422, Aldrich). Three model ink solutions were prepared with different concentrations of these products, chosen according to criteria already largely described in a previous work [26]. All solutions were stirred for 3 days in closed vessels, and then, paper sheets (Whatman No 1, 10 cm large square) were immersed for 10 min. After-

wards, the sheets were placed between two Cobb blotting papers [27], and the excess of ink was mopped up by using a 10-kg Cobb roll back and forth. This procedure allows an even deposition of the solution, with a lateral dispersion of  $\pm 5\%$ . The concentration of iron deposited on the samples, determined by atomic absorption spectroscopy [28], is close to 0.8 % w/w for both Fe and Fe + Ac paper sheets. After impregnation, the papers were dried overnight for 17 h at 23 °C. The sample names and concentrations of solutions used for their impregnation are given in Table 2 with pH measurements of cold paper extracts according to standard protocol [29].

Ageing at ambient temperature was performed in a small glove box placed in an air-conditioned room (23 °C) and buffered at 50 % RH with silica gel (PROSorb, Long Life for Art, Germany) pre-conditioned in a climatic chamber at 50 % RH. For artificial ageing at higher temperature, samples were cut in smaller pieces (avoiding edges) and placed in closed vessels with an experimental set-up described elsewhere [30] yet using silica gel (PROSorb, Long Life for Art, Germany; pre-conditioned at 50 % RH) instead of paper for humidity buffering. Humidity was monitored during ageing (50  $\pm$  5 % RH) by small sensors placed in the vessel (Hygrobutton, ProgesPlus, USA). In order to avoid temperature and humidity fluctuation during sample transfer, each vessel was filled with one sample only, meaning that there were as many samples as measurements (~85, 12 and 60 samples for Fe + Ac, Fe + Ac conc and Fe solutions, respectively).

## 2.2 Degree of polymerization

The degree of polymerization (DP) was determined by standard viscosity measurements using cupriethylenediamine (CED) as solvent [31]. The limiting viscosity number  $[\eta]$  was measured 10–15 min after paper dissolution. In order to evaluate possible artefacts due to cellulose-oxidized groups, preliminary tests were performed implementing a sodium borohydride reducing treatment prior CED dissolution. Similar values of  $[\eta]$  were obtained compared with

**Table 2** Sample preparation

Name of paper samples	Composition of solution used for impregnation (g L <sup>-1</sup> )		ink pH	paper pH
	Gallic acid monohydrate	Iron(II) sulphate heptahydrate		
Fe	–	4	3.6	4.2
Fe + Ac	0.9	4	3.2	3.7
Fe + Ac conc	9	40	2.6	3.2

Composition and pH of solutions used for impregnation; the pH of paper was measured on cold extracts [29] after drying at 23 °C and 50 % RH for 17 h

those without reducing treatment. The viscosity measurements were therefore taken without reducing treatment.

An accurate determination of the amount of dry cellulose solubilized in CED was achieved by the use of a temperature- and humidity-controlled microbalance equipped with a heating resistance (DVS Advantage, SMS Ltd, UK) that offers the possibility to heat the sample at 120 °C in order to remove residual water and thus estimate the amount of dry matter.

The limiting viscosity number  $[\eta]$  was converted to DP values (i.e. the average number of monomers per macromolecule) using the Mark–Houwink–Sakurada equation:

$$[\eta] = K \cdot (DP_v)^\alpha \quad (4)$$

In Eq. (4),  $K$  and  $\alpha$  are two constants given for a polymer/solvent system and  $DP_v$  stands for an approximation of the average number of monomers per macromolecule, as measured by viscosimetry.

The values  $K = 0.91$  and  $\alpha = 0.85$  were chosen in this study. They were initially proposed by Evan et al. [32] and have largely been used in the cellulose chemistry community for the cellulose/CED system. They lead to  $DP_v$  values that are (i) experimentally consistent with  $M_w$  values determined by size exclusion chromatography and (ii) proportional to average number of monomer per macromolecule (DP) with a proportionality factor that is relatively close to 1 [33]. Eq. (2) shows that two proportional quantities will lead to similar activation energy values. Therefore,  $DP_v$ , as determined with Eq. (4), appears appropriate for the determination of activation energy values of chain scission and will be hereafter more simply referred to as DP.

## 2.3 Mechanical properties

Loss of mechanical properties was evaluated with a zero-span tensile tester [34] (Pulmac, TS-100) on dried papers, pre-conditioned at 23 °C and 50 % of relative humidity (RH). This test consists in measuring the failure load necessary to break a strip of paper maintained by two joint clamps. The load, also called zero-span tensile strength, is expressed in kg per 15 mm. For each sample, 10 measurements were taken and the average was considered. Standard deviation was ranging from 2 % up to 6 %.

## 3 Results

### 3.1 Determining the amount of dry cellulose for DP measurements

DP measurements largely rely on an accurate determination of the amount of solubilized cellulose. It appeared useless to weight samples before ink impregnation to

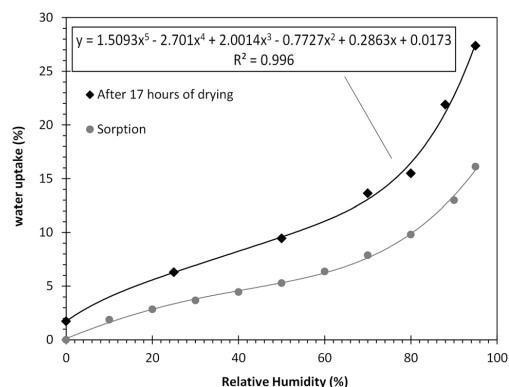


**Fig. 1** Water uptake versus humidity at 23 °C. *Filled circle* sorption isotherm starting with a paper that was previously heated at 120 °C for 15 min; *filled diamond* desorption isotherm corresponding to a paper that was immersed for 10 min in water, pressed between two Cobb paper and then exposed for 17 h to specific values of relative humidity; (—) polynomial fit. All measurements were taken on approximately 10 mg of pure Whatman paper

estimate the amount of dry cellulose because paper edges appeared darker and relatively heterogeneous and had therefore to be taken apart. Samples were also cut out of the central part of the sheets that had a homogeneous aspect. Moreover, when paper is immersed in water and then dried overnight at ambient temperature, a large hysteresis effect is expected, meaning that a sorption isotherm (Fig. 1, grey data) between 0 and 95 % RH is not appropriate.

Dry cellulose weights were also estimated by the use of the microbalance mentioned above, considering 10 mg of Whatman samples impregnated with pure water and then exposed to fixed humidity conditions. After impregnation, paper retains water to a ratio of approximately 115 % of its own weight. When it is afterwards exposed to air, the water uptake rapidly decreases. The microbalance monitored this weight decrease versus time until equilibrium is reached at requested conditions. It was always observed that an exposure for 17 h was largely long enough to reach equilibrium. Afterwards, the sample was heated at 120 °C in order to remove residual water, leading to the determination of dry cellulose weight and water uptake. Several humidity conditions ranging from 0 % RH up to 97 % RH were tested this way, and measurements were interpolated (Fig. 1, diamond-shaped data). The Brunauer–Emmett–Teller (BET) model was not considered here because it is mainly valid for low moistures (below 40 % RH) and does not allow fitting in the whole range of humidity values. A fifth-order polynomial interpolation was preferred although it has no physical meaning.

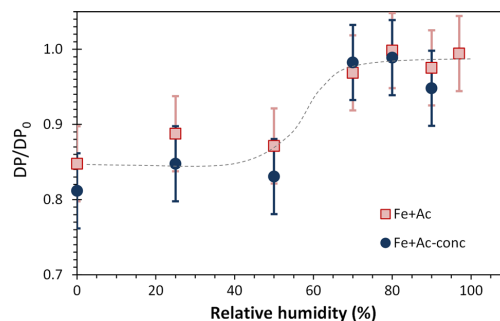


**Fig. 2** Retention of DP after 17 h of drying at 23 °C and different humidity conditions. *Filled square* samples Fe + Ac; *filled circle* samples Fe + Ac conc (see Table 2)

### 3.2 Measuring initial degree of polymerization ( $DP_0$ )

The DP of blank Whatman paper is close to 3100. Preliminary measurements (not detailed) taken on IGI impregnated papers showed that this value was not stable during drying, which may bring errors in the kinetics measurements. Therefore, the change in DP was also measured in drying conditions with fixed humidity conditions in the range from 0 to 97 % RH and considering the above-mentioned desorption curve (Fig. 1). A significant DP loss (10–20 %) was observed for the driest conditions (0–50 % RH), whereas DP remained unchanged for the highest humidity conditions (70–97 % RH) (Fig. 2). Moreover, this phenomenon was more pronounced on the concentrated samples (Fe + Ac conc). In order to avoid confusion on  $DP_0$  values in the Ekenstam model, we decided to let dry all IGI papers at 50 % RH and chose a starting point ( $t = 0$ ) corresponding to 17 h after impregnation for all artificial ageing experiments.

### 3.3 Kinetic approach of chain breaking

Artificial ageing of IGI impregnated papers was performed at increasing temperatures from 23 to 90 °C. The evolution of DP values was monitored to plot  $1/DP(t) - 1/DP_0$  versus time (Fig. 3). These curves were linearly interpolated without imposing a fixed value for the origin. The resulting  $k(T)$  slopes values were then reported in an Arrhenius plot (Fig. 4), leading to the determination of the following activation energies:  $E_a = 95.3 \pm 1.7 \text{ kJ mol}^{-1}$  for the Fe + Ac sample and  $E_a = 98.6 \pm 2.5 \text{ kJ mol}^{-1}$  for the Fe sample. These two values are similar within experimental uncertainties.

**Fig. 3** Ekenstam plots at temperature of ageing ranging 23–90 °C. 23 °C (*plus symbol*); 41 °C (*times symbol*); 70 °C (*filled triangle*); 80 °C (*filled square*); 90 °C (*filled circle*); Ageing was performed at 50 % RH

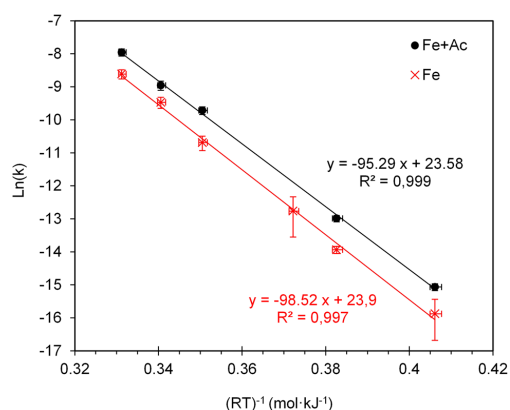
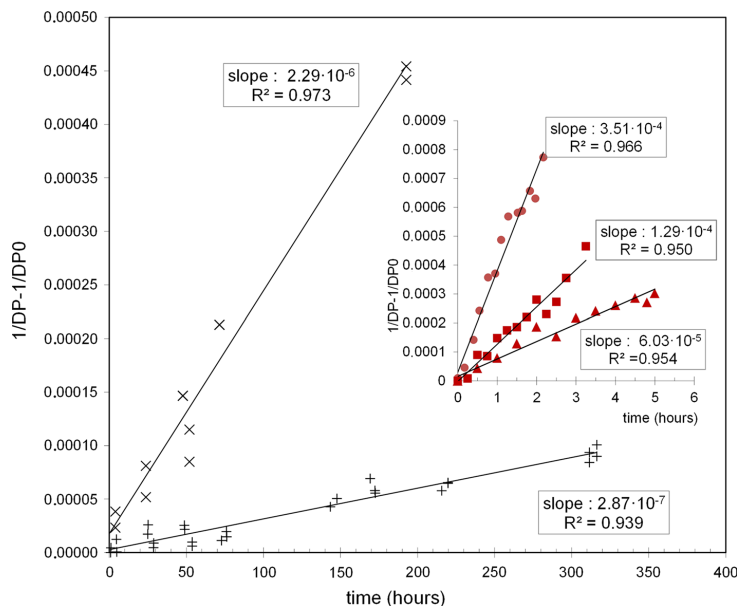


**Fig. 4** Arrhenius plot of DP measurements. Samples Fe + Ac (*black filled circle*); samples Fe (*red times symbol*)

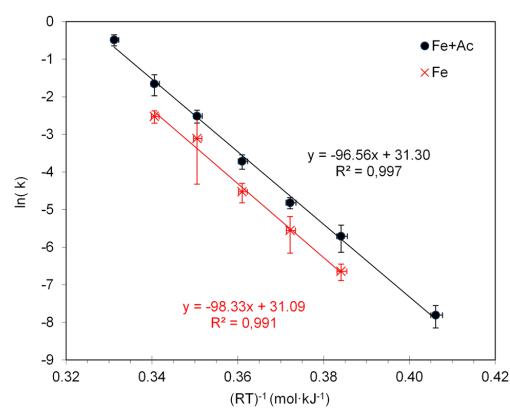


**Fig. 5** Arrhenius plot of zero-span measurements. Samples Fe + Ac (*black filled circle*); samples Fe (*red times symbol*)

### 3.4 Kinetic approach of mechanical decay

The evolution of zero-span tensile strength  $Z(t)$  was monitored during ageing on samples that were similar to those used for viscosity measurements, yet aged for longer ageing periods (3000 h at 23 °C; 550 h at 40–50 °C; 125 h at 60 °C; 70 h at 70 °C; 10 h at 80 °C; 7 h at 90 °C). Arrhenius plots (Fig. 5) were drawn using Eq. (3a).

Activation energies  $E_a = 96.6 \pm 2.4$  and  $E_a = 98.3 \pm 3.1$  kJ mol<sup>-1</sup> were, respectively, obtained for the Fe + Ac

and Fe samples. These values are similar to those obtained with DP measurements following the Ekenstam approach.

## 4 Discussion

### 4.1 Oxidation versus hydrolysis?

IGI are acidic. The solutions Fe and Fe + Ac studied in this work have pH values 3.6 and 3.2, respectively

(Table 2). As a result, papers impregnated with these inks are acidic with pH values 4.2 and 3.7, respectively. Sulphuric acid is often put forward as the main cause of acidity [10], but this interpretation is not convincing: inks are not made with sulphuric acid, but with sulphate salts and released sulphate ions cannot account for low pH value of the ink that is more probably attributable to formation of iron(II)/iron(III) solvation complexes and to gallic acid dissociation ( $pK_a = 4.5$ ). Anyway, whatever the cause of acidity, the low pH values of our samples give substantial reasons to suspect acid-catalysed hydrolysis as the main cause of chain scission.

This first interpretation does not stand when examining paper behaviour in further details: in previous work [26], ink impregnated papers were conditioned in anoxia and their degradation was delayed. Moreover, papers impregnated with pure gallic acid did not show significant depolymerization at ambient temperature despite showing a low pH value (3.6). Also pH is certainly an important factor, but it does not alone account for the depolymerization observed on ink impregnated papers.

On these papers, the most surprising aspect of the depolymerization lies in its rapidity that makes the phenomenon perceptible overnight. Here again, damages depend on environmental conditions: when wet samples are exposed overnight to high humidity conditions (>60 % RH), they still contain a significant amount of water (over 10 % w/w) (Fig. 1) and no significant variation of DP is observed (Fig. 2). Conversely, when these samples are exposed overnight to low humidity conditions (<60 % RH), their drying is more advanced, they contain much less water (below 10 % w/w) (Fig. 1), and the cellulose DP decreases by 10–20 % (Fig. 2). This behaviour suggests that reactive sites become accessible to oxygen in low humidity conditions, whereas they remain protected by water in high humidity conditions. It is consistent with a mechanism of depolymerization in which oxygen is a key factor.

One could think that the decrease in DP recalls the “initial rapid change in DP, before linear kinetics are established” [12] which corresponds to the juxtaposition of a fast and slow kinetic several times observed in the literature (Table 1, Daruwalla et al. [13], Rychly et al. [35]). This change has in the past been “attributed to rapid breaking of a small number of weak bonds” [12]. The concept of weak bonds (or weak links) is often questioned in the paper research community, most of the time driving scepticism. Zou et al. [14] did not find any experimental evidence of weak links on bleached kraft and bleached bisulphite pulps. Calvini [36] proposes to include the notion of weak bond in his kinetic model, but does not appear fully convinced by this notion as he mentions that “apparent weak link degradation can also be attributed to

[...] variation of the polydispersity index for specimens [papers] that do not follow the most probable distribution of Mw (e.g. [...] pulp with relatively high hemicellulose content)”. Finally, Emsley, in his editorial on cellulose degradation [37, 38], clearly maintains not being in “favour of the concept of weak bonds” but prefers to “think in terms of a spectrum of reactivities”.

Considering the above-mentioned literature, there is no objective reason to attribute the DP decrease observed on IGI impregnated papers to an eventual content of “weak links” as Whatman No 1 paper is one of the best linear cellulose models showing a Gaussian distribution of molar mass.

Our experiments show that the DP loss is directly linked to the presence of oxygen (and probably his accessibility to reactive sites). It is also related to the presence of iron(II) ions a significant proportion of which (20–30 %) is transformed to iron(III) during drying at 50 % RH [26]. This transformation implies reactive oxygen species that might have an impact on cellulose chain scissions.

#### 4.2 Discussing the reliability of artificial ageing experiments

The Arrhenius plots obtained from DP measurements data between 23 and 90 °C (Figs. 4, 5) show an excellent linear correlation, with  $R^2$  factors over 0.99, providing experimental evidence of the reliability of the Arrhenius law to extrapolate to room temperature kinetic studies performed with artificial ageing. Interestingly, activation energies measured in this study, the average value of which is  $97 \pm 2 \text{ kJ mol}^{-1}$ , are close to the value of  $92 \text{ kJ mol}^{-1}$  taken as an average of published activation energies by Reilly et al. [18] for evaluating the impact of temperature increase on short-lived organic materials.

This positive result should, however, be considered with great care for collection management purpose: the model samples of this study are designed to reproduce the main chemical degradation occurring on paper fibres that are in contact with ink, but they remain inappropriate to reproduce the decay of an original manuscript. Indeed on most original manuscripts, the ink is concentrated on top of the paper sheet (because of the initial paper size) and a few fibres only are concerned by the degradation that is reproduced on our samples. It should be kept in mind for collection management that the physical distribution of ink is the first key point of manuscript conservation. Paper degradation starts with humidity-driven migrations of iron in the sheet and around the ink line. The samples designed for this study do not model these migrations, because they are already fully impregnated with the ink. Moreover, the Arrhenius approach is not appropriate to model these phenomena that are mainly governed by physics and occur when the manuscript is exposed to high humidity

conditions [39]. It has been shown, for instance, that these migrations become significant above 85 % RH even for a few hours of exposure [40, 41]. Keeping collections in dry environments remains the first precaution to be taken, long before speculating on temperature impact.

#### 4.3 DP measurements versus zero-span testing

The data obtained in this work with zero-span and DP measurements lead to comparable values of activation energies, close to  $97 \pm 2 \text{ kJ mol}^{-1}$ . This point may at first appear surprising, not to say suspicious when considering the numerous values of activation energies available in the literature, a small selection of which is reported in Table 1. It is, however, consistent with the fact that activation energy values measured with zero-span testing by Shahani et al. are similar to those found with DP measurements (Table 1, Shahani et al. [16]).

This coincidence finds a simple explanation: the first term  $1/DP(t) - 1/DP_0$  of the Ekenstam approach (Eq. 1) actually corresponds to the average number of broken bonds per anhydroglucose unit. It is intuitive to suppose that the loss of zero-span tensile strength is correlated with the number of broken bonds. This correlation is in fact linear at least for loss of zero-span breaking strength below 60 % as shown by the re-computation of data published by Zou et al. [14] (Fig. 6) or by other literature data [17, 42]. Considering this linear behaviour, one should expect similar activation energies for zero-span and DP measurements.

These observations lead to a second conclusion: DP measurements make it possible to quantify the early stage of degradation, a stage for which zero-span testing is not sensitive. On the opposite zero-span testing enables the measurement of a more advanced stage of degradation for which DP is poorly discriminant. The fact that similar

activation energies were found on DP and zero-span measurements proves that the mechanism of chain breaking remains unchanged all along the degradation.

#### 4.4 Discussing Activation energy values

A large range of activation energy values have been proposed to model cellulose depolymerization, ranging from  $55 \text{ kJ mol}^{-1}$  [43] to  $180 \text{ kJ mol}^{-1}$  [44] depending on cellulosic materials and physical/chemical parameters taken to monitor degradation. Table 1 shows a selection of these activation energies that are believed to be the most relevant to this study.

As pointed out by Zou et al. [14], chain breaking may be produced by several reactions simultaneously occurring in the material, each of these at a different rate depending on reagent concentrations. In a limited range of temperature around a fixed value  $T_0$ ,  $\text{Ln}(k)$  can be expressed in Taylor's series. The global activation energy appears then as a weighted average of activation energies of each independent reaction:

$$E_a = \frac{\sum_i E_i k_i^0}{\sum_i k_i^0} \quad (5)$$

where  $E_i$  is the activation energy of reaction  $i$  and  $k_i^0$  its rate at  $T_0$ .

This point radically impairs interpretation of activation energies. It is, however, generally considered that higher activation energy values refer to pure acid-catalysed hydrolysis while lower values are correlated with oxidative mechanisms. These general considerations rely on several factors: first, activation energies measured in air condition are generally lower than those measured on similar samples but under nitrogen (Table 1, Shafizadeh et al. [11]); second, activation energies measured in dry environment (air without water) are lower than those measured in humid environment (Table 1, Kocar et al. [21]); third, low activation energies below  $100 \text{ kJ mol}^{-1}$  are measured by chemiluminescence, a technique sensitive to radical production (Table 1, Rychly et al. [35]); fourth, the decomposition of cellobiose in an oxidative Fenton reaction system leads to low activation energy of  $55 \text{ kJ mol}^{-1}$  (Table 1, Kwon et al. [43]); and fifth, high values of activation energy (in the range  $127\text{--}179 \text{ kJ mol}^{-1}$ ) are measured for cellulose hydrolysis in sulphuric acid solutions as reviewed by SriBala et al. [44] (see also Table 1, Kwon et al. [43]).

On IGI impregnated papers, intermediate values of activation energies (approx.  $97 \pm 2 \text{ kJ mol}^{-1}$ ) are measured, questioning a possible superimposition via Eq. (5) of two independent reactions, one corresponding to oxidative chain breaking (low  $E_a$ ) and the other to acidic hydrolysis (high  $E_a$ ). This scenario appears doubtful since reaction rates of IGI impregnated papers are between one and two

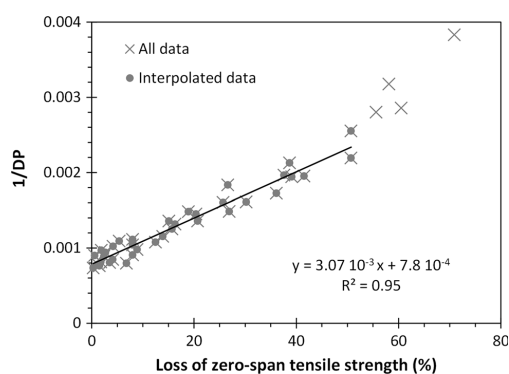


**Fig. 6** Re-computation of zero-span tensile strength and DP data from Zou et al. [14] showing a linear correlation. Selection of some activation energy values related to paper degradation

orders of magnitude above those of blank papers. Indeed, reaction rates measured by Zou et al. [20] at 23 °C (natural ageing) on acidic papers (pH 3.7) are around  $4 \times 10^{-9} \text{ h}^{-1}$  ( $9.98 \times 10^{-8} \text{ day}^{-1}$ ), a value, respectively, 70 and 30 times below reaction rates of Fe + Ac and Fe samples at similar temperature. In these conditions, the weight of acidic hydrolysis terms in Eqs. (3a, 3b) is negligible, meaning that the measured activation energy corresponds to a dominant mechanism. It remains below but not far from the values found for pure acidic hydrolysis. This suggests a mechanism partly related to acidic hydrolysis, but with a catalytic effect of iron implying different reaction intermediates that lower the activation energy.

## 5 Conclusion

This work assesses the reliability of Arrhenius law for IGI chemical damage in temperature range 20–90 °C. It confirms the possibility to extrapolate artificial ageing results to natural ageing conditions. This point is crucial for scientists involved in the chemical aspects of paper degradation. It should, however, be considered with great care by paper conservators and curators as the samples were designed to reproduce the chemical reactions occurring during paper decay by IGI but are not relevant to test the initial step of degradation occurring on original manuscripts, i.e. the migration of iron within the paper sheet because of humidity.

Our measurements show that the mechanism of chain breaking is driven by the combined impact of pH, oxygen and iron. The activation energy of IGI impregnated paper depolymerization ( $97 \pm 2 \text{ kJ mol}^{-1}$ ) is relatively close but inferior to activation energies measured on naturally aged lignin-free acidic papers ( $109 \text{ kJ mol}^{-1}$ ). On the opposite, reaction rates of IGI impregnated papers are 1–2 orders of magnitude above those of lignin-free acidic papers. These observations are not consistent with the superimposition of two different pathways such as acidic hydrolysis and cellulose oxidation, but suggest a dominant hydrolytic process that involves directly or indirectly oxygen and iron.

**Acknowledgments** This work was supported by French state funds managed by the Ile de France Region (DIM Oxymore) and ANR within the “Investissements d’Avenir program” under reference ANR-11-IDEX-0004-02, and more specifically within the framework of the Cluster of Excellence MATISSE led by Sorbonne Universités.

## References

- J. Kolar, M. Strlic, (eds.), *Iron Gall Inks: On Manufacture, Characterisation, Degradation and Stabilisation* (National and University Library, Ljubljana. 2006)
- J. Gust, J. Suwalski, *Corrosion*. **50**, 355 (1994)
- C. Krekel, *Int. J. Forensic Doc. Exam.* **5**, 54 (1999)
- C.H. Wunderlich, R. Weber, G. Bergerhoff, *Zeitschrift für Anorganische und Allgemeine Chemie*. **598/599**, 371 (1991)
- A. Kongdee, T. Bechtold, *Cellulose* **16**, 53 (2009)
- C. Burgaud, V. Rouchon, A. Wattiaux, J. Bleton, R. Sabot, P. Refait, *J. Electroanal. Chem.* **650**, 16 (2010)
- J.G. Neevel, *Restaurator*. **16**, 143 (1995)
- M. Strlic, J. Kolar, (eds.), *Ageing and Stabilisation of Paper* (National and University Library, Ljubljana. 2005)
- P. Calvini, *Cellulose* **12**, 445 (2005)
- S. Zervos, in *Cellulose: Structure and Properties, Derivatives and Industrial Uses*, ed. by A. Lejeune and T. Deprez (Nova Science, 2010), p. 155–203
- F. Shafizadeh, A.G.W. Bradbury, *J. Appl. Polym. Sci.* **23**, 1431 (1979)
- A.M. Emsley, G.C. Stevens, *Cellulose* **1**, 26 (1994)
- E.H. Daruwalla, M.G. Narsian, *Tappi J.* **49**, 106 (1966)
- X. Zou, T. Uesaka, N. Gurnagul, *Cellulose* **3**, 243 (1996)
- P.L. Bégin, E. Kaminska, *Restaurator*. **23**, 89 (2002)
- J. Shahani, S.B. Lee, F.H. Hengemihle, G. Harrison, P. Song, *Accelerated Aging of Paper. I: Chemical Analysis of Degradation Products, II: Application of Arrhenius Relationship, III: Proposal for a new Accelerated Aging Test*, ASTM research Program, Library of Congress, Washington, 2001
- E. Kaminska, P. Bégin, D. Grattan, D. Woods, A. Bülow, *Accelerated aging test method development for American Society for Testing and Materials Institute for Standards Research*, ASTM Research Program, Canadian Conservation Institute, Ottawa, 2001
- J. M. Reilly, D. W. Nishimura, E. Zinn, *New tools for preservation: assessing long-term environmental effects on library and archives collections* (Commission of Preservation and Access, Washington, 1995), [www.clir.org/pubs/reports/pub59/pub59.pdf](http://www.clir.org/pubs/reports/pub59/pub59.pdf). Accessed 15 July 2015
- Standard BSI PAS 198 (2012)
- X. Zou, T. Uesaka, N. Gurnagul, *Cellulose* **3**, 269 (1996)
- D. Kocar, M. Strlic, J. Kolar, J. Rychly, L. Matisova-Rychla, B. Pihlar, *Polym. Degrad. Stabil.* **88**, 407 (2005)
- M. Strlic, J. Kolar, (eds.), *Ageing and Stabilisation of Paper* (National and University Library, Ljubljana. 2005)
- J. Kolar, A. Stolfa, M. Strlic, M. Pompe, B. Pihlar, M. Budnar, J. Simcic, B. Reissland, *Anal. Chim. Acta.* **555**, (2006). doi:10.1016/j.aca.2005.08.073
- V.S. Selih, M. Strlic, J. Kolar, B. Pihlar, *Polym. Degrad. Stabil.* **92**, 1476 (2007)
- M. Strlic, J. Kolar, B. Pihlar, *Polym. Degrad. Stabil.* **73**, 535 (2001)
- V. Rouchon, M. Duranton, C. Burgaud, E. Pellizzi, B. Lavedrine, K. Janssens, W. de Nolf, G. Nuyts, F. Vanmeert, K. Hellemans, *Anal. Chem.* **83**, 2589 (2011)
- Standart ISO 535 (2014)
- Standart ISO 17812 (2007)
- Standard ISO 6588-1 (2005)
- T. Sawoszczuk, A. Baranski, J.M. Lagan, T. Lojewski, K. Zieba, *J. Cult. Herit.* **9**, 401 (2008)
- Standart ISO 5351 (2010)
- R. Evans, A.F.A. Wallis, in 4th International Symposium on Wood and Pulping Chemistry, Paris, Palais des Congrès, 27th–30th April 1987 (1987)
- J. Tetreault, A.L. Dupont, P. Bégin, S. Paris, *Polym. Degrad. Stabil.* **98**, 1827 (2013)
- Standard TAPPI T 231 cm-96 (1996)
- J. Rychly, M. Strlic, L. Matisova-Rychla, J. Kolar, *Polym. Degrad. Stabil.* **78**, 357 (2002)
- P. Calvini, *Cellulose* **21**, 1127 (2014)
- A.M. Emsley, *Cellulose* **15**, 187 (2008)

38. A.M. Emsley, *Cellulose* **15**, 239 (2008)
39. V. Rouchon, B. Durocher, E. Pellizzi, J. Stordiau-Pallot, *Stud. Conserv.* **54**, 236 (2009)
40. V. Rouchon, M. Duranton, O. Belhadj, M. Bastier Desroches, V. Duplat, C. Walbert, B. Vinther Hansen, *Polym. Degrad. Stabil.* **98**, 1339 (2013)
41. O. Belhadj, C. Phan Tan Luu, E. Jacobi, S. Meslet-Struyve, S. Vez, B. Reissland, V. Rouchon, *J. Pap. Conserv.* **15**, 9 (2014)
42. A.L. Dupont, Le patrimoine culturel sur papier: de la compréhension des processus d'altération à la conception de procédés de stabilisation, Chemical Sciences, Evry Val d'Essonne University, 85 p. (2014) <https://tel.archives-ouvertes.fr/tel-01115774/document>. Accessed 20th July 2015
43. Y. Kwon, S.E.F. Kleijn, K.J.P. Schouten, M.T.M. Koper, *ChemSusChem*. **5**, 1935 (2012)
44. G. SriBala, R. Vinu, *Ind. Eng. Chem. Res.* **53**, 8714 (2014)

# Appendix I

## Sugar calibration by electrophoresis

Standard mother solutions of cellobiose and glucose were prepared in milli-Q water at 5000 ppm and 1000 ppm, respectively. In order to prepare a stock solution, 4 mL of these mother solutions were derivatized 1 h at 80 °C by adding 4 mL of ABEE reagent solution (mixture of 100 mg · mL<sup>-1</sup> of ABEE (benzocaïne) and 100 mg · mL<sup>-1</sup> of acetic acid 99.6 %, Carlo Erba Reagents dissolved in MeOH) and 40 mL of sodium cyanoborohydride (95 %, Aldrich). At the end of the reaction, 12 mL of borate buffer (450 mmol · L<sup>-1</sup>, pH 8.6)<sup>1</sup> were added to precipitate excess of ABEE and filtrated (0.20 µm PTFE, Macherey-Nagel).

The derivatized sugar solutions were then diluted in volumetric flasks using a mixture of milli-Q water, acidified methanol and borate buffer pH 8.6 (1:1:3) as solvent of dilution to keep the same proportions as the ones in the sample solution. Concentrations of standards were determined by weighting solutions in order to be more accurate than by using volumes.

Analysis with capillary electrophoresis with the protocol described in part c led to the calibrations curves of cellobiose (Fig. I.1A) and glucose (Fig. I.1B).

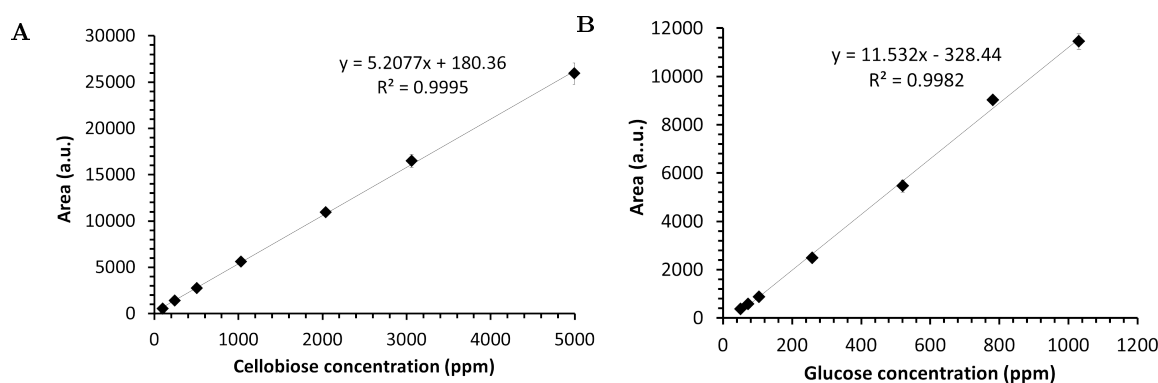


FIG. I.1 – Calibration curve of (A) cellobiose and (B) glucose.

<sup>1</sup>prepared by dissolving boric acid (99.79 %, Fisher Chemicals) in milli-Q water and adjusting pH with sodium hydroxide 1 mol · L<sup>-1</sup> (Fisher Chemicals)



# Appendix J

## Test of iron elimination with cation exchange resin

The use of a resin was tested to try to eliminate iron from the cellobiose mixture at the end of the measurement (in order to attempt NMR analysis). The resin 50W from Biorad was tested. This resin is composed of copolymer matrix styren-divinylbenzen and sulfonate groups are used to do the cation exchange. Iron ions are replaced by protons with this resin type and thus led to an acidification of the medium.

Preliminary tests were done without cellobiose to see how much the resin could remove of iron. The resin was available in the laboratory and had been used before. Consequently, before use, the resin was regenerated to be sure all sites are be available. This was done with HCl, as recommended by Biorad [279].

Iron sulfate solutions at the same concentration in iron as the cellobiose mixture were prepared.

### J.1 Estimation of the amount of resin needed

The volume of sample to filtrate was 4 mL. Iron concentration in the sample was around  $42 \text{ mmol} \cdot \text{L}^{-1}$  which equalizes  $2.35 \text{ g} \cdot \text{L}^{-1}$  in total iron concentration. In 4 mL of the sample, there are 9.4 mg of iron.

$$Eq = \frac{\text{weight(g)}}{\frac{M_w}{\text{average ion valence}}} \quad (\text{J.1})$$

In terms of equivalent, it represents 0.42 mEq if an average of the valence between iron(II) and iron(III) is taken (2.5).

The resin capacity being  $0.6 \text{ mEq mL}^{-1}$ , at least 0.7 mL of the resin should be taken. This is equivalent to 0.49 g of wet resin (resin density 0.7).

1.5 g were chosen in order to be sure to have enough resin to chelate all cations.

### J.2 Test in batch mode

The batch method was chosen. 1.5 g were weighted in a beaker and 4 mL of iron sulfate solution was added. The solution was stirred one hour and then filtrated onto a whatman filter on a buchner flask. Three successive batches were done on the same solution. Improvement of iron elimination was observed (FIG. J.1).

The first batch allows the elimination of 99 % of the ionic iron present in solution. After three batches one per thousand of the ionic iron present in solution has disappeared. Although this is quite good, this concentration is still too high to do for example NMR measurements and help products characterization. This elimination of iron could also have been of interest regarding HPLC-TPA analysis, to avoid column blockage. However, in this latter case, paper extracts are obtained in so small a volume that batch purification would have led to a loss of sample. Other commercial cartridges (CHROMAFIX PS-H<sup>+</sup>, Macherey Nagel) were tested for this particular application but led to impurities detectable on the chromatogram.

<b>Batch</b>	<b>[Total ionic Iron] mmol · L<sup>-1</sup></b>	<b>Elimination factor</b>
Initial solution	43.5	
Batch 1	0.398	109
Batch 2	0.0962	452
Batch 3	0.042	1035

TAB. J.1 – *Monitoring of iron elimination.*

# Appendix K

## STXM

### K.1 Conversion of exposure times to dose

The dose  $D$  is the total amount of deposited energy per mass of material. It can be expressed in Gy ( $\text{J} \cdot \text{kg}^{-1}$ ) using the exposure time  $t$  of the sample to X-rays beam and the absorbed flux of X-rays  $F$ , which is the number of absorbed photons per second (IV.2). The flux  $F$  is also defined as function of the intensity  $I$  by the equation K.1:

$$F = \frac{I_0 - I_t}{\epsilon} = \frac{I_0 \cdot (1 - \exp(-OD))}{\epsilon} \quad (\text{K.1})$$

with:

$\epsilon$ , the detector efficiency;

$OD$ , the optical density.

Parameters values of our measurements are reported in the table K.1. Some of them have been roughly estimated since accurate data were not available. By using the equation K.1, the dose rate was evaluated for the two energies used to map the “ink<sub>O</sub>+gum drop” sample, i.e. 707.8 eV and 709.8 eV. These values of the dose-rate were then used to obtain the absorbed doses, multiplying by the exposure time. Since the dose-rate is energy-dependant, the dose deposited in the sample during the cumulative scans at each energy has been evaluated (table K.3, column 4). Next, the total dose received by the sample when alternating scans at 707.8 eV and 709.8 eV was obtained by the combination of doses at single energy (table K.3, column 6).

Symbol	Property	Value	Source
$I_0$	Incident intensity	20 MHz $\pm$ 0.05	average value during shifts
	slits	20/20	logbook
	Spot size	43 nm	35 nm zone plate spot size
$d$	sample thickness	100 nm $\pm$ 2	FIB section
$\rho$	sample density	1.8 g $\cdot$ cm <sup>-3</sup> $\pm$ 0.01	prussian blue value
$\epsilon$	detector efficiency	0.5 $\pm$ 0.01	estimated
$E$	energy	708.8 eV $\pm$ 0.2	average
$V$	sample volume irradiated	1.452 $\cdot$ 10 <sup>5</sup> nm <sup>3</sup> $\pm$ 2.9 $\cdot$ 10 <sup>3</sup>	calculation with round spot
$m$	sample mass	2.61 $\cdot$ 10 <sup>-19</sup> kg $\pm$ 5.43 $\cdot$ 10 <sup>-21</sup>	calculated
$OD$	optical density	0.16 $\pm$ 0.01	average of first & last values
$I_0 - I_t$	absorbed flux per volume	2.93 MHz $\pm$ 0.03	calculated
$d_R$	Dose rate	2540.0 MGy $\cdot$ s <sup>-1</sup> $\pm$ 77.8	calculated

 TAB. K.1 – *Parameters used to convert exposure time to dose.*

E	Maps @ E	time (ms)	Dose (MGy)
707.8 eV	1	1	2.54
	2	2	5.08
	3	3	7.62
	4	4	10.16
	5	5	12.70
	6	6	15.24
	7	7	17.78
	8	8	20.32
	9	9	22.86
	10	10	25.40
	15	15	38.10
	20	20	50.80
	25	25	63.50
	30	30	76.20
	35	35	88.90
	40	40	101.61
45	45	114.31	
50	50	127.01	
55	55	139.71	
60	60	152.41	

 TAB. K.2 – *Doses calculation at one energy.*

E	Total maps	Cumulative dose (MGy)	OD	Dmg	$Dmg_{\infty} - Dmg$	$\ln(Dmg_{\infty} - Dmg)$
707.8 eV			0.137*			
	1	2.54	0.145	0.008	0.042	-3.170
	3	7.62	0.155	0.018	0.032	-3.442
	5	12.70	0.161	0.024	0.026	-3.650
	7	17.78	0.166	0.029	0.021	-3.863
	9	22.86	0.168	0.031	0.019	-3.963
	11	27.94	0.169	0.032	0.018	-4.017
	13	33.02	0.170	0.033	0.018	-4.046
	15	38.10	0.172	0.035	0.015	-4.200
	17	43.18	0.173	0.036	0.014	-4.269
	19	48.26	0.173	0.036	0.014	-4.269
	25	63.50	0.178	0.041	0.009	-4.711
	35	88.90	0.180	0.043	0.007	-4.962
	45	114.30	0.182	0.045	0.005	-5.298
	55	139.70	0.182	0.045	0.005	-5.298
	65	165.10	0.179	0.042	0.008	-4.828
	75	190.50	0.180	0.043	0.007	-4.962
85	215.90	0.182	0.045	0.005	-5.298	
95	241.30	0.183	0.046	0.004	-5.221	
105	266.70	0.184	0.047	0.003	-5.809	
115	292.10	0.185	0.048	0.002	-6.215	
			$Dmg_{\infty} = 0.050$			
709.8 eV			0.188*			
	2	5.08	0.181	0.007	0.048	-3.037
	4	10.16	0.170	0.023	0.032	-3.442
	6	15.24	0.165	0.023	0.032	-3.442
	8	20.32	0.160	0.028	0.027	-3.612
	10	25.40	0.155	0.033	0.022	-3.817
	12	30.48	0.153	0.035	0.020	-3.912
	14	35.56	0.149	0.039	0.016	-4.135
	16	40.64	0.150	0.038	0.017	-4.075
	18	45.72	0.150	0.039	0.017	-4.104
	20	50.80	0.148	0.040	0.015	-4.200
	30	76.20	0.146	0.042	0.013	-4.343
	40	101.60	0.143	0.045	0.010	-4.605
	50	127.00	0.142	0.046	0.009	-4.711
	60	152.40	0.142	0.046	0.009	-4.711
	70	177.80	0.135	0.053	0.002	-6.215
	80	203.20	0.136	0.052	0.003	-5.809
90	228.60	0.137	0.051	0.004	-5.521	
100	254.00	0.136	0.052	0.003	-5.809	
110	279.40	0.137	0.051	0.004	-5.221	
120	304.80	0.138	0.050	0.005	-5.298	
			$Dmg_{\infty} = 0.055$			

\* Estimated undamage.

TAB. K.3 – Doses calculation and damage estimation.

## K.2 Critical doses estimation

The critical dose is the dose that attenuates (or increments) a specific spectroscopic feature by 63 %. The critical dose was determined from the dose–damage data by fitting it with the following equation K.2:

$$Dmg = Dmg_{\infty} + A \cdot \exp\left(\frac{D}{D_c}\right) \quad (\text{K.2})$$

with:

$Dmg$ , a measure of damage;

$Dmg_{\infty}$ , the saturation damage in the same scale;

$A$ , a constant;

$D$ , radiation dose;

$D_c$ , the critical dose.

The  $Dmg$  value was evaluated with the optical density. It was obtained by subtracting an estimation of undamaged  $OD$  with the actual  $OD$  value. The  $Dmg_{\infty}$  value is the maximum value of the damage. If the damage process follows first-order kinetics, a plot of  $\ln(Dmg - Dmg_{\infty})$  versus dose  $D$  (in MGy) should be linear with a slope of  $\frac{1}{D_c}$ .

Figures K.1 and K.2 plot  $\ln(Dmg - Dmg_{\infty})$  versus dose  $D$  for the two energies and corresponding linear fit. The two linear fits have the same slope from which is calculated a first-order critical dose of 125 MGy. Adequation of the data and the linear fit is approximative, suggesting that the radiation damage does not really follow a first-order kinetic. It probably involves other pathways, such as mass loss, new bonding formation . . . . Hence the obtained first-order critical dose gives a raw approximation of the radiation sensitivity the sample.

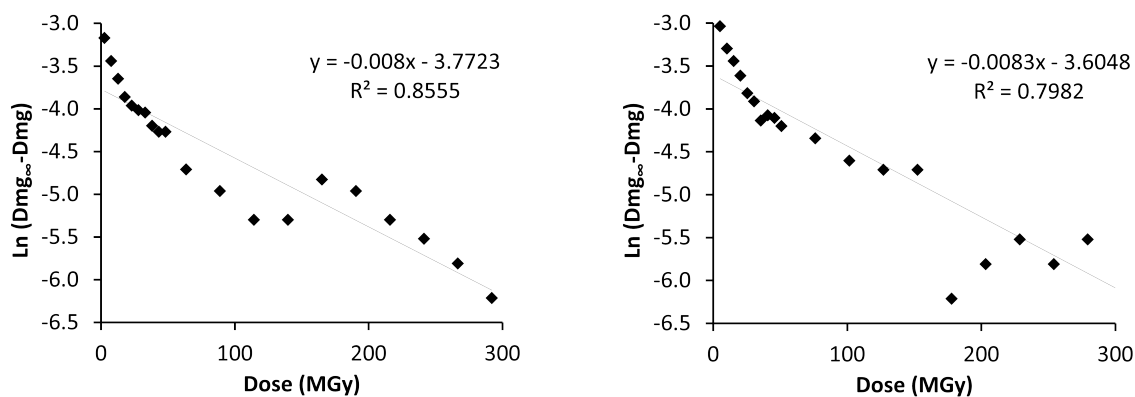


FIG. K.2 –  $\ln(Dmg - Dmg_{\infty})$  versus dose  $D$  for the peak at 709.8 eV.

## K.3 Parameters for stack acquisition

### K.3.1 Iron edge

	Start E (eV)	End E (eV)	Range (eV)	Points	Step (eV)	Dwell time (ms)
1	700	706	6	7	1	1
2	706.2	714	7.8	40	0.2	1
3	714.2	720	5.8	7	0.967	1

TAB. K.4 – Parameters used for recording of stacks at iron edge.

### K.3.2 Carbon edge

	Start E (eV)	End E (eV)	Range (eV)	Points	Step (eV)	Dwell time (ms)
1	270	283	13	15	1	1
2	283.2	292	8.8	89	0.1	1
3	292.2	305	12.8	27	0.492	1
4	305.2	325	19.8	14	1.523	1

TAB. K.5 – Parameters used for recording of stacks at carbon edge.

### K.3.3 Nitrogen edge

	Start E (eV)	End E (eV)	Range (eV)	Points	Step (eV)	Dwell time (ms)
1	395	398	3	7	0.5	1
2	398.2	408	9.8	66	0.151	1
3	408.2	415	6.8	15	0.486	1
4	415.5	435	19.5	21	0.975	1

TAB. K.6 – Parameters used for recording of stacks at carbon edge.



# Résumé

Les collections muséales refferment de nombreux objets historiques. Ils ne sont cependant pas toujours dans un bon état de préservation dû à une dégradation des matériaux qui les constituent. Concernant plus particulièrement les documents graphiques, les encres ferro-galliques posent notamment problème au sein des collections en engendrant une dégradation du support papier. Elles ont été utilisées majoritairement pour l'écriture jusqu'au vingtième siècle et bien que de nombreuses recettes existent, elles sont constituées majoritairement de trois ingrédients: un extrait de noix de galles, du sulfate de fer(II) et de la gomme Arabique. Ce dernier ingrédient sert de liant et aide à la dispersion du précipité ferro-gallique bleu-noir qui se forme par complexation du fer avec de l'acide gallique contenu dans l'extrait de noix de galles.

Lors de l'application de ces encres sur le support papier ou après une exposition à une forte humidité, une partie des constituants peut diffuser et entraîner des réactions chimiques conduisant à la dégradation de la cellulose, principal composant du papier. Ce phénomène est communément appelé corrosion du papier par les encres ferro-galliques. Cette altération va se manifester visuellement par la formation de halos bruns autour des lignes d'écriture et une fragilisation du papier qui peut entraîner la formation de lacunes au cours de la manipulation des pages des manuscrits.

Cette fragilisation provient de la dépolymérisation des chaînes de cellulose, suite à la rupture de liaisons glycosidiques reliant les monomères (unité anhydroglucose) entre eux. Concernant les encres ferro-galliques, deux mécanismes sont suspectés être à l'origine de ces coupures de chaînes: l'hydrolyse acide dûe au faible pH des encres et l'oxydation radicalaire à cause de la présence de fer.

En ce qui concerne les papiers acides non-imprégnés de fer, l'hydrolyse acide est considérée comme majoritaire en dessous de 100 °C, alors que l'oxydation est majoritaire au dessus de 100 °C. Dans des conditions d'humidité et de températures pas trop drastiques, l'hydrolyse acide est considérée comme prédominante et l'oxydation comme jouant un rôle mineur.

Dans le cas des encres ferro-galliques, la présence de fer pourrait promouvoir la formation de radicaux hydroxyles via des réactions de Fenton et ainsi favoriser les coupures de chaînes. Ces radicaux hydroxyles ont été mis en évidence dans le cas de la dégradation de la cellulose en milieu basique mais pas en milieu acide tel que celui des encres ferro-galliques. Une étude récente [111] au sein du CRC a montré le rôle primordial de l'oxygène dans la dépolymérisation à température ambiante des papiers encrés. Ces observations semblent remettre en question la prédominance du mécanisme d'hydrolyse par rapport à celui d'oxydation. Cette étude nous a conduits à entreprendre ce travail de thèse dont l'objectif vise à mieux comprendre les mécanismes en jeu dans la dégradation de la cellulose en présence de fer. Ce travail se découpe en trois parties complémentaires. Les

deux premières parties concernent les aspects chimiques de la dégradation : l'étude des Espèce réactive de l'oxygène (ERO) et des coupures de chaînes alors que la dernière partie concerne la distribution des différents constituants de l'encre au sein de fibres de papier.

## Étude des espèces réactives de l'oxygène

Les ERO sont des espèces formées à partir de l'oxygène moléculaire. Il peut s'agir d'espèces radicalaires ou d'entités non-radicalaires électrophiles : i) *espèces produites par activation de l'oxygène* : oxygène singulet, ion superoxyde  $O_2^{\cdot-}$ , radicaux hydroxyles  $OH^{\cdot}$ , peroxyde d'hydrogène  $H_2O_2$  ; ii) *espèces organiques*: hydroperoxydes  $R-OOH$ , radicaux hydroperoxydes  $R-OO^{\cdot}$  ; iii) *espèces metal-oxo* : ion perferryle  $(Fe^{IV}-O_2)^{2+}$ , ion ferryle  $(Fe^{IV}=O)^{2+}$ , anion-radical superoxo  $Fe^{III}-O_2^{\cdot-}$ , ou d'autres espèces telles que les  $\mu$  peroxy,  $\mu$  oxo, alkylperoxy, hydroperoxy.

Ces espèces sont très réactives et ont des durées de vie assez courtes (1 ns). Il est donc nécessaire d'utiliser des réactions de piégeage pour les observer. Dans ce travail, nous avons décidé d'utiliser deux techniques pour l'étude des ERO, la chromatographie liquide haute performance et la spectroscopie de Résonance paramagnétique électronique (RPE) pour rechercher la présence de ERO dans la dégradation de papiers encrés. La première technique a été utilisée pour la détection et quantification des radicaux hydroxyles avec une méthode spécifique basée sur la réaction de l'acide téréphtalique (TPA) avec les radicaux hydroxyles pour former l'acide hydroxytéréphtalique (HTPA). Elle est sensible (de l'ordre de  $nmol \cdot L^{-1}$ ) et cumulative, permettant donc le piégeage de radicaux hydroxyles au fur et à mesure de leur formation sur une période de vieillissement donnée. La seconde technique, la RPE, permet la détection de plusieurs ERO. Des piègeurs de radicaux (SP), tel que le DMPO et le POBN, ont été utilisés afin de détecter d'éventuelles ERO. En effet, ces piègeurs permettent la formation d'adduits radicalaires de plus grande durée de vie que celles des ERO et donc leur observation. L'utilisation additionnelle de molécule relais (telle que le formiate de sodium ou des alcools) permet la détection d'un spectre plus large d'espèces électrophiles, au détriment de la détermination de la nature exacte de l'espèce. Ces piègeurs sont utilisés en solution et dans le cas de nos expériences, ont été mis en contact avec des papiers imprégnés vieillis naturellement à 50 % d'humidité et 23 °C en enceinte climatique. Afin de comparer les résultats obtenus, des tests de lixiviation du fer ont aussi été réalisés et des solutions modèles ont été préparées.

En l'absence de molécules relais dans les échantillons, aucun adduit, notamment avec les radicaux hydroxyles, n'a été détecté par spectroscopie RPE. Lors de tests effectués en chromatographie liquide, des radicaux hydroxyles ont été identifiés sur des papiers imprégnés de sulfate de fer(II) mais pas sur des papiers encrés. Cela pourrait être dû au caractère anti-oxydant de l'acide gallique, présent dans l'encre. Les concentrations détectées sont cependant très faibles ( $8 nmol \cdot g^{-1}$  après 48 jours de vieillissement). Cela est cohérent avec l'absence de signal en spectroscopie RPE, technique dont la limite de détection est de l'ordre du  $\mu mol \cdot L^{-1}$ .

Cependant, l'utilisation combinée du piègeur de radicaux avec le formiate de sodium a donné lieu à la formation de l'adduit radicalaire correspondant ( $DMPO-CO_2^{\cdot-}$ ) en présence de papiers imprégnés de sulfate de fer et d'encre, suggérant ainsi la présence d'une autre espèce que les radicaux hydroxyles (FIG. 1). L'analyse de solutions modèles a montré que la formation de l'adduit nécessitait la présence de fer(II) et d'oxygène, ainsi qu'un pH quasi neutre.

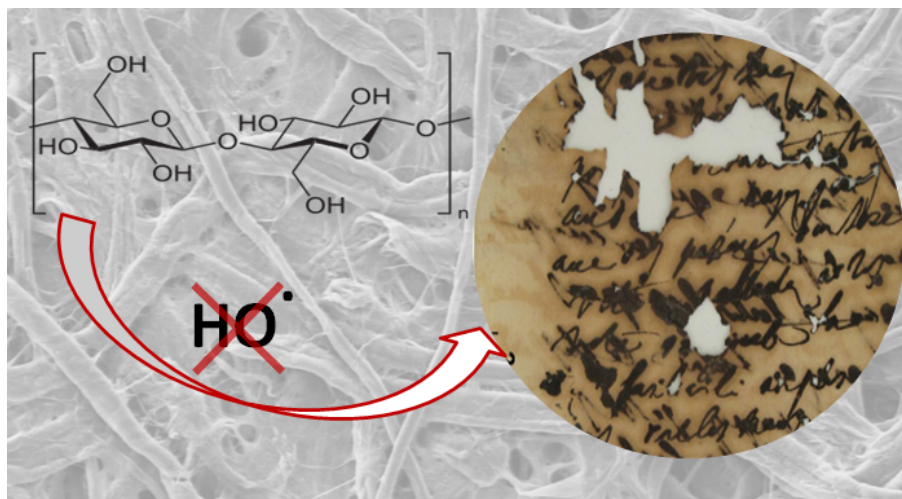


FIG. 1 – Les espèces réactives de l'oxygène en jeu dans la corrosion du papier par les encres ferrogalliques ne sont pas des radicaux hydroxyles.

La concentration en adduits  $\text{DMPO} - \text{CO}_2^-$  varie en fonction du vieillissement du papier : elle augmente durant les vingt-quatre premières heures, puis diminue au cours des vingt jours suivants pour finalement se stabiliser. Cela pourrait être corrélé à la dépolymérisation des papiers et à l'oxydation du fer(II).

Au vu de l'importance du fer sur les signaux obtenus, des tests de lixiviation du fer en solution ont été effectués. Des extractions aqueuses des papiers imprégnés de sulfate de fer (II) et d'encre ont été réalisées afin de mesurer les concentrations de fer en solution par spectroscopie UV-visible. Les échantillons de papier ont aussi été analysés par spectroscopie RPE solide avant et après lavage afin de déterminer la présence éventuelle de radicaux organiques et les environnements du fer (III). Ces analyses ont montré que la lixiviation du fer en solution est importante mais diminue avec le temps de vieillissement du papier. Cette diminution peut s'expliquer par un attachement plus fort du fer à la cellulose.

L'impact du fer(II) sur la concentration de l'adduit  $\text{DMPO} - \text{CO}_2^-$  a été étudié à l'aide de solutions modèles entre  $0.01 \text{ mmol} \cdot \text{l}^{-1}$  to  $10 \text{ mmol} \cdot \text{l}^{-1}$ . Pour une concentration en fer supérieure à  $10 \text{ mmol} \cdot \text{l}^{-1}$ , une disparition du signal est observée. Cette disparition pourrait être due à une diminution du pH ou à la présence de fer(II).

L'utilisation du TEMPOL, un radical nitroxyde stable, a permis de montrer que dans la gamme de pH utilisée, celui-ci a peu d'influence contrairement à la présence de fer. Ce dernier peut réduire le radical nitroxyde en une hydroxylamine, non détectable par spectroscopie RPE.

## Coupage de la liaison glycosidique

La coupure de la liaison glycosidique est à l'origine du processus de dépolymérisation de la cellulose. Dans un premier temps, l'étude s'est portée sur la dépolymérisation d'échantillons modèles de papiers imprégnés d'encre, qui ont la particularité de se dégrader à température ambiante et permettent ainsi d'étudier la stabilité de la loi d'Arrhenius à cette température. Dans un second temps, la dégradation d'une molécule modèle, la cellobiose, a été étudiée. La cellobiose est la plus petite unité répétitive de la cellulose. Elle est plus simple à étudier que la cellulose grâce au large éventail de techniques d'analyse

auxquelles elle peut se prêter. Bien que le choix de cette molécule modèle ne puisse fournir qu'une compréhension partielle des processus de dégradation intervenant dans un matériau aussi complexe que le papier, il paraît tout à fait approprié pour clarifier la combinaison de paramètres favorisant la coupure de la liaison osidique dans le cas de la dépolymérisation induite par le fer. A la lumière des observations faites dans la partie précédente, le fer, l'oxygène et le pH sont les trois paramètres qui ont été étudiés afin de déterminer leur rôle dans la dégradation de la cellobiose. Des tests préliminaires ont d'abord effectués sur des systèmes solides en imprégnant la cellobiose avec du sulfate de fer. En raison de sa tendance à cristalliser, les systèmes solides se sont finalement révélés inappropriés et les études se sont poursuivies sur des systèmes en solution dans lesquels une bonne mise en contact entre la cellobiose et le fer (ferrique/ferreux) a pu être réalisée.

La dégradation d'échantillons de papier Whatmann modèles imprégnés d'encre a été suivie par viscosimétrie et des tests de résistance mécanique du double pli (zero-span mechanical testing). Ces échantillons ont été préparés par imprégnation avec une encre modèle constitué d'un mélange de en sulfate de fer(II) heptahydraté à  $40 \text{ g} \cdot \text{L}^{-1}$  et d'acide gallique monihydraté à  $9 \text{ g} \cdot \text{L}^{-1}$ . Ainsi préparés, les papiers encrés modèles manière à subir une dépolymérisation rapide même à température ambiante. Le modèle d'Ekenstam a été utilisé pour déterminer la constante de vitesse des coupures de chaînes cellulosiques. Cette constante cinétique s'est révélée beaucoup plus que celle reportée dans la littérature pour des papiers acides (1-2 ordres de grandeur au-dessus). Ces constantes de vitesse mesurées à différentes températures ont ensuite permis la détermination des énergies d'activation grâce à la loi d'Arrhenius. Il a été montré que : l'extrapolation de la loi d'arrhénius à température ambiante est valide ; les énergies d'activation des papiers encrés modèles sont proches de celles reportées dans la littérature pour des papiers acides sans lignine. L'ensemble de ces observations sont cohérentes avec un processus d'hydrolyse acide prédominant dont la barrière d'énergie est réduite par la présence d'oxygène et de fer.

Afin de poursuivre les investigations sur ces mécanismes de dégradation, une molécule plus simple est choisie comme modèle, la cellobiose.

L'étude de la dégradation de la cellobiose en solution montre que le pH est le paramètre ayant le plus d'impact : pour un pH fixé à 3.6, aucune modification n'est observée, indépendamment des autres paramètres (présence de fer et/ou d'oxygène). A un pH de 1.6, une conversion de la cellobiose est observée pour tous les échantillons, signifiant que l'hydrolyse acide est le principal mécanisme de coupure de la liaison glycosidique. Lorsque le fer et l'oxygène sont présents simultanément, des réactions additionnelles se produisent et consomment le glucose et/ou la cellobiose. Ces réactions sont liées aux réactions d'oxydo-réduction impliquant le fer et l'oxygène, mais requièrent elles aussi un pH faible.

La caractérisation des différents produits des réactions intervenant dans la solution contenant du fer à pH 1.6 a été effectuée par spectroscopie infrarouge et spectroscopie de masse.

Durant les trois premiers jours de vieillissement, l'hydrolyse est prédominante, en lien avec l'oxydation du fer qui acidifie le milieu et conduit à la formation d'hydroxyde de fer. Après sept jours de vieillissement, des produits autres que le glucose sont observés par électrophorèse capillaire et spectroscopie infrarouge, attestant de la formation de groupes C=O provenant majoritairement d'oxydation ou de déshydratation. De l'acide formique et de l'acide acétique ont aussi été détectés, mais en raison de leur volatilité, il est peu probable qu'ils soient responsables des bandes infrarouges observées, sachant que les échantillons

ont été lyophilisés avant les mesures de spectroscopie infrarouge.

Les études menées sur les échantillons modèles de papier imprégné d'encre et sur la cellobiose en solution ont conduit à une même conclusion que l'hydrolyse (favorisée par l'oxydation du fer et la précipitation de composés ferriques) est le mécanisme prédominant lors de la coupure des chaînes. Cependant, le faible pH auquel les coupures sont observées pour la cellobiose (pH 1.6) est largement inférieur au pH classiquement mesuré lors des extractions aqueuses du papier (pH 3-4). Ces pH d'extractions aqueuses correspondant à une moyenne des espèces acides lixiviées en solutions, des valeurs de pH plus faibles pourraient exister localement dans le papier. Cela pourrait être le cas s'il y avait une répartition inhomogène du fer. Il est alors utile de déterminer la répartition de fer, et plus particulièrement de fer(II), dans les fibres de papier serait utile pour confirmer cette hypothèse. Le diamètre des fibres de papier étant de l'ordre du dixième de micromètre, une technique à l'échelle du nanomètre telle que la spectro-microscopie de rayons X en transmission semblait prometteuse pour poursuivre cet objectif. Cette technique permet en outre de cartographier la spéciation de plusieurs éléments comme le carbone, l'azote, le fer, etc. La partie suivante abordera les différentes possibilités offertes par cette technique pour déterminer la répartition de plusieurs ingrédients de l'encre dans les fibres de papier.

## **Distribution des constituants de l'encre au sein des fibres de papier**

La dégradation du papier par les encres ferro-galliques n'est pas seulement gouvernée par les réactions chimiques de coupures de liaisons glycosidiques mais aussi par la pénétration de l'encre à l'intérieur du papier et plus particulièrement des fibres de cellulose. Les fibres de papiers sont très hydrophiles, c'est pour cela que lors de la fabrication du papier, un encollage est nécessaire. Cette opération consiste en l'ajout d'un adhésif, comme par exemple de la gélatine, pour rendre le papier moins perméable à l'eau et en faire un support adéquat pour l'écriture. Par conséquent, l'encollage est un paramètre clé pouvant empêcher la pénétration de l'encre ferro-gallique à l'intérieur du papier au moment de l'écriture. En outre, il a été montré que, sur des manuscrits, le papier est plus perméable à l'eau au niveau du verso des traits d'écritures que dans une zone vierge [49] : l'encollage est donc altéré par les encres ferro-galliques. La migration de l'eau au sein d'une feuille de papier résulte de différents processus qui incluent non seulement les pores à l'intérieur de la feuille mais aussi la sorption et diffusion à l'intérieur des fibres de papier (de diamètre compris entre 5 et 20  $\mu\text{m}$ ). C'est pourquoi il est important d'étudier la distribution des constituants de l'encre et en particulier du fer à une échelle microscopique et nanoscopique. Des études ont déjà été menées sur la distribution de l'encre à l'échelle d'une feuille de papier. Concernant plus particulièrement les encres ferro-galliques, l'émission de rayons X induite par des particules (PIXE) a été utilisée pour déterminer des profils de concentration en éléments métalliques, mais avec une résolution ne permettant pas l'analyse au sein d'une fibre. L'absorption de rayons X (XANES) à la raie K du fer a été très utilisée pour la détermination des états d'oxydation du fer de manière ponctuelle sans permettre d'imager une zone d'intérêt. Cependant, la technique du STXM, spectro-microscopie basée sur l'absorption des rayons X, semble prometteuse dans le but de cartographier à l'échelle nanométrique la distribution des constituants de l'encre et l'encollage à la gélatine. La distribution de l'encollage au sein d'une feuille de papier a aussi été étudiée par fluorescence et microscopie infrarouge. Dans ce travail, il a été décidé de tester la spectroscopie infrarouge couplée à la microscopie à force atomique (AFM-IR) pour cartographier

la distribution de la gélatine au sein d'une fibre.

La préparation des échantillons modèles a été réalisée avec un papier préparé selon un procédé artisanal à partir de chiffons de lin non blanchis. Les fibres ont été individualisées et imprégnées de différentes solutions de gélatine ou d'encre modèle utilisées seules ou l'une après l'autre, la gélatine étant appliquée avant ou après l'encre. Les échantillons n'ont pas été inclus dans une résine afin d'éviter la présence de signatures parasites. Pour la préparation de coupes transversales, deux techniques ont été utilisées : l'ultramicrotomie et les faisceaux d'ions focalisés (FIB). La première technique a été utilisée dans un premier temps car plus accessible et moins coûteuse. La préparation de coupes sans enrobage s'est cependant avérée longue et délicate. Ces premières coupes réalisées sur des fibres imprégnées de gélatine ont été analysées par AFM-IR. Cette technique s'est révélée peu adéquate, premièrement car les fibres étaient souvent endommagées (fissures), deuxièmement car il est difficile d'imager le bord de la coupe et troisièmement car le contact entre les coupes et le cristal d'analyse IR n'était pas uniforme, rendant les résultats des cartographies difficiles à interpréter.

La préparation par FIB a conduit à des coupes globalement en meilleur état et permettant une cartographie du bord de la coupe par STXM. Afin de déterminer la capacité du STXM à être utilisée pour cartographier la distribution des divers composants de l'encre et de l'encollage, des échantillons de références ont aussi été préparés et analysés.

Les spectres d'absorption de rayons X au seuil K du carbone (XANES) sont différents pour la cellulose, la gélatine et les constituants de l'encre, permettant par conséquent de cartographier la distribution de ces constituants dans les échantillons de fibres. Cela est réalisé en choisissant des énergies appropriées, spécifiques au constituant. Des analyses aux seuils K de l'azote et L du fer apportent des informations complémentaires sur la répartition de la gélatine, de l'encre ou du fer libre.

Le fer étant sensible à l'irradiation et son état d'oxydation pouvant varier sous le faisceau, des vérifications ont été réalisées afin de définir les conditions d'analyses les plus adaptées (détaillées dans l'annexe K) pour limiter sa photo-réduction sous le faisceau. L'entièreté de la coupe de l'échantillon a d'abord été analysée avec faible résolution spatiale au seuil L du fer pour des énergies de 700 eV, 707.8 eV, 709.8 eV et 730 eV afin de localiser des zones d'intérêt riches en Fe(II) et en Fe(III). Ces zones ont ensuite subi un balayage complet, toujours au seuil L du fer, mais avec une résolution permettant l'extraction de spectres XANES. Des analyses complémentaires au seuil K du carbone et/ou de l'azote ont été effectuées dans ces mêmes zones. Cela a permis l'identification de régions d'intérêt en limitant l'irradiation de l'échantillon au seuil L du fer. Il est alors possible de déterminer la distribution, dans une même zone, de Fe(II), Fe(III), cellulose, gélatine et composants de l'encre ferro-gallique. La spéciation du fer reste néanmoins qualitative et cette méthodologie peut être améliorée en travaillant à plus basse température afin de limiter les effets secondaires liés à la radiation et les modifications dans la spéciation d'éléments. L'échantillon pourrait alors supporter de plus grandes doses avant d'atteindre le même état de dégradation [253, 254]. Ce refroidissement n'était pas disponible sur la ligne de faisceau au moment des expériences, mais pourrait être explorée lors d'une prochaine étude.

Pour les fibres imprégnées de gélatine (FIG. 2, gauche), le STXM a permis de montrer la présence d'une couche de gélatine à l'extérieur de la fibre, qui ne semble pas pénétrer à l'intérieur de manière suffisamment importante pour être détectée. Dans le cas de fibres non encollées imprégnées d'encre, des composés riches en fer(III) ont été détectés à la

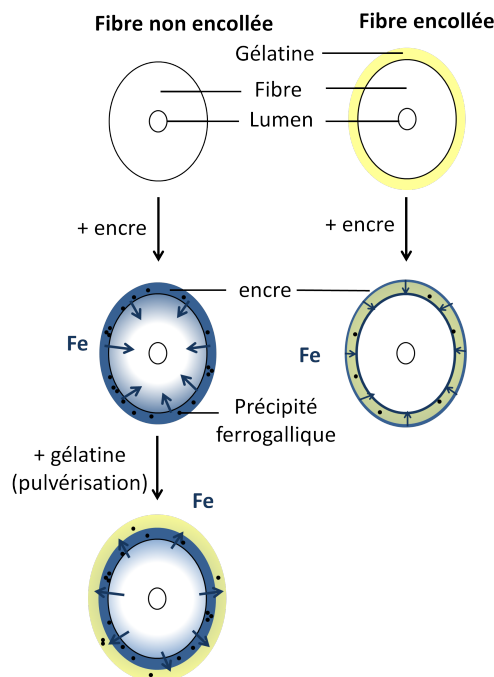


FIG. 2 – *Schema des coupes transversales de fibres de papier et leur comportement après imprégnation encre selon le type de fibre (encollée ou non). Effet de la gélatine application on the diffusion of iron in an inked fiber.*

surface externe de la fibre, correspondant probablement au précipité ferro-gallique. Du fer est aussi présent à l'intérieur de la fibre sous forme d'un mélange de fer(II) et fer(III). Sa répartition est hétérogène : les fissures contiennent beaucoup de fer et les parois de la fibre présentent de plus faibles concentrations. Le fer présent pourrait aussi bien correspondre à des sulfates de fer, des oxo-hydroxydes ou à du fer lié à la cellulose car aucune signature de l'acide gallique ni du précipité ferro-gallique n'a été détectée.

Pour les fibres encollées et imprégnées d'encre (FIG. 2 , droite), la gélatine n'a pas été détectée au seuil du carbone ou de l'azote. Cela est probablement dû à une dissolution dans le bain d'encre réalisé après celui de gélatine ou à une distribution hétérogène le long de la fibre. Cependant, il semblerait que l'encollage ait eu un effet bénéfique, limitant la pénétration de fer au cœur de la fibre. Sur cet échantillon, la signature du précipité n'a pas été détectée, mais la signature de l'acide gallique est clairement visible à l'extérieur de la fibre avec un mélange de fer(II) et de fer(III). Cela pourrait être dû à la compétition de la gélatine pour la chélation du fer.

Concernant les fibres encrées puis imprégnées dans un second temps de gélatine par pulvérisation (FIG. 2 , bas), l'analyse STXM a montré la présence de gélatine à l'extérieur des fibres sans pénétration notable à l'intérieur. Des grains riches en fer(III) majoritairement ont été identifiés à l'extérieur des fibres, piégés dans la gélatine : les signatures XANES au seuil K du carbone pourraient correspondre au précipité ferrogallique. Le fer est également présent au sein de la gélatine, ce qui est cohérent avec sa capacité à chélater le fer. Par contre, aucune trace de fer n'a été détectée à l'intérieur des fibres de papier, suggérant un effet protecteur de la pulvérisation de gélatine post-écriture. Cela est cohérent avec des observations précédentes qui ont montré un ralentissement de la dépolymérisation de papiers encrés après l'application de gélatine par pulvérisation [258].

L'ensemble de ces conclusions est basé sur l'analyse d'un seul échantillon. D'autres échantillons doivent être analysés afin de confirmer ces tendances. Des mesures au seuil K

du soufre serait également intéressantes afin d'estimer la migration des sulfates au cœur des fibres de papier. L'étude d'autres échantillons permettrait également de répondre aux questions suivantes : comment l'encre et le fer se répartissent aux seins d'échantillons anciens ? Est-ce que les composants de l'encre pénètrent différemment lorsqu'ils sont utilisés ensemble ou séparément ? Est-ce que le dépôt de gélatine sur une fibre encrée est aussi bénéfique avec une encre ancienne ? La plupart des échantillons ont été préparés mais pas analysés dû à un temps de faisceau limité. Cette étude a néanmoins montré que le fer est capable de pénétrer à l'intérieur de fibre de papier alors que la gélatine reste plutôt à la surface.

## Conclusion

Les encres ferro-galliques étant à la fois acides et riches en fer, deux mécanismes principaux sont proposés dans la littérature à l'heure actuelle pour expliquer la dépolymérisation des papiers : l'hydrolyse acide et l'oxydation radicalaire. Parmi les radicaux, les radicaux hydroxyles, pouvant être produits par réaction de Fenton, sont souvent présentés comme responsable de la dégradation. Bien que leur présence ai été montrée en milieu basique, la question de leur présence dans un milieu acide tel que celui des encres ferro-gallique est toujours en suspens. Trois approches complémentaires ont été mises en œuvre pour clarifier les mécanismes en jeu dans le cas de la corrosion par les encres ferrogalliques.

Des expériences préliminaires [111] ont montré que la présence combinée de fer(II) et d'oxygène était un paramètre clé provoquant la dépolymérisation des papiers, suggérant l'importance de mécanisme d'oxydation, qui fût ensuite confirmé par la détection de groupements carbonyles dû à l'oxydation de la cellulose. Ces résultats ont conduit à l'étude dans un premier temps des espèces réactives de l'oxygène (ERO) pouvant être impliquées dans la dépolymérisation de la cellulose par oxydation radicalaire.

Deux techniques ont été utilisées afin de rechercher les ERO éventuellement présentes : la spectroscopie de résonance paramagnétique (RPE) et la chromatographie liquide haute performance (HPLC). La première technique a été utilisée sur des échantillons liquides et solides. L'analyse directe d'échantillons de papier par RPE n'a pas révélé la présence de radicaux organiques. Cependant, le fer(III), paramagnétique, a été observé en site pseudo-octaédrique (sous forme de complexe hydraté) et en site rhombique, attribué au fer lié aux groupements carbonyles ou hydroxyles. Ces sites pourraient favoriser la dégradation de la cellulose environnante. La RPE en milieu liquide a été réalisée sur des échantillons de papiers mis en contact avec une solution de piègeur de radicaux (en particulier le DMPO). Ce dernier, utilisé seul, n'a pas permis la détection de radicaux hydroxyles, ni d'autres radicaux (hydroperoxydes, superoxydes). Cependant, l'ajout d'une molécule relai de formiate a conduit à une formation importante d'adduits, pouvant provenir de différentes ERO. Des tests complémentaires ont montré que ce signal était dû à la présence de fer(II) en solution lixivié par le papier et qu'il dépendait de la concentration en fer(II) et de la présence d'oxygène. Ce signal ne peut cependant pas provenir de radicaux hydroxyles. En effet, la chromatographie liquide avec la méthode de l'acide téréphtalique a révélé la formation de radicaux hydroxyles en faibles concentration et uniquement dans les papiers imprégnés de sulfate de fer.

La quantité importante d'ERO produite au sein de solutions de sulfate de fer(II) ou d'encre, pourraient être à l'origine de la coupure de la liaison glycosidique. Afin d'approfondir les mécanismes en jeu, la cinétique de dépolymérisation des papiers encrés

a été étudiée. Cela n'avait pas été précédemment dans la littérature à notre connaissance. Des mesures de viscosité et de résistance mécanique ont été réalisées à différentes températures et les énergies d'activations ont été estimées. Les constantes de vitesses mesurées sur les papiers encrés sont supérieures d'un à deux ordres de grandeur à celles obtenues pour des papiers acides. Pourtant les énergies d'activations sont proches (légèrement inférieures) à celles reportées dans la littérature pour l'hydrolyse acide. Cela suggère un mécanisme d'hydrolyse acide prédominant avec un petit effet catalytique du fer. Cette étude a été complétée par des tests sur une molécule modèle, la cellobiose, afin de mesurer les effets de la présence de fer, du pH et de l'oxygène. La dégradation a été suivie par électrophorèse capillaire et spectroscopie infrarouge. Le pH s'est révélé être le paramètre clé. Le fer et l'oxygène ont provoqué l'acidification du milieu conduisant à la coupure de la liaison glycosidique. La présence de sulfate de fer a induit la formation de co-produits avec des groupes carbonyles, probablement suite à la dégradation du glucose.

Le faible pH (1.5) atteint lors de ces expériences en présence d'oxygène et de fer(II) est très inférieur à celui de papiers imprégnés de sulfate de fer. Cela nous a conduits à envisager la présence de spots localisés riches en fer pouvant provoquer une forte acidité locale. Cette hypothèse de répartition inhomogène du fer dans le papier a été étudiée par STXM. Des coupes transversales de fibres de papiers ont été réalisées par FIB. Pour des échantillons non encollés, du fer a été mesuré au sein des fibres, renforçant la thèse de l'hydrolyse acide comme mécanisme prédominant. La spectro-microscopie STXM s'est montrée adéquate pour cartographier la distribution des éléments à l'échelle nanoscopique au sein d'une fibre de papier. La répartition de la gélatine, de l'acide gallique et du fer(II) et fer(III) a donné des informations clé pour mieux comprendre le phénomène de corrosion des encres ferro-galliques.



# Bibliography

- [1] G. André et al. L'un des plus anciens papiers du monde exhumé récemment en Mongolie – découverte, analyses physico-chimiques et contexte scientifique. *Arts asiatiques*. 2010, **65**(1), pp. 27–42. ISSN: 0004-3958. DOI: 10.3406/arasi.2010.1699.
- [2] G. Coste. *Le papier, un matériau complexe*. url: <http://cerig.pagora.grenoble-inp.fr/dossier/papier-materiau/page01.htm>. 2004.
- [3] C. H. Stephens et al. Composition and condition of naturally aged papers. *Journal of the American Institute for Conservation*. 2008, **47**(3), pp. 201–215. ISSN: 0197-1360.
- [4] T. Barrett. Early European Papers, Contemporary Conservation Papers. *Paper conservator*. 1989, **13**, pp. 32–38.
- [5] T. Barrett and C. Mosier. The Role of Gelatin in Paper Permanence. *Journal of the American Institute for Conservation*. Oct. 1, 1995, **34**(3), pp. 173–186. ISSN: 0197-1360. DOI: 10.2307/3179538.
- [6] I. Brückle. *The Role of Alum in Historical Papermaking*. Sept. 1993.
- [7] P. H. F. Pereira et al. Vegetal fibers in polymeric composites: a review. *Polímeros*. Feb. 2015, **25**(1), pp. 9–22. ISSN: 0104-1428. DOI: 10.1590/0104-1428.1722.
- [8] W. Haworth, E. Hirst, and H. Thomas. The Existence of the Cellobiose Residue in Cellulose : Abstract : Nature. *Nature*. 1930, **126**, p. 438.
- [9] K. Freudenberg. Nachtrag zu der Mitteilung über Methylcellulose. Zugleich 6. Mitteilung über Lignin und Celluloses. *Justus Liebigs Annalen der Chemie*. Jan. 1, 1928, **461**(1), pp. 130–131. ISSN: 1099-0690. DOI: 10.1002/jlac.19284610107.
- [10] Y. Nishiyama et al. Crystal structure and hydrogen bonding system in cellulose I(alpha) from synchrotron X-ray and neutron fiber diffraction. *Journal of the American Chemical Society*. Nov. 26, 2003, **125**(47), pp. 14300–14306. ISSN: 0002-7863. DOI: 10.1021/ja037055w.
- [11] Y. Nishiyama, P. Langan, and H. Chanzy. Crystal structure and hydrogen-bonding system in cellulose Ibeta from synchrotron X-ray and neutron fiber diffraction. *Journal of the American Chemical Society*. Aug. 7, 2002, **124**(31), pp. 9074–9082. ISSN: 0002-7863.
- [12] J. W. Rowen and R. Blaine. Sorption of nitrogen and water vapor on textile fibers. *Journal of Research of the national bureau of standards*. RP1842 1947, **39**, pp. 479–486.

- 
- [13] A. Bismarck et al. Surface characterization of flax, hemp and cellulose fibers; Surface properties and the water uptake behavior. *Polymer Composites*. 2002, **23**(5), pp. 872–894. ISSN: 1548-0569. DOI: 10.1002/pc.10485.
- [14] G. Zografi et al. Surface area and water vapor sorption of macrocrystalline cellulose. *International Journal of Pharmaceutics*. Jan. 1984, **18**(1), pp. 99–116. ISSN: 0378-5173. DOI: 10.1016/0378-5173(84)90111-X.
- [15] S. Zervos. Characterization of changes induced by ageing to the microstructure of pure cellulose paper by use of a gravimetric water vapour adsorption technique. *Cellulose*. Aug. 1, 2007, **14**(4), pp. 375–384. ISSN: 0969-0239, 1572-882X. DOI: 10.1007/s10570-007-9125-0.
- [16] G. Banik and I. Brückle. *Paper and water: a guide for conservators*. OCLC: 716844327. Amsterdam: Butterworth-Heinemann, 2011. ISBN: 978-0-7506-6831-6.
- [17] I. D. Hartley, F. A. Kamke, and H. Peemoeller. Cluster theory for water sorption in wood. *Wood Science and Technology*. Jan. 1, 1992, **26**(2), pp. 83–99. ISSN: 0043-7719, 1432-5225. DOI: 10.1007/BF00194465.
- [18] S. Lequin et al. Adsorption Equilibria of Water Vapor on Cork. *Journal of Agricultural and Food Chemistry*. Mar. 24, 2010, **58**(6), pp. 3438–3445. ISSN: 0021-8561. DOI: 10.1021/jf9039364.
- [19] J. Leisen et al. In-Plane Moisture Transport in Paper Detected by Magnetic Resonance Imaging. *Drying Technology*. Jan. 31, 2001, **19**(1), pp. 199–206. ISSN: 0737-3937. DOI: 10.1081/DRT-100001361.
- [20] A. H. Bedane et al. Theoretical modeling of water vapor transport in cellulose-based materials. *Cellulose*. Apr. 6, 2016, **23**(3), pp. 1537–1552. ISSN: 0969-0239, 1572-882X. DOI: 10.1007/s10570-016-0917-y.
- [21] H. Gupta and S. G. Chatterjee. Parallel Diffusion of Moisture in Paper. Part 1: Steady-State Conditions. *Industrial & Engineering Chemistry Research*. Dec. 2003, **42**(25), pp. 6582–6592. ISSN: 0888-5885, 1520-5045. DOI: 10.1021/ie030413j.
- [22] Gelatin manufacturers institute of America. *Gelatin handbook*. Url: [http://www.gelatin-gmia.com/images/GMIA\\_Gelatin\\_Manual\\_2012.pdf](http://www.gelatin-gmia.com/images/GMIA_Gelatin_Manual_2012.pdf). 2012.
- [23] A.-L. Dupont. *Gelatine sizing of paper and its impact on the degradation of cellulose during ageing*. PhD thesis. Amsterdam: Universiteit van Amsterdam, 2003. 256 pp.
- [24] J. Waterhouse and T. Barrett. The aging characteristics of european handmade papers: 1400-1800. *Tappi journal*. 1991, pp. 207–212.
- [25] A.-L. Dupont. “The role of gelatine/alum sizing in the degradation of paper: a study by size exclusion chromatography in lithium chloride/N,N-dimethylacetamide using multiangle light scattering detection”. In: *Works of art on paper: books, documents and photographs: techniques and conservation*. ICC Congress. Baltimore, 2002, pp. 59–64.
- [26] C. A. ( A. Mitchell and T. C. Hepworth. *Inks: their composition and manufacture*. In collab. with University of California Libraries. London : C. Griffin & company, limited, 1904. 282 pp.
-

- [27] M. Zerdoun Bat-Yehouda. *Les encres noires au Moyen Age*. CNRS Editions, 1983. 437 pp. ISBN: 2-222-02972-4.
- [28] A. Stijnman. “Reconstructions of iron-gall ink recipes for the InkCor project.” In: *Art of the past : sources and reconstruction*. Proceedings of the first symposium of the Art Technological Source Research Study Group. M. Clarke, J. Townsend, and A. Stijnman, eds. London, 2005, pp. 125–134.
- [29] D. Champour and F. Malepeyre. *Nouveau manuel complet de la fabrication des encres de toute sorte; suivi de La fabrication du cirage*. Librairie encyclopédique de Roret. Paris, 1875.
- [30] D. N. Carvalho. *Forty Centuries of Ink: Or, A Chronological Narrative Concerning Ink and Its Backgrounds, Introducing Incidental Observations and Deductions, Parallels of Time and Color Phenomena, Bibliography, Chemistry, Poetical Effusions, Citations, Anecdotes and Curiosa Together with Some Evidence Respecting the Evanescent Character of Most Inks of To-day and an Epitome of Chemico-legal Ink*. Banks law publishing Company, 1904.
- [31] F. Flieder, R. Barroso, and C. Oruezabal. “Analyse des tannins hydrolysables susceptibles d’entrer dans la composition des encres ferro-galliques”. In: *Icom committee for conservation. 4th triennial meeting, Venice, 13-18 October. Preprints*. Icom committee for conservation triennial meeting. 6. Venice, 1975, pp. 751512–1–16.
- [32] E. D. Verink. “Simplified Procedure for Constructing Pourbaix Diagrams”. In: *Uhlig’s Corrosion Handbook*. R. W. Revie, ed. John Wiley & Sons, Inc., 2011, pp. 93–101. ISBN: 978-0-470-87286-4.
- [33] A. Kongdee and T. Bechtold. Influence of ligand type and solution pH on heavy metal ion complexation in cellulosic fibre: model calculations and experimental results. *Cellulose*. Aug. 14, 2008, **16**(1), pp. 53–63. ISSN: 0969-0239, 1572-882X. DOI: 10.1007/s10570-008-9248-y.
- [34] C. Burgaud et al. Determination of the Fe(II)/Fe(III) ratio in iron gall inks by potentiometry: A preliminary study. *Journal of Electroanalytical Chemistry*. Dec. 15, 2010, **650**(1), pp. 16–23. ISSN: 1572-6657. DOI: 10.1016/j.jelechem.2010.09.015.
- [35] M. Darbour. *Les encres metallogalliques : étude de la préparation de l’acide gallique et analyse du complexe ferrogallique*. PhD thesis. Paris: Paris IV, Oct. 29, 1980. 74 pp.
- [36] C. Krekel. “Chemische Struktur historischer Eisengallustinten”. In: *Tintenfrassschäden und ihre Behandlung*. Stuttgart, Germany: Banik G., 1999, pp. 25–37.
- [37] R. K. Feller and A. K. Cheetham. Fe(III), Mn(II), Co(II), and Ni(II) 3,4,5- trihydroxybenzoate (gallate) dihydrates; a new family of hybrid framework materials. *Solid State Sciences*. Sept. 2006, **8**(9), pp. 1121–1125. ISSN: 1293-2558. DOI: 10.1016/j.solidstatesciences.2006.04.013.
- [38] C.-H. Wunderlich, R. Weber, and G. Bergerhoff. Über Eisengallustinte. *Zeitschrift für anorganische und allgemeine Chemie*. June 1, 1991, **598**(1), pp. 371–376. ISSN: 1521-3749. DOI: 10.1002/zaac.19915980134.

- [39] A. Ponce, K. J. Gaskell, and L. B. Brostoff. “New insights into the chemistry and structure of iron gall ink”. Preservation Science Symposia: New Research on Iron Gall Ink. Url: <https://www.loc.gov/preservation/outreach/symposia/IGIPonce.pdf>. Library of Congress, Washington DC, Oct. 11, 2012.
- [40] A. Ponce et al. Elucidation of the Fe(III) Gallate Structure in Historical Iron Gall Ink. *Analytical Chemistry*. Apr. 8, 2016, ISSN: 0003-2700. DOI: 10.1021/acs.analchem.6b00088.
- [41] Z. T. Maqsood. *Formation and reactivity of iron III complexes with gallic acid*. PhD thesis. University of Karachi, 1991.
- [42] L. L. Lu, Y. H. Li, and X. Y. Lu. Kinetic study of the complexation of gallic acid with Fe(II). *Spectrochimica acta. Part a, Molecular and biomolecular spectroscopy*. Oct. 2009, **74**(3), pp. 829–834. ISSN: 1386-1425. DOI: 10.1016/j.saa.2009.08.025.
- [43] M. J. Hynes and M. Ó Coinceanainn. The kinetics and mechanisms of the reaction of iron(III) with gallic acid, gallic acid methyl ester and catechin. *Journal of Inorganic Biochemistry*. June 2001, **85**(2), pp. 131–142. ISSN: 0162-0134. DOI: 10.1016/S0162-0134(01)00205-7.
- [44] A. E. Fazary, M. Taha, and Y. H. Ju. Iron Complexation Studies of Gallic Acid. *Journal of Chemical and Engineering Data*. Jan. 2009, **54**(1), pp. 35–42. ISSN: 0021-9568. DOI: 10.1021/jc800441u.
- [45] H. Powell and M. Taylor. Interactions of iron(II) and iron(III) with gallic acid and its homologues: a potentiometric and spectrophotometric study. *Australian Journal of Chemistry*. Jan. 1, 1982, **35**(4), pp. 739–756.
- [46] M. Andjelković et al. Iron-chelation properties of phenolic acids bearing catechol and galloyl groups. *Food Chemistry*. 2006, **98**(1), pp. 23–31. ISSN: 0308-8146. DOI: 10.1016/j.foodchem.2005.05.044.
- [47] S. Khokhar and R. K. Owusu Apenten. Iron binding characteristics of phenolic compounds: some tentative structure–activity relations. *Food Chemistry*. May 2003, **81**(1), pp. 133–140. ISSN: 0308-8146. DOI: 10.1016/S0308-8146(02)00394-1.
- [48] M. C. Sistach, J. M. Gibert, and R. Areal. Ageing of laboratory iron gall inks studied by reflectance spectrometry. *Restaurator-International Journal for the Preservation of Library and Archival Material*. 1999, **20**(3), pp. 151–166. ISSN: 0034-5806.
- [49] V. Rouchon et al. The Water Sensitivity of Iron Gall Ink and its Risk Assessment. *Studies in Conservation*. 2009, **54**(4), pp. 236–254. ISSN: 0039-3630.
- [50] V. Rouchon et al. The use of halide charged interleaves for treatment of iron gall ink damaged papers. *Polymer Degradation and Stability*. July 2013, **98**(7), pp. 1339–1347. ISSN: 0141-3910. DOI: 10.1016/j.polyimdegstab.2013.03.028.
- [51] O. Belhadj et al. The Dutch Fe-Migration Mending Test. *ResearchGate*. Jan. 1, 2014, **15**(1).
- [52] B. Reissland. *Visible progress of paper degradation caused by iron gall inks*. University of Northumbria, 2000. ISBN: 978-0-9541165-0-7.

- [53] O. Posse and International conference for the preservation and restoration of old manuscripts. *Handschriften-Konservierung. Nach der St. Galler Konferenz 1898 sowie der Dresdener Konferenz 1899. Bearbeitet von Otto Posse.* OCLC: 913404096. Kopenhagen: Restaurator Press, 1969.
- [54] G. Banik and H. Weber. *Tintenfrassschäden und ihre Behandlung.* Kohlhammer, 1999. 308 pp. ISBN: 978-3-17-015377-6.
- [55] J. Kolar and M. Strlic. *Iron Gall Inks : on Manufacture, Characterisation, Degradation and Stabilisation.* 1 vols. Ljubljana: National and University Library, 2006. 252 pp.
- [56] W. Koppenol. The centennial of the Fenton reaction. *Free Radical Biology and Medicine.* Dec. 1993, **15**(6), pp. 645–651. ISSN: 08915849. DOI: 10.1016/0891-5849(93)90168-T.
- [57] F. Haber and J. Weiss. The Catalytic Decomposition of Hydrogen Peroxide by Iron Salts. *Proceedings of the Royal Society of London A: Mathematical, Physical and Engineering Sciences.* Nov. 15, 1934, **147**(861), pp. 332–351. ISSN: 1364-5021, 1471-2946. DOI: 10.1098/rspa.1934.0221.
- [58] W. H. Koppenol. The Haber-Weiss cycle—70 years later. *Redox Report: Communications in Free Radical Research.* 2001, **6**(4), pp. 229–234. ISSN: 1351-0002. DOI: 10.1179/135100001101536373.
- [59] J. C. Williams et al. “Metallic Catalysts in the Oxidative Degradation of Paper”. In: *Preservation of Paper and Textiles of Historic and Artistic Value.* Vol. 164. Advances in Chemistry 164. American Chemical Society, Dec. 17, 1978, pp. 37–61. ISBN: 0-8412-0360-1.
- [60] C. J. Shahani and F. H. Hengemihle. “The Influence of Copper and Iron on the Permanence of Paper”. In: *Historic Textile and Paper Materials.* Vol. 212. Advances in Chemistry 212. American Chemical Society, Feb. 1, 1986, pp. 387–410. ISBN: 0-8412-0900-6.
- [61] U. Henniges et al. Copper Corrosion: Comparison between Naturally Aged Papers and Artificially Aged Model Papers. *Macromolecular Symposia.* 2006, **244**(1), pp. 194–203. ISSN: 1521-3900. DOI: 10.1002/masy.200651218.
- [62] J. A. Emery and H. A. Schroeder. Iron-catalyzed oxidation of wood carbohydrates. *Wood Science and Technology.* June 1, 1974, **8**(2), pp. 123–137. ISSN: 0043-7719, 1432-5225. DOI: 10.1007/BF00351367.
- [63] K. Messner et al. “Comparison of Possible Chemical and Microbial Factors Influencing Paper Decay by Iron-Gall Inks”. In: *Biodeterioration 7.* D. R. Houghton, R. N. Smith, and H. O. W. Egging, eds. DOI: 10.1007/978-94-009-1363-9\_60. Springer Netherlands, 1988, pp. 449–454. ISBN: 978-94-010-7107-9 978-94-009-1363-9.
- [64] J. G. Neevel. Phytate : a Potential Conservation Agent for the Treatment of Ink Corrosion Caused by Iron Gall Inks. *Restaurator.* 1995, **16**(3), pp. 143–160.
- [65] J. Neevel. The Development of a New Conservation Treatment for Ink Corrosion, Based on the Natural Anti-oxidant Phytate. *International Journal of Forensic Document Examiners.* 1999, **5**, pp. 130–137.
- [66] A. Potthast, U. Henniges, and G. Banik. Iron gall ink-induced corrosion of cellulose: aging, degradation and stabilization. Part 1: model paper studies. *Cellulose.*

- Dec. 1, 2008, **15**(6), pp. 849–859. ISSN: 0969-0239, 1572-882X. DOI: 10.1007/s10570-008-9237-1.
- [67] U. Henniges et al. Iron gall ink-induced corrosion of cellulose: aging, degradation and stabilization. Part 2: application on historic sample material. *Cellulose*. Dec. 1, 2008, **15**(6), pp. 861–870. ISSN: 0969-0239, 1572-882X. DOI: 10.1007/s10570-008-9238-0.
- [68] U. Henniges et al. Studies into the Early Degradation Stages of Cellulose by Different Iron Gall Ink Components. *Macromolecular Symposia*. 2008, **262**(1), pp. 150–161. ISSN: 1521-3900. DOI: 10.1002/masy.200850215.
- [69] M. Strlič et al. Emission of reactive oxygen species during degradation of iron gall ink. *Polymer Degradation and Stability*. Jan. 2010, **95**(1), pp. 66–71. ISSN: 0141-3910. DOI: 10.1016/j.polymdegradstab.2009.10.011.
- [70] X. Zou, T. Uesaka, and N. Gurnagul. Prediction of paper permanence by accelerated aging I. Kinetic analysis of the aging process. *Cellulose*. Dec. 1996, **3**(1), pp. 243–267. ISSN: 0969-0239, 1572-882X. DOI: 10.1007/BF02228805.
- [71] X. Zou, T. Uesaka, and N. Gurnagul. Prediction of paper permanence by accelerated aging II. Comparison of the predictions with natural aging results. *Cellulose*. 1996, **3**(1), pp. 269–279. ISSN: 0969-0239, 1572-882X. DOI: 10.1007/BF02228806.
- [72] C. J. Shahani et al. *Accelerated aging of paper: I: Chemical analysis of degradation products, II: Application of Arrhenius relationship, III: Proposal for a new accelerated aging test*. American Society for Testing and Materials Research Report D06-1006. Washington, DC: Preservation Research and Testing Division, Library of Congress, 2000.
- [73] D. Kočar et al. Chemiluminescence from paper III: the effect of superoxide anion and water. *Polymer Degradation and Stability*. June 2005, **88**(3), pp. 407–414. ISSN: 0141-3910. DOI: 10.1016/j.polymdegradstab.2004.12.005.
- [74] D. Fengel and G. Wegener. *Wood: chemistry, ultrastructure, reactions*. Walter de Gruyter, Jan. 1, 1983. 633 pp. ISBN: 978-3-11-083965-4.
- [75] G. SriBala and R. Vinu. Unified Kinetic Model for Cellulose Deconstruction via Acid Hydrolysis. *Industrial & Engineering Chemistry Research*. 2014, **53**(21), pp. 8714–8725. ISSN: 0888-5885. DOI: 10.1021/ie5007905.
- [76] Y. Kwon et al. Cellobiose Hydrolysis and Decomposition by Electrochemical Generation of Acid and Hydroxyl Radicals. *ChemSusChem*. Oct. 1, 2012, **5**(10), pp. 1935–1943. ISSN: 1864-564X. DOI: 10.1002/cssc.201200250.
- [77] P. M. Whitmore and J. Bogaard. Determination of the Cellulose Scission Route in the Hydrolytic and Oxidative Degradation of Paper. *Restaurator*. 1994, **15**(1). ISSN: 0034-5806, 1865-8431. DOI: 10.1515/rest.1994.15.1.26.
- [78] A. Potthast et al. “Hydrolysis and surface modification during paper ageing”. In: 2nd European workshop on cultural heritage preservation. J. Brown, ed. Kjeller, Norway: Norwegian Institute for air research, Sept. 24, 2012, pp. 158–163.
- [79] M. Strlic and J. Kolar. *Ageing and stabilisation of paper*. National and University Library. Ljubljana, 2005. ISBN: 961-6551-03-5.

- [80] T. Rosenau et al. Confirmation of the presence of hydroxyl radicals during pre-ripening of alkali cellulose. *Journal of Wood Chemistry and Technology*. 2006, **26**(1). WOS:000237021100005, pp. 53–63. ISSN: 0277-3813. DOI: 10.1080/02773810600580263.
- [81] X. Zou et al. Accelerated aging of papers of pure cellulose: mechanism of cellulose degradation and paper embrittlement. *Polymer Degradation and Stability*. 1994, **43**(3), pp. 393–402. ISSN: 0141-3910. DOI: 10.1016/0141-3910(94)90011-6.
- [82] W. D. Major. *The degradation of cellulose in oxygen and nitrogen at high temperatures*. PhD thesis. Appleton, Wisconsin: Lawrence College, 1958. 110 pp.
- [83] J. Arney and A. Jacobs. Accelerated aging of paper-relative importance of atmospheric oxidation. *Tappi Press*. 1979, **62**(7).
- [84] P. Calvini and A. Gorassini. FTIR – Deconvolution Spectra of Paper Documents. *Restaurator*. 2002, **23**(1), pp. 48–66. DOI: 10.1515/REST.2002.48.
- [85] T. Łojewski et al. Evaluating paper degradation progress. Cross-linking between chromatographic, spectroscopic and chemical results. *Applied Physics A*. 2010, **100**(3), pp. 809–821. ISSN: 0947-8396, 1432-0630. DOI: 10.1007/s00339-010-5657-5.
- [86] J. Łojewska et al. Kinetic approach to degradation of paper: in situ FTIR transmission studies on hydrolysis and oxidation. *e-Preservation Science*. 2005, (2), pp. 1–12. ISSN: 1581-9280.
- [87] J. Röhrling et al. A Novel Method for the Determination of Carbonyl Groups in Cellulosics by Fluorescence Labeling. 1. Method Development. *Biomacromolecules*. Sept. 1, 2002, **3**(5), pp. 959–968. ISSN: 1525-7797. DOI: 10.1021/bm020029q.
- [88] J. Röhrling et al. A Novel Method for the Determination of Carbonyl Groups in Cellulosics by Fluorescence Labeling. 2. Validation and Applications. *Biomacromolecules*. Sept. 1, 2002, **3**(5), pp. 969–975. ISSN: 1525-7797. DOI: 10.1021/bm020030p.
- [89] A. Potthast et al. A Novel Method for the Determination of Carbonyl Groups in Cellulosics by Fluorescence Labeling. 3. Monitoring Oxidative Processes. *Biomacromolecules*. May 1, 2003, **4**(3), pp. 743–749. ISSN: 1525-7797. DOI: 10.1021/bm025759c.
- [90] R. Bohrn et al. The FDAM Method: Determination of Carboxyl Profiles in Cellulosic Materials by Combining Group-Selective Fluorescence Labeling with GPC. *Biomacromolecules*. June 1, 2006, **7**(6), pp. 1743–1750. ISSN: 1525-7797. DOI: 10.1021/bm060039h.
- [91] A.-L. Dupont. Degradation of Cellulose at the Wet/Dry Interface. II. An Approach to the Identification of the Oxidation Compounds. *Restaurator*. 1996, **17**(3). ISSN: 0034-5806, 1865-8431. DOI: 10.1515/rest.1996.17.3.145.
- [92] M. C. Sistach, N. Ferrer, and M. Romero. Fourier Transform Infrared Spectroscopy Applied to the Analysis of Ancient Manuscripts. *Restaurator*. 1998, **19**(4). ISSN: 0034-5806, 1865-8431. DOI: 10.1515/rest.1998.19.4.173.
- [93] J. Kolar. Mechanism of Autoxidative Degradation of Cellulose. *Restaurator*. 1997, **18**(4), pp. 163–176.

- [94] T. N. Kleinert, Marraccini, and L. M. Aging and colour reversion of bleached pulps, part 2: influence of air and moisture. *Svensk papperstidning*. 1963, **66**(6), pp. 189–195.
- [95] J. L. Bolland and G. Gee. Kinetic studies in the chemistry of rubber and related materials. II. The kinetics of oxidation of unconjugated olefins. *Transactions of the Faraday Society*. Jan. 1, 1946, **42**, pp. 236–243. ISSN: 0014-7672. DOI: 10.1039/TF9464200236.
- [96] D. Entwistle, E. H. Cole, and N. S. Wooding. The Autoxidation of Alkali Cellulose Part II. *Textile Research Journal*. Jan. 10, 1949, **19**(10), pp. 609–624. ISSN: 0040-5175, 1746-7748. DOI: 10.1177/004051754901901003.
- [97] F. Shafizadeh and A. G. W. Bradbury. Thermal degradation of cellulose in air and nitrogen at low temperatures. *Journal of Applied Polymer Science*. Mar. 1, 1979, **23**(5), pp. 1431–1442. ISSN: 1097-4628. DOI: 10.1002/app.1979.070230513.
- [98] W. H. Koppenol, D. M. Stanbury, and P. L. Bounds. Electrode potentials of partially reduced oxygen species, from dioxygen to water. *Free Radical Biology and Medicine*. Aug. 1, 2010, **49**(3), pp. 317–322. ISSN: 0891-5849. DOI: 10.1016/j.freeradbiomed.2010.04.011.
- [99] M. Anbar and P. Neta. A compilation of specific bimolecular rate constants for the reactions of hydrated electrons, hydrogen atoms and hydroxyl radicals with inorganic and organic compounds in aqueous solution. *The International Journal of Applied Radiation and Isotopes*. July 1, 1967, **18**(7), pp. 493–523. ISSN: 0020-708X. DOI: 10.1016/0020-708X(67)90115-9.
- [100] C. Sonntag. *Free-Radical-Induced DNA Damage and Its Repair: A Chemical Perspective*. Springer, Mar. 20, 2006. 528 pp. ISBN: 978-3-540-30592-7.
- [101] D. F. Guay et al. Mechanisms of Oxidative Degradation of Carbohydrates During Oxygen Delignification. II. Reaction of photochemically generated hydroxyl radicals with methyl  $\beta$ -cellobioside. *Journal of Wood Chemistry and Technology*. Feb. 28, 2001, **21**(1), pp. 67–79. ISSN: 0277-3813. DOI: 10.1081/WCT-100102655.
- [102] M. N. Schuchmann and C. von Sonntag. The Effect of Oxygen on the OH-radical-induced Scission of the Glycosidic Linkage of Cellobiose. *International Journal of Radiation Biology*. Jan. 1, 1978, **34**(4), pp. 397–400. ISSN: 0955-3002. DOI: 10.1080/09553007814551051.
- [103] C. von Sonntag. “Free-Radical Reactions of Carbohydrates as Studied by Radiation Techniques”. In: *Advances in Carbohydrate Chemistry and Biochemistry*. R. Stuart Tipson and Derek Horton, ed. Vol. Volume 37. Academic Press, 1980, pp. 7–77. ISBN: 0065-2318.
- [104] J. Kolar, M. Strlic, and B. Pihlar. New colourimetric method for determination of hydroxyl radicals during ageing of cellulose. *Analytica Chimica Acta*. Mar. 2001, **431**(2), pp. 313–319. ISSN: 0003-2670.
- [105] L. Marraccini and T. Kleinert. Aging and Colour Reversion of Bleached Pulps. Part 1. Peroxide Formation During Aging. *Svensk papperstidning*. 1962, **65**(4), pp. 126–131.
- [106] D. Kocar et al. A new method for determination of hydroperoxides in cellulose.

- Analytical and bioanalytical chemistry*. Dec. 2002, **374**(7), pp. 1218–1222. ISSN: 1618-2642. DOI: 10.1007/s00216-002-1641-z.
- [107] M.-J. Jeong, A.-L. Dupont, and E. R. de la Rie. Degradation of cellulose at the wet–dry interface. II. Study of oxidation reactions and effect of antioxidants. *Carbohydrate Polymers*. Jan. 30, 2014, **101**, pp. 671–683. ISSN: 0144-8617. DOI: 10.1016/j.carbpol.2013.09.080.
- [108] C. Lu and W. H. Koppenol. Inhibition of the Fenton reaction by nitrogen monoxide. *JBIC Journal of Biological Inorganic Chemistry*. Oct. 6, 2005, **10**(7), pp. 732–738. ISSN: 0949-8257, 1432-1327. DOI: 10.1007/s00775-005-0019-z.
- [109] H. Bataineh, O. Pestovsky, and A. Bakac. pH-induced mechanistic changeover from hydroxyl radicals to iron(IV) in the Fenton reaction. *Chemical Science*. Apr. 2, 2012, **3**(5), pp. 1594–1599. ISSN: 2041-6539. DOI: 10.1039/C2SC20099F.
- [110] T. Kishimoto and F. Nakatsubo. Non-chlorine bleaching of kraft pulp. IV. Oxidation of methyl 4-O-ethyl--d-glucopyranoside with Fenton’s reagent: Effects of pH and oxygen. *Holzforschung-International Journal of the Biology, Chemistry, Physics and Technology of Wood*. 1998, **52**(2), pp. 180–184.
- [111] V. Rouchon et al. Room-Temperature Study of Iron Gall Ink Impregnated Paper Degradation under Various Oxygen and Humidity Conditions: Time-Dependent Monitoring by Viscosity and X-ray Absorption Near-Edge Spectrometry Measurements. *Analytical Chemistry*. Apr. 1, 2011, **83**(7), pp. 2589–2597. ISSN: 0003-2700. DOI: 10.1021/ac1029242.
- [112] V. Rouchon-Quillet et al. The impact of gallic acid on iron gall ink corrosion. *Applied Physics a-Materials Science & Processing*. July 2004, **79**(2), pp. 389–392. ISSN: 0947-8396. DOI: 10.1007/s00339-004-2541-1.
- [113] O. I. Aruoma et al. Evaluation of the antioxidant and prooxidant actions of gallic acid and its derivatives. *Journal of Agricultural and Food Chemistry*. Nov. 1, 1993, **41**(11), pp. 1880–1885. ISSN: 0021-8561. DOI: 10.1021/jf00035a014.
- [114] M. Strlic et al. Anti- and prooxidative properties of gallic acid in Fenton-type systems. *Journal of Agricultural and Food Chemistry*. Oct. 2002, **50**(22), pp. 6313–6317. ISSN: 0021-8561. DOI: 10.1021/jf025636j.
- [115] R. Lo Scalzo. Measurement of free radical scavenging activity of gallic acid and unusual antioxidants as sugars and hydroxyacids. *Electronic Journal of Environmental, Agricultural and Food chemistry*. 2010, **9**(8), pp. 1360–1371. ISSN: 1579-4377.
- [116] G.-C. Yen, P.-D. Duh, and H.-L. Tsai. Antioxidant and pro-oxidant properties of ascorbic acid and gallic acid. *Food Chemistry*. Nov. 2002, **79**(3), pp. 307–313. ISSN: 0308-8146. DOI: 10.1016/S0308-8146(02)00145-0.
- [117] M. Strlic et al. A comparative study of several transition metals in Fenton-like reaction systems at circum-neutral pH. *Acta Chimica Slovenica*. 2003, **50**(4), pp. 619–632.
- [118] S. Ardo. *Dégradation oxydative d’une quinolone par la nano-magnétite via l’interaction Fe(II) / O<sub>2</sub>*. Paris 6, Dec. 18, 2014.
- [119] Venny, S. Gan, and H. K. Ng. Current status and prospects of Fenton oxidation for the decontamination of persistent organic pollutants (POPs) in soils. *Chemical*

- Engineering Journal*. Dec. 1, 2012, **213**, pp. 295–317. ISSN: 1385-8947. DOI: 10.1016/j.cej.2012.10.005.
- [120] J. Herney-Ramirez, M. A. Vicente, and L. M. Madeira. Heterogeneous photo-Fenton oxidation with pillared clay-based catalysts for wastewater treatment: A review. *Applied Catalysis B: Environmental*. July 20, 2010, **98**(1), pp. 10–26. ISSN: 0926-3373. DOI: 10.1016/j.apcatb.2010.05.004.
- [121] J. Rychlý et al. Thermal oxidation of cellulose investigated by chemiluminescence. The effect of water at temperatures above 100 °C. *Carbohydrate Polymers*. Nov. 25, 2004, **58**(3), pp. 301–309. ISSN: 0144-8617. DOI: 10.1016/j.carbpol.2004.07.006.
- [122] H. Mimoun. The synthesis, reactions, properties & applications of coordination compounds. In: G. Wilkinson. *Comprehensive coordination chemistry*. Pergamon Press, 1987, pp. 317–340.
- [123] P. Brandhuber and G. Korshin. *Methods for Detection of Residual Concentrations of Hydrogen Peroxide in Advanced Oxidation Processes*. WateReuse, 2009. 72 pp. ISBN: 978-1-934183-15-1.
- [124] E. Graf and J. T. Penniston. Method for determination of hydrogen peroxide, with its application illustrated by glucose assay. *Clinical chemistry*. 1980, **26**(5), pp. 658–660.
- [125] Q. Zhang et al. A Novel Method for the Determination of Hydrogen Peroxide in Bleaching Effluents by Spectroscopy. *BioResources*. May 24, 2013, **8**(3), pp. 3699–3705. ISSN: 1930-2126. DOI: 10.15376/biores.8.3.3699-3705.
- [126] E. Kontturi et al. Quantification method for hydrogen peroxide formation during oxygen delignification of kraft pulp. *Nordic Pulp & Paper Research Journal*. 2005, **20**(4), pp. 490–495. ISSN: 0283-2631.
- [127] M. C. Dobarganes and J. Velasco. Analysis of lipid hydroperoxides. *European Journal of Lipid Science and Technology*. July 1, 2002, **104**(7), pp. 420–428. ISSN: 1438-9312. DOI: 10.1002/1438-9312(200207)104:7<420::AID-EJLT420>3.0.CO;2-N.
- [128] M. Strlic, J. Kolar, and B. Pihlar. Some preventive cellulose antioxidants studied by an aromatic hydroxylation assay. *Polymer Degradation and Stability*. 2001, **73**(3), pp. 535–539. ISSN: 0141-3910.
- [129] J. Zhang and Y. Nosaka. Quantitative Detection of OH Radicals for Investigating the Reaction Mechanism of Various Visible-Light TiO<sub>2</sub> Photocatalysts in Aqueous Suspension. *The Journal of Physical Chemistry C*. Jan. 24, 2013, **117**(3), pp. 1383–1391. ISSN: 1932-7447. DOI: 10.1021/jp3105166.
- [130] C. L. Hawkins and M. J. Davies. Detection and characterisation of radicals in biological materials using EPR methodology. *Biochimica et Biophysica Acta (BBA) - General Subjects*. Current methods to study reactive oxygen species - pros and cons. Feb. 2014, **1840**(2), pp. 708–721. ISSN: 0304-4165. DOI: 10.1016/j.bbagen.2013.03.034.
- [131] X. Huang et al. Ferrous ion autoxidation and its chelation in iron-loaded human liver HepG2 cells. *Free Radical Biology and Medicine*. Jan. 1, 2002, **32**(1), pp. 84–92. ISSN: 0891-5849. DOI: 10.1016/S0891-5849(01)00770-5.

- [132] R. Zalma et al. Formation of oxy radicals by oxygen reduction arising from the surface activity of asbestos. *Canadian journal of chemistry*. 1987, **65**(10), pp. 2338–2341.
- [133] L. ( Yu and Z. Cheng. Application of electron spin resonance (ESR) spectrometry in nutraceutical and food research. *Molecular Nutrition & Food Research*. Jan. 1, 2008, **52**(1), pp. 62–78. ISSN: 1613-4133. DOI: 10.1002/mnfr.200700395.
- [134] N. Senesi. “Application of Electron Spin Resonance (ESR) Spectroscopy in Soil Chemistry”. In: *Advances in Soil Science*. B. A. Stewart, ed. Advances in Soil Science 14. Springer New York, 1990, pp. 77–130. ISBN: 978-1-4612-7978-5 978-1-4612-3356-5.
- [135] C. J. Rhodes. Electron spin resonance. Part two: a diagnostic method in the environmental sciences. *Science Progress*. Pt 4 2011, **94**, pp. 339–413. ISSN: 0036-8504.
- [136] J. C. Arthur, O. Hinojosa, and M. S. Bains. ESR study of reactions of cellulose with  $\cdot\text{OH}$  generated by  $\text{Fe}^{+2}/\text{H}_2\text{O}_2$ . *Journal of Applied Polymer Science*. June 1, 1968, **12**(6), pp. 1411–1421. ISSN: 1097-4628. DOI: 10.1002/app.1968.070120613.
- [137] A. Zoleo, F. Vecchia, and M. Brustolon. Characterization of ancient and modern papers by CW-EPR spectroscopy. *Applied Magnetic Resonance*. 2009, **35**(2), pp. 213–220. ISSN: 0937-9347, 1613-7507. DOI: 10.1007/s00723-008-0155-z.
- [138] D. Capitani et al. H-1 NMR relaxation study of cellulose and water interaction in paper. *Tappi journal*. 1999, **82**(9), pp. 117–124. ISSN: 0734-1415.
- [139] Tappi, ed. *Standard T 441 om-09: Water absorptiveness of sized (non-bibulous) paper, paperboard, and corrugated fiberboard (Cobb test)*. 2013.
- [140] ISO/TC6/SC2, ed. *ISO standard 535:1991 - Paper and board – Determination of water absorptiveness – Cobb method*. 1991.
- [141] W. Freinbichler et al. Highly reactive oxygen species: detection, formation, and possible functions. *Cellular and Molecular Life Sciences*. May 2, 2011, **68**(12), pp. 2067–2079. ISSN: 1420-682X, 1420-9071. DOI: 10.1007/s00018-011-0682-x.
- [142] P. R. Marriot, M. Perkins, and D. Griller. Spin trapping for hydroxyl in water: a kinetic evaluation of two popular traps. *Canadian Journal of Chemistry*. 1980, **58**, pp. 803–807.
- [143] A. Technologies. “HPLC Basics: Fundamentals of Liquid Chromatography”. 2011.
- [144] J. C. Thompsen and H. A. Mottola. Kinetics of the complexation of iron(II) with ferrozine. *Analytical Chemistry*. Apr. 1, 1984, **56**(4), pp. 755–757. ISSN: 0003-2700. DOI: 10.1021/ac00268a037.
- [145] W. Fresenius and W. Schneider. *For the determination of iron (II) and total iron with 2,2'-dipyridyl in mineral waters. Reduction of iron (III) with ascorbic acid [Translation from: Zeitschrift fur Analytische Chemie 209 340-341, 1965]*. 1976.
- [146] G. Charlot. *Dosages colorimétriques des éléments minéraux: principes et méthodes*. Masson, 1961. 396 pp.
- [147] F. M. Najib and O. I. Hayder. Study of Stoichiometry of Ferric Thiocyanate Complex for Analytical Purposes Including F- - Determination. *Iraqi National Journal of Chemistry*. 2011, **42**, pp. 135–155.

- [148] L. A. Reinke, J. M. Rau, and P. B. McCay. Characteristics of an oxidant formed during iron (II) autoxidation. *Free Radical Biology and Medicine*. Apr. 1994, **16**(4), pp. 485–492. ISSN: 0891-5849. DOI: 10.1016/0891-5849(94)90126-0.
- [149] K. Makino et al. Cautionary note for DMPO spin trapping in the presence of iron ion. *Biochemical and Biophysical Research Communications*. Nov. 15, 1990, **172**(3), pp. 1073–1080. ISSN: 0006-291X.
- [150] L. Ebersson. Formation of hydroxyl spin adducts via nucleophilic addition-oxidation to 5,5 dimethyl-1-pyrroline N-Oxide. *Acta Chemica Scandinavica*. 1999, **53**, pp. 584–593.
- [151] P. M. Hanna and R. P. Mason. Direct evidence for inhibition of free radical formation from Cu(I) and hydrogen peroxide by glutathione and other potential ligands using the EPR spin-trapping technique. *Archives of Biochemistry and Biophysics*. May 15, 1992, **295**(1), pp. 205–213. ISSN: 0003-9861. DOI: 10.1016/0003-9861(92)90507-S.
- [152] K. Ranguelova and R. P. Mason. The Fidelity of Spin Trapping with DMPO in Biological Systems. *Magnetic resonance in chemistry : MRC*. Apr. 2011, **49**(4), pp. 152–158. ISSN: 0749-1581. DOI: 10.1002/mrc.2709.
- [153] V. Rouchon et al. Etude du vieillissement naturel de papiers imprégnés d'encre ferrogalliques. *Techné*. 2008, pp. 60–67.
- [154] A. Zoleo, L. Speri, and M. Bronzato. Electron Paramagnetic Resonance as a Probe for Metal Ions and Radicals in Paper. *Restaurator*. 2015, **36**(4), pp. 269–282.
- [155] V. Rouchon and S. Bernard. Mapping iron gall ink penetration within paper fibres using scanning transmission X-ray microscopy. *Journal of Analytical Atomic Spectrometry*. Feb. 25, 2015, **30**(3), pp. 635–641. ISSN: 1364-5544. DOI: 10.1039/C4JA00358F.
- [156] B. P. Soule et al. The chemistry and biology of nitroxide compounds. *Free Radical Biology and Medicine*. June 1, 2007, **42**(11), pp. 1632–1650. ISSN: 0891-5849. DOI: 10.1016/j.freeradbiomed.2007.02.030.
- [157] M. Shiga et al. 4-Hydroxy-2,2,6,6-tetramethyl-1-piperidinyloxy Free Radical as a Novel Ascorbic Acid Quencher. *Analytical Communications*. Jan. 1, 1997, **34**(4), pp. 115–118. ISSN: 1364-5536. DOI: 10.1039/A701274H.
- [158] P. M. Wood. The potential diagram for oxygen at pH 7. *Biochemical Journal*. July 1, 1988, **253**(1), pp. 287–289. ISSN: 0264-6021.
- [159] M. Ilbert and V. Bonnefoy. Insight into the evolution of the iron oxidation pathways. *Biochimica et Biophysica Acta (BBA) - Bioenergetics*. The evolutionary aspects of bioenergetic systems. Feb. 2013, **1827**(2), pp. 161–175. ISSN: 0005-2728. DOI: 10.1016/j.bbabi.2012.10.001.
- [160] M. Uchimiya and A. T. Stone. Redox reactions between iron and quinones: Thermodynamic constraints. *Geochimica et Cosmochimica Acta*. Mar. 15, 2006, **70**(6), pp. 1388–1401. ISSN: 0016-7037. DOI: 10.1016/j.gca.2005.11.020.
- [161] C. Jiang, S. Garg, and T. D. Waite. Hydroquinone-Mediated Redox Cycling of Iron and Concomitant Oxidation of Hydroquinone in Oxidic Waters under Acidic Conditions: Comparison with Iron–Natural Organic Matter Interactions. *Environmental*

- Science & Technology*. Dec. 15, 2015, **49**(24), pp. 14076–14084. ISSN: 0013-936X, 1520-5851. DOI: 10.1021/acs.est.5b03189.
- [162] W. Stumm and G. F. Lee. Oxygenation of Ferrous Iron. *Industrial & Engineering Chemistry*. Feb. 1, 1961, **53**(2), pp. 143–146. ISSN: 0019-7866. DOI: 10.1021/ie50614a030.
- [163] L. Li et al. Distinguishing the 5,5-dimethyl-1-pyrroline N-oxide (DMPO)-OH radical quenching effect from the hydroxyl radical scavenging effect in the ESR spin-trapping method. *Analytica Chimica Acta*. June 4, 2004, **512**(1), pp. 121–124. ISSN: 0003-2670. DOI: 10.1016/j.aca.2004.02.020.
- [164] L. Linxiang et al. An HPLC assay of hydroxyl radicals by the hydroxylation reaction of terephthalic acid. *Biomedical Chromatography*. 2004, **18**(7), pp. 470–474. ISSN: 1099-0801. DOI: 10.1002/bmc.339.
- [165] K. Yamaguchi, Y. Takahara, and T. Fueno. “The role of oxygen chemistry and biochemistry.” In: *Studies in Inorganic chemistry*. Elsevier. Vol. 33. 1988, pp. 263–268.
- [166] D. Sawyer. *Oxygen Chemistry*. Oxford University Press, USA, Sept. 19, 1991. 238 pp. ISBN: 978-0-19-536332-6.
- [167] S. Y. Qian and G. R. Buettner. Iron and dioxygen chemistry is an important route to initiation of biological free radical oxidations: an electron paramagnetic resonance spin trapping study. *Free Radical Biology and Medicine*. June 1999, **26**(11), pp. 1447–1456. ISSN: 0891-5849. DOI: 10.1016/S0891-5849(99)00002-7.
- [168] Z. Sroka and W. Cisowski. Hydrogen peroxide scavenging, antioxidant and anti-radical activity of some phenolic acids. *Food and Chemical Toxicology*. June 2003, **41**(6), pp. 753–758. ISSN: 0278-6915. DOI: 10.1016/S0278-6915(02)00329-0.
- [169] C. Popovici, I. Saykova, and B. Tylkowski. Evaluation de l’activité antioxydant des composés phénoliques par la réactivité avec le radical libre DPPH. *Revue de Génie Industriel*. 2009, **4**, pp. 25–39. ISSN: 1313-8871.
- [170] C.-S. Wu. *Handbook Of Size Exclusion Chromatography And Related Techniques: Revised And Expanded*. CRC Press, Nov. 4, 2003. 721 pp. ISBN: 978-0-8247-5779-3.
- [171] R. Evans and A. F. A. Wallis. Cellulose molecular weights determined by viscometry. *Journal of Applied Polymer Science*. Apr. 1, 1989, **37**(8), pp. 2331–2340. ISSN: 1097-4628. DOI: 10.1002/app.1989.070370822.
- [172] P. L. Bégin and E. Kaminska. Thermal Accelerated Ageing Test Method Development. *Restaurator*. 2008, **23**(2), pp. 89–105. DOI: 10.1515/REST.2002.89.
- [173] D. Erhardt, D. Von Endt, and W. Hopwood. The comparison of accelerated aging conditions through the analysis of extracts of artificially aged paper. *Preprints of papers presented at the fifteenth annual meeting of the American Institute for Conservation of Historic and Artistic Works. Vancouver, British Columbia, Canada, May 20-24, 1987*. 1987, pp. 43–55. ISSN: 0272-3727.
- [174] A. Barański, J. Lagan, and T. Lojewski. “Acid-catalyzed degradation”. In: *Ageing and stabilisation of paper*. National and University Library. Ljubljana: Strilc M., 2005, pp. 93–108. ISBN: 961-6551-03-5.

- [175] A. Barański et al. On the applicability of Arrhenius equation to accelerated ageing tests. The case of alum-impregnated cellulose. *Polish Journal of Chemical Technology*. nr 1 2004, **Vol. 6**, pp. 1–8. ISSN: 1509-8117.
- [176] J. Rychlý et al. Chemiluminescence from paper I. Kinetic analysis of thermal oxidation of cellulose. *Polymer Degradation and Stability*. 2002, **78**(2), pp. 357–367. ISSN: 0141-3910. DOI: 10.1016/S0141-3910(02)00187-8.
- [177] R. M. Rowell et al. Oxidative alkaline degradation of cellobiose. *Carbohydrate Research*. 1969, **11**(1), pp. 17–25. ISSN: 0008-6215. DOI: 10.1016/S0008-6215(00)80637-0.
- [178] L. Löwendahl, G. Petersson, and O. Samuelson. Oxygen-Alkali Treatment of cellobiose. *Acta Chemica Scandinavica B*. 1975, **29**, pp. 975–980.
- [179] H. S. Isbell and H. L. Frush. Mechanisms for hydroperoxide degradation of disaccharides and related compounds. *Carbohydrate Research*. Apr. 1, 1987, **161**(2), pp. 181–193. ISSN: 0008-6215. DOI: 10.1016/S0008-6215(00)90076-4.
- [180] G. Bonn et al. The alkaline degradation of cellobiose to glucose and fructose. *Monatshefte für Chemie / Chemical Monthly*. Aug. 1, 1985, **116**(8), pp. 961–971. ISSN: 0026-9247, 1434-4475. DOI: 10.1007/BF00809189.
- [181] W. M. Corbett and J. Kenner. The degradation of carbohydrates by alkali. Part IX. Cellobiose, cellobiulose, cellotetraose, and laminarin. *Journal of the Chemical Society (Resumed)*. Jan. 1, 1955, pp. 1431–1435. ISSN: 0368-1769. DOI: 10.1039/JR9550001431.
- [182] D. J. MacLaurin and J. W. Green. Carbohydrates in alkaline systems. II. Kinetics of the transformation and degradation reactions of cellobiose, cellobiulose, and 4-O-*eta*-D-glucopyranosyl-D-mannose in 1M sodium hydroxide at 22 °C. *Canadian Journal of Chemistry*. Nov. 1, 1969, **47**(21), pp. 3957–3964. ISSN: 0008-4042. DOI: 10.1139/v69-659.
- [183] M. Pincu, B. Brauer, and R. B. Gerber. When a Proton Attacks Cellobiose in the Gas Phase: Ab Initio Molecular Dynamics Simulations. *Physical Chemistry Chemical Physics*. 2013, ISSN: 1463-9076.
- [184] J. Zhang et al. Catalytic oxidative conversion of cellulosic biomass to formic acid and acetic acid with exceptionally high yields. *Catalysis Today*. Catalytic Materials And Catalysis For Low Carbon Technology. Sept. 15, 2014, **233**, pp. 77–82. ISSN: 0920-5861. DOI: 10.1016/j.cattod.2013.12.010.
- [185] M. Hernández et al. A small change in the surface polarity of cellulose causes a significant improvement in its conversion to glucose and subsequent catalytic oxidation. *Applied Catalysis B: Environmental*. Jan. 2014, **144**, pp. 528–537. ISSN: 0926-3373. DOI: 10.1016/j.apcatb.2013.07.061.
- [186] M. Marzo, A. Gervasini, and P. Carniti. Hydrolysis of disaccharides over solid acid catalysts under green conditions. *Carbohydrate Research*. Jan. 10, 2012, **347**(1), pp. 23–31. ISSN: 0008-6215. DOI: 10.1016/j.carres.2011.10.018.
- [187] V. Degirmenci et al. Sulfated Zirconia Modified SBA-15 Catalysts for Cellobiose Hydrolysis. *Catalysis Letters*. Jan. 1, 2011, **141**(1), pp. 33–42. ISSN: 1011-372X, 1572-879X. DOI: 10.1007/s10562-010-0466-1.

- [188] W. Deng et al. Oxidative Hydrolysis of Cellobiose to Glucose. *Catalysis Letters*. Apr. 1, 2011, **141**(4), pp. 498–506. ISSN: 1011-372X, 1572-879X. DOI: 10.1007/s10562-010-0532-8.
- [189] J. Łojewska et al. FTIR in situ transmission studies on the kinetics of paper degradation via hydrolytic and oxidative reaction paths. *Applied Physics A*. June 1, 2006, **83**(4), pp. 597–603. ISSN: 0947-8396, 1432-0630. DOI: 10.1007/s00339-006-3529-9.
- [190] H.-b. Xie et al. Raman and infrared spectra of cellobiose in the solid state: What can be learned from single-molecule calculations? *Chemical Physics Letters*. Oct. 6, 2011, **514**(4), pp. 284–290. ISSN: 0009-2614. DOI: 10.1016/j.cpllett.2011.08.082.
- [191] N. A. Nikonenko et al. Investigation of stretching vibrations of glycosidic linkages in disaccharides and polysaccharides with use of IR spectra deconvolution. *Biopolymers*. 2000, **57**(4), pp. 257–262. ISSN: 0006-3525. DOI: 10.1002/1097-0282(2000)57:4<257::AID-BIP7>3.0.CO;2-3.
- [192] V. Rouchon et al. Application of Arrhenius law to DP and zero-span tensile strength measurements taken on iron gall ink impregnated papers: relevance of artificial ageing protocols. *Applied Physics A*. July 30, 2016, **122**(8), p. 773. ISSN: 0947-8396, 1432-0630. DOI: 10.1007/s00339-016-0307-1.
- [193] F. K. Bedu-Addo. Understanding lyophilization formulation development. *Pharmaceutical technology*. 2004, pp. 10–18.
- [194] G. R. Nireesha et al. Lyophilization/freeze drying-An review. *International journal of novel trends in pharmaceutical sciences*. 2013, **3**(4), pp. 87–93.
- [195] J. Cartenensen and K. Van Scoik. Amorphous-to-Crystalline Transformation of Sucrose. *pharmaceutical research*. 1990, **7**(12), pp. 1278–1281.
- [196] V. P. Heljo et al. The effect of water plasticization on the molecular mobility and crystallization tendency of amorphous disaccharides. *Pharmaceutical Research*. 2012, **29**(10), pp. 2684–2697. ISSN: 1573-904X. DOI: 10.1007/s11095-011-0658-4.
- [197] C. Remazeilles et al. PIXE elemental mapping on original manuscripts with an external microbeam. Application to manuscripts damaged by iron-gall ink corrosion. *Nuclear Instruments and Methods in Physics Research Section B: Beam Interactions with Materials and Atoms*. 7th International Conference on Nuclear Microprobe Technology and Applications. July 2001, **181**(1), pp. 681–687. ISSN: 0168-583X. DOI: 10.1016/S0168-583X(01)00364-0.
- [198] O. Dahlman et al. Analysis of carbohydrates in wood and pulps employing enzymatic hydrolysis and subsequent capillary zone electrophoresis. *Journal of Chromatography A*. Sept. 1, 2000, **891**(1), pp. 157–174. ISSN: 0021-9673. DOI: 10.1016/S0021-9673(00)00619-1.
- [199] J. Sjöberg et al. An optimized CZE method for analysis of mono- and oligomeric aldose mixtures. *Carbohydrate Research*. Aug. 2, 2004, **339**(11), pp. 2037–2043. ISSN: 0008-6215. DOI: 10.1016/j.carres.2004.06.003.
- [200] A.-L. Dupont et al. Comprehensive characterisation of cellulose- and lignocellulose-degradation products in aged papers: Capillary zone electrophoresis of low-molar mass organic acids, carbohydrates, and aromatic lignin derivatives. *Carbohydrate*

- Polymers*. Mar. 1, 2007, **68**(1), pp. 1–16. ISSN: 0144-8617. DOI: 10.1016/j.carbpol.2006.07.005.
- [201] R. Weinberger. *Practical Capillary Electrophoresis*. Academic Press, Apr. 18, 2000. 503 pp. ISBN: 978-0-08-053934-8.
- [202] F. Parker. *Applications of Infrared Spectroscopy in Biochemistry, Biology, and Medicine*. Springer Science & Business Media, Dec. 6, 2012. 612 pp. ISBN: 978-1-4684-1872-9.
- [203] M. Fan, D. Dai, and B. Huang. “Fourier transform infrared spectroscopy for natural fibres”. In: *Fourier transform–materials analysis*. Dr. Salih Salih, 2012, p. 260. ISBN: 978-953-51-0594-7.
- [204] A. M. Faure. *Hydroxyl radical mediated degradation of cereal eta-glucan*. PhD thesis. Zurich: ETH ZURICH, 2013. 179 pp.
- [205] G. Socrates. *Infrared and Raman Characteristic Group Frequencies: Tables and Charts*. Google-Books-ID: LDoAAjMnwEIC. John Wiley & Sons, 2001. 372 pp. ISBN: 978-0-470-09307-8.
- [206] A. Ricci et al. Acid-catalysed glucose dehydration in the gas phase: a mass spectrometric approach. *Journal of Mass Spectrometry*. Jan. 1, 2015, **50**(1), pp. 228–234. ISSN: 1096-9888. DOI: 10.1002/jms.3525.
- [207] D. Eklund and P. Salminen. Water sorption in paper during short times. *Appita journal*. Jan. 1, 1987, **40**(5), pp. 340–346. ISSN: 1038-6807.
- [208] U. H. C. Kappel. “Measurement of printing ink penetration in uncoated papers and its influence on print quality”. In: *94th annual meeting preprints*. 94th annual meeting Pulp and paper technical association of Canada. Montreal, QC, Canada, Feb. 6, 2008, B539–B542.
- [209] L. Yang et al. A novel method for studying ink penetration of a print. *Nordic Pulp & Paper Research Journal*. 2005, **20**(4). WOS:000235258200008, pp. 423–429. ISSN: 0283-2631.
- [210] Y. Li and B. He. Characterization of ink pigment penetration and distribution related to surface topography of paper using confocal laser scanning microscopy. *BioResources*. May 27, 2011, **6**(3), pp. 2690–2702. ISSN: 1930-2126. DOI: 10.15376/biores.6.3.2690-2702.
- [211] Ø. Eriksen and Ø. W. Gregersen. A study of ink pigment penetration and optical properties of laboratory sheets using scanning electron microscope. *ResearchGate*. Jan. 1, 2004,
- [212] M. Myllys et al. X-ray microtomography and laser ablation in the analysis of ink distribution in coated paper. *Journal of Applied Physics*. Apr. 14, 2015, **117**(14), p. 144902. ISSN: 0021-8979, 1089-7550. DOI: 10.1063/1.4916588.
- [213] M. Budnar et al. Analysis of iron gall inks by PIXE. *Nuclear Instruments and Methods in Physics Research Section B: Beam Interactions with Materials and Atoms*. Feb. 2006, **243**(2), pp. 407–416. ISSN: 0168-583X. DOI: 10.1016/j.nimb.2005.10.013.
- [214] K. J. K. Proost. Determination of localized Fe<sup>2+</sup>/Fe<sup>3+</sup> ratios in inks of historic documents by means of -XANES. *Nuclear Instruments and Methods in Physics*

- Research Section B: Beam Interactions with Materials and Atoms.* 2004, **213**, pp. 723–728. ISSN: 0168-583X. DOI: 10.1016/S0168-583X(03)01693-8.
- [215] B. Kanngießler et al. Investigation of oxidation and migration processes of inorganic compounds in ink-corroded manuscripts. *Spectrochimica Acta Part B: Atomic Spectroscopy*. 17th International Congress on X-Ray Optics and Microanalysis. Oct. 8, 2004, **59**(10), pp. 1511–1516. ISSN: 0584-8547. DOI: 10.1016/j.sab.2004.07.013.
- [216] I. Arčon et al. XANES analysis of Fe valence in iron gall inks. *X-Ray Spectrometry*. May 1, 2007, **36**(3), pp. 199–205. ISSN: 1097-4539. DOI: 10.1002/xrs.962.
- [217] M. Wilke et al. The oxidation state of iron determined by Fe K-edge XANES-application to iron gall ink in historical manuscripts. *Journal of Analytical Atomic Spectrometry*. Sept. 23, 2009, **24**(10), pp. 1364–1372. ISSN: 1364-5544. DOI: 10.1039/B904438H.
- [218] V. Rouchon, E. Pellizzi, and K. Janssens. FTIR techniques applied to the detection of gelatine in paper artifacts: from macroscopic to microscopic approach. *Applied Physics A*. Sept. 1, 2010, **100**(3), pp. 663–669. ISSN: 0947-8396, 1432-0630. DOI: 10.1007/s00339-010-5649-5.
- [219] G. Kolbe. Gelatine in Historical Paper Production and as Inhibiting Agent for Iron-Gall Ink Corrosion on Paper. *Restaurator*. 2004, **25**(1), pp. 26–39. DOI: 10.1515/REST.2004.26.
- [220] E. Hummert, U. Henniges, and A. Potthast. Fluorescence labeling of gelatin and methylcellulose: monitoring their penetration behavior into paper. *Cellulose*. Jan. 22, 2013, **20**(2), pp. 919–931. ISSN: 0969-0239, 1572-882X. DOI: 10.1007/s10570-013-9864-z.
- [221] C. by design limited. *Hand Made Cover Paper Workshop with Christopher Clarkson and Jacques Brejoux at Moulin Du Verger Paper Mill*.
- [222] V. Rouchon, H. Capodano-Cordonnier, and E. Pellizzi. Détection par spectrométrie infrarouge des encollages à la gélatine dans les papiers anciens. *PapierS*. 2010, (2), pp. 5–6.
- [223] R. Oraji et al. X-ray spectromicroscopy of the effect of chemical treatment on flax fibres. *Canadian Light Source Activity Report*. 2008, pp. 118–119.
- [224] A. Dazzi et al. AFM-IR: combining atomic force microscopy and infrared spectroscopy for nanoscale chemical characterization. *Applied Spectroscopy*. Dec. 2012, **66**(12), pp. 1365–1384. ISSN: 1943-3530. DOI: 10.1366/12-06804.
- [225] C. L. Source. *Albums de Canadian Light Source / Flickr - Photo Sharing!* Url: <https://www.flickr.com/photos/97079436@N04/sets/>.
- [226] J. T. Francis and A. P. Hitchcock. Inner-shell spectroscopy of p-benzoquinone, hydroquinone, and phenol: distinguishing quinoid and benzenoid structures. *The Journal of Physical Chemistry*. Aug. 1, 1992, **96**(16), pp. 6598–6610. ISSN: 0022-3654. DOI: 10.1021/j100195a018.
- [227] G. D. Cody et al. Determination of chemical-structural changes in vitrinite accompanying luminescence alteration using C-NEXAFS analysis. *Organic Geochemistry*. May 5, 1998, **28**(7), pp. 441–455. ISSN: 0146-6380. DOI: 10.1016/S0146-6380(98)00010-2.

- [228] J. Lehmann et al. Near-edge X-ray absorption fine structure (NEXAFS) spectroscopy for mapping nano-scale distribution of organic carbon forms in soil: Application to black carbon particles. *Global Biogeochemical Cycles*. Mar. 1, 2005, **19**(1), GB1013. ISSN: 1944-9224. DOI: 10.1029/2004GB002435.
- [229] P. R. Haberstroh et al. Chemical composition of the graphitic black carbon fraction in riverine and marine sediments at sub-micron scales using carbon X-ray spectroscopy. *Geochimica et Cosmochimica Acta*. Mar. 15, 2006, **70**(6), pp. 1483–1494. ISSN: 0016-7037. DOI: 10.1016/j.gca.2005.12.001.
- [230] G. D. Cody et al. Inner-Shell Spectroscopy and Imaging of a Subbituminous Coal: In-Situ Analysis of Organic and Inorganic Microstructure Using C(1s)-, Ca(2p)-, and Cl(2s)-NEXAFS. *Energy & Fuels*. May 1, 1995, **9**(3), pp. 525–533. ISSN: 0887-0624. DOI: 10.1021/ef00051a018.
- [231] G. D. Cody et al. The application of soft X-ray microscopy to the in-situ analysis of sporinite in coal. *International Journal of Coal Geology*. Dec. 1996, **32**(1), pp. 69–86. ISSN: 0166-5162. DOI: 10.1016/S0166-5162(96)00031-6.
- [232] C. K. Boyce et al. Organic chemical differentiation within fossil plant cell walls detected with X-ray spectromicroscopy. *Geology*. 2002, **30**(11), pp. 1039–1042.
- [233] K. Benzerara et al. Nanoscale environments associated with bioweathering of a Mg-Fe-pyroxene. *Proceedings of the National Academy of Sciences of the United States of America*. Jan. 25, 2005, **102**(4), pp. 979–982. ISSN: 0027-8424, 1091-6490. DOI: 10.1073/pnas.0409029102.
- [234] K. Benzerara et al. Scanning transmission X-ray microscopy study of microbial calcification. *Geobiology*. Oct. 1, 2004, **2**(4), pp. 249–259. ISSN: 1472-4669. DOI: 10.1111/j.1472-4677.2004.00039.x.
- [235] S. G. Urquhart and H. Ade. Trends in the Carbonyl Core (C 1S, O 1S)  $\rightarrow$  \*C=O Transition in the Near-Edge X-ray Absorption Fine Structure Spectra of Organic Molecules. *The Journal of Physical Chemistry B*. Aug. 1, 2002, **106**(34), pp. 8531–8538. ISSN: 1520-6106. DOI: 10.1021/jp0255379.
- [236] M. W. Buckley and N. A. Besley. A theoretical study of the near edge X-ray absorption fine structure of amino acids and proteins. *Chemical Physics Letters*. Jan. 7, 2011, **501**(4), pp. 540–546. ISSN: 0009-2614. DOI: 10.1016/j.cpllett.2010.12.004.
- [237] J. A. Brandes et al. Carbon K-edge XANES spectromicroscopy of natural graphite. *Carbon*. Sept. 2008, **46**(11), pp. 1424–1434. ISSN: 0008-6223. DOI: 10.1016/j.carbon.2008.06.020.
- [238] J. J. Dynes et al. Speciation and quantitative mapping of metal species in microbial biofilms using scanning transmission X-ray microscopy. *Environmental Science & Technology*. Mar. 1, 2006, **40**(5), pp. 1556–1565. ISSN: 0013-936X.
- [239] S. Bernard et al. Exceptional preservation of fossil plant spores in high-pressure metamorphic rocks. *Earth and Planetary Science Letters*. Oct. 15, 2007, **262**(1), pp. 257–272. ISSN: 0012-821X. DOI: 10.1016/j.epsl.2007.07.041.
- [240] F. Bourdelle et al. Quantification of the ferric/ferrous iron ratio in silicates by scanning transmission X-ray microscopy at the Fe L<sub>2,3</sub> edges. *Contributions to*

- Mineralogy and Petrology*. June 4, 2013, **166**(2), pp. 423–434. ISSN: 0010-7999, 1432-0967. DOI: 10.1007/s00410-013-0883-4.
- [241] A. P. Hitchcock. *aXis2000*.
- [242] B. Ravel. *Demeter*. url= <https://bruceravel.github.io/demeter/>.
- [243] B. Ravel and M. Newville. ATHENA, ARTEMIS, HEPHAESTUS: data analysis for X-ray absorption spectroscopy using IFEFFIT. *Journal of Synchrotron Radiation*. July 1, 2005, **12**(4), pp. 537–541. ISSN: 1600-5775. DOI: 10.1107/S0909049505012719.
- [244] D. Solomon et al. Carbon (1s) NEXAFS Spectroscopy of Biogeochemically Relevant Reference Organic Compounds. *Soil Science Society of America Journal*. 2009, **73**(73), pp. 1817–1830. ISSN: 0361-5995. DOI: 10.2136/sssaj2008.0228.
- [245] G. D. Cody et al. Soft X-ray induced chemical modification of polysaccharides in vascular plant cell walls. *Journal of Electron Spectroscopy and Related Phenomena*. Mar. 2009, **170**(1), pp. 57–64. ISSN: 0368-2048. DOI: 10.1016/j.elspec.2008.09.007.
- [246] G. D. Cody. “Probing chemistry within the membrane structure of wood with soft X-ray spectral microscopy”. In: vol. 507. AIP, 2000, pp. 307–312. DOI: 10.1063/1.1291162.
- [247] C. Karunakaran et al. Introduction of Soft X-Ray Spectromicroscopy as an Advanced Technique for Plant Biopolymers Research. *PLOS ONE*. Mar. 26, 2015, **10**(3), e0122959. ISSN: 1932-6203. DOI: 10.1371/journal.pone.0122959.
- [248] G. D. Cody et al. Soft X-ray induced chemical modification of polysaccharides in vascular plant cell walls. *Journal of Electron Spectroscopy and Related Phenomena*. Radiation Damage. Mar. 2009, **170**(1), pp. 57–64. ISSN: 0368-2048. DOI: 10.1016/j.elspec.2008.09.007.
- [249] G. N. George et al. X-ray-induced photo-chemistry and X-ray absorption spectroscopy of biological samples. *Journal of Synchrotron Radiation*. Pt 6 Nov. 1, 2012, **19**, pp. 875–886. ISSN: 0909-0495. DOI: 10.1107/S090904951203943X.
- [250] A. Karlsson et al. The reduction of the Rieske iron–sulfur cluster in naphthalene dioxygenase by X-rays. *Journal of Inorganic Biochemistry*. Jan. 15, 2000, **78**(1), pp. 83–87. ISSN: 0162-0134. DOI: 10.1016/S0162-0134(99)00213-5.
- [251] C. Gervais et al. Radiation damages during synchrotron X-ray micro-analyses of Prussian blue and zinc white historic paintings: detection, mitigation and integration. *Applied Physics A*. Sept. 9, 2015, **121**(3), pp. 949–955. ISSN: 0947-8396, 1432-0630. DOI: 10.1007/s00339-015-9462-z.
- [252] M. M. v. Schooneveld and S. DeBeer. A close look at dose: Toward L-edge XAS spectral uniformity, dose quantification and prediction of metal ion photoreduction. *Journal of Electron Spectroscopy and Related Phenomena*. 2015, **Complete**(198), pp. 31–56. ISSN: 0368-2048. DOI: 10.1016/j.elspec.2014.12.001.
- [253] A. Meents et al. Reduction of X-ray-induced radiation damage of macromolecular crystals by data collection at 15K: a systematic study. *Acta Crystallographica Section D*. Mar. 1, 2007, **63**(3), pp. 302–309. ISSN: 1399-0047. DOI: 10.1107/S0907444906053261.

- [254] M. Warkentin and R. E. Thorne. Glass transition in thaumatin crystals revealed through temperature-dependent radiation-sensitivity measurements. *Acta Crystallographica Section D*. Oct. 1, 2010, **66**(10), pp. 1092–1100. ISSN: 1399-0047. DOI: 10.1107/S0907444910035523.
- [255] C. V. Smythe and C. L. A. Schmidt. Studies on the Mode of Combination of Iron with Certain Proteins, Amino Acids, and Related Compounds. *Journal of Biological Chemistry*. Jan. 8, 1930, **88**(1), pp. 241–269. ISSN: 0021-9258, 1083-351X..
- [256] R. H. H. Wolf et al. The influence of amphoteric polyelectrolyte gelatin on the formation of Cobalt(II), Nickel(II), Magnesium(II), Manganese(II), Iron(III) and Aluminium(III) hydroxide). *Colloid and Polymer Science*. July 1974, **252**(7), pp. 570–573. ISSN: 0303-402X, 1435-1536. DOI: 10.1007/BF01558154.
- [257] M. Helminger et al. Synthesis and Characterization of Gelatin-Based Magnetic Hydrogels. *Advanced Functional Materials*. June 1, 2014, **24**(21), pp. 3187–3196. ISSN: 1616-3028. DOI: 10.1002/adfm.201303547.
- [258] V. Rouchon et al. “Gelatine and iron gall ink corrosion”. IADA, 13<sup>th</sup> Congress. Berlin, 2015.
- [259] E. Jacobi et al. Rendering the Invisible Visible. *Journal of Paper Conservation*. 2011, **12**(2), pp. 25–34.
- [260] M. Qian, M. Liu, and J. W. Eaton. Transition Metals Bind to Glycated Proteins Forming Redox Active “Glycochelates”: Implications for the Pathogenesis of Certain Diabetic Complications. *Biochemical and Biophysical Research Communications*. Sept. 18, 1998, **250**(2), pp. 385–389. ISSN: 0006-291X. DOI: 10.1006/bbrc.1998.9326.
- [261] T. Beetz and C. Jacobsen. Soft X-ray radiation-damage studies in PMMA using a cryo-STXM. *Journal of Synchrotron Radiation*. May 1, 2003, **10**(3), pp. 280–283. ISSN: 0909-0495. DOI: 10.1107/S0909049503003261.
- [262] P. Bertrand. *La spectroscopie de résonance paramagnétique électronique-Fondements*. EDP Sciences, 2010. ISBN: 978-2-7598-0554-9.
- [263] P. Bertrand. *La spectroscopie de résonance paramagnétique électronique - Applications*. EDP Sciences, July 3, 2014. 441 pp. ISBN: 978-2-7598-1292-9.
- [264] E. G. Janzen, Y. Kotake, and H. Randall D. Stabilities of hydroxyl radical spin adducts of PBN-type spin traps. *Free Radical Biology and Medicine*. 1992, **12**(2), pp. 169–173. ISSN: 0891-5849. DOI: 10.1016/0891-5849(92)90011-5.
- [265] E. Levevre-Drouet and R. Betremieux. Amélioration d’une méthode de dosage colorimétrique de Fe(II) en présence de Fe(III) Importance des phénomènes de photoréduction. *Association française pour l’étude du sol*. 1984, pp. 213–224.
- [266] G. F. Lee and W. Stumm. Determination of Ferrous Iron in the Presence of Ferric Iron With Bathophenanthroline. *Journal (American Water Works Association)*. Dec. 1, 1960, **52**(12). ArticleType: research-article / Full publication date: DECEMBER 1960 / Copyright © 1960 American Water Works Association, pp. 1567–1574. ISSN: 0003-150X..

- [267] L. L. Stookey. Ferrozine—a new spectrophotometric reagent for iron. *Analytical Chemistry*. June 1, 1970, **42**(7), pp. 779–781. ISSN: 0003-2700. DOI: 10.1021/ac60289a016.
- [268] J. Im, J. Lee, and F. E. Löffler. Interference of ferric ions with ferrous iron quantification using the ferrozine assay. *Journal of Microbiological Methods*. Dec. 2013, **95**(3), pp. 366–367. ISSN: 01677012. DOI: 10.1016/j.mimet.2013.10.005.
- [269] M. J. AHMED and U. K. ROY. A simple spectrophotometric method for the determination of iron(II) aqueous solutions. *Turk J Chem*. 2009, **33**, pp. 709–726. DOI: 10.3906/kim-0802-9.
- [270] T. N. Kiran Kumar and H. D. Revanasiddappa. Rapid and sensitive spectrophotometric determination of trace amounts of iron(III) using leuco Xylene cyanol FF. *Analytical and Bioanalytical Chemistry*. Aug. 1, 2003, **376**(7), pp. 1126–1130. ISSN: 1618-2642, 1618-2650. DOI: 10.1007/s00216-003-2023-x.
- [271] C. D. Stalikas et al. Simple and Selective Spectrophotometric Method for the Determination of Iron (III) and Total Iron Content, Based on the Reaction of Fe(III) with 1,2-Dihydroxy-3,4-Diketocyclo-Butene (Squaric Acid). *Microchimica Acta*. June 1, 2003, **142**(1), pp. 43–48. ISSN: 0026-3672, 1436-5073. DOI: 10.1007/s00604-002-0950-4.
- [272] D. G. Karamanev, L. N. Nikolov, and V. Mamatarkova. Rapid simultaneous quantitative determination of ferric and ferrous ions in drainage waters and similar solutions. *Minerals Engineering*. May 2002, **15**(5), pp. 341–346. ISSN: 0892-6875. DOI: 10.1016/S0892-6875(02)00026-2.
- [273] F. Daumarie, P. Griesmar, and S. Salzard. *Florilège de chimie pratique*. Hermann, 1999. 282 pp. ISBN: 978-2-7056-6373-5.
- [274] O. L. Barak Morgan. The effect of pH on the kinetics of spontaneous Fe(II) oxidation by O<sub>2</sub> in aqueous solution—basic principles and a simple heuristic description. *Chemosphere*. 2007, **68**(11), pp. 2080–4. ISSN: 0045-6535. DOI: 10.1016/j.chemosphere.2007.02.015.
- [275] S. D. Aust, L. A. Morehouse, and C. E. Thomas. Role of metals in oxygen radical reactions. *Journal of Free Radicals in Biology & Medicine*. 1985, **1**(1), pp. 3–25. ISSN: 0748-5514. DOI: 10.1016/0748-5514(85)90025-X.
- [276] V. Vancova, G. Ondrejovic, and J. Gazo. Oxidation of triphenylphosphine in chloro-iron(III) complexes. *Chemicke Zvesti*. 1976, **30**(1), pp. 86–89.
- [277] C. Ercolani et al. Dioxygen activation and catalytic oxidation of triphenylphosphine by iron phthalocyanine compounds. *Journal of Molecular Catalysis*. May 1985, **30**(1), pp. 135–144. ISSN: 0304-5102. DOI: 10.1016/0304-5102(85)80023-7.
- [278] J.-M. Noël. *Analyse dynamique de surfaces fonctionnelles par électrochimie localisée*. Rennes 1, 2011.
- [279] B. Laboratories. *AG 50W and AG MP-50, cation exchange resins Instruction manual*. Url: <http://www.bio-rad.com/webroot/web/pdf/lsr/literature/9118AG50.pdf>.



# List of Figures

I.1	3-D representation of cellulose macromolecule. . . . .	6
I.2	Cellulose arrangement in parallel layer. . . . .	7
I.3	Cellulose arrangement in cristalline and amorphous regions. . . . .	7
I.4	(A) Representation of morphological structure of a cotton fiber and B Scanning electron microscopy images of Whatman paper I. . . . .	7
I.5	Water vapor sorption (in black) and desorption (in blue) curves of What- man paper upon humidity exposure. The red curve represents the BET model. . . . .	8
I.6	Water arrangements between cellulose chains depending on relative hu- midity (adapted from [16]. . . . .	9
I.7	Typical structure of gelatin. . . . .	10
I.8	Iron gall ink main composition. . . . .	11
I.9	Raspberry ellagotannins. . . . .	12
I.10	Iron gall ink complex formation according to Krekel [36]. Note the release of two protons in step 1. . . . .	13
I.11	Structure and partial charge of the iron gallate complexe proposed by Ponce et al. [40]. . . . .	14
I.12	Manucripts corroded by iron gall ink. . . . .	15
I.14	Steps of progression in degradation of a manuscript by iron gall ink ac- cording to Reissland[52]. . . . .	16
I.15	Acid catalyzed hydrolysis of cellulose. . . . .	17
I.16	Sites of possible oxidation on cellulose[91]. . . . .	18
I.17	Cellulose autoxidation adapted from [97]. I stands for an initiator. . . . .	20
I.18	Radical oxidation of carbohydrate (black scheme)and the impact of iron and Fenton reaction (blue scheme). . . . .	20
I.19	Hydroxyl radical attack at the anomeric carbon during delignification pro- posed by Guay et al.[101]. . . . .	21
I.21	The Fenton-Hamilton hypothesis [48]. . . . .	23
II.1	Iron oxo species formation [122]. . . . .	27
II.2	Monitoring of model ink pH with time (black circle). Red circle represents pH of gallic acid solution. . . . .	29
II.3	The spin-trapping of hydroxyl radicals by DMPO: (A) reaction of spin- trapping and (B) protocol 1. . . . .	31
II.4	Detection of electrophilic species with DMPO and sodium formate:(A) reaction of the electrophilic specie with formate, (B) reaction of spin- trapping and (C) protocol 2. . . . .	32

II.5	Scheme of ESR spectrometer principle. . . . .	33
II.6	(A) JEOL <i>FA</i> – 300 series ESR spectrometer and (B) JEOL quartz flat cell. . . . .	34
II.7	Hydroxyl radicals detection on paper samples: (A) reaction of terephthalic acid (TPA) hydroxylation and (B) protocol for hydroxyl radicals detection on paper. . . . .	35
II.8	Agilent 1100 series HPLC system. . . . .	35
II.9	(A) Typical ESR signals of Ink-P <sub>7</sub> solutions in presence of DMPO alone (top) or used in combination with formate (bottom) and schemes of the related expected DMPO – OH• and DMPO – COO• <sup>-</sup> radical adducts, if present; (B) Typical evolution with time of the DMPO – COO• <sup>-</sup> signal intensity (taking as example the Ink-P <sub>7</sub> solution after 60 min of mixing). . . . .	37
II.10	Typical ESR signals of Ink-P <sub>7</sub> solutions in presence of POBN alone (top) or used in combination with formate (bottom) and schemes of the related expected POBN – OH• and POBN – COO• <sup>-</sup> radical adducts, if present. . . . .	37
II.11	HTPA concentrations (normalized with respect to paper weight) detected by HPLC upon ageing of a blank paper (cross) and paper impregnated with Ink (full circle) or Fe2 (empty circle). . . . .	38
II.12	Evolution with paper ageing of ESR measurements (A), degree of polymerization (B) and proportion of ferrous iron (C). (A) DMPO – CO <sub>2</sub> • <sup>-</sup> concentrations determined by ESR on ink-P <sub>y</sub> solutions following protocol 2. Values are normalized with respect to paper weight; (B) Viscosimetry measurements; (C) XANES measurements at the Fe K-Edge (from Rouchon et al.[111]). Inked (full circle) or Fe2 impregnated papers (empty circle). . . . .	41
II.13	Solid-state ESR spectra recorded at room temperature (a,b) and at 77 K (c-f) before (plain lines) and after (dotted lines) water washing. Red (a,b) and blue curves (e,f) correspond to Fe2-P <sub>21</sub> sample and black curves (c,d) to Fe2-P <sub>1</sub> sample. . . . .	43
II.14	DMPO – CO <sub>2</sub> • <sup>-</sup> adducts concentrations versus initial iron II sulfate concentration in Fe2-M <sub>z</sub> (empty circle) and Ink-M <sub>z</sub> (full circle) solutions. . . . .	45
II.15	Final pH versus initial <i>Fe<sup>II</sup></i> concentrations in the Ink-M <sub>z</sub> (full circle) and Fe2-M <sub>z</sub> (empty circle) solutions studied by ESR with protocol 2, and in the Fe2-M <sub>z</sub> solution analyzed according to protocols 3 (full triangle) and 4 (empty triangle). . . . .	46
	47figure.caption.51	
	47figure.caption.52	
III.1	Arrhenius plot of (A) DP measurements and (B) zero-span measurements. Samples of paper impregnated with Ink are represented with black filled circle and those imprgenated with Fe2 with red cross. . . . .	57
III.2	Attenuated total reflectance FTIR spectroscopy: (A) NICOLET 6700 FTIR spectrometer (Thermo Scientific) equipped with a diamond ATR module and (B) ATR principle. . . . .	59
III.3	Infrared spectra of Pwd_Fe2_Ink_ratio2.6 sample before (green spectrum) and after (red spectrum) ageing one week at 80 °C. . . . .	60

---

III.4	X-rays powder diffraction of cellobiose sample freeze-dried and kept one week under: (A) 50 % relative humidity or (B) 0 % relative humidity in P <sub>2</sub> O <sub>5</sub> with the protocol [196]. . . . .	61
III.5	SEM observation of Pwd_Fe2_Ink_ratio3 after ageing. . . . .	62
III.6	Experimental set-up for cellobiose degradation study. . . . .	65
III.7	Capillary electrophoresis principle. . . . .	66
III.8	Steps of the protocol for sugar analysis: (A) derivatization of the sugar, (B) then analysis on the P/ACE™ MDQ instrument from Beckman Coulter. . . . .	67
III.10	Monitoring of (A) cellobiose concentration and (B) pH in samples solutions at pH3.6. Orange curves represent sulfuric acid mixture with (plain lines) or without (dotted lines) oxygen. Grey curves represent iron (II) sulfate mixture with (plain lines) or without (dotted lines) oxygen. . . . .	71
	71figure.caption.73	
III.12	Evolution of (A) pH and (B) iron concentrations in the Fe2_pH1.6_O <sub>2</sub> sample versus ageing time. Soluble iron(II) and iron(III) are monitored by UV-vis spectroscopy. Concentrations are normalized with respect to initial amount of iron. . . . .	72
	73figure.caption.77	
III.14	Monitoring of cellobiose concentration (in blue) and glucose yield (in red) in (A) Fe3_pH1.6_O <sub>2</sub> and (B) Ink_pH2_O <sub>2</sub> samples. . . . .	73
III.15	Evolution of (A) pH and (B) iron concentrations of Fe3_pH1.6_O <sub>2</sub> sample versus ageing time. Soluble iron(II) and iron(III) are monitored by UV-vis spectroscopy. Concentrations are normalized with respect of initial amount of iron. . . . .	74
III.16	ATR-IRTF spectra of H <sub>2</sub> SO <sub>4</sub> _pH1.6_O <sub>2</sub> before ageing (green curve) and after seven days of ageing (red curve). . . . .	75
	75figure.caption.81	
III.18	Deconvolution of the infrared spectra of the Fe2_pH1.6_O <sub>2</sub> sample in component peaks (A) before and (B) after 15 days of ageing and (C) follow-up of absorption peaks at 1729 cm <sup>-1</sup> and 1775 cm <sup>-1</sup> . . . . .	77
III.19	Molecules formation from degradation pathways of glucose in acidic medium [76]. . . . .	78
III.20	Analysis of organic acids in Fe2_pH1.6_O <sub>2</sub> by capillary electrophoresis. . . . .	78
III.21	Mass spectra obtained in positive ion mode of Fe2_pH1.6_O <sub>2</sub> (top) and H <sub>2</sub> SO <sub>4</sub> _pH1.6_O <sub>2</sub> samples (bottom) after seven days of ageing. In green are represented adducts of cellobiose and in red adducts of glucose. . . . .	80
IV.1	Picture and infrared microscopy maps of the cross-section of a paper impregnated with gelatin and embedded in a resin: (A) Infrared mapping of resin, gelatin and cellulose (one pixel=10 μm×10 μm, dark regions correspond to high absorption); (B) Characteristic infrared spectrum; (C) gelatin concentration profile [218]. . . . .	84
IV.2	Moulin du Verger Papermill [221]. . . . .	85
IV.3	Water adsorption properties of Whatman paper sized with gelatin solution of different concentrations. The absorption time corresponds to the time necessary for a 0.1 μL drop of water to be absorbed by the paper [49]. . . . .	86

---

---

IV.4	Evaluation of water absorption time of <i>Brejoux</i> papers impregnated with 4 % <i>gelatin K</i> and washed different duration in a water bath. . . . .	88
IV.5	Ultramicrotome LEICA EM UC6 of IPANEMA, Saclay. . . . .	89
IV.6	Protocol of fiber preparation for ultramicrotomy cross-section process: (A) preparation of the sample bloc;(B) cutting of the sample bloc;(C) thin cross-sections cutting with a diamond knife; (D) Cross-section deposit onto an ZnSe prism. . . . .	90
IV.7	FIB of the Institut d'Electronique, de Microelectronique et de Nanotechnologies, Lille. . . . .	90
IV.8	Protocol of fiber preparation and FIB cross-section process: (A) deposit of the fiber on a silicium wafer; (B) platinumium deposit on the fiber; (C) FIB cutting of the cross-section with trenches on each side of the foil;(D) Raw fiber cross-section obtained by FIB. (E) FIB foils on the two wide posts in V-shaped of the lift-out grid, on which letters A to C serve as marks to locate the sample. Red circles highligh two FIB foils. . . . .	91
IV.9	Structure of a fiber cross-section. . . . .	91
IV.10	Observation of <i>Verger</i> paper fibers with an optical microscope, showing fibers in good condition (green arrows) and defibrilated fibers (red aarrows). 91	
IV.11	SEM image of a well preserved fiber (A) and of a defibrillated fiber (B) extracted from <i>Verger</i> paper. . . . .	92
IV.12	AFM topography images of the cross-sections of a <i>gel<sub>4</sub> fiber</i> and of a <i>79/9 fiber</i> obtained by ultramicrotomy. . . . .	92
IV.14	Description of the AFM-IR technique. . . . .	94
IV.15	Pictures of (A) the CLS experimental floor [225] and of (B) the SM beamline. 95	
IV.16	(A) Picture and (B) scheme of the STXM experimental setup showing the position of the sample and of the focusing and detecting tools in the SM end station. . . . .	96
IV.17	(A) XANES absorption edges of typical organic compounds and (B) electronic transitions at the origin of the spectrum. . . . .	96
IV.18	Scheme of a STXM stack recorded at the C K-edge on an enlarged region (black square) of a fiber cross-section (SEM sample image). Maps of the enlarged zone are recorded while scanning in energy. The green and red spectra correspond to data extracted from all the maps in the green and red regions, respectively. . . . .	98
IV.19	C K-edge spectra of cellulose and gelatin model compounds. . . . .	100
IV.20	C K-edge spectra of ink components. . . . .	101
IV.21	N K-edge spectrum of gelatin. . . . .	103
IV.22	Fe L-edge spectra of iron(II) and iron(III) references, in yellow and blue, respectively. . . . .	103
IV.23	Iron reduction test on “ink <sub>O</sub> +gum drop”: evolution of OD with (A) the time of exposure and (B) with the dose. . . . .	104

---

IV.26	C K-edge STXM mapping of $gel_{1.5}$ and $gel_4$ fibers, enlarged area of analysis (yellow squares, top images) and regions of spectra extraction (dashed zones). Related C K-edge RGB compositionnal maps obtained from comparison with gelatin and <i>raw fiber</i> reference spectra. Red represents cellulose (region with spectra matching mostly raw fiber reference spectra) and green gelatin (region with spectra matching mostly gelatin reference spectra). Blue represents region of the metal coating and also regions where residual components of the fit is high. . . . .	110
IV.28	N K-edge extracted spectra from $gel_{1.5}$ fibers. The colours of the spectra correspond to those of the regions chosen for spectra extraction (dashed zones in FIG. IV.26). . . . .	111
IV.29	Iron penetration in $ink_R$ fiber. Top image correspond to SEM image of the cross-section. The three other images are Fe L-edge STXM mappings of iron distributions: iron(II), iron(III) and total iron, respectively from top to bottom. . . . .	113
IV.31	Fit of the spectrum extracted from an iron dot using the linear regression analysis of the Axis2000 software as done for the entire stack with the stack fit option. . . . .	115
IV.32	Spectra extracted from inked-fiber Fe L-edge stacks (dashed areas). The spectra colors correspond to those of the dashed areas. On the left are represented raw spectra and on the right normalized spectra. . . . .	115
IV.33	Spectra obtained on $ink_R$ fiber at C K-edge. The spectra colors correspond to those of the dashed areas of FIG. IV.32. . . . .	116
IV.34	Images of $gel_4+ink_R$ fiber. Top image correspond to SEM image of the cross-section. The two other images are Fe L-edge STXM mappings of iron distributions: iron(II) and iron(III), respectively from top to bottom. . . . .	117
IV.35	Comparison of Fe and C edges maps of an enlarged area of $gel_4+ink_R$ fiber and repartition of ink ingredients. On the RGB compositionnal maps, regions in blue and in yellow are rich in iron(III) and iron(II), respectively. Red and green areas represent regions matching cellulose and gallic acid references, respectively. No signal is detected at the N K-edge. . . . .	118
IV.36	Comparison of Fe L-edge spectra recorded in different regions of the $gel_4+ink_R$ fiber. The spectra colors correspond to those of the dashed areas. On the left are represented raw spectra and on the right normalized spectra. . . . .	119
IV.37	Comparison of C K-edges spectra recorded in different regions of the $gel_4+ink_R$ fiber. The spectra colors correspond to those of the dashed areas of FIG. IV.36. . . . .	119
IV.38	N K-edge spectrum extracted from inked regions c and d in an enlarged area of the $gel_4+ink_R$ fiber (see FIG. IV.36). . . . .	120
IV.39	Comparison of Fe(III) and gallic acid distribution on the enlarged area of $gel_4+ink_R$ fiber. . . . .	120
IV.40	Comparison of Fe K-edge spectra on the $ink_R$ fiber and $gel_4+ink_R$ fiber. . . . .	121
IV.41	Comparison of N, C and Fe K-edges maps on $ink_R+gel_4$ fiber. . . . .	122
IV.42	Comparison of N, C and Fe K-edges maps on $ink_R+gel_4$ fiber. Gelatin is represented in green and located in the central part of the image. Cellulose is showed in red and the iron gall ink precipitate in blue. . . . .	123

IV.43	Comparison of Fe L-edge spectra extracted from the dashed areas on ink <sub>R</sub> + gel <sub>4</sub> fiber. The spectra colors correspond to those of the dashed areas. . . . .	124
IV.44	Comparison of C K-edge spectra on ink <sub>R</sub> + gel <sub>4</sub> fiber. The spectra colors correspond to those of the dashed areas of FIG. IV.43. . . . .	124
IV.45	Component maps of ink <sub>R</sub> + gel <sub>4</sub> fiber obtained with a stack fit at C K-edge using extracted spectra. . . . .	125
IV.46	Scheme of fiber cross-section, and its behaviour upon ink impregnation depending on the fiber type (sized or unsized). Effect of gelatin application on the diffusion of iron in an inked fiber. . . . .	126
B.1	a) Splitting of energy levels of a paramagnetic specie with $S = \frac{3}{2}$ and evolution with B magnetic field. b) Formation of an absorption signal at the field of resonance $B_0$ . Adapted from [262]. . . . .	140
	adduct due to hyperfine coupling leading to lines splitting. 141figure.caption.140	
B.3	Main artefact reactions with spin-trapping: (A) Forrester-Hepburn mechanism, (B) inversed spin-trapping and (C) DMPO adduct decomposition after superoxide trapping. . . . .	142
B.4	Scheme of decomposition reaction of POBN – OH• adduct leading to formation of MNP spin-trap, which could also decompose into tert-butyl hydroaminoxyl radical. . . . .	143
B.5	Spectra of POBN – OH• after 2 min mixing with H <sub>2</sub> O <sub>2</sub> . . . . .	143
B.6	Decomposition of DMPO – OH• adducts in hydroxylamine (left) and nitron (right). . . . .	144
C.1	Flask for iron(II) quantification. . . . .	148
C.2	Calibration curve for iron(II) quantification. . . . .	148
C.3	Monitoring of spectra evolution with various molar SCN-/Iron(III) ratio. . . . .	149
C.4	Flask for iron(III) quantification. . . . .	150
C.5	Calibration curve for Iron(III) quantification. . . . .	150
D.1	Pourbaix diagram of iron species $1 \cdot 10^{-2} \text{ mol} \cdot \text{L}^{-1}$ . . . . .	151
D.2	Impact of pH on the oxidation kinetic of total iron(II) species in infinite dilution (adapted from [274]). . . . .	152
D.3	Impact of the medium on the oxidation kinetic of iron(II) sulfate solution at $1 \text{ mmol} \cdot \text{L}^{-1}$ . Blue, red and green curves represent water, (4 mol · L <sup>-1</sup> ) formate solution and phosphate buffer, respectively. . . . .	152
D.4	Effect of the iron concentration on iron oxidation in 4 mol · L <sup>-1</sup> formate solution. Blue, red and green curves represent iron sulfate solution at 10 mmol · L <sup>-1</sup> , 1 mmol · L <sup>-1</sup> and 0.1 mmol · L <sup>-1</sup> , respectively. . . . .	153
E.1	Reaction of Triphenylphosphine (TPP) with peroxides. . . . .	155
E.2	Calibration curve for TPPO quantification. . . . .	156
F.1	Calibration curve for HTPA quantification. . . . .	157
G.1	Cyclic voltametry of Fe <sup>III</sup> Cl <sub>3</sub> at $1 \text{ mmol} \cdot \text{L}^{-1}$ , HCl $100 \text{ mmol} \cdot \text{L}^{-1}$ . . . . .	160
G.2	Principle of the experiments carried out with SECM. . . . .	160
G.3	Typical approach curves obtained with a conductive (red) or non conductive (green) surface [278]. . . . .	161

---

G.4	Approach curve obtained before and after oxygen reduction (300 pulses of one second) in a solution of Fe(II) 50 mL, and HCl 100 mL). . . . .	162
	162figure.caption.165	
G.6	Observations of one fiber after 20 reductions in a Fenton system. The red arrow show the region of analysis in (A) optical microscopy and (B) SEM.	163
I.1	Calibration curve of (A) cellobiose and (B) glucose. . . . .	175
K.1	$\ln(Dmg - Dmg_{\infty})$ versus dose $D$ for the peak at 707.8 eV. . . . .	182
K.2	$\ln(Dmg - Dmg_{\infty})$ versus dose $D$ for the peak at 709.8 eV. . . . .	182
1	Les espèces réactives de l'oxygène en jeu dans la corrosion du papier par les encres ferrogalliques ne sont pas des radicaux hydroxyles. . . . .	187
2	Schema des coupes transversales de fibres de papier et leur comportement après imprégnation encre selon le type de fibre (encollée ou non). Effet de la gélatine application on the diffusion of iron in an inked fiber. . . . .	191



# List of Tables

I.1	Main composition of cotton, flax, hemp and wood [7]. . . . .	6
I.2	Litterature review of nitrogen and water sorption by cellulosic substrates. . . . .	8
I.3	Composition of iron gall ink precipitate (adapted from Ponce, Gaskell, and Brostoff [39]) . . . . .	13
II.1	Protocols and compositions of the mixed solutions used for the ESR analyses (the total analyzed volume is 2 mL in each protocol). . . . .	32
II.2	Concentration of $\text{DMPO} - \text{CO}_2^-$ adducts in solution samples as estimated from ESR measurements carried out with protocol 2. Reported values are average values of 3 samples with standard deviations. <i>n.d.</i> : no detected signal. . . . .	39
II.3	Iron quantification in leaching solutions as determined by UV/VIS spectroscopy (precision $\pm 0.05$ ). . . . .	42
III.1	Activation energies from several published data. Values from experiments obtained on cellobiose solutions are added for comparison with the values obtained for other cellulosic solids. . . . .	56
III.2	Description of cellobiose solid samples preparation. . . . .	58
III.3	Coding of the three factors studied. . . . .	63
III.4	Trial matrix. Fe stands for total iron, Ar for argon bubbling and $\text{O}_2$ for oxygen bubbling. . . . .	63
III.5	Matrix of the model ( $X$ ), vector of the response $Y$ and vector $A$ of the $a_x$ coefficients. . . . .	64
III.6	Description of samples for cellobiose degradation prepared according to the trial matrix. . . . .	65
III.7	Additional samples. . . . .	65
III.8	Changes observed during ageing of cellobiose samples. . . . .	70
III.9	Main peaks found on mass spectra of $\text{Fe2\_pH1.6\_O}_2$ and $\text{H}_2\text{SO}_4\text{\_pH1.6\_O}_2$ samples . . . . .	79
III.10	(A) <i>Response matrix of normalized cellobiose concentration at 10 days and (B) factors of the first order model for minimal [cellobiose]</i> . . . . .	81
IV.1	Description of fibers samples and model compounds. Except powders, all samples are cut in thin cross-sections. . . . .	87
IV.2	Main energy values at C (K), N (K) and Fe (L) edges. . . . .	97
C.1	Main quantification techniques of iron(II) described in litterature . . . . .	146
C.2	Main quantification techniques of iron(III) described in litterature. . . . .	147

---

E.1	Description of samples preparation for cellobiose degradation. . . . .	156
G.1	Description of samples preparation for cellobiose degradation. . . . .	162
J.1	Monitoring of iron elimination. . . . .	178
K.1	Parameters used to convert exposure time to dose. . . . .	180
K.2	Doses calculation at one energy. . . . .	180
K.3	Doses calculation and damage estimation. . . . .	181
K.4	Parameters used for recording of stacks at iron edge. . . . .	183
K.5	Parameters used for recording of stacks at carbon edge. . . . .	183
K.6	Parameters used for recording of stacks at carbon edge. . . . .	183



---

## Comprehension of cellulose depolymerisation mechanisms induced by iron ions

---

**Abstract :** Degradation of paper by iron gall inks (IGI) is a challenging issue for written heritage conservation. These inks consist of a mixture of iron(II) sulphate, tannins and gum Arabic, and are therefore acidic and iron-rich. Hence, paper degradation by IGI is often attributed to a combination of acid hydrolysis and of iron-catalyzed oxidation involving hydroxyl radicals ( $\text{HO}^\bullet$ ) formed by Fenton reaction. Nevertheless, which of these two mechanisms prevails on cellulose depolymerisation remains a largely open question, which is addressed in the present work.

The first step was to look at reactive oxygen species (ROS), especially  $\text{HO}^\bullet$ , by trapping reactions coupled with ESR and HPLC. Traces of  $\text{HO}^\bullet$  were identified on some samples, but their presence was not consistent with paper damage. Another type of ROS was detected in higher quantity, but correlated more to oxidation of iron leached species rather than to paper decay itself.

The determination of depolymerisation kinetics at different temperatures led, on inked papers, to activation energies only slightly below those obtained on acidic papers, suggesting a dominant acid hydrolysis mechanism with a limited catalytic effect of iron. This is also supported by the detailed study of the respective effects of iron, oxygen and pH towards degradation of cellobiose taken as a model molecule. This approach gave evidence that acidification of the solution during iron oxidation is the driving force for glycosidic bond cleavage. To reach this pH, localized iron spots have to be present in the paper as was indeed confirmed by the STXM nano-imaging technique that allowed mapping the distribution of ink components and gelatin within a paper fiber.

**Keywords :** Cellulose, iron, radicals, acid-catalyzed hydrolysis, oxidation

---

## Compréhension des mécanismes de dépolymérisation de la cellulose induits par les ions fer

---

**Résumé :** La dégradation du papier par les encres ferrogalliques (EFG) est un défi important pour la conservation du patrimoine écrit. Ces encres, composées d'un mélange de sulfate de fer (II), de tannins et de gomme Arabique, sont acides et riches en fer. Par conséquent, les mécanismes de dégradation des manuscrits par les EFG proposés dans la littérature combinent souvent hydrolyse acide et oxydation radicalaire catalysée par le fer, celle-ci impliquant la formation de radicaux  $\text{HO}^\bullet$  par réaction de Fenton. Le mécanisme prédominant reste cependant une question encore largement ouverte, qui est au coeur de ce travail de thèse.

Dans un premier temps, l'étude cherchait à identifier les espèces réactives de l'oxygène (ERO) par RPE et HPLC, en particulier les radicaux  $\text{HO}^\bullet$ , détectés sur certains échantillons mais en faible quantité et sans corrélation avec la dégradation du papier. La formation d'autres ERO a par contre été mise en évidence, mais reliée à l'oxydation de fer libéré en solution plutôt qu'à la dégradation même du papier.

La détermination des cinétiques de dépolymérisation à différentes températures a conduit à des énergies d'activation proches sur papier encré et sur papier acide, suggérant une prédominance du mécanisme d'hydrolyse acide dans les deux cas. Ceci est confirmé par l'étude des effets de l'oxygène, du pH et du fer sur la dégradation d'une molécule modèle, la cellobiose, qui révèle que la coupure de la liaison glycosidique est liée à l'acidification du milieu lors de l'oxydation du fer. L'atteinte de tels pH acides au sein du papier suppose une présence localisée du fer, effectivement confirmée par des mesures de la distribution des éléments de l'encre et de la gélatine dans une fibre de papier par nanomicroscopie STXM.

**Mots clés :** Cellulose, fer, radicaux, hydrolyse acide, oxydation